upna Universidad Pública de Navarra Nafarroako Unibertsitate Publikoa

NEUTRONS FOR SOCIETY

Influence of microstructure in the martensitic transformation and in the physical and magnetic properties in metamagnetic shape memory alloys

Memory presented by:

Javier López García

Supervisors:

Vicente Recarte Callado

José Alberto Rodríguez Velamazán

Acknowledgments

This thesis was carried out with the support of institutions as Institut Laue-Langevin (ILL), which financed my contract during this three years, and Public University of Navarra as academic institution, and also a lot of people that I would like to acknowledge in the following lines.

First of all, I want to thank my thesis directors, José Alberto Rodríguez Velamazán and Vicente Recarte, for the opportunity they have given to me to work in this project. Above all, I would like to highlight the great accessibility and dedication they have shown and the trust placed in me throughout the thesis, showing their great human quality, making working with them a pleasure. Likewise, I would like to thank Iñaki Pérez de Landazábal and Vicente Sánchez Alarcos that, as part of the research group, have shown great availability by providing a critical view of the project, the experiments and the publications.

On the other hand, to thank Iraultza Unzueta, Jose Ángel García and Ferrnando Plazaola of the University of the Basque Country (UPV / EHU), a group that has worked hand in hand with me in the synthesis and treatment of samples and in the characterization using Mössbauer spectroscopy.

In addition to thanking the ILL for the phD contract, I cannot forget all my fellow students that I have met in Grenoble, especially my colleagues Stass, Joao, Gaynor, Quentin (little fights for the leg gap) with which the disconnected chats in the office made it a very friendly place to work. Special mention deserves Lidia Mazzuca, who helped me to integrate both in the group of students and in the life in Grenoble and with whom we became united by a great friendship at the end of these three years. The "Spanish community" was growing with the arrival of Palmerina, Javier Murias, Ángel and María Pedrosa with whom the talks at the time of rest helped to change the chip and even to de-stress from the long days of work; I think we have not left any topic that we have not talked about in our bench. Finally, the life in Grenoble would not have been the same if I had not met a great scientist like my Polish friend Rafał Wawrzyńczak (after three years I still do not know how to pronounce your family name) with whom, in addition to discussing the problems that arose during the thesis, the hours spent in the D'enfer on Fridays combining beer and pool evaded us from the problems of the week and allowed beginning the weekend with joy.

Outside the scientific field, although I met him at the ILL, I wanted to thank Willy, my fatigue partner on the bike, for the great moments (and especially the bad times) that we have spent touring the mountains of Grenoble preparing for the Marmotte. Beatings shared with other great cyclists like Pablo and Thomas. Furthermore, I have to acknowledge the football team “Los Latinos” for welcoming me in this great team where I had the opportunity to improve my poor French and win the local league. In this team I had the opportunity to meet another good

friend, Jesús Pavón, with whom I spent really good times playing indoor football and knowing more about Grenoble and their places, growing in this way a good friendship and what we can call the iberic-italian group also formed by Cinzia De Cesare and Marta Crisanti.

On the other hand, I remember many people in Pamplona that I can not forget to acknowledge them. Starting for the people that I shared office with, as Adrián and Isaac among others. Specially, I have to present my acknowledgement to Jesús Beato who made my stay in Pamplona much easier by introducing me in such an amazing group of people "Tercio Stalker" where I had the opportunity to meet good people and know more about the night of Pamplona, renaming some of its streets.

Cambiamos de idioma para agradecer a esas otras personas que posiblemente no dominen el inglés. Empezar este agradecimiento a toda la cuadrilla de Cruces/Zorroza, amigos con los que he crecido y compartido toda mi vida y que me han mostrado su apoyo durante toda la tesis, aunque no acabo de estar seguro si alguno ha llegado a entender lo que hago.

También agradecer los ánimos recibidos por otro gran grupo de amigos desde hace mucho tiempo en Pedrosa de Río Úrbel, gente con la que he crecido desde bien pequeño y que siempre han estado al pie del cañón animando y aguantándome a partes iguales. Por otro lado, también pertenecientes a este pequeño pueblo de la provincia de Burgos, agradecer a Rodrigo y Blanca todo el interés y el apoyo mostrado durante estos tres años y esa visita medio inesperada a Grenoble.

Volviendo al norte de la península, mostrar mi agradecimiento a la familia Hérnandez-Mejía, familia con la que he compartido gran parte de mi vida y algunos que otros malos momentos pedaleando bien desde Bilbao hasta Burgos o por las interminables subidas de los Alpes franceses. Agradecer también a sus hijas Sara y Ester destacando sus palabras de aliento durante la parte final de la tesis.

Por otro lado, no me puedo olvidar de Janire Escolar por los años que hemos pasado juntos y el apoyo y ayuda ofrecida durante los años de tesis, carrera y máster.

Por último, pero no por ello lo último, sino todo lo contrario, agradecer a toda mi familia por el apoyo mostrado, desde mi abuela, que aún me sigue preguntando por el colegio, pasando por mis tíos Juanjo y Tomás y por supuesto mis padres y mi hermano, que no ha habido un día en el que no me hayan animado a seguir trabajando y peleando para llegar al objetivo final.

Summary

Ferromagnetic shape memory alloys have raised substantial interest from both fundamental and applied points of view, due to the unique properties they show related to the occurrence of a first-order structural transformation – the martensitic transformation – between magnetically ordered phases. In particular, in Ni-Mn-Z (Z=In, Sn, and Sb) Heusler alloys, the so-called metamagnetic shape memory alloys, the transformation takes place between a ferromagnetic austenite and a weakly magnetic martensitic phase, in such a way that a large magnetization drop occurs at the martensitic transformation. This allows the induction of the martensitic transformation by an applied magnetic field, thus giving rise to multifunctional properties (namely giant magnetoresistance, magnetic shape memory effect and large inverse magnetocaloric effect) of great technical interest for practical applications, like sensing or magnetic refrigeration. The transformation temperatures, the magnetization of the different structural phases, the entropy change associated to the martensitic transformation and, in general, all the magnetostructural features giving rise to those functional properties depend on the composition, the structure and the microstructure of the alloys. The compositional dependence has been deeply studied in ferromagnetic shape memory alloys, being directly related to the electronic concentration. Variations in the composition like doping with different magnetic atoms (cobalt doping, in particular) have shown a strong influence in the magnetism of these materials. Also, the effect of the atomic order has been thoroughly analyzed in several previous works and shown to be a parameter of great influence to tune the magnetostructural properties of this kind of systems, although some metamagnetic shape memory alloys present an extraordinary high stability of the atomic order. The role of the microstructure, in turn, has been less investigated, in spite of its potential for tuning the magnetostructural properties of these systems, in particular as a suitable alternative in cases with highly stable atomic order. Therefore, in this work we have focused in the study of the influence of the microstructure in metamagnetic shape memory alloys (Ni-Mn-In and Ni-Mn-Sn systems) together with the effect of Co-doping, in order to gain insight into these effects and to control and improve the properties of these materials.

Ni-Mn-In and Ni-Mn-Sn ternary alloys, and the corresponding quaternary (Co-doped) alloys have been prepared and subsequently subjected to thermo-mechanical treatments (hand milling, ball milling, and thermal annealing at different temperatures) in order to modify their microstructure in a controlled way. The alloys have been characterized macroscopically by calorimetric and magnetic measurements, and studied at the microscopic level mainly through X-ray and neutron diffraction, which provided us information about the crystal structures, the atomic order in the alloys, the microstructural parameters as grain size and internal strains and the magnetic structures. The combination of the results obtained in the microscopic study with the calorimetric and magnetic macroscopic characterization allowed us to gain a better understanding of the role of the microstructure and cobalt doping in the magnetostructural properties of these metamagnetic shape memory alloys and identify routes to obtain improved functional properties.

Starting with the ternary Ni-Mn-Sn system, we have stablished the correlation between microstructural parameters and magnetostructural properties in these alloys. We have characterized the different microstructural states induced by thermo-mechanical treatments and correlated them with the properties of the alloys (in particular, the magneto-caloric effect). First, we have used laboratory X-rays diffraction to obtain the microstructural parameters of a $Ni_{50}Mn_{35}Sn_{15}$ alloy subjected to different thermal treatments after hand-milling, and we have related the defects on the sample with the internal strains state induced by the milling and annealing processes. Then, powder neutron diffraction has been used to determine the crystal and magnetic structures of the alloys, allowing relating the magnetocaloric effect with the magnetic coupling. Finally, the magnetic characterization of the set of samples was completed by Mössbauer spectroscopy, showing also the suitability of this technique for microstructural characterization.

The cobalt-doped quaternary system, Ni-Co-Mn-Sn-Co has been the next subject of study. We have determined the magnetostructural properties in milled and in annealed samples of the in $Ni_{45}Co_5Mn_{35}Sn_{15}$ alloy, showing an improvement of the magnetostructural properties by Co addition, related with a change in the magnetic coupling of the Mn atoms, and an unconventional improved magnetocaloric effect in a soft-milled alloy. Therefore, the presence of a small amount of defects affects in a different way to the ternary and quaternary alloys: while in the Ni-Mn-Sn system the introduction of defects such as vacancies or antiphase boundaries reduces the entropy change associated to the martensitic transformation, the effect is opposite in Ni-Co-Mn-Sn. This unusual result incited further investigation of the effect of milling, with a systematic study on the microstructure by synchrotron X-rays powder diffraction in ball-milled samples, showing the evolution of the microstructural parameters and the magnetostructural properties with the milling time. The increase of the milling time produces amorphization of the material and induces the martensitic phase, reducing in this way the amount of austenite with martensitic transformation and decreasing the enthalpy associated to the transition. Moreover, neutron powder diffraction has shown that the magnetic structure in austenite remains ferromagnetic upon milling but with a significant decrease of the ordered magnetic moments.

With the aim of obtaining further understanding of the effect of Cobalt doping the magnetic coupling, we have selected the Ni-Mn-In system as case study. $Ni_{50}Mn_{34}In_{16}$ and $Ni_{45}Co_5Mn_{37}In_{13}$ alloys with two different thermal treatments were macroscopically characterized by magnetometry and calorimetry measurements and the atomic order and magnetic structures studied by neutron diffraction. It has been shown the variation in the Curie and martensitic transformation temperatures due to the different thermal treatments and Co doping and, more relevantly, the increase produced in the saturation magnetization of the austenite phase, reaching ca. 60% when Co-doping and thermal treatment by slow cooling are combined. As shown by neutron diffraction in austenite phase, slow cooling thermal treatments produce a higher degree of atomic order, together with a reduction of strains and defects, which cause an increase in the total ordered magnetic moment and a slight enhancement of the ferromagnetic coupling, while cobalt doping has a stronger effect in increasing the ferromagnetic coupling, which explains the noticeable effect in the magnetization. The spin density maps obtained from polarized neutron diffraction have revealed the magnetic interaction pathways responsible for this coupling scheme.

Since in the systematic study of the effect of milling we have observed that long milling times lead to amorphous states, we have extended our study to the recrystallization processes in Ni-Co-Mn-Sn and Ni-Co-Mn-In alloys, with the analysis of the evolution of the different phases, the cell parameters and microstrutural parameters as grain size, micro and macrostrains.

Index

Chapter 1. Introduction

1.1.MARTENSITIC TRANSFORMATION

Hardening of steels by quenching is one of the most important technological processes in metallurgy. If the steel is quenched rapidly enough from the austenite state there is no time for eutectoidal decomposition and the steel undergoes a diffusionless structural transformation. The first observation of this transformation was carried out by the german metallurgist Adolf Martens, after who both the transformation and the steel final structure are known as martensitic transformation (MT) and martensitic phase, respectively. Although the term "martensitic" was initially used to describe the structural transition in steels, nowadays it is applied to all diffussionless structural changes in metallic alloys.

Actually, the MT is a solid-solid shear-dominant displacive diffusionless fist order transition between two different crystallographic structures; a high temperature phase known as *austenite* and another crystallographic structure with lower symmetry at lower temperatures called *martensite*. Due to its diffussionless nature, atomic bonds are not broken during the MT, and as consequence the atomic displacements are limited by the interatomic distance, the atomic order remaining constant in both phases [1–8]. This mechanism, where thermal activation is not necessary, allows the MT to take place at low temperature. However, for alloys where the MT occurs at high temperature, the thermal energy can produce diffusive phenomena, thus altering the stability of the transforming phases and the transformation properties themselves.

As a first order transition, it has associated an enthalpy, a change of volume, a hysteresis of transformation, the presence of an interface and the possibility of the coexistence of phases in thermodynamic equilibrium. The MT can be understood as the superposition of two processes; a homogeneous deformation of the crystal lattice and an invariant shear of the new lattice. The homogeneous deformation of the lattice, which leads to the change of crystallographic structure, is produced by a shearing process of certain atomic planes of the austenitic phase. This deformation implies the appearance of elastic and superficial energies in the surrounding volume of the transformed zone that impedes the transformation, and can even stop it. To accommodate the new structure and minimize the emergent energies, a deformation of the new lattice is produced by an invariant shearing process. This is a process of accommodation, without change of structure, which can occur either by gliding or by twinning, as shown in Figure 1. 1.

The fact that the high temperature phase has a greater symmetry than the low temperature one means that several orientations of the martensite are compatible with the austenitic phase and, therefore, that the martensitic phase is structurally inhomogeneous. This inhomogeneous character is general for ferroic materials (ferromagnetic, ferroelectric, ferroelastic, etc ...).

As the growth of the martensitic phase implies an increase in the elastic energy associated with the deformation, during the transformation a self-compensating distribution of domains (called "martensitic variants") occurs in order to decrease the overall macroscopic deformation and, therefore, minimize the energy of the deformation. Thus, each variant is formed with an orientation that counteracts the accumulated energy in the formation of the previous variant.

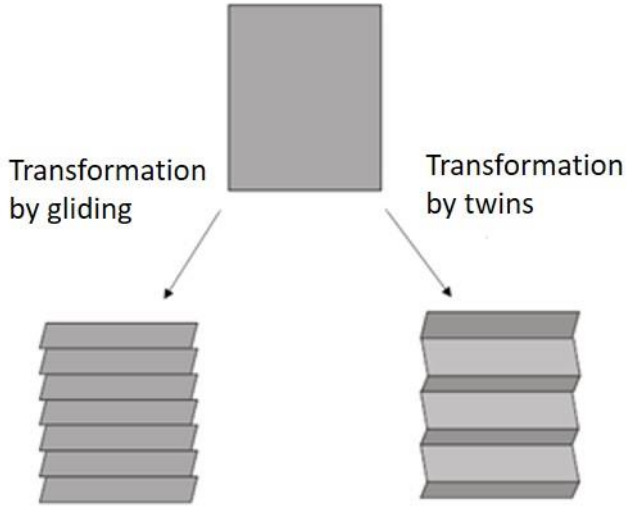

Figure 1. 1. Schematic representation of the gliding and twining accommodation processes during the transformation.

1.1.1. Thermoelastic transformation

Two types of martensitic transformation can be distinguished taking into account the kinetics of the transformation, the *burst-type* (*non thermoelastic*) and the *thermoelastic martensitic transformations*. The first ones are characterized by a large volume change that implies the presence of plastic deformation and a wide thermal hysteresis (hundreds of Kelvins). This type of transformations are typical on quenched steels and iron alloys. On the other hand, the thermoelastic martensitic transformations have a small volume change associated, a small mismatch between the cell parameter of both phases (that favors the absence of plastic deformation) and consequently low hysteresis (tens of Kelvins), and a complete reversibility. In this type of transformation, the martensite is formed by nucleation and growth on cooling. The nucleation and growing of new martensite variants stops when cooling is interrupted, the processes resuming on further cooling. On heating, the inverse transformation takes place by means of the backward motion of the austenite-martensite interfaces formed in the direct transformation, the martensite plates disappearing in the reverse order of their appearance. In this way, the structure of the austenite is restored in the inverse transformation, recovering the original orientation. According to this formation kinetics, thermoelastic martensitic

transformations are considered athermic, which implies that the transformation is solely a function of temperature and, therefore, independent of time [3].

From the macroscopic point of view, it is possible to explain the reversibility of the transformation considering the atomic order of the crystal structures. The retransformation path, the last variants to be formed being the first to disappear, ensures maintaining the atomic order of the austenite phase. So the reversibility associated to the shape memory alloy corresponds to the retransformation of the martensitic structure that minimizes the energy of the system.

From the thermodynamic point of view, the term "thermoelastic" means that, for any temperature and applied stress in the temperature range in which the transformation extends, a state of thermoelastic equilibrium is established, defined by a local balance of the forces acting on the interfaces that separate the martensitic phase from the austenitic phase. The difference in the Gibbs free energy between the two phases gives the driving force of the transformation. As can be seen in figure 1.2, at a temperature above the equilibrium temperature T_0 the Gibb's free energy is lower in austenite than in martensite, so the cubic phase is more stable. On the other hand, the martensite is more stable below T_0 due to its lower Gibb's energy. During the *direct transformation* (austenite → martensite), there is a balance between the difference in free energy, which favors the transformation, and the increase in elastic energy that inhibits the transformation. The contribution of the elastic energy makes it necessary to supercool below the critical temperature T_0 in which the Gibbs energies of the austenitic and martensitic phases are equal (Figure 1. 2.). The *reverse transformation* (martensite → austenite) is favored both by the elastic energy stored in the direct transformation and by the free energy difference of the two phases. In addition, the presence of dissipative mechanisms linked to the movement of austenite-martensite interphases and the accommodation of the domains of martensite supposes a loss of energy that causes the occurrence of hysteresis [9].

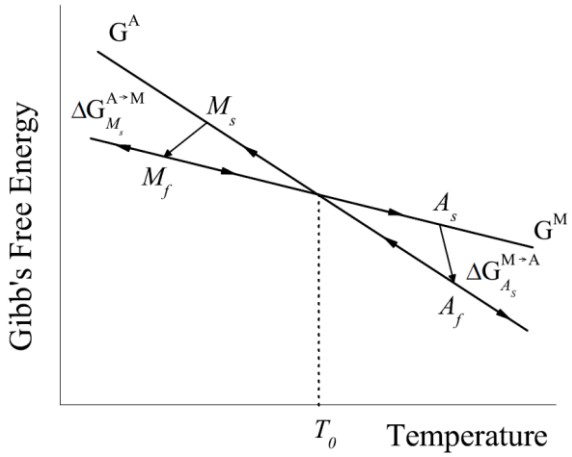

Figure 1. 2. Schematic diagram of the Gibb's free energy of martensite and austenite in the martensitic transformation region.

On cooling from austenite to martensite (*direct transformation*) the structural change starts at the first critical temperature known as *martensite start* (M_s), where the variants start to grow, and finishes at temperatures lower than *martensite finish* (M_f) where the whole sample is in martensitic state. On the other hand, the transformation from martensite to austenite (*reverse transformation*) starts at a temperature called *austenite start* (A_s) and finishes at *austenite finish* (A_f) temperature, where the whole specimen is in the parent phase. Figure 1. 3. shows all these characteristic temperatures in the reverse and direct transformation. As it has been pointed out previously, there is a thermal hysteresis, so $A_s > M_f$ and $A_f > M_s$ where the martensitic transformation temperature for the forward transition is defined as $T_M = \frac{(M_s + M_f)}{2}$.

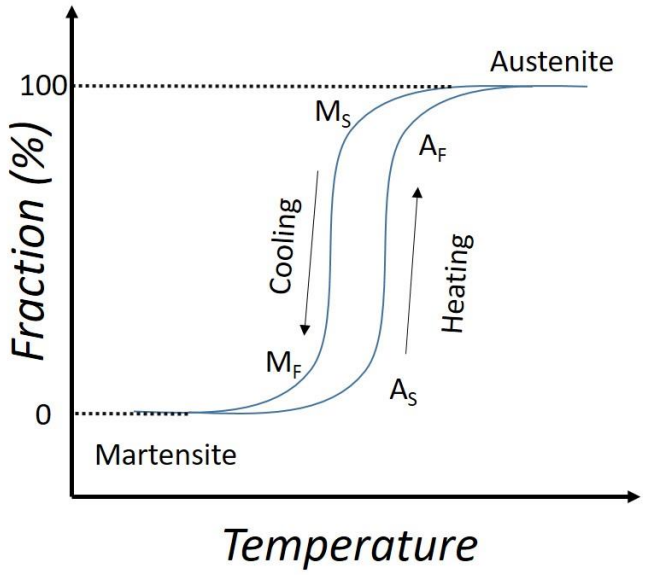

Figure 1. 3. Fraction of transformed austenite as a function of the temperature.

1.2. SHAPE MEMORY ALLOYS

The alloys that experience a thermoelastic martensitic transformation are called Shape Memory Alloys. The characteristics of such a reversible structural transformation and the high mobility of the martensitic variants confer these materials some peculiar and interesting properties such as the Shape Memory Effect or the Superelasticity [4].

- **Shape memory effect**

Due to the high mobility of the interphases between the variants, the martensitic phase is easily deformable under an applied stress. If a deformed alloy is heated up to temperatures above A_f, the reverse MT occurs, resulting in the recovery of the crystallographic austenitic structure. This leads to the elimination of the stress-induced deformation and therefore to the recovery of the initial shape. This effect is known as *shape memory effect*.

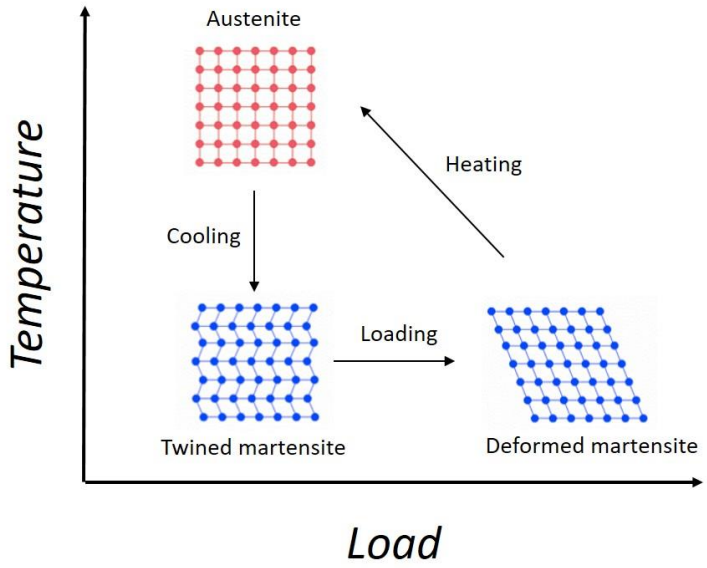

Figure 1. 4. Illustration of the shape memory mechanism.

Starting in the austenite phase, the martensitic structure is obtained on cooling down the sample below M_S. The martensite appears with a specific variants structure, composed by self-accommodating groups, in such a way that the sample does not experiment any macroscopic change of shape. The reorientation of variants, which accommodate the strain induced by an applied stress, gives rise to a macroscopic deformation and consequently a change of shape. Finally, heating the alloy above A_f results on recovery of the austenitic structure and initial shape.

The formation of martensite nuclei in the alloy occurs non-homogeneously. Bearing this in mind, the creation of preferential nucleation sites, such as network defects or precipitates, can determine the sequence of appearance of the martensite. The controlled creation of these nucleation centers can make possible the control of the MT process under cyclic variations of temperature, allowing the control of the transformation path. This process is known as a double-form memory effect. The introduction of nucleation centers in the crystal can be achieved in various ways, such as, for example (i) by deforming above the elastic limit, either in austenite or in martensite, (ii) by multiple repetitions of the cycle composed by cooling → deformation → heating, (iii) through repetitions of charge cycles at temperatures greater than A_f that induce transformation (iv) cooling under load from temperatures greater than A_f up to temperatures lower than M_f and heating again without load until temperatures greater than A_f, or (v) introducing precipitates in the sample by heat treatment, among others. These processes of creating nucleation centers, called training processes, can produce an increment of the deformation during the MT of 0.48% by application of magnetic field in different cycles in Ni-Fe-Mn-Ga [10] or an increase of 6% in the deformation stabilizing two-way shape memory alloys in Cu-Zn-Al [11]. These properties increment the possible applications of these alloys in

fields as different as actuators, thermo- and magnetosensors, medicine or civil structures [12–16].

- **Superelastic effect**

When a mechanical stress is applied to the alloy at temperatures higher than A_f the alloy may transform to martensite. This is due to the fact that the work carried out by this stress supposes an additional contribution to the driving force responsible for the transformation, making it possible to promote the transformation at temperatures higher than the one corresponding to the transformation induced by temperature. Once the stress is removed, the sample recovers the deformation without any residual strain, since at that temperature the stable phase is the austenitic structure instead of the martensite. This superelastic effect can be described by the Clausius-Clapeyron equation:

$$\frac{d\sigma}{dT_0} = \frac{\Delta S}{\varepsilon} \tag{1.1}$$

where σ is the external strain, ΔS is the entropy change associated to the MT and ε is the macroscopic deformation associated also to the structural change. In case of single-crystal, the application of stress at temperatures higher than A_f can provide a monovariant martensite in the alloy producing an strain close to 10% [17]. Furthermore, a tensile strain of 21.3% was found in Cu-Al-Ni polycrystalline alloy, where the grain growth was controlled by continuous unidirectional solidification [18].

1.3.Ni-Mn-Z ALLOYS

The alloys that undergo thermoelastic MT between magnetically ordered phases can have certain special characteristics due to the coupling of their structural and magnetic properties. In this case, if the magnetic properties of the austenite and the martensite are different, the structural transformation (the martensitic one) involves a change in the magnetic properties, giving rise to a magnetostructural first-order transformation, where the elastic and magnetic subsystems are coupled. Then, magnetic field appears as another stimulus to which the MT is sensitive.

Among the magnetic shape memory alloys, Ni-Mn-Z (Z = Ga, In, Sn, Sb) are by far the most studied systems due to the interesting effects they show, as the magnetic-field-induced strain, the magnetic shape memory effect or the magnetic-field-induced martensitic transformation. The main characteristics of these materials, subject of study in this thesis, are described below.

1.3.1. Structure

- **High-temperature phases**

Ni-Mn-Z alloys with compositions close to Ni2MnZ are a particular type of Heusler alloys. Heusler alloys are intermetallic compounds with general composition X_2YZ, where X and Y are 3d elements corresponding to transition metals as Fe, Co, Cu, Ni, etc., and Z can be an element for IIIA, IVA or VA groups of the periodic table. The typical crystallographic structure of these materials is a cubic $L2_1$ structure (space group $F\,m\bar{3}m$) with next-nearest-neighbors long-range atomic order [19–22]. Such structure can be described by four fcc interpenetrated sublattices, *i, ii , iii* and *iv*, where the origin of each sublattice is located at the $(0,0,0), \left(\frac{1}{2},\frac{1}{2},\frac{1}{2}\right), \left(\frac{1}{4},\frac{1}{4},\frac{1}{4}\right)\ and\ \left(\frac{3}{4},\frac{3}{4},\frac{3}{4}\right)$ positions, respectively. As illustrated in Figure 1. 5, in the Ni-Mn-Z case, the Mn atoms are located at the $(0,0,0)$ position (4*a* Wykoff position), the Z element at the $\left(\frac{1}{2},\frac{1}{2},\frac{1}{2}\right)$ position (4*b* Wykoff position) and Ni atoms occupy the $\left(\frac{1}{4},\frac{1}{4},\frac{1}{4}\right)\ and\ \left(\frac{3}{4},\frac{3}{4},\frac{3}{4}\right)$ positions (8*c* Wykoff position).

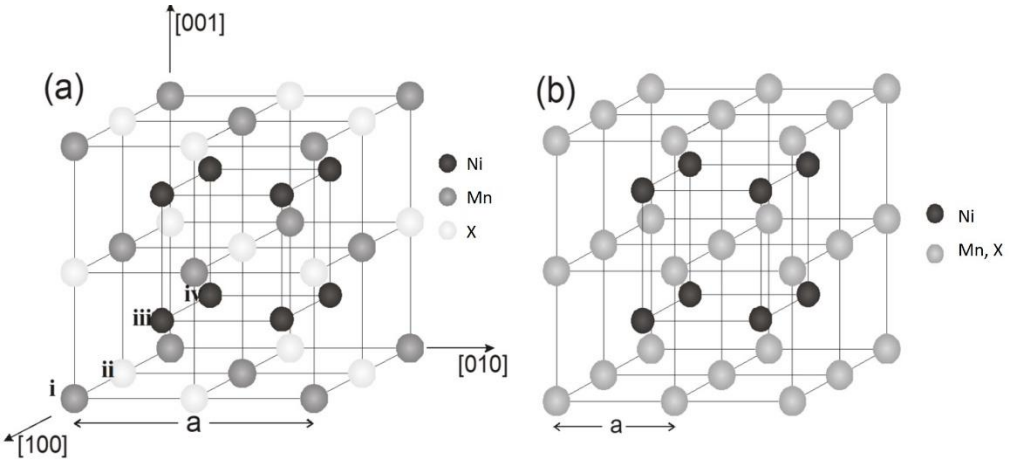

Figure 1. 5. a) $L2_1$ Heusler structure composed by the interpenetrated sublattices i, ii , iii and iv where, in the case of Ni_2MnZ, the i sublattice is occupied by Mn atoms, ii by Z element and iii and iv are occupied by Ni atoms. b) B2 structure where there are only two different sublattices; one is occupied by Ni atoms and the other by Mn and Z element indistinctly.

These alloys do not solidify directly from melt to the Heusler $L2_1$ structure. During the solidification they pass from liquid to a cubic ClCs-type B2 structure with nearest-neighbor atomic ordering and space group $Pm\bar{3}m$. This is a disordered structure with only two different atomic occupancies among the four sublattices, $Occ(i) = Occ(ii) \neq Occ(iii) = Occ(iv)$,Figure 1. 5.b. The $L2_1$ structure is obtained through a second-order B2-$L2_1$ transition taking place at different temperatures depending on both the composition and the Z element [23]–[27]. The next nearest-neighbor atomic ordering implies that the cell parameter is twice

that in the B2 structure. Recently, the presence of the B2-$L2_1$ order transition has been confirmed by neutron diffraction measurements in Ni-Mn-Ga [26, 28], Ni-Mn-In [29, 30] and Ni-Mn-In-Co [31] alloys, thus corroborating the calorimetric curves previously measured in Ni_2Mn-Ga and Ni-Mn-In systems. In Ni-Mn-Sn and Ni-Mn-Sb alloys, in turn, no B2-$L2_1$ transition has been detected, the $L2_1$ structure being stable up to temperatures close to the melting point [32].

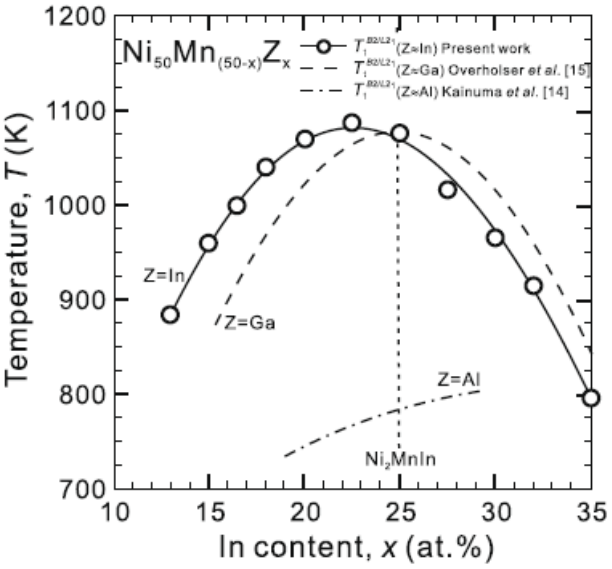

Figure 1. 6. Critical temperatures for B2-$L2_1$ order-disorder transformation determined by differential scanning calorimetry by Miyamoto et al. [27]

- **Martensitic phase**

According to the studies carried by Webster et. al, the MT is the result of the structural instability that appears due to the Fermi-surface nesting at the limit of the Brillouin zone [33]. At this point, the austenite structure is not stable and transforms to a lower symmetry structure. The vibrational contribution of the austenite, which is the responsible for the stabilization of the Heusler structure at high temperatures (diminishing the Gibb's free energy) is compensated by the lower Gibb's free energy of the martensitic structure [34]. Due to the presence of Ni and Mn atoms, that are 3d atoms, the idea of the Jahn-Teller mechanism as the responsible of the MT was assumed by Fujii et. al in Ni_2MnGa and Co_2NbSn [35]. This idea was corroborated by Brown et. al in 1999 from polarized neutron diffraction measurements in Ni_2MnGa, which showed that the degeneracy of the *d* states of the austenite close to the Fermi energy level produces a redistribution of the conduction electrons minimizing the Gibb's free energy and changing the magnetism associated to the structure from Mn to Ni atoms [36]. Finally, studies in Ni-Mn-Sn and N-Mn-In alloys carried out by Bhobe et. al have shown from *extended x-ray absorption fine structure (EXAFS)* that the origin of the Jahn-Teller mechanism comes from the increase of the hybridization of the *p* and *d* orbitals from the Z element and Ni as consequence of the reduced length of the Ni-Z bond with respect to the Ni-Mn one [37, 38].

Thus, on further cooling below the B2-$L2_1$ transition temperature, the thermoelastic MT can take place from the austenite phase to a martensitic structure. In all the magnetic Heusler shape memory alloys, inelastic neutron scattering studies reveal a softening of the TA_2 phonon

branch of the austenite, that corresponds to the [110] acoustic phonon [39–41], on approaching the MT. This softening was firstly observed in Ni_2MnGa by Zheludev et. al. [39] as a decreasing of the phonon energy on cooling, with a minimum energy value for the wave vector $q = (2\pi/a)(\xi, \xi, 0)$ whit $\xi = 1/3$, as illustrated in Figure 1. 7. Irrespectively of the crystallographic structure, in all the martensitic structures the (100) direction of the martensite corresponds to the (110) plane in the austenite, the direction of the TA_2 acoustic phonon showing the soft mode at temperatures close to the M_S.

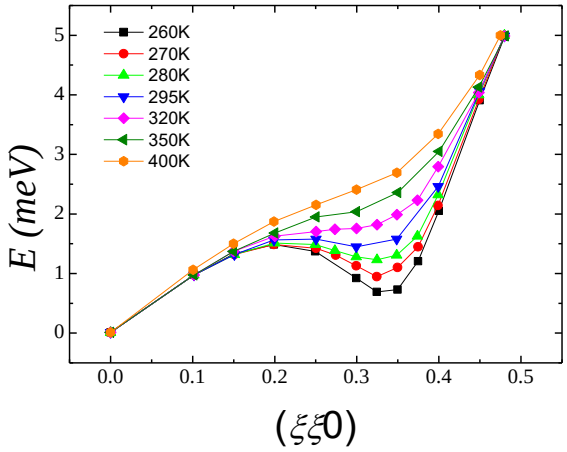

Figure 1. 7. Temperature dependence of the phonon anomaly in the (ξξ0) TA_2 branch in austenite [39].

- **Ni-Mn-Ga system**

The first martensitic structure observed in the stoichiometric alloy Ni_2MnGa was a body centered tetragonal structure with lattice parameters $a = b = 5.920$ Å and $c = 5.566$ Å (c/a=0.94<1) associated to a modulated superstructure [33]. In that work, it was established that MT is due to shears on the (110) planes along the direction $[1\bar{1}0]$ of the austenite $L2_1$. The tetragonal distortion of the cubic lattice results in a macroscopic contraction of the material (around 1%) along the [100] axis of the austenite. The observation, in X-ray diffraction measurements, of four satellites between the main reflections of the tetragonal lattice suggested a superstructure modulated with a period of five unit cells. The modulation of this structure, called 5M martensite, consists in a displacement of the planes $(110)_{aust}$ along the directions $[1\bar{1}0]_{aust}$ with a modulation period of ten atomic planes, in such a way that the tenth plane $(110)_{aus}$ has the same position as the first. Subsequent neutron diffraction studies carried out by Brown et. al [42] revealed a 7M orthorhombic martensite more complex than the 5M tetragonal previously obtained by Martinov et. al [43]. In both cases, two consecutive transformations were observed on cooling: a first transformation from austenite to a premartensitic cubic 3M modulated structure, and then the transformation to the 7M or 5M martensites. In more recent studies, high resolution X-rays powder diffraction measurements have revealed a 7M incommensurate structure with space group $Immm\,(00\gamma)$ and propagation vector $q = 0.33701c^*$ [44–46].

This structure was confirmed also by Righi et. al, who found the same structure but with a larger propagation vector $q = 0.4248c^*$ [47]. Moreover, again Righi et. al have shown that off stoichiometric Ni-Mn-Ga presents a 5M commensurate structure with a fundamental monoclinic lattice [48].

- **Ni-Mn-Z (Z=In, Sn, Sb)**

In these alloys, the martensitic phase may show many different crystallographic structures depending on the Z element and the alloy composition.

In Ni-Mn-Sn system, an orthorhombic structure with a four-layered modulation (called 4O) and $Pmma$ space group was determined by Sutou et. al. from transmission electron microscopy observations [49], where the presence of three new satellites around the main reflection gave information about the modulation of the structure. This structure was corroborated from powder neutron diffraction measurements performed by Brown et. al. in Ni-Mn-Sn and Ni-Mn-Sb [50, 51] and by Rama Rao et. al [52] in Ni-Mn-Sb alloys. In Ni-Mn-In system, Krenke et. al [53] found, from neutron diffraction measurements, that the martensitic structure at 5 K was a 10M monoclinic structure. For similar compositions, Brown et. al. [54] found a three-fold modulated monoclinic structure with space group $P2/m$. In fact, further systematic studies have revealed the coexistence of several crystallographic structures (4O, 3M, 5M, 7M, commensurate and incommensurate, orthorhombic and monoclinic… [55–57]) in martensites of different alloys. In Table 1. I, the different martensitic structures obtained in Ni-Mn based Heusler alloys are summarized. The relationship between the austenitic and the 4O and 3M martensitic structures is schematically illustrated in Figure 1. 8.

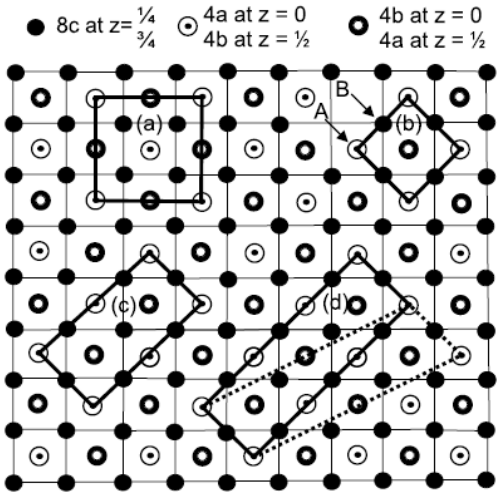

Figure 1. 8. Schematic representation of martensitic transformation in the (001) projection showing: a) the ideal $L2_1$ Heusler structure with $Fm\bar{3}m$ space group, b) the tetragonal structure with $I4/mmm$ space group, c) the transformed orthorhombic structure with $Pmma$ space group referred as four layered modulation, 4O [50, 51] and d) three-fold modulated structures, 3M: the solid line represents a three-fold orthorhombic structure with space group $Pnnm$, while the broken line represents a three-fold monoclinic cell with space group $C2/m$. Representation obtained from [54].

Table 1. I. Crystallographic structures in austenite and martensite.

Systems	Austenite	Martensite	
		Structure	Space group
Ni-Mn-Ga	$L2_1$	Tetragonal	*I4/mmm* [58–60]
		Orthorhombic	*Pnnm* [26, 42, 60, 61]
		Orthorhombic	*Immm*(00 γ) [47]
		Monoclinic	*I2/m*(α0γ) [48]
		Monoclinic	*I2/m* [48]
NiMnSb	$L2_1$	Orthorhombic	*Pmma* [49, 50]
NiMnSn	$L2_1$	Tetragonal	*I4/mmm* [55]
		Orthorhombic	*Pmma* [49, 51, 62]
NiMnIn	$L2_1$	Tetragonal	*I4/mmm* [56]
		Monoclinic	*P2/m* [54]
		Monoclinic	*I2/m*(α0γ) [63]
Ni-Co-Mn-Ga	$L2_1$	Tetragonal	*I4/mmm* [64, 65]
Ni-Co-Mn-Sb	$L2_1$	Orthorhombic	*Pmma* [66]
Ni-Co-Mn-Sn	$L2_1$	Tetragonal	*I4/mmm* [67]
		Orthorhombic	*Pmma* [68]
Ni-Co-Mn-In	$L2_1$	Monoclinic	*P2/m* [69]

1.3.1. Magnetism

The majority of the Heusler alloys have a ferromagnetic behavior and saturate at weak magnetic fields. These compounds have localized magnetic moments, so they are ideal model systems for study the effects of both atomic disorder and changes in the electron concentration on magnetic properties. In the particular case of X_2MnZ compounds, a magnetic moment close to $4\mu_B$ is provided by Mn atoms.

The 3*d* and *sp* elements occupying the (X) position and (Z) position, respectively, have and important role on the magnetic properties of Heusler alloys [70]. It has been shown that *sp* electron concentration is primarily important in establishing magnetic properties, influencing both the magnetic moment formation and the type of the magnetic order [33, 71]. On the other hand, antiferromagnetic behavior was also discovered in Heusler alloys with B2 structure, where the Mn-Mn distances are smaller than in the $L2_1$ structure. In particular, antiferromagnetic magnetic structure was found in alloys with X=Ni, Pd and Z=Al showing B2-type crystal structure [70].

Focusing in Ni-Mn-Z Heusler alloys, it has been shown that the variations on the *Z* element change the electronic contribution of the *sp* electrons, thus producing a variation in the Curie temperature, as shown by Şaşisoğlu et. al. [72]. In this work, they also shown that the interaction between the Mn-Ni sublattices plays an important role in those compounds, even though Ni atoms provide a magnetic contribution lower than $0.3\mu_B$.

Two main groups of magnetic alloys may be distinguished according to the magnetic behavior: ferromagnetic (mainly the Ni-Mn-Ga systems), characterized by presenting ferromagnetic behavior in both the austenite and martensite phases, and metamagnetic (Ni-Mn-Z systems with Z = Sn, Sb, In) characterized by a weak magnetic behavior in the martensite phase and therefore by a large magnetization drop at the MT. This large magnetization drop occurring at the MT allows the induction of the MT by an applied magnetic field, thus giving rise to multifunctional properties (namely giant magnetoresistance, magnetic shape memory and large inverse magnetocaloric effect) of great technical interest for practical applications in fields like sensing or magnetic refrigeration.

Brown et. al. developed a thorough study on the magnetic coupling in the austenite in ferromagnetic (Ni-Mn-Ga) and metamagnetic (Ni-Mn-Sn, Ni-Mn-Sb and Ni-Mn-In) Heusler alloys, those last ones with excess of Mn and presenting MT. In the case of an excess of Mn, which is usual for compositions undergoing the MT at temperatures of technological interest, some Mn atoms are located at *4b* sites (*ii* sublattice). In all the experiments, the observed magnetic structure was ferromagnetic, which means that the coupling between the 4*a* and 4*b* sites where the Mn atoms are located is ferromagnetic. The calculated magnetic moment values lied close to $2\mu_B$ and $1\mu_B$, respectively, and $0.33\mu_B$ in the 8*c* position assigned to Ni atom [42, 50, 51, 54]. However, other powder neutron diffraction experiments in Ni-Mn-Sn alloy carried out by Umetsu et. al. showed an antiferromagnetic coupling between de Mn atoms located in 4*a* and 4*b* sites [73]. The main difference between both alloys is the amount of Mn atoms, having higher Mn concentration in the case of Brown's study. In addition, another important result was obtained by Umetsu et. al. in Co-doped alloy (substitution of Ni by Co), where the magnetic coupling suffers a variation from antiferromagnetic to ferromagnetic. The explanation of this change, proposed by Kurtulus et. al by density-functional theory studies, is related to the fact that the interactions between Co and Mn are stronger than the interactions between Ni and Mn [74]. Other studies have been carried out to clarify the magnetic structure of the martensite of metamagnetic shape memory alloys from neutron scattering measurements. Antiferromagnetic correlations were deduced in Ni-Mn-Sn and Ni-Mn-Sb by Aksoy et. al. from diffuse scattering measurements with neutron polarization analysis [75, 76]. The presence of short-range antiferromagnetic correlations in martensite is supported by the observation of exchange bias at low temperatures in some Ni-Mn-based Heusler alloys [77–83]. In Ni-Mn-Sn system, however, recent Mössbauer spectroscopy studies seem to give evidence of a paramagnetic state [84], hence the exact nature of the magnetic correlations in martensite is also still under discussion.

In summary, the magnetism in these alloys mainly arises from the coupling between the Mn atoms, in which the magnetic moment is chiefly confined, so the magnetic exchangeinteractions (which can be treated in the framework of a Ruderman-Kittel-Kasuya-Yoshida model) strongly depend on the Mn–Mn distance, and therefore different sequences of magnetostructural transformations can be observed depending on both the third alloying element and the change in interatomic distances caused by the MT. In particular, in Ni-Mn-Z (Z=In, Sn, and Sb) alloys, as mentioned before, the MT takes place between a ferromagnetic austenite and a weak magnetic martensitic phase. This behavior is thought to be related to a

development of local antiferromagnetic correlations promoted by the variation of the distance between Mn atoms taking place as a result of the MT.

1.4. MAGNETOSTRUCTURAL EFFECTS IN Ni-Mn-Z ALLOYS

The alloys that undergo thermoelastic martensitic transformation and are also ferromagnetic can have certain special characteristics due to the coupling of their structural and magnetic properties. In this case, if the magnetic properties of the austenite and the martensite are different, the structural transformation (the martensitic one) involves a change in the magnetic properties, giving rise to a magnetostructural 1st order transformation, where elastic and magnetic subsystems are coupled. Then, magnetic field appears as another stimulus to which the MT is sensitive. As a consequence, new effects linked to the MT may arise, as the magnetic-field-induced strain, the magnetic shape memory effect or the magnetic-field-induced MT.

1.4.1. Magnetic-field induced strain (MFIS). Magnetic shape memory effect (MSME)

In ferromagnetic alloys, the MT promotes the formation of a structure of magnetic domains linked to the structure of crystallographic domains. In this case, the application of a magnetic field may cause the movements of the martensitic variants and hence a large macroscopic deformation on the alloy. This particular effect, consequence of the coupling between the structural and magnetic degrees of freedom in ferromagnetic martensitic structures, can be only possible at temperatures below the MT (A_S) and Curie temperature (T_C).

The magnetic shape memory alloys are characterized by a net magnetic moment or spontaneous magnetization (Ms). When a magnetic field is applied on the alloy, a magnetostatic energy known as Zeeman energy tends to align the magnetic moments with the applied magnetic field, which can be described with the equation:

$$E_{magnetostatic} = -\mu_0 \boldsymbol{H} \cdot \boldsymbol{M_S} \tag{1.2}$$

where μ_0 is the permeability in the vacuum, $\boldsymbol{H}$ is the external magnetic field and the $\boldsymbol{M_s}$ the spontaneous magnetization.

On the other hand, the energy of magnetocrystalline anisotropy opposes to the displacement of magnetization out of certain directions, the so-called directions of easy magnetization or easy axes. For materials with a uniaxial anisotropy, this energy can be expressed as:

$$E_{anisotropy} = K_u sin^2\theta \tag{1.3}$$

where K_u is the constant of uniaxial anisotropy and θ is the angle between the magnetization and the easy axis of magnetization.

When an external magnetic field is applied, the magnetization tends to rotate from the directions of easy magnetization to the direction of the external magnetic field, this tendency being greater the greater the saturation magnetization (M_{sat}). If the energy of anisotropy is high, the magnetizations are strongly fixed to the crystallographic orientations of each variant, changing the direction of easy magnetization along the interface. In this case, the application of a magnetic field creates a Zeeman energy difference along the boundary between the variants that causes a pressure on the boundary. If this pressure is greater than the de-twinning stress, the movement of the twin boundary will occur resulting in the growth of those variants that are favorably oriented with respect to the direction of the external field, in order to minimize the Zeeman energy. The condition for the movement of variants can be formulated as:

$$\sigma_{mag} = \frac{K_U}{\varepsilon_O} > \sigma_{dtw} \tag{1.4}$$

where σ_{mag} is the magnetic stress, ε_O is the maximum deformation induced by the magnetic field and σ_{dtw} corresponds is de-twinning stress [38].

As in the case of stress-induced deformation, the strain will persist after removing the magnetic field. Now, if the magnetically-deformed martensite is heated up to temperatures above A_f, the reverse MT takes place and the austenitic structure, and hence the original shape, are recovered. This is called the "Magnetic Shape Memory Effect".

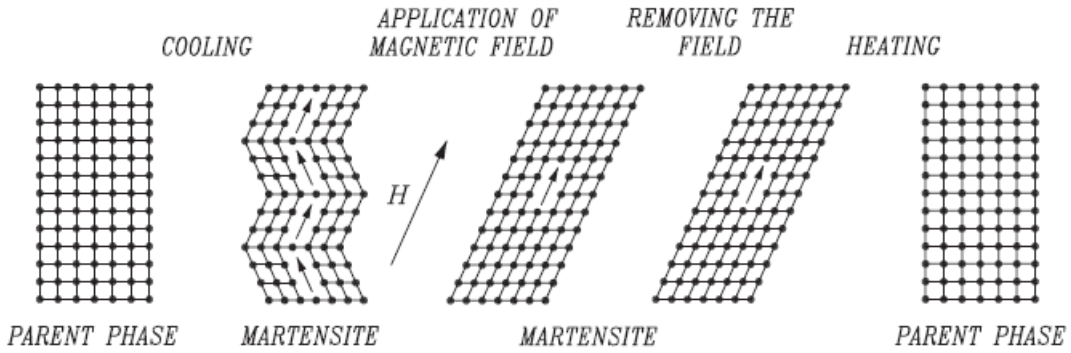

Figure 1. 9. Schematic representation of the magnetic shape memory effect [85].

1.4.2. Magnetic-field Induced Martensitic Transformation (MFIMT)

As a first order transition, the application of an external field may shift the transformation temperatures according to the Clausius-Clapeyron equation. The expression for the case of a magnetic field is

$$\frac{dT_M}{dH} = -\mu_0 \frac{\Delta M}{\Delta S} \tag{1.5}$$

where ΔM and ΔS are the magnetization and entropy changes linked to the transformation. Taking into account that the entropy of the martensite is lower than that of austenite, the transformation temperature will shift to higher or lower temperatures depending on the sign of

the magnetization change. In the case of metamagnetic shape memory alloys, the large magnetization drop occurring at the MT leads to very large negative shifts in the transformation temperature under the application of high magnetic fields. Hence, if the magnetic field is applied in the martensitic state at temperatures close to A_S, it can result in the magnetic induction of the reverse MT.

This phenomenon was firstly studied in $Ni_{45}Co_5Mn_{36.7}In_{13.3}$ Heusler single-crystal, where it was demonstrated not only the induction of the austenite by the applied magnetic field but also the almost full recovery of the induced strain with the applied magnetic field [86]. After this first discovery, the magnetic induction of the MT has been observed and studied in all the Ni-Mn-based metamagnetic systems; Ni-Mn-In [87], Ni-Mn-Sn [88], Ni-Mn-Sb [89], Ni-Co-Mn-Sn [90], Ni-Co-Mn-Al [91] or Ni-Co-Mn-Ga [92]. The weak magnetic state in martensite, and consequently the huge change in magnetization at the martensitic transformation, is the main responsible of the possibility of inducing the reverse transformation by magnetic field. The evolution of the martensitic transformation leading to the magnetic induction of the transformation is illustrated in Figure 1. 10.

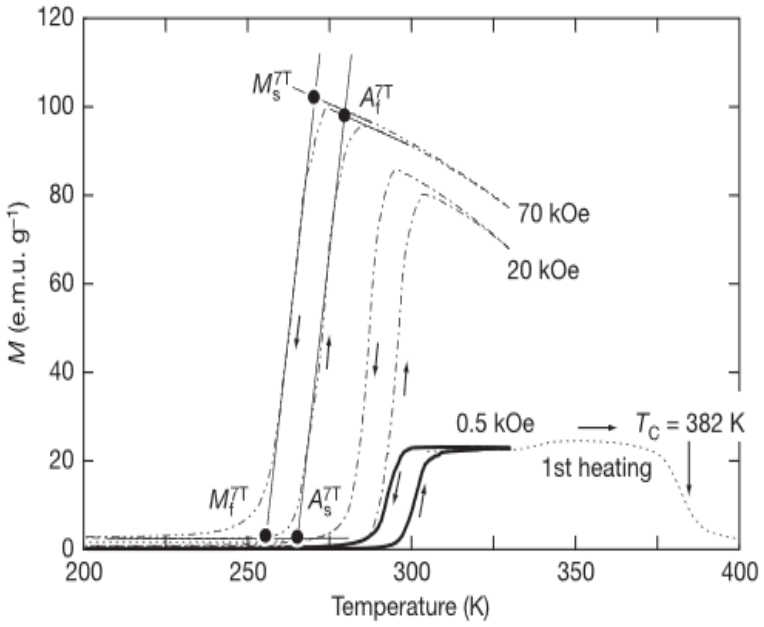

Figure 1. 10. Temperature dependence of magnetization for a Ni-Co-Mn-In metamagnetic shape memory alloy [86].

Taking into account the different magnetic characteristics of the austenitic and martensitic phases, the magnetic induction of the MT may give rise to large inverse magnetocaloric effects [85, 89, 93–96] or to giant magnetoresistance [97–99], very interesting for practical application in magnetic refrigeration or sensing, respectively.

1.4.3. Magnetocaloric effect

The magnetocaloric effect can be defined as the variation in the temperature that a magnetic material suffers when a magnetic field is applied on it. Depending of the measuring conditions, the magnetocaloric effect can be expressed as a temperature change in adiabatic conditions or as an entropy change in isothermal conditions, caused by the application of a magnetic field. This phenomenon is intrinsic for all magnetic materials and is produced as a result of the coupling of the magnetic sublattice with the applied magnetic field, giving a variation in the magnetic contribution to the entropy of the solid [100].

The effect of the application of the magnetic field in the temperature and entropy of a magnetic material can be obtained from thermodynamic considerations. The total differential of the total entropy can be written as:

$$dS = \left(\frac{\partial S}{\partial T}\right)_{H,P} dT + \left(\frac{\partial S}{\partial H}\right)_{T,P} dH + \left(\frac{\partial S}{\partial P}\right)_{T,H} dP \tag{1.6}$$

where *T*,*H* and *P* are the thermodynamic variables temperature, magnetic field and pressure, respectively. Focusing only in an isobaric process, that is, at constant pressure, and taking into account that the partial derivative of entropy with respect to the magnetic field can be related to magnetization through the Maxwell equation

$$\left(\frac{\partial S}{\partial H}\right)_T = \left(\frac{\partial M}{\partial T}\right)_H \tag{1.7}$$

and the partial derivative of entropy with respect to temperature can be expressed as

$$\left(\frac{\partial S}{\partial T}\right)_H = \frac{C}{T} \tag{1.8}$$

where C is the heat capacity of the material, the equation (1.6) results in

$$dS(T,H) = \frac{C(T,H)}{T} dT + \left(\frac{\partial M(T,H)}{\partial T}\right)_H dH \tag{1.9}$$

where the entropy is expressed in terms of easily measurable variables. In this expression, the entropy can be assumed to be the total entropy of the material as long as all the contributions to the entropy (vibrational, electronic, etc…) are included in the value of *C*, which provides all the degrees of freedom of the system.

Figure 1. 11 shows a schematic representation of the magnetocaloric effect in a *S*-*T* diagram. By applying a magnetic field in a conventional magnetic material (or by increasing the intensity of the magnetic field), the magnetic contribution to the entropy is modified as a consequence of the increment of the magnetic order on the alloy. There are two different ways to vary the magnetic field: adiabatically or isothermally. If the variation of the magnetic field is carried out under adiabatic conditions, in a reversible process, the system experiments a variation in the temperature ΔT_{ad} that corresponds to the adiabatic difference between the functions $S(H_f)$ *and* $S(H_i)$. Applying the adiabatic condition (*dS=0*) in the equation (1.9), the expression for the adiabatic temperature change as a function of the applied magnetic field is expressed as:

$$\Delta T_{ad}(T,H) = -\int_{H_i}^{H_f} \frac{T}{C(T,H)} \left(\frac{\partial M(T,H)}{\partial T}\right)_H dH \tag{1.10}$$

where the integration limits correspond to the initial and final magnetic fields.

On the other hand, the variation on the magnetic field can be carried out in isothermal conditions, thus producing a variation in the entropy of the system ΔS_{iso}. If we impose the condition $dT=0$, the isothermal variation in the entropy can be expressed as follows:

$$\Delta S_{iso}(T,H) = \int_{H_i}^{H_f} \left(\frac{\partial M(T,H)}{\partial T}\right)_H dH \quad (1.11)$$

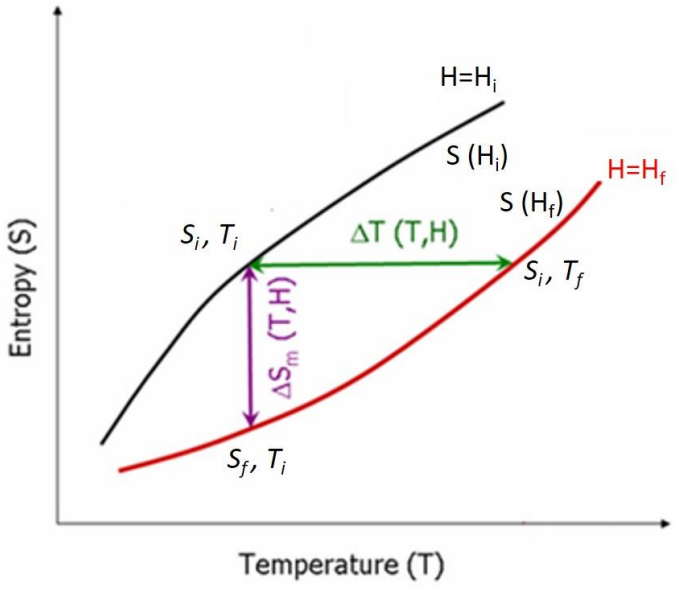

Figure 1. 11. Schematic representation of the magnetocaloric effect showing the variation in the temperature and entropy of a magnetic material when a magnetic field is applied.

Therefore, ΔT_{ad} and ΔS_{iso} are the two magnitudes representative of the magnetocaloric effect. As shown in figure 1.11, both variations are dependent on the initial temperature and on the magnetic field variation. Both ΔT_{ad} and ΔS_{iso} can be positive or negative depending of the sign of the partial derivative of the magnetization with the temperature: i) $\Delta T_{ad}>0$ and $\Delta S_{iso}<0$, when $\partial M(T,H)/\partial T < 0$, as it happens in the ferromagnetic materials around T_C, or ii) $\Delta T_{ad}<0$ and $\Delta S_{iso}>0$, when $\partial M(T,H)/\partial T < 0$. The latter case is known as *inverse magnetocaloric effect*.

As previously explained and as the expressions 1.10 and 1.11 state, the higher values of magnetocaloric effect will appear in those regions where the variation of the magnetization with the temperature is larger, i.e., in the proximities of phase transitions. For example, in ferromagnetic materials the highest values in ΔT_{ad} and ΔS_{iso} are at Curie temperature (T_C). In fact, the magnetocaloric effect has been studied in the vicinity of the second order magnetic transition in a large number of materials. Gd has appeared as particularly useful for applications at room temperature [94, 101, 102]. However, in the last years, the research is focusing in materials where the magnetic coupling is related with a first order transition, as is in $Gd_5(Si_xGe_{1-x})_4$ [103–106]. In these materials, the steep variation that the magnetization undergoes during the first order transition drives to huge values of ΔT_{ad} and ΔS_{iso}, thus taking the name of *giant magnetocaloric effect*. Moreover, they present the advantage that the transition temperatures can be shifted by controlling the composition. In the case of shape memory alloys, the entropy of the system as a function of the temperature suffers a discontinuity linked to the entropy

change at the MT, ΔS_{MT}. As previously explained, the application of a magnetic field promotes a shift in the transformation temperature, expressed by the Clausius–Clapeyron equation, resulting in the magnetic induction of an entropy change, that is, in a magnetocaloric effect. If the effect of the magnetic field is strong enough to induce the whole first order transition (and its effect on the heat capacities of the two phases is small) a limit value of the MCE with $\Delta S \approx \Delta S_{MT}$ should be expected.

The magnetocaloric effect has been widely studied in the Heusler alloys (Ni-Mn-Ga [96, 107–109], Ni-Mn-Sn [88, 110, 111], Ni-Mn-In [53, 88, 112], Ni-Mn-Sb[89, 113, 114] and Ni-Fe-Ga[93, 115]). The highest values of magnetocaloric effect in Ni-Mn-Ga systems have been observed in alloys close to the stoichiometry and have been obtained in those alloys where the magnetic and structural transitions overlap, reaching values of direct magnetocaloric effect close to $\Delta S = 23 J/kgK$ at 5T [116]. The largest reported values of inverse magnetocaloric effect in ternary metamagnetic alloys are $\Delta S = 19\ J/kgK$, obtained in $Ni_{50}Mn_{37}Sn_{13}$ [117] and $Ni_{50}Mn_{34}In_{16}$ [88], while the values obtained in $Ni_{50}Mn_{37}Sb_{13}$ reach $\Delta S = 9.1\ J/kgK$ [89]. The introduction of another 3d element such as Co, which produces an increment of magnetization in austenite and reduces the magnetic coupling in martensite, produces an increase of ΔM that implies the increase of the ΔS in the MT. In this way the large variations in the entropy have been obtained, reaching $31.9 J/kgK$, $34 J/kgK$ and $30/kgK$ for Ni-Co-Mn-Sn [118], Ni-Co-Mn-Sb [119] and Ni-Co-Mn-In [120], respectively.

There are two different ways to measure the magnetocaloric effect: directly and indirectly. The direct methods consist in the direct measurement (by calorimetry) of the adiabatic change on the temperature or the isothermal entropy variation that the material undergoes when a magnetic field is applied. On the other hand, indirect methods are based in the calculation of the values of ΔT_{ad} and ΔS_{iso} from magnetization measurements using the previous equations. In the present work, the MCE values (that is, the values of the entropy change) have been estimated indirectly from thermomagnetization curves at different applied magnetic fields, using equation 1.11.

1.4.4. Giant magnetoresistance.

Magnetoresistance is the variation of the electric resistance when a magnetic field is applied on a material. This behavior was discovered by William Thomson for iron in 1857. Depending on the variation in the resistance it is possible to have giant magnetoresistance or even colossal magnetoresistance [121–123] reaching variations of 1300% at room temperature in La-Ca-Mn-O films. The magnetoresistance is attributed to the influence of the state of spin on the dispersion of conduction electrons [124]. This phenomenon has been observed and studied in some ferromagnetic and metamagnetic shape memory alloys [97–99, 125]. For example, negative magnetoresistance was measured in Ni-Mn-Fe-Ga system in a broad range of temperatures, being mostly relevant in the range of temperatures close to the MT. This behavior was ascribed to the electronic redistribution and the increment in the dispersion in the presence of interphases. Due to the difference in the resistivity between structural phases, a huge change

in the magnetoresistance can be expected in the MT in metamagnetic shape memory systems, which show values up to -80% linked to the induction of the MT in Ni-Mn-In [126] or -48% in Ni-Mn-Sn [127] systems.

1.5. TUNNING THE MULTIFUNCTIONAL PROPERTIES

The MT characteristics and the magnetic properties of Ni-Mn-Z alloys depend on composition, atomic order and microstructure. This makes possible to properly tune the multifunctional features linked to the magnetostructural properties in these materials.

1.5.1. Composition

As the MT occurs when the Fermi surface coincides with the Brillouin zone, the concentration of electrons in the conduction band (e/a) can be considered as one of the main factors in the structural stability. In this sense, the compositional dependence of the Ni-Mn-Z Heusler alloys affects to the MT temperature and to the martensitic and austenitic Curie temperatures modifying in this way the magnetic and physical properties.

To obtain the e/a value we assume that each atom contributes with the most external electrons, considering the configuration of the electronic band structure in Heusler alloys [128]. In this way, Ni ($3d^8 4d^2$) provides 10 electrons, Mn ($3d^5 4d^2$) contributes with 7 and, depending of the Z element, it contributes with 3 in the case of Ga ($4s^2 4p^1$) and In ($5s^2 5p^1$), 4 for Sn ($5s^2 5p^2$) and 5 electrons for Sb ($5s^2 5p^3$).

In the case of Ni-Mn-Ga alloys, V. A. Chernenko was the first to establish empirically the relation between the MT and e/a, resolving in this way the phase diagram of those alloys [129]. Since then, many systematic studies were carried out analyzing the magnetic and structural properties as a function of e/a. In this study it was revealed that the temperatures of the martensitic and premartensitic transformations increase significantly when the value of e/a increases, while the Curie temperature of the austenite remains nearly constant. A critical value e/a≈7.7 is reached when $M_S=T_C$. Below and above this value, $M_S<T_C$ when e/a<7.7 and $M_S>T_C$ when e/a>7.7. Additionally, the enthalpy and entropy associated to this structural transition increase with the e/a value [130]. It was also demonstrated the importance of e/a in the martensitic structures, affecting the symmetry and the type of modulation [131]. More in detail, as Figure 1. 12 shows, Çakir et. al [132] have demonstrated the relation between e/a and the structure in the martensite by replacing Ga by Mn, showing the existence of intermartensitic transitions. The authors found that intermartensitic transitions take place following the sequence 7M→$L1_0$, 5M→7M, and 5M→7M→$L1_0$ on decreasing temperature and that the $L1_0$ (non-modulated tetragonal phase with space group *I4/mmm*) tends to be the ground state as it was previously considered theoretically [133].

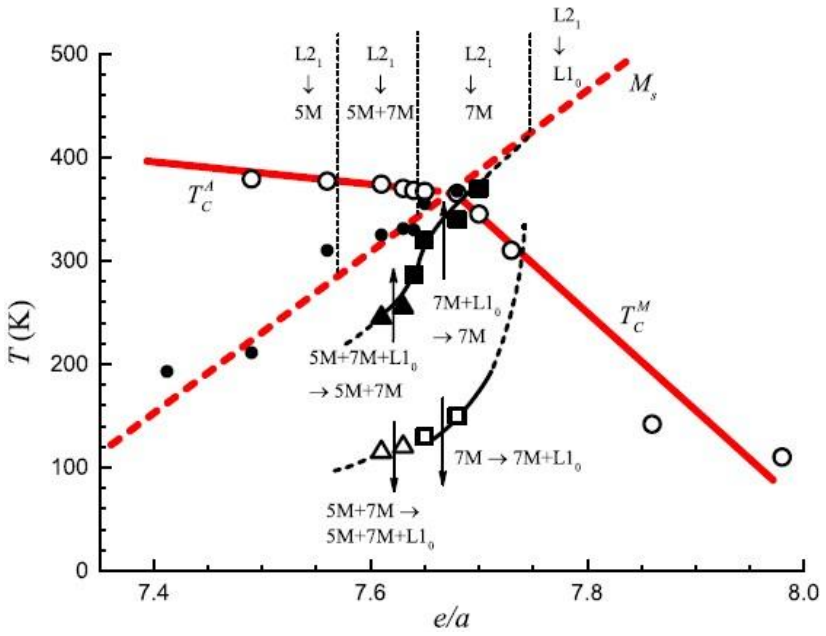

Figure 1. 12. Phase diagram of $Ni_{50}Mn_{50-x}Ga_x$ system where the filled circles indicates the temperature of the martensitic transformation and the open circles correspond to austenite and martensite Curie temperatures, squares denote 7M↔7M+L1$_0$ transition and open and filled triangles represent the forward and reverse transformation 5M+7M↔5M+7M+L1$_0$, respectively [132].

The effect of e/a variation in the case of Ni-Mn-In system was systematically studied by replacing In by Mn – thus increasing the e/a ratio – and analyzing the magnetic and structural properties of the resulting alloys [56, 134]. Three regions can be distinguished in the phase diagram (Figure 1. 13). For values of e/a ≤ 7.869, the MT is absent. The stoichiometric alloy, with e/a=7.526, lies in this region and does not present MT. The Curie temperature of the austenite, T_C^A, remains almost constant and an increase of saturation magnetization is observed as Mn replaces In in the 4*b* sublattice, with values of saturation magnetization that vary from 80 emu/g in the stoichiometric alloy to 120 emu/g for the alloy with e/a=7.834. This is an indication of a coupling of ferromagnetic character between the Mn atoms located in their own sublattice with the Mn atoms located in the In sublattice. The MT appears at 264K when e/a≥7.869, marking a critical point. Moreover, the alloy with e/a=7.869 is the only one in the series where the reverse transformation can be induced by applying magnetic field at temperatures close to A_S. In this region of the phase diagram (7.869 ≤ e/a ≤ 8.1) the martensitic phase presents modulated monoclinic crystal structures at room temperature. A shift of the magnetic ordering temperature of the martensite, T_C^M, to lower temperatures is observed as e/a increases, while the magnetism in austenite weakens, presenting linear behavior in the M(H) curves. Finally, the alloys with e/a > 8.1, present the MT at high temperature and the big amount of Mn in the alloy produces a change to antiferromagnetic coupling as found in $Ni_{50}Mn_{50}$ [135]. The martensitic phase of the alloys in this region shows a non-modulated L1$_0$ tetragonal structure at room temperature.

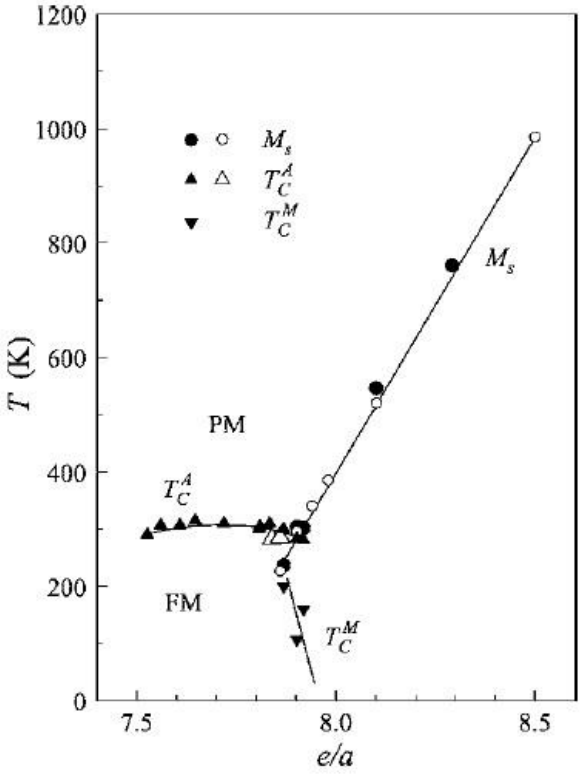

Figure 1. 13. Phase diagram of Ni-Mn-In system as a function of e/a [49, 56, 135].

Regarding the Ni-Mn-Sn system, Krenke et. al [55] carried out a systematic study of the compositional dependence of the physical and magnetic properties in the $Ni_{50}Mn_{50-x}Sn_x$ series, where the e/a ratio increases as the concentration of Sn decreases. The stoichiometric alloy does not show MT. The MT is present for values of e/a ≥ 8.041, starting at 190 K and showing a continuous increase in temperature with the increase of Mn concentration, linked to an increment in the entropy and enthalpy associated to the transformation. On the other hand, as Mn is the main responsible of the magnetism in these alloys, its concentration affects the magnetic coupling, with the saturation magnetization being reduced by the increase in Mn concentration, while the T_C shows a slight decrease in austenite and a marked reduction in martensite. The crystal structure of the martensitic phases as a function of the composition has been studied by X-rays diffraction by Çakir et. al [57] , showing that the martensitic structures can present different symmetries according to the amount of Mn in the alloy and that different structures can coexist in the same alloy, giving rise to intermartensitic transitions. In this way, the analysis has revealed the presence of orthorhombic 5M commensurate and incommensurate structures, incommensurate 7M monoclinic structures and non-modulated tetragonal $L1_0$ structures (Figure 1. 14). For e/a between 8.011 and 8.17 the martensitic structures show an incommensurate 5M orthorhombic structructure, with an intermartensitic transition to $L1_0$ for the lowest values of e/a and to incommensurate 7M for the higher ones. For e/a=8.2 the martensitic structure is pure 7M incommensurate, and for e/a=8.25 and 8.30 intermatensitic transitions from 7M to $L1_0$ are observed. Finally, the martensite is pure tetragonal for e/a=8.34. It is worth noting that the propagation vector of the incommensurate orthorhombic 5M structure

is very close to q=0.5c*, which would correspond to the commensurate 4O crystal structure showed previously by Sutou et. al [49] and corroborated by Brown with neutron powder diffraction [51]. Figure 1.14 shows the phase diagram of Ni-Mn-Sn system representing the evolution of MT, austenite and martensite Curie temperatures and the structures present in martensite as a function of e/a.

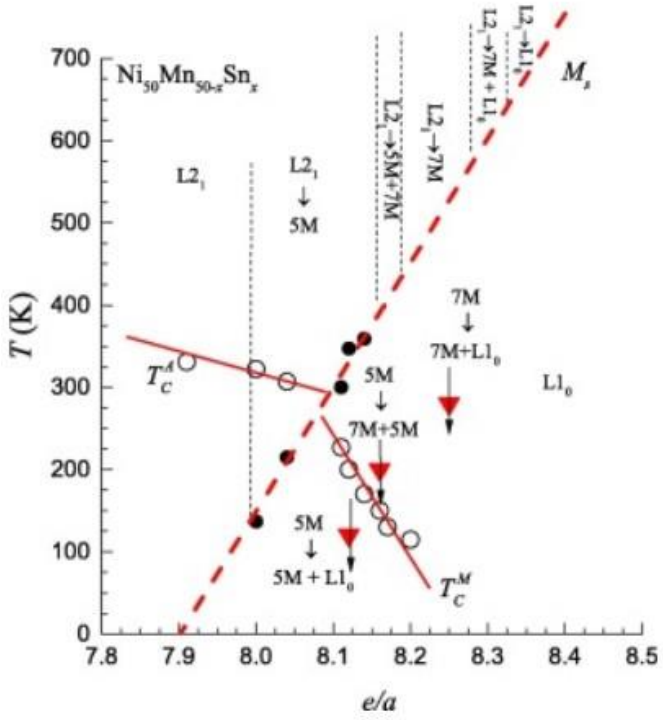

Figure 1. 14. Phase diagram of Ni-Mn-Sn system where the filled circles indicate the temperature of the martensitic transformation, the open circles correspond to austenite and martensite Curie temperature and triangles correspond to the intermartensitic transitions [57].

In the case of Ni-Mn-Sb system, a similar systematic study was performed modifying the composition by replacing Sb by Mn atoms [76, 136] in the $Ni_{50}Mn_{50-x}Sb_x$ series. Like in the case of Ni-Mn-In and Ni-Mn-Sn, the stoichiometric Ni-Mn-Sb alloy does not present MT, the transformation appearing for valence-electron concentrations e/a≥8.185. In this way, for lower values of e/a, the alloy presents an austenite structure, undergoing only a magnetic ordering transition that takes place at temperatures ranging from 360K in the stoichiometric sample to 340K in the case of the alloy with e/a=8.173. The M(H) curves measured at 5K in those alloys show that the saturation magnetization is reduced with the increase of Mn in the alloy, which is attributed to the tendency of the extra Mn located in Sb sublattice to couple antiferromagnetically with the Mn located in its own sublattice. With the decrease of the value of x and the increase in the valence-electron concentration, the MT appears first for the sample with e/a=8.185 at 170K, with T_C at 339K. As Figure 1. 15 shows, as e/a increases, the temperature of the MT shows a clear increase, while T_C^A and T_C^M decrease (slightly and markedly, respectively). For high values of e/a the MT rises to high temperatures (up to 709K) and the alloys show antiferromagnetic coupling between Mn atoms as in the case of $Ni_{50}Mn_{50}$.

On the other hand, the crystallographic structures obtained by X-ray diffraction reveal $L2_1$ structures in the austenite phase and different types of structure in martensite, from the tetragonal $L1_0$ structure with *P4/mmm* space group and the 4O orthorhombic structure obtained by Sutou [49], with space group *Pnnm* and *Pmma,* to 7-fold modulated orthorhombic structures [42].

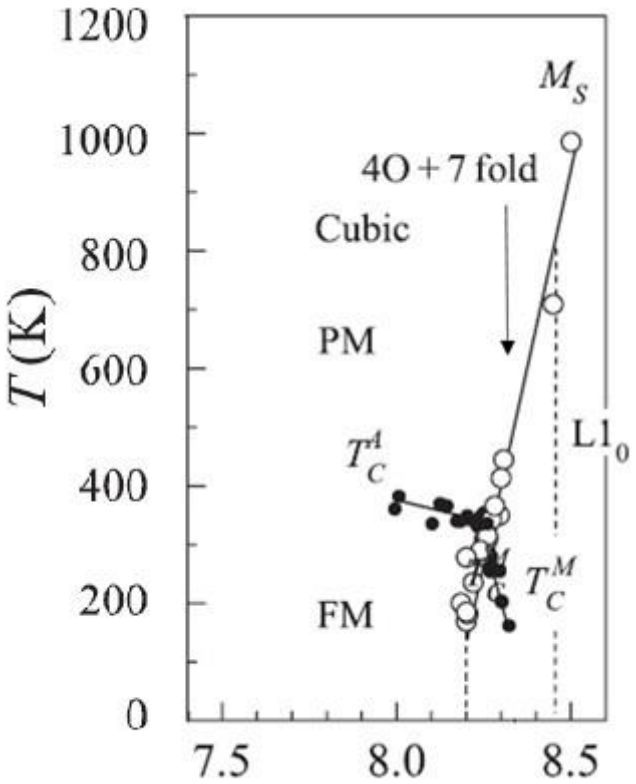

Figure 1. 15. Phase diagram of Ni-Mn-Sb system as a function of e/a [76].

Figure 1. 16 shows a comparative of the phase diagrams of Ni-Mn-Z (Z= Ga, In, Sn, Sb) alloys. The reason for the differences in the *e/a* dependencies of M_S for different Z-elements is attributed to the differences in both the density of conduction electrons and the unit cell parameters of the austenite phase. According to the band model, the Fermi surface just touches the (110) Brillouin zone boundary to achieve a stable $L2_1$ [137]. With increasing valence electron number, the energy of the conduction electrons exceeds the Fermi level and moves to the corners of the Brillouin zone giving rise to an increase in the energy of the system. In such a case, the system tends to minimize the free energy by creating the distortions. The new Brillouin zone pattern corresponds to the new crystal structure, which is martensite [129, 138]. The increase in the density of the valence electron number leads to a higher M_S and, depending on the excess in the conduction electrons at the Fermi level, the different martensite structures form. For the set of alloys series, T_C^M decreases more rapidly than T_C^A with e/a because of the fact that the lower unit-cell volume in the martensite state leads to strengthened antiferromagnetic interactions. The strength of the magnetic interactions between Mn atoms is

also strongly correlated with the number of conduction electrons [139]. The reason of the decrease of T_C^M and T_C^A lies in the rise in significance of antiferromagnetic interactions as Z content decreases, due to the increase in the number of Mn–Mn nearest neighbors and to the decrease in Mn–Mn distances (see below), with the magnetic coupling becoming antiferromagnetic at low Z contents like in $Ni_{50}Mn_{50}$.

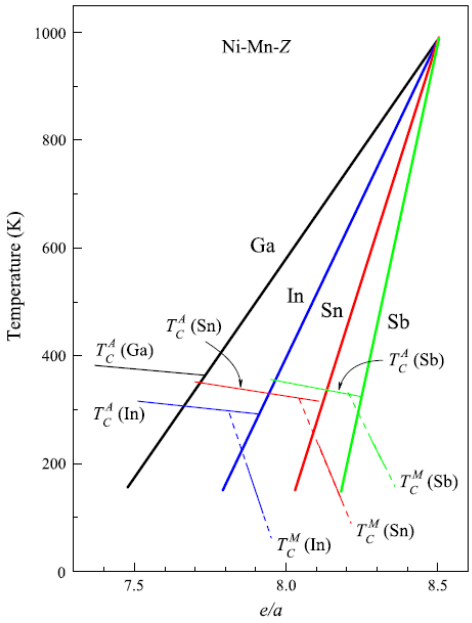

Figure 1. 16. Dependence of e/a relation with martensitic transformation and the Curie temperature for austenite (T_C^A) and martensite (T_C^M) [85].

The e/a dependence of the magnetic moment for Ni–Mn–Z alloys in cubic phase is shown in Figure 1. 17. This figure shows how the magnetic moment increases continuously with e/a as we increase the amount of magnetic atoms (Mn), up to a certain inflection point, where it starts decreasing. This inflection occurs when antiferromagnetic interactions become significant, essentially due to the excess of Mn. Comparing the different series, it becomes evident that, when the atomic radius of the Z element is smaller (and therefore the lattice parameters and interatomic distances are smaller), the inflection point occurs for lower values of e/a, since a smaller Mn-Mn distance favors antiferromagnetic interactions. [55, 140].

The interatomic distances represent clearly a key parameter in the properties of these alloys and, in particular, for the magnetic coupling. In order to assess the effect of e/a in the interatomic distances, we can compare the lattice constant in the $L2_1$ phase for the set of series $Ni_{50}Mn_{50-x}Z_x$ (Figure 1. 18) [85]. For a given Z, the lattice constant of the austenite phase decreases with decreasing Z content. Also, if we compare the series with Z = In, Sn, Sb – in the same row of the periodic table – the values of the lattice parameter show a continuous decrease with increasing e/a. When comparing Z = In with Z = Ga series, since In and Ga are isoelectronic, replacing one of these elements by the other causes a change in the lattice constant without altering the electron concentration (series $Ni_{50}Mn_{25}Ga_{25-x}In_x$ in Figure 1. 18). The whole picture

shows that MT is present for alloys with lattice constant in austenite below a critical value around 6 Å.

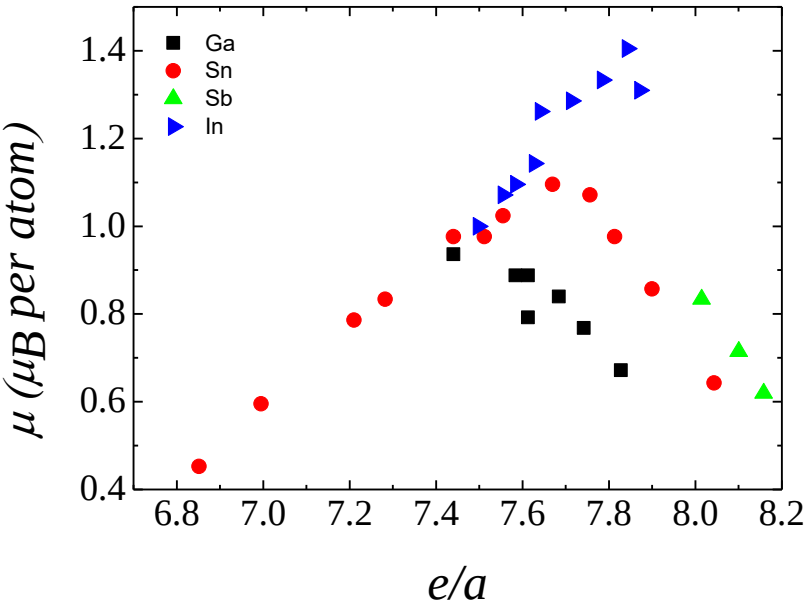

Figure 1. 17. The e/a dependence of the magnetic moment per atom [85, 132].

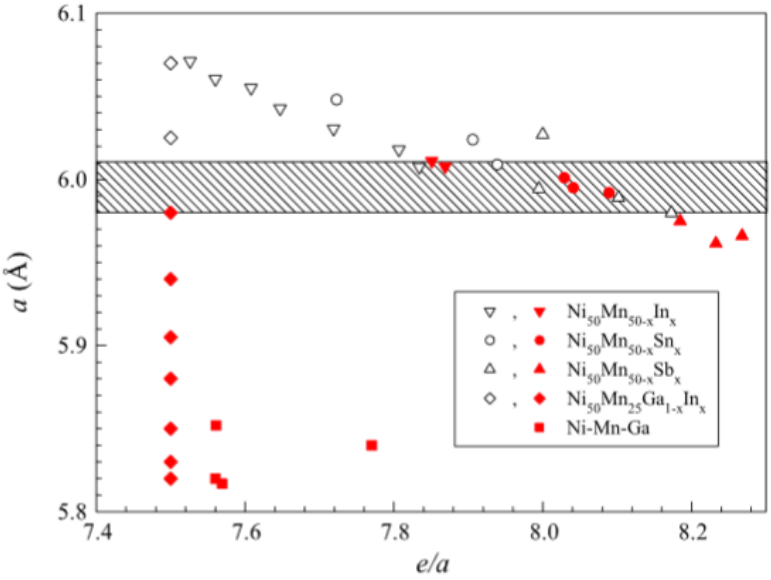

Figure 1. 18. The e/a dependence of the lattice parameter of the cubic phase at room temperature in Ni-Mn-based Heusler alloys. The alloys that does not present martensitic transformation are represented by open symbols [85].

The addition of another 3d element was studied also in the Ni-Mn-Z alloys in order to investigate the effect that this doping produces in the physical properties [141–148]. In particular, the doping with Co has been shown to enhance the magnetism of the austenite,

increasing the ΔM associated to the MT and therefore improving the magnetic properties relevant for applications (producing larger magnetically-induced shifts of the MT temperatures and higher associated magnetocaloric effect) [73, 86, 90, 119, 149–151]. Co doping in Ni-Mn-In and Ni-Mn-Sn systems has been proved to increase both the Curie temperature and the spontaneous magnetization of the austenite by the enhancement of the ferromagnetic coupling [73, 152], leading to an increase of the variation of the magnetization at the MT. Neutron powder diffraction in Ni-Mn-Sn and Ni-Co-Mn-Sn has shown that the Co atoms share 8*c* sites with Ni while the magnetic coupling between the Mn moments on the 4*a* (Mn sublattice) and 4*b* (Sn sublattice) of the austenitic cubic structure becomes more ferromagnetic [73]. Density-functional theory studies in Co-Mn-Sn and Ni-Mn-Sn show that the ferromagnetic exchange interaction between Co and Mn is several times larger than the exchange interaction between Ni and Mn [74]. Therefore, the substitution of Ni by Co increases the ferromagnetic interactions, favoring the ferromagnetic coupling of the Mn moments. The magnetism of the martensite is also affected by the Co doping. For example, in the case of Ni-Co-Mn-Ga it has been demonstrated by neutron powder diffraction that the martensitic phase presents long-range antiferromagnetic order in the range of $T_C^M < T < M_f$ [153], which results in a larger ΔM at the MT.

1.5.2. Atomic order

The structural and magnetic properties of the Ni–Mn based Heusler alloys depend on the atomic order as long as the variations on the configurational ordering of the constituting elements in the crystal lattice affect both the MT and the magnetic moment of the alloy. This is related to the modification of both the electronic structure and the lattice site occupancy by the magnetic atoms. The long-range atomic order can be modified either by changing the composition or, once the composition is fixed, by means of different thermal treatments, such as quenching from high temperature or post-quench aging.

Due to its dependence on Mn-Mn distance, the exchange interactions in the cubic $L2_1$ austenitic phase of these alloys are directly related to atomic order (the Mn moments on the regular 4*a* sites are ferromagnetically coupled, whereas different Mn-Mn exchange interactions may appear between Mn atoms at the 4*b* sites and those in the 4*a* sublattice). Therefore, a complete correlation between long-range atomic order and exchange interactions is needed in order to properly tune the magnetic properties of these alloys. Such a correlation has been recently stablished in Ni-Mn-In alloys, in which the atomic order was modified by means of thermal treatments [29]. In Ni-Mn-Sn, in turn, the extraordinary high stability of the $L2_1$ structure precludes the variation of atomic order by means of conventional thermal treatments, and therefore no analogous study has been performed. In fact, previous studies based on configurational disorder in off-stoichiometric alloys points out to both ferromagnetic [51] and antiferromagnetic [73] coupling between Mn moments at 4*a* and 4*b* sites, so some controversy concerning the nature of the exchange interactions in the austenitic phase of Ni-Mn-Sn alloys still persists.

The characteristic $L2_1$ structure corresponding to the Heusler alloy, presenting a complete next-nearest-neighbor atomic order, is only possible in stoichiometric compounds

Ni_2-Mn-Z (Z= Ga, In, Sn, Sb), in which all atoms are located in its own sublattice. The first studies on the influence of the atomic order on the MT were carried out by Kreissl et. al. on the Ni_2MnGa compound. In this analysis they quenched the alloy from 1073 K and 1273K showing a shift of ~100K to lower temperature in the MT temperature for the alloy quenched from higher temperature, accompanied by a reduction in the ferromagnetic moment [21, 154].

Several systematic studies have been performed in Ni-Mn-Z alloys out of the stoichiometry, aiming at determining the long-range atomic order and its dependence on thermal treatments. In this sense, neutron powder thermo-diffraction measurements have been proven to be a powerful tool to quantify the atomic order from the analysis of the integrated intensity of the (111) and (200) reflections, which correspond to $L2_1$ and B2 structure, respectively [155]. In fact, the order parameter corresponding to the $L2_1$ structure, η_{L21} (which ranges from 0, for the B2 structure, to 1, for the maximum next-nearest-neighbor atomic order), can be assumed as $\eta_{L21} \approx (I_{(111)})^{1/2}$ [155].

In the case of Ni-Mn-Ga, Sanchez-Alarcos et. al. [26, 28, 156] analyzed the effect of the thermal treatments and its relation with the atomic order in two different ways: i) by quenching the alloy from different temperatures and ii) by post-quenching aging treatments at moderate temperatures. Both types of thermal treatment produce changes in the long-range atomic order of the alloy, retaining different degrees of disorder by quenching or recovering the order by aging. Both kinds of treatments are equivalent since the final parameter, which controls the MT and magnetic properties, is the degree of long-range atomic order. It was found that the MT and Curie temperatures shift to lower temperatures after quenching from high temperatures, where the atomic order degree is low. In the case of the post-quench aging, both critical temperatures increase as a consequence of the recovery of atomic order. The calorimetric measurements carried on the quenched samples have shown the presence of an exothermic peak at temperatures around 600K linked to the recovery of the metastable quenched state. In the second heating, this peak does not appear again, what implies the irreversibility of this process. Neutron experiments were carried out starting from the as quenched state at room temperature and heating up to 1173K (Figure 1. 19). A slight increase in the integrated intensity of the peak (111), linked to $L2_1$ order, is observed in the temperature range where the exothermic process takes place. At higher temperature, the order $L2_1$ disappears according to the order-disorder transition $L2_1$-B2. During the second heating ramp, the integrated intensity shows the maximum degree of long-range atomic order allowed by the stoichiometry at each temperature.

Rietveld refinement in paramagnetic austenite was carried out in both states, before and after heating the alloy to 1173K, and the result revealed a small amount of Ga atoms ~0.5% in Mn sublattice displacing the same amount of Mn to the Ga sublattice for the as-quench sample; this disorder induced by quenching treatments is recovered on further heating. The migration of Mn – the main responsible of the magnetic behavior – to its own sublattice produces an increment in the ferromagnetic coupling. This increment in the ferromagnetic coupling is the cause of the increment of the saturation magnetization and the shift of the magnetic ordering to higher temperatures. In the case of Ni-Mn-Ga, the effect of atomic order is particularly pronounced for the martensitic structure, stabilizing this structure with respect to austenite. The final result is an increase of the MT temperature as consequence of the atomic ordering [20, 26, 140, 157].

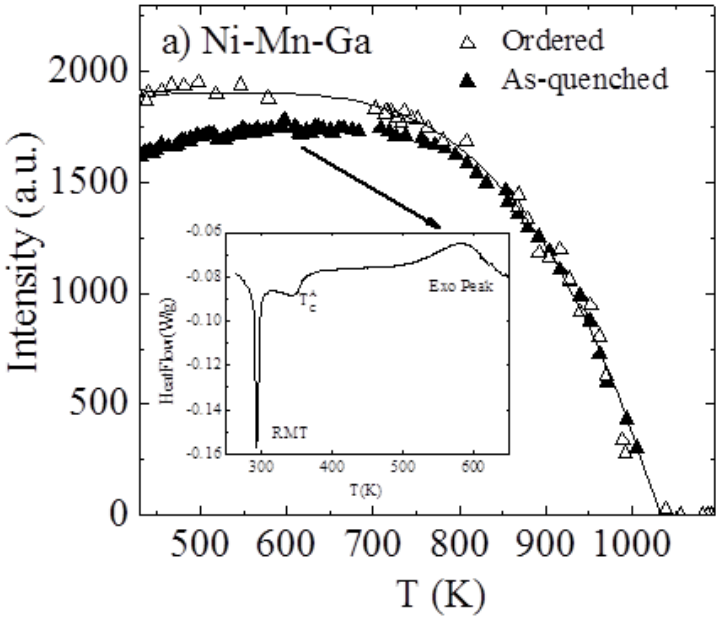

Figure 1. 19. Evolution of the integrated intensity of the (111) peak of a Ni-Mn-Ga alloy, linked to $L2_1$ atomic order, as a function of temperature. As-quenched state corresponds to the first heating ramp and ordered state to the second one. Inset: Exothermic peak only observed during the first heating linked to irreversible recovery of the as-quenched induced atomic disordering.

Recarte et al [29] reported an analogous study in Ni-Mn-In system, presenting its response to the thermal treatments. As happens in Ni-Mn-Ga alloys, the Curie temperature decreases with the increase of the quenching temperature, but the MT has an opposite variation, increasing with quenching temperature. Concerning post-quench aging, the MT and Curie temperature have also opposite displacements, with the magnetic order temperature going to higher temperatures and the MT shifting to lower temperatures as the aging temperature (and therefore the degree of atomic ordering) increases. Again, the exothermic peak observed by calorimetric measurements, which disappears during a second heating ramp, has been related with the increased atomic order that is observed by "in situ" neutron thermo-diffraction. The evolution of the (111) peak integrated intensity shows the maximum value during the first heating at the temperatures of the exothermic peak, and decreases on further heating as a result of the order-disorder transition $L2_1$-B2 (Fig. 1.20), while during the second heating ramp, the integrated intensity shows a higher degree of long-range atomic order at all temperatures [29]. Once more, the displacement of the Mn atoms to their own sublattice enhances the ferromagnetic coupling and increases the Curie temperature. However, for this metamagnetic alloy the enhancement of magnetism of the austenite stabilizes this phase against martensite and the MT shifts to lower temperatures as the degree of atomic order increases.

On the other hand, similar studies in Ni-Mn-Ga and Ni-Mn-In alloys with high values of e/a ratio, [158] with the MT occurring between a paramagnetic austenite and a paramagnetic

martensite, which orders magnetically at lower temperatures, demonstrated that atomic ordering only affects the Curie temperature. Again, the increase of the atomic order modifies the magnetic coupling between Mn atoms increasing the magnetic order temperature. Nevertheless, the MT is not modified since no magnetically ordered state is involved in the MT.

Then, it is found that the atomic order variations associated to the thermal treatments affect the structural transformation in a different way depending on the character of the magnetic ordering in the austenitic and the martensitic phases. The variation on the atomic order only affects the MT temperature in those alloys in which at least one of the structural phases shows magnetic order at the transformation temperature, whereas those transformations taking place between paramagnetic phases remain unaffected. The observed behaviors are explained in terms of the effect of the magnetic exchange coupling variations on the free energy difference between austenite and martensite. In particular, it has been proposed that the increase of the atomic order degree stabilizes the structural phase showing higher magnetic moment. The obtained results demonstrate the key role of magnetism on the MT [158].

Completing the investigation of the atomic order effect in the metamagnetic shape memory alloys, analogous studies have been reported for in Ni-Mn-Sn and Ni-Mn-Sb systems, showing different behavior. Neutron powder diffractograms were measured from room temperature to 1173K revealing that the (111) peak does not disappear (Figure 1. 20), meaning that there is no $L2_1$-B2 order-disorder transition. The evolution of the intensity of the (111) peak shows a small and continuous decrease in the integrated intensity. Extrapolating the curve, the value for the $L2_1$-B2 transition temperatures would be at temperatures higher than the melting point (1300K), which implies that in these alloys the $L2_1$ structure is exceptionally stable. Furthermore, the different thermal treatment carried out do not modify neither the MT nor the Curie temperature of the austenitic phase.

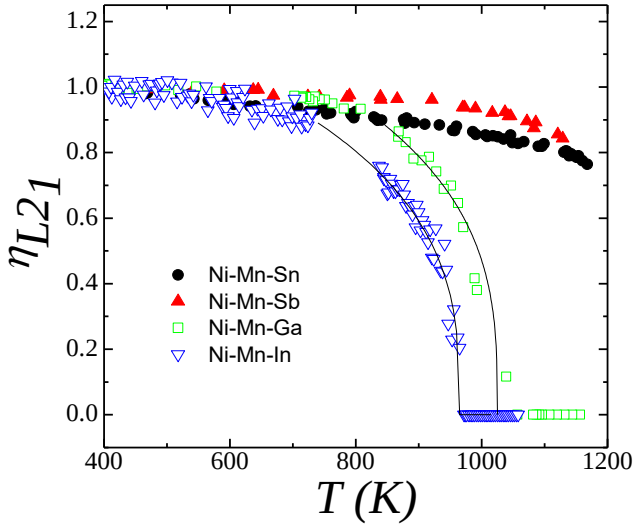

Figure 1. 20. Temperature dependence of the $L2_1$ atomic order parameter in Ni-Mn-Sn, Ni-Mn-Sn, Ni-Mn-Ga and Ni-Mn-In [32].

Figure 1. 21 summarizes the general behavior of Ni-Mn-Z shape memory alloys under modification of the atomic order degree. In this figure, the evolution of T_C, of the MT temperature, T_M and of the change of the saturation magnetization at the MT, ΔM, as a function of quenching temperature are shown. As it has been previously explained, the higher the quenching temperature the lower the degree of atomic order. ΔM corresponds to the absolute value at the MT, i.e. $\Delta M = M_{mart} - M_{aust}$ for Ni-Mn-Ga and $\Delta M = M_{aust} - M_{mar}$ for the three metamagnetic systems. The enhancement of Mn-Mn ferromagnetic coupling through the increase of atomic order produces an increase T_C for the systems where the atomic order can be significantly modified, i.e. Ni-Mn-Ga and Ni-Mn-In. Also, ΔM increases with atomic order for both systems. Finally, the magnetic coupling enhancement promoted by atomic order stabilizes the structural phase showing higher magnetic moment, producing and increase and a decrease of the MT temperature for the Ni-Mn-Ga and Ni-Mn-In alloys, respectively. On the other hand, the Z = Sn, Sb alloys show a null variation of T_C, T_M and ΔM, due to the exceptional stability of their atomic order degree.

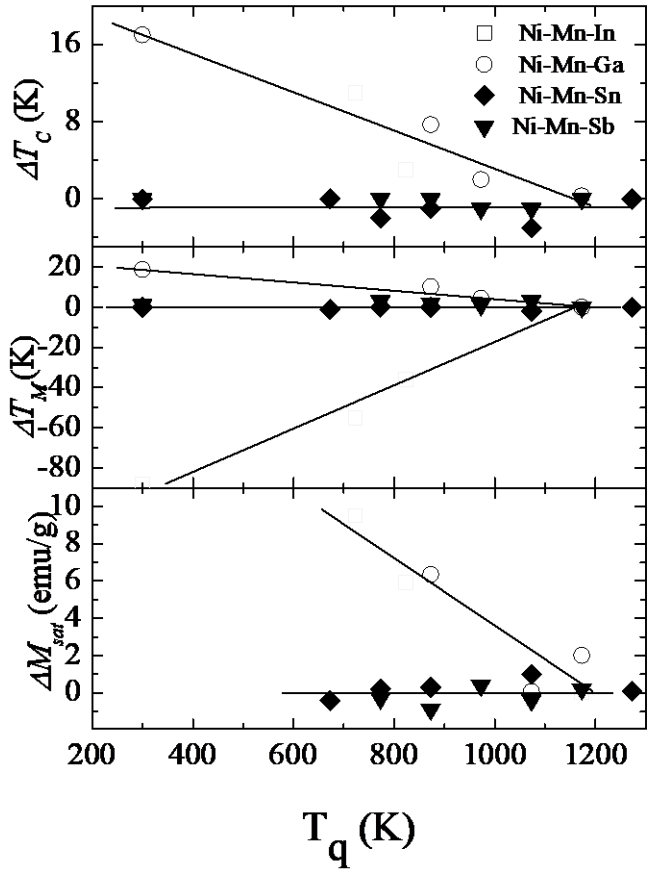

Figure 1. 21. Shift of the Curie temperature, ΔT_C, the martensitic transformation temperature, ΔT_M, and the magnetization change at the MT, ΔM, as a function of the quenching temperature. Values for the highest quenching temperature have been taken as reference. ΔM is the absolute value at the MT, i.e. $\Delta M = M_{mart} - M_{aust}$ for Ni-Mn-Ga and $\Delta M = M_{aust} - M_{mar}$ for the three metamagnetic systems.

1.5.3. Microstructure

The microstructure of the alloy may also affect the magnetostructural properties of metamagnetic shape memory alloys as long as the variations in the microstructural parameters (grain size, vacancies, grain boundaries, dislocations, internal stresses, precipitates, antiphase boundaries, etc …) may result in a local modification of composition, interatomic distances or atomic order. The influence of microstructure is especially interesting in Ni-Mn-Sn and Ni-Mn-Sb alloys, in which the $L2_1$ structure is highly stable and the atomic order is then hardly modifiable by means of conventional thermal treatments [32]. In these alloys, the modification of the microstructural parameters appears as the only way to modify the functional properties for a selected alloy composition.

Mechanical milling and subsequent annealing treatments are among the simplest and most used methods to modify the microstructure. Typically, the grain size reduction and the presence of defects and internal stresses induced by milling degrade the MT and the magnetic properties, which can be then partially restored upon microstructural recovery processes brought by subsequent annealing [68, 83, 159–162]. Even though the grain size and the state of internal tensions are known to be two parameters highly influencing the characteristics of the MT through the variation of the elastic energy term [163], up to now, less work has been devoted to the analysis of the MT and the magnetic properties at reduced sizes tending to nanoscale. In this sense, it has been recently proposed that below a critical size, shape memory alloy nanoparticles show non hysteretic behavior [164]. Taking into account that the transformation hysteresis linked to a first order transition is an important drawback for magnetocaloric applications, nanoparticle alloys seem to be a promising alternative procedure to improve simultaneously the mechanical behavior (see below) and the MCE required for refrigeration systems.

On the other hand, one of the main drawbacks of the metamagnetic shape memory alloys is the poor mechanical properties they show. These alloys are very brittle and difficult to handle, and cracks form very easily when the crystal is being thermally cycled through the phase transformation [165, 166]. Alloys in form of films, ribbons, wires or foams [167–170] have been studied as an alternative to overcome the mechanical limitations of the bulk material. In particular, the integration of powder alloys into a polymer to form composites has been found to be especially interesting for the development of magnetically-controlled dampers and actuators. Such composites may show low cost, large mechanical energy absorption and good mechanical properties [171, 172]. In this case, a previous complete characterization of the powder alloy is needed in order to properly tune the response of the composites.

Ball milling technique is one of the simplest and cheapest methods to produce nanostructured materials. The use of ball milling as a reduction method to nanoscale size has been studied in multiple systems, and interesting physical and chemical phenomena have been

found to appear. A considerable modification of the magnetic behavior and the synthesis of new phases have been reported [173–175]. For instance, the reduction in the size of particles by ball milling may optimize the MCE in different magnetic systems, either by increasing the temperature range [176] or by reducing the hysteretic losses linked to a magnetostructural first order transformation [177]. On the other hand, together with grain size reduction, ball milling produces a huge amount of defects (vacancies, dislocations, chemical disorder, strains…) in the material. A proper analysis of the milled powder may therefore provide valuable information concerning the influence of those defects on both the MT and the magnetic properties.

The effect of ball milling on the magnetostructural properties has been studied in Ni-Mn-Ga, where the effect of thermal treatments has been widely characterized and different sequences of structural transition (different from those in the corresponding bulk) have been found in the achieved nanoparticles [178–181]. Likewise, nanoparticles of Ni-Mn-Sn and Ni-Mn-In have been recently obtained by ball milling [159, 161, 182, 183]. As in Ni-Mn-Ga, atomic disorder and lattice strain inhibit the MT in the as-milled alloys, while post-mill annealing treatments are needed to restore the MT. A significant influence of annealing on the ferromagnetic exchange interaction, exchange bias and MCE, has been also reported in these alloys. In any case, a systematic study of the effect of mechanically-induced microstructural defects on the structural and magnetic properties of metamagnetic shape memory alloys is still absent.

1.6. OBJECTIVES AND THESIS STRUCTURE

The aim of this thesis is the study of routes to obtain improved magnetostructural properties in metamagnetic shape memory alloys, mainly through the modification of the microstructural parameters. This thesis is organized in seven chapters including an introduction, the techniques used and all the results. In this way, Chapter 1 provides a general introduction to the main concepts and a summary of the most relevant work related with the topic of the thesis published up to the present date. Chapter 2 explains the different experimental techniques employed during this thesis, starting from the synthesis of the alloys and the mechanical and thermal treatments performed in the samples, following with the macroscopic (calorimetric and magnetic) characterization, and finishing with the microscopic study, mainly through diffraction experiments. The results obtained during this research are reported in Chapters 3, 4, 5 and 6, structured as follows:

- Correlation between microstructure and magnetostructural properties in Ni-Mn-Sn system. Characterization of the microstructure induced by thermo-mechanical treatments and its relation with the properties of the alloys (particularly the magneto-caloric effect). (Chapter 3)
- Improvement of magnetostructural properties by Co addition. Correlation between microstructure and magnetostructural properties in Ni-Mn-Sn-Co system. Improvement of magnetocaloric effect in a Ni-Mn-Sn-Co alloy subjected to soft milling. Evolution of

the microstructural parameters and the magnetostructural properties with the milling time. (Chapter 4)

- Understanding the effect of Co-doping in the magnetic coupling using the Ni-Mn-In system as case study. (Chapter 5)
- Study of the recrystallization process in Co doped Ni-Mn-In and Ni-Mn-Sn alloys amorphized by milling. (Chapter 6)

Chapter 3 is divided in three parts. The first part consists in obtaining the microstructural parameters of a $Ni_{50}Mn_{35}Sn_{15}$ alloy subjected to different thermal treatments after hand-milling in agate mortar by using laboratory X-rays and its magnetic characterization, relating the defects on the sample with the internal strains state induced by the milling and annealing processes. In the second part, the crystal and magnetic structures of the alloys were obtained by powder neutron diffraction, allowing relating the magnetocaloric effect with the magnetic coupling in austenite and martensite. In the last part, Mössbauer spectroscopy was used to complete the magnetic characterization on the sample set, showing that it is possible to use this technique to characterize the microstructure. In Chapter 4, the magnetostructural properties were studied in $Ni_{45}Co_5Mn_{35}Sn_{15}$ alloy in milled and in annealed samples, showing an improvement of the magnetostructural properties by Co addition and an improved magnetocaloric effect in the soft-milled alloy. Due to this unconventional result, a systematic study on the microstructure was undergone by mechanical ball-milling, showing the evolution of the microstructural parameters and the magnetostructural properties with the milling time. The microstructure parameters were analyzed by powder diffraction using synchrotron radiation. In Chapter 5, the atomic order and the magnetic structure for $Ni_{50}Mn_{34}In_{16}$ and $Ni_{45}Co_5Mn_{37}In_{13}$ alloys with two different thermal treatments were studied by neutron diffraction in order to understand the effect of thermal treatments and Co-doping on the austenite magnetism. Polarized neutron single-crystal diffraction in $Ni_{45}Co_5Mn_{37}In_{13}$ contributes to clarify the interaction pathways between the different atomic positions in the high temperature phase. Since long milling times lead to amorphous states, the recrystallization processes have been studied in Chapter 6, with the analysis of the evolution of the different phases, the cell parameters and the parameters as grain size, micro and macrostrains. Finally, a summary of the main conclusions is presented in Chapter 7.

Bibliography.

[1] C. M. Wayman, *Introduction to the crystallography of martensitic transformations*. New York: Macmillan, 1964.

[2] M. Cohen, *Proceedings of the International Conference on Martensitic Transformations: ICOMAT 1979 : Cambridge, Massachusetts, 24-29 June, 1979*. Department of Materials Science and Engineering, MIT, 1979.

[3] Z. Nishiyama, *Martensitic Transformation*. Elsevier, 2012.

[4] K. Otsuka, C. M. Wayman, Shape Memory Materials-Cambridge University Press (1998) | Shape Memory Alloy | Crystal Structure.

[5] C. M. Wayman, *Physical Metallurgy*, Elsevier Science publisher BV. R. W. Cahn, P. Haasen, 1983.

[6] C. M. Wayman, *Engineering Aspects of Shape Memory Alloys*, Butterworth-Heinemann Ldt. T. W, Duering, K.N Melton, D. Stöckel, C. M. Wayman, 1990.

[7] K Bhattacharya, *Microstructure of Martensite*, Oxford University Press. A. P. Sutton, R. E. Rudd, 2003.

[8] J. W. Christian, *The theory of transformations in metals and alloys*, Pergarmon Press. Oxford, 1975.

[9] Q.-P. Sun, *IUTAM Symposium on Mechanics of Martensitic Phase Transformation in Solids*. Springer Science & Business Media, 2013.

[10] A. A. Cherechukin, V. V. Khovailo, R. V. Koposov, E. P. Krasnoperov, T. Takagi, and J. Tani, "Training of the Ni–Mn–Fe–Ga ferromagnetic shape-memory alloys due cycling in high magnetic field," *J. Magn. Magn. Mater.*, vol. 258–259, pp. 523–525, Mar. 2003.

[11] L. Contardo and G. Guénin, "Training and two way memory effect in Cu-Zn-Al alloy," *Acta Metall. Mater.*, vol. 38, no. 7, pp. 1267–1272, Jul. 1990.

[12] M. Kohl, *Shape Memory Microactuators*. Springer Science & Business Media, 2013.

[13] N. B. Morgan, "Medical shape memory alloy applications—the market and its products," *Mater. Sci. Eng. A*, vol. 378, no. 1, pp. 16–23, Jul. 2004.

[14] S. A. Shabalovskaya, "On the nature of the biocompatibility and on medical applications of NiTi shape memory and superelastic alloys," *Biomed. Mater. Eng.*, vol. 6, no. 4, pp. 267–289, Jan. 1996.

[15] L. G. Machado and M. A. Savi, "Medical applications of shape memory alloys," *Braz. J. Med. Biol. Res.*, vol. 36, no. 6, pp. 683–691, Jun. 2003.

[16] G. Song, N. Ma, and H.-N. Li, "Applications of shape memory alloys in civil structures," *Eng. Struct.*, vol. 28, no. 9, pp. 1266–1274, Jul. 2006.

[17] T. W. Duerig, K. N. Melton, and D. Stöckel, *Engineering Aspects of Shape Memory Alloys*. Butterworth-Heinemann, 2013.

[18] H. Fu, S. Song, L. Zhuo, Z. Zhang, and J. Xie, "Enhanced mechanical properties of polycrystalline Cu–Al–Ni alloy through grain boundary orientation and composition control," *Mater. Sci. Eng. A*, vol. 650, pp. 218–224, Jan. 2016.

[19] F. A. Hames, "Ferromagnetic-Alloy Phases Near the Compositions Ni2MnIn, Ni2MnGa, Co2MnGa, Pd2MnSb, and PdMnSb," *J. Appl. Phys.*, vol. 31, no. 5, pp. S370–S371, May 1960.

[20] M. L. Richard *et al.*, "Chemical order in off-stoichiometric Ni–Mn–Ga ferromagnetic shape-memory alloys studied with neutron diffraction," *Philos. Mag.*, vol. 87, no. 23, pp. 3437–3447, Aug. 2007.

[21] M. Kreissl, K.-U. Neumann, T. Stephens, and K. R. A. Ziebeck, "The influence of atomic order on the magnetic and structural properties of the ferromagnetic shape memory compound Ni 2 MnGa," *J. Phys. Condens. Matter*, vol. 15, no. 22, p. 3831, 2003.

[22] W. Ito, M. Nagasako, R. Y. Umetsu, R. Kainuma, T. Kanomata, and K. Ishida, "Atomic ordering and magnetic properties in the Ni45Co5Mn36.7In13.3 metamagnetic shape memory alloy," *Appl. Phys. Lett.*, vol. 93, no. 23, p. 232503, Dec. 2008.

[23] R. W. Overholser, M. Wuttig, and D. A. Neumann, "Chemical ordering in Ni-Mn-Ga Heusler alloys," *Scr. Mater.*, vol. 40, no. 10, pp. 1095–1102, Apr. 1999.

[24] D. L. Schlagel, R. W. McCallum, and T. A. Lograsso, "Influence of solidification microstructure on the magnetic properties of Ni–Mn–Sn Heusler alloys," *J. Alloys Compd.*, vol. 463, no. 1, pp. 38–46, Sep. 2008.

[25] V. V. Khovailo, T. Takagi, A. N. Vasilev, H. Miki, M. Matsumoto, and R. Kainuma, "On Order–Disorder (L21 → B2′) Phase Transition in Ni2+xMn1—xGa Heusler Alloys," *Phys. Status Solidi A*, vol. 183, no. 2, pp. R1–R3, 2001.

[26] V. Sánchez-Alarcos, V. Recarte, J. I. Pérez-Landazábal, and G. J. Cuello, "Correlation between atomic order and the characteristics of the structural and magnetic transformations in Ni–Mn–Ga shape memory alloys," *Acta Mater.*, vol. 55, no. 11, pp. 3883–3889, Jun. 2007.

[27] T. Miyamoto, W. Ito, R. Y. Umetsu, R. Kainuma, T. Kanomata, and K. Ishida, "Phase stability and magnetic properties of Ni50Mn50−xInx Heusler-type alloys," *Scr. Mater.*, vol. 62, no. 3, pp. 151–154, Feb. 2010.

[28] V. Sánchez-Alarcos, J. I. Pérez-Landazábal, and V. Recarte, "Influence of Long-Range Atomic Order on the Structural and Magnetic Properties of Ni-Mn-Ga Ferromagnetic Shape Memory Alloys," *Materials Science Forum*, Vol. 684, pp. 85-103, 2011.

[29] V. Recarte, J. Pérez-Landazábal, V. Sánchez-Alarcos, and J. A. Rodriguez-Velamazán, "Dependence of the martensitic transformation and magnetic transition on the atomic order

in Ni–Mn–In metamagnetic shape memory alloys," *Acta Mater.*, vol. 60, pp. 1937–1945, Mar. 2012.

[30] V. Sánchez-Alarcos, V. Recarte, J.I. Pérez-Landazábal, S. Larumbe, R. Caballero-Flores, I. Unzueta, J.A. García, F. Plazaola, J.A. Rodríguez-Velamazán, "Mechanically induced disorder and crystallization process in Ni-Mn-In ball-milled alloys," *J. Alloys Compd.*, vol. 689, pp. 983–991, Dec. 2016.

[31] V. Sánchez-Alarcos, V. Recarte, J. I. Pérez-Landazábal, E. Cesari, and J. A. Rodríguez-Velamazán, "Long-Range Atomic Order and Entropy Change at the Martensitic Transformation in a Ni-Mn-In-Co Metamagnetic Shape Memory Alloy," *Entropy*, vol. 16, no. 5, pp. 2756–2767, May 2014.

[32] V. Sánchez-Alarcos, J. I. Pérez-Landazábal, V. Recarte, I. Lucia, J. Vélez, and J. A. Rodríguez-Velamazán, "Effect of high-temperature quenching on the magnetostructural transformations and the long-range atomic order of Ni–Mn–Sn and Ni–Mn–Sb metamagnetic shape memory alloys," *Acta Mater.*, vol. 61, no. 12, pp. 4676–4682, Jul. 2013.

[33] P. J. Webster, K. R. A. Ziebeck, S. L. Town, and M. S. Peak, "Magnetic order and phase transformation in Ni2MnGa," *Philos. Mag. B*, vol. 49, no. 3, pp. 295–310, Mar. 1984.

[34] A. Planes and L. Mañosa, "Vibrational properties of shape-memory alloys," in *Solid State Physics*, vol. 55, H. Ehrenreich and F. Spaepen, Eds. Academic Press, 2001, pp. 159–267.

[35] S. Fujii, S. Ishida, and S. Asano, "Electronic Structure and Lattice Transformation in Ni2MnGa and Co2NbSn," *J. Phys. Soc. Jpn.*, vol. 58, no. 10, pp. 3657–3665, Oct. 1989.

[36] P. J. Brown, A. Y. Bargawi, J. Crangle, K.-U. Neumann, and K. R. A. Ziebeck, "Direct observation of a band Jahn-Teller effect in the martensitic phase transition of Ni2MnGa," *J. Phys. Condens. Matter*, vol. 11, no. 24, pp. 4715–4722, Jan. 1999.

[37] P. A. Bhobe, K. R. Priolkar, and P. R. Sarode, "Local atomic arrangement and martensitic transformation in Ni 50 Mn 35 In 15 : an EXAFS study," *J. Phys. Appl. Phys.*, vol. 41, no. 4, p. 045004, 2008.

[38] P. A. Bhobe, K. R. Priolkar, and P. R. Sarode, "Factors influencing the martensitic transformation in Ni 50 Mn 35 Sn 15 : an EXAFS study," *J. Phys. Condens. Matter*, vol. 20, no. 1, p. 015219, 2008.

[39] A. Zheludev, S. M. Shapiro, P. Wochner, A. Schwartz, M. Wall, and L. E. Tanner, "Phonon anomaly, central peak, and microstructures in Ni_2MnGa," *Phys. Rev. B*, vol. 51, no. 17, pp. 11310–11314, May 1995.

[40] J. I. Pérez-Landazábal, V. Recarte, V. Sánchez-Alarcos, J. A. Rodríguez-Velamazán, M. Jiménez-Ruiz, P. Link, E. Cesari, and Y. I. Chumlyakov, "Lattice dynamics and external magnetic-field effects in Ni-Fe-Ga alloys," *Phys. Rev. B*, vol. 80, no. 14, p. 144301, Oct. 2009.

[41] X. Moya, D. González-Alonso, L. Mañosa, A. Planes, V.O. Garlea, T.A. Lograsso, D. L. Schlagel, J.L. Zarestky, S. Aksoy and M. Acet, "Lattice dynamics in magnetic superelastic Ni-Mn-In alloys: Neutron scattering and ultrasonic experiments," *Phys. Rev. B*, vol. 79, no. 21, p. 214118, Jun. 2009.

[42] P. J. Brown, J. Crangle, T. Kanomata, M. Matsumoto, K-U. Neumann, B. Oularddiaf and K. R. A. Ziebekck *et al.*, "The crystal structure and phase transitions of the magnetic shape memory compound Ni 2 MnGa," *J. Phys. Condens. Matter*, vol. 14, no. 43, p. 10159, 2002.

[43] V. V. Martynov and V. V. Kokorin, "The crystal structure of thermally- and stress-induced Martensites in Ni2MnGa single crystals," *J. Phys. III*, vol. 2, no. 5, pp. 739–749, May 1992.

[44] S. Singh, J. Bednarcik, S. R. Barman, C. Felser, and D. Pandey, "Premartensite to martensite transition and its implications for the origin of modulation in Ni2MnGa ferromagnetic shape-memory alloy," *Phys. Rev. B*, vol. 92, no. 5, p. 054112, Aug. 2015.

[45] S. Singh, V. Petricek, Parasmani Rajput, Adrian H. Hill, E. Suard, S. R. Barman and Dhananjai Pandey, "High-resolution synchrotron x-ray powder diffraction study of the incommensurate modulation in the martensite phase of Ni2MnGa: Evidence for nearly 7M modulation and phason broadening," *Phys. Rev. B*, vol. 90, no. 1, p. 014109, Jul. 2014.

[46] S. Singh, J Nayak, Abhishek Rai, Parasmani Rajput, Adrian H Hill, S R Barman and Dhananjai Pandey, "(3 + 1)D superspace description of the incommensurate modulation in the premartensite phase of Ni2MnGa: a high resolution synchrotron x-ray powder diffraction study," *J. Phys. Condens. Matter*, vol. 25, no. 21, p. 212203, May 2013.

[47] L. Righi, F. Albertini, G. Calestani, L. Pareti, A. Paoluzi, C. Ritter, P.A. Algarabel, L. Morellon, M. R. Ibarra, "Incommensurate modulated structure of the ferromagnetic shape-memory Ni2MnGa martensite," *J. Solid State Chem.*, vol. 179, no. 11, pp. 3525–3533, Nov. 2006.

[48] L. Righi, F. Albertini, L. Pareti, A. Paoluzi, and G. Calestani, "Commensurate and incommensurate '5M' modulated crystal structures in Ni–Mn–Ga martensitic phases," *Acta Mater.*, vol. 55, no. 15, pp. 5237–5245, Sep. 2007.

[49] Y. Sutou, Y. Imano, N. Koeda, T. Omori, R. Kainuma, K. Ishida and K. Oikawa., "Magnetic and martensitic transformations of NiMnX(X=In,Sn,Sb) ferromagnetic shape memory alloys," *Appl. Phys. Lett.*, vol. 85, no. 19, pp. 4358–4360, Nov. 2004.

[50] P. J. Brown, A.P. Gandy, K. Ishida, W. Ito, R. Kainuma, T. Kanomata, K. U. Neumann, K. Oikawa, B. Ouladdiaf, A. Sheikh, and K. R. A. Ziebeck, "Magnetic and structural properties of the magnetic shape memory compound Ni 2 Mn 1.48 Sb 0.52," *J. Phys. Condens. Matter*, vol. 22, no. 9, p. 096002, 2010.

[51] P. J. Brown, A.P. Gandy, K. Ishida, R. Kainuma, T. Kanomata, K. U. Neumann, K. Oikawa, B. Ouladdiaf, and K. R. A. Ziebeck, "The magnetic and structural properties of the magnetic shape memory compound Ni 2 Mn 1.44 Sn 0.56," *J. Phys. Condens. Matter*, vol. 18, no. 7, p. 2249, 2006.

[52] N. V. Rama Rao, J. A. Chelvane, V. Chandrasekaran, A. V. Morozkin, J. Lamsal, W. B. Yelon, R. Nirmala, K. G. Suresh, and S.K. Malik, "Neutron diffraction studies on the Heusler alloy Ni50Mn37Sb13," *J. Appl. Phys.*, vol. 109, no. 7, p. 07A907, Mar. 2011.

[53] T. Krenke, E. F. Wassermann, X. Moya, L. Manosa, and A. Planes, E. Suard, and B. Oularddiaf, "Magnetic superelasticity and inverse magnetocaloric effect in Ni-Mn-In," *Phys. Rev. B*, vol. 75, no. 10, p. 104414, Mar. 2007.

[54] P. J. Brown, A.P. Gandy, R. Kainuma, T. Kanomata, K. U. Neumann, K. Oikawa, B. Ouladdiaf, A. Sheikh, and K. R. A. Ziebeck, "The field and temperature dependence of the magnetic and structural properties of the shape memory compound Ni 1.84 Mn 1.64 In 0.52," *J. Phys. Condens. Matter*, vol. 23, no. 45, p. 456004, 2011.

[55] T. Krenke, M. Acet, E. F. Wassermann, X. Moya, L. Manosa, and A. Planes, "Martensitic transitions and the nature of ferromagnetism in the austenitic and martensitic states of Ni-Mn-Sn alloys," *Phys. Rev. B*, vol. 72, no. 1, p. 014412, Jul. 2005.

[56] T. Krenke, M. Acet, E. F. Wassermann, X. Moya, L. Manosa, and A. Planes, "Ferromagnetism in the austenitic and martensitic states of Ni-Mn-In alloys," *Phys. Rev. B*, vol. 73, no. 17, p. 174413, May 2006.

[57] A. Çakır, L. Righi, F. Albertini, M. Acet, and M. Farle, "Intermartensitic transitions and phase stability in Ni50Mn50−xSnx Heusler alloys," *Acta Mater.*, vol. 99, pp. 140–149, Oct. 2015.

[58] B. Wedel, M. Suzuki, Y. Murakami, C. Wedel, T. Suzuki, D. Shindo, and K. Itagaki, "Low temperature crystal structure of Ni–Mn–Ga alloys," *J. Alloys Compd.*, vol. 290, no. 1, pp. 137–143, Aug. 1999.

[59] D. Y. Cong, Y. D. Zhang, Y. D. Wang, M. Humbert, X. Zhao, T. Watanabe, L. Zuo, and C. Esling, "Experiment and theoretical prediction of martensitic transformation crystallography in a Ni–Mn–Ga ferromagnetic shape memory alloy," *Acta Mater.*, vol. 55, no. 14, pp. 4731–4740, Aug. 2007.

[60] V. Sanchez-Alarcos, Perez-Landazabal, V. Recarte, C. Gomez-Polo, and J. A. Rodriguez-Velamazan, "Correlation between composition and phase transformation temperatures in Ni–Mn–Ga–Co ferromagnetic shape memory alloys," *Acta Mater.*, vol. 56, no. 19, pp. 5370–5376, Nov. 2008.

[61] R. Ranjan, S. Banik, S. R. Barman, U. Kumar, P. K. Mukhopadhyay, and D. Pandey, "Powder x-ray diffraction study of the thermoelastic martensitic transition in $Ni_2Mn_{1.05}Ga_{0.95}$," *Phys. Rev. B*, vol. 74, no. 22, p. 224443, Dec. 2006.

[62] K. Fukushima, K. Sano, T. Kanomata, H. Nishihara, Y. Furutani, T. Shishido, W. Ito, R. Y. Umetsu, R. Kainuma, K. Oikawa, and K. Ishida, "Phase diagram of Fe-substituted Ni–Mn–Sn shape memory alloys," *Scr. Mater.*, vol. 61, no. 8, pp. 813–816, Oct. 2009.

[63] H. Yan, Y. Zhang, A. Senyshyn, H-G. Brokmeier, C. Esling, X. Zhao, and L. Zuo, "Crystal structure determination of incommensurate modulated martensite in Ni–Mn–In Heusler alloys," *Acta Mater.*, vol. 88, pp. 375–388, Apr. 2015.

[64] V. Recarte, J. I. Pérez-Landazábal, V. Sánchez-Alarcos, and J. A. Rodríguez-Velamazán, "Study of the transformation sequence on a high temperature martensitic transformation Ni-Mn-Ga-Co shape memory alloy," *J. Phys. Conf. Ser.*, vol. 549, no. 1, p. 012017, 2014.

[65] D. Y. Cong, S. Wang, Y. D. Wang, Y. Ren, L. Zuo, and C. Esling, "Martensitic and magnetic transformation in Ni–Mn–Ga–Co ferromagnetic shape memory alloys," *Mater. Sci. Eng. A*, vol. 473, no. 1, pp. 213–218, Jan. 2008.

[66] A. K. Nayak, K. G. Suresh, and A. K. Nigam, "Correlation between reentrant spin glass behavior and the magnetic order–disorder transition of the martensite phase in Ni–Co–Mn–Sb Heusler alloys," *J. Phys. Condens. Matter*, vol. 23, no. 41, p. 416004, Sep. 2011.

[67] S. C. Ma, C.W. shih *et al.*, "Wheel speed-dependent martensitic transformation and magnetocaloric effect in Ni–Co–Mn–Sn ferromagnetic shape memory alloy ribbons," *Acta Mater.*, vol. 90, pp. 292–302, May 2015.

[68] X. Wang, F. Sun, J. Wang, Q. Yu, Y. Wu, H. Hua, and C. Jiang, "Influence of annealing temperatures on the magnetostructural transition and magnetocaloric effect of Ni40Co10Mn40Sn10 powders," *J. Alloys Compd.*, vol. 691, pp. 215–219, Jan. 2017.

[69] H. Yan, C Zhang, Y. Zhang, X. Wang, C. Sling, X. Xhao, and L. Zuo, "Crystallographic insights into Ni–Co–Mn–In metamagnetic shape memory alloys," *J. Appl. Crystallogr.*, vol. 49, no. 5, pp. 1585–1592, Oct. 2016.

[70] P. J. Webster and K. R. A. Ziebeck, "1.5.5.1.2.2 Antiferromagnetic order," in *Alloys and Compounds of d-Elements with Main Group Elements. Part 2*, H. P. J. Wijn, Ed. Berlin, Heidelberg: Springer Berlin Heidelberg, 1988, pp. 86–86.

[71] Z. Islam, D. Haskel, J.C. Lang, G. Srajer, Y. Lee, B.N. Harmon, A.I. Goldman, D.L. Schlagel and T.A. Lograsso, "An X-ray study of non-zero nickel moment in a ferromagnetic shape-memory alloy," *J. Magn. Magn. Mater.*, vol. 303, no. 1, pp. 20–25, Aug. 2006.

[72] E. Şaşıoğlu, L. M. Sandratskii, and P. Bruno, "First-principles calculation of the intersublattice exchange interactions and Curie temperatures of the full Heusler alloys Ni_2MnX (X=Ga, In, Sn, Sb," *Phys. Rev. B*, vol. 70, no. 2, p. 024427, Jul. 2004.

[73] Umetsu, R. Y, A. Sheikh, B. Ouladdiaf, K. R. A. Ziebeck, T. Kanomata, and R. Kainuma, "The effect of Co substitution on the magnetic properties of the Heusler alloy Ni50Mn33Sn17," *Appl. Phys. Lett.*, vol. 98, no. 4, p. 042507, Jan. 2011.

[74] Y. Kurtulus, R. Dronskowski, G. D. Samolyuk, and V. P. Antropov, "Electronic structure and magnetic exchange coupling in ferromagnetic full Heusler alloys," *Phys. Rev. B*, vol. 71, no. 1, Jan. 2005.

[75] S. Aksoy, M. Acet, P. P. Deen, L. Mañosa, and A. Planes, “Magnetic correlations in martensitic Ni-Mn-based Heusler shape-memory alloys: Neutron polarization analysis,” *Phys. Rev. B*, vol. 79, no. 21, p. 212401, Jun. 2009.

[76] S. Aksoy, M. Acet, E. Wassermann, T. Krenke, X. Moya, L. Mañosa, A. Planes, and P. P. Deen, “Structural properties and magnetic interactions in martensitic Ni-Mn-Sb alloys,” *Philos. Mag.*, vol. 89, no. 22–24, pp. 2093–2109, Aug. 2009.

[77] M. Khan, I. Dubenko, S. Stadler, and N. Ali, “Exchange bias in bulk Mn rich Ni–Mn–Sn Heusler alloys,” *J. Appl. Phys.*, vol. 102, no. 11, p. 113914, Dec. 2007.

[78] M. Khan, I. Dubenko, S. Stadler, and N. Ali, “Exchange bias behavior in Ni–Mn–Sb Heusler alloys,” *Appl. Phys. Lett.*, vol. 91, no. 7, p. 072510, Aug. 2007.

[79] Z. Li, C. Jing, J. Chen, S. Yuan, S. Cao, and J. Zhang, “Observation of exchange bias in the martensitic state of Ni50Mn36Sn14 Heusler alloy,” *Appl. Phys. Lett.*, vol. 91, no. 11, p. 112505, Sep. 2007.

[80] J. L. S. Llamazares, B. Hernando, J. J. Suñol, C. García, and C. A. Ross, “Kinetic arrest of direct and reverse martensitic transformation and exchange bias effect in Mn49.5Ni40.4In10.1 melt spun ribbons,” *J. Appl. Phys.*, vol. 107, no. 9, p. 09A956, May 2010.

[81] J. Sharma and K. G. Suresh, “Martensitic transition, magnetic, magnetocaloric and exchange bias properties of Fe-substituted Mn-Ni-Sn Heusler alloys,” *Solid State Commun.*, vol. 248, pp. 1–5, Dec. 2016.

[82] B. M. Wang, Y. Liu, L. Wang, S.L. Huang, Y. Zhao, Y. Yang, and H. Zhang, “Exchange bias and its training effect in the martensitic state of bulk polycrystalline Ni49.5Mn34.5In16,” *J. Appl. Phys.*, vol. 104, no. 4, p. 043916, Aug. 2008.

[83] P. Czaja, J. Przewoźnik, M. Fitta, M. Bałanda, A. Chrobak, B. Kania, P. Zackiewicz, A. Wójcik, M.Szlezynger, and W. Maziarz, “Effect of ball milling and thermal treatment on exchange bias and magnetocaloric properties of Ni48Mn39.5Sn10.5Al2 ribbons,” *J. Magn. Magn. Mater.*, vol. 401, pp. 223–230, Mar. 2016.

[84] R. Y. Umetsu, R. Kainuma, Y. Amako, Y. Taniguchi, T. Kanomata, K. Fukushima, A. Fujita, K. Oikawa, and K. Ishida, “Mössbauer study on martensite phase in Ni50Mn36.5Fe0.557Sn13 metamagnetic shape memory alloy,” *Appl. Phys. Lett.*, vol. 93, no. 4, p. 042509, Jul. 2008.

[85] A. Planes, L. Mañosa, and M. Acet, “Magnetocaloric effect and its relation to shape-memory properties in ferromagnetic Heusler alloys,” *J. Phys. Condens. Matter*, vol. 21, no. 23, p. 233201, 2009.

[86] R. Kainuma, Y. Imano, W. Ito, Y. Sutou, H. Morito, S. Okamoto, O. Kitakami, K. Oikawa, A. Fujita, T. Kanomata, and K. Ishida, “Magnetic-field-induced shape recovery by reverse phase transformation,” *Nature*, vol. 439, no. 7079, pp. 957–960, Feb. 2006.

[87] K. Oikawa, W. Ito, Y. Imano, Y. Sutou, R. Kainuma, K. Ishida, S. Okamoto, O. Kitakami, and T. Kanomata, "Effect of magnetic field on martensitic transition of Ni46Mn41In13 Heusler alloy," *Appl. Phys. Lett.*, vol. 88, no. 12, p. 122507, Mar. 2006.

[88] T. Krenke, E. Duman, M. Acet, X. Moya, L. Mañosa, and A. Planes, "Inverse magnetocaloric effect in ferromagnetic Ni–Mn–Sn alloys," *Nat. Mater.*, vol. 4, no. 6, pp. 450–454, Jun. 2005.

[89] J. Du, Q. Zheng, W. J. Ren, W. J. Feng, X. G. Liu, and Z. D. Zhang, "Magnetocaloric effect and magnetic-field-induced shape recovery effect at room temperature in ferromagnetic Heusler alloy Ni–Mn–Sb," *J. Phys. Appl. Phys.*, vol. 40, no. 18, p. 5523, 2007.

[90] R. Kainuma, Y. Imano, W. Ito, H. Morito, Y. Sutou, K. Oikawa, A. Fujita, K. Ishida, S. Okamoto, O. Kitakami, and T. Kanomata, "Metamagnetic shape memory effect in a Heusler-type Ni43Co7Mn39Sn11 polycrystalline alloy," *Appl. Phys. Lett.*, vol. 88, no. 19, p. 192513, May 2006.

[91] R. Kainuma, W. Ito, R. Y. Umetsu, K. Oikawa, and K. Ishida, "Magnetic field-induced reverse transformation in B2-type NiCoMnAl shape memory alloys," *Appl. Phys. Lett.*, vol. 93, no. 9, p. 091906, Sep. 2008.

[92] G. Porcari, S. Fabbrici, C. ênechele, F. Albertini, M. Buzzi, A. Paoluzi, J. Kamarad, Z. Arnold, and M. Solzi, "Reverse magnetostructural transformation and adiabatic temperature change in Co- and In-substituted Ni-Mn-Ga alloys," *Phys. Rev. B*, vol. 85, no. 2, p. 024414, Jan. 2012.

[93] V. Recarte, J. I. Pérez-Landazábal, C. Gómez-Polo, E. Cesari, and J. Dutkiewicz, "Magnetocaloric effect in Ni–Fe–Ga shape memory alloys," *Appl. Phys. Lett.*, vol. 88, no. 13, p. 132503, Mar. 2006.

[94] A. Tishin, A.V. Derkach, Y.I. Spichkin, M.D. Kuz´min, A. Chernyshov, K.A. Gschneidner, and V.K. Pecharsky, "Magnetocaloric effect near a second-order magnetic phase transition," *J. Magn. Magn. Mater.*, vol. 310, pp. 2800–2804, Mar. 2007.

[95] V. D. Buchelnikov and V. V. Sokolovskiy, "Magnetocaloric effect in Ni-Mn-X (X = Ga, In, Sn, Sb) Heusler alloys," *Phys. Met. Metallogr.*, vol. 112, no. 7, pp. 633–665, Dec. 2011.

[96] A. Aliev, A. Batdalov, S. Bosko, V. Buchelnikov, I. Dikstein, V. Kovailo, V. Koledov, R. Levitin, V. Shavrov, and T. Takagi, "Magnetocaloric effect and magnetization in a Ni–Mn–Ga Heusler alloy in the vicinity of magnetostructural transition," *J. Magn. Magn. Mater.*, vol. 272–276, pp. 2040–2042, May 2004.

[97] M. Khan, A. K. Pathak, M. R. Paudel, I. Dubenko, S. Stadler, and N. Ali, "Magnetoresistance and field-induced structural transitions in Ni50Mn50−xSnx Heusler alloys," *J. Magn. Magn. Mater.*, vol. 320, no. 3, pp. L21–L25, Feb. 2008.

[98] A. K. Pathak, I. Dubenko, C. Pueblo, S. Stadler, and N. Ali, "Magnetoresistance and magnetocaloric effect at a structural phase transition from a paramagnetic martensitic state

to a paramagnetic austenitic state in Ni50Mn36.5In13.5 Heusler alloys," *Appl. Phys. Lett.*, vol. 96, no. 17, p. 172503, Apr. 2010.

[99] S. Singh and C. Biswas, "Magnetoresistance origin in martensitic and austenitic phases of Ni2Mn1+xSn1−x," *Appl. Phys. Lett.*, vol. 98, no. 21, p. 212101, May 2011.

[100] V. K. Pecharsky and K. A. Gschneidner Jr, "Magnetocaloric effect and magnetic refrigeration," *J. Magn. Magn. Mater.*, vol. 200, no. 1, pp. 44–56, Oct. 1999.

[101] S. M. Benford and G. V. Brown, "T-S diagram for gadolinium near the Curie temperature," *J. Appl. Phys.*, vol. 52, pp. 2110–2112, Apr. 1981.

[102] S. Yu. Dan'kov, A. M. Tishin, V. K. Pecharsky, and K. A. Gschneidner, "Magnetic phase transitions and the magnetothermal properties of gadolinium," *Phys. Rev. B*, vol. 57, no. 6, pp. 3478–3490, Feb. 1998.

[103] V. K. Pecharsky and K. A. Gschneidner, Jr., "Giant Magnetocaloric Effect in Gd 5 (Si 2 Ge 2)," *Phys. Rev. Lett.*, vol. 78, no. 23, pp. 4494–4497, Jun. 1997.

[104] L. Morellon, Z. Arnold, P. A. Algarabel, C. Magen, M. R. Ibarra, and Y. Skorokhod, "Pressure effects in the giant magnetocaloric compounds Gd 5 (Si x Ge 1− x) 4," *J. Phys. Condens. Matter*, vol. 16, no. 9, p. 1623, 2004.

[105] P. J. von Ranke, N. A. de Oliveira, and S. Gama, "Understanding the influence of the first-order magnetic phase transition on the magnetocaloric effect: application to Gd5(SixGe1−x)4," *J. Magn. Magn. Mater.*, vol. 277, no. 1, pp. 78–83, Jun. 2004.

[106] L. Morellon, P. A. Algarabel, C. Magen, and M. R. Ibarra, "Giant magnetoresistance in the Ge-rich magnetocaloric compound, Gd5(Si0.1Ge0.9)4," *J. Magn. Magn. Mater.*, vol. 237, no. 2, pp. 119–123, Dec. 2001.

[107] Z. Li, Y. Zhang, C. F. Sánchez-Valdés, J.L. Sánchez-Llamazares, C. Esling, X. Zhao, and L. Zuo, "Giant magnetocaloric effect in melt-spun Ni-Mn-Ga ribbons with magneto-multistructural transformation," *Appl. Phys. Lett.*, vol. 104, no. 4, p. 044101, Jan. 2014.

[108] J. Marcos, L. Mañosa, A. Planes, F. Casanova, X. Batlle, and A. Labarta, "Multiscale origin of the magnetocaloric effect in Ni-Mn-Ga shape-memory alloys," *Phys. Rev. B*, vol. 68, no. 9, p. 094401, Sep. 2003.

[109] X. Zhou, W. Li, H. P. Kunkel, and G. Williams, "A criterion for enhancing the giant magnetocaloric effect: (Ni–Mn–Ga)—a promising new system for magnetic refrigeration," *J. Phys. Condens. Matter*, vol. 16, no. 6, pp. L39–L44, Feb. 2004.

[110] A. Ghosh and K. Mandal, "Effect of structural disorder on the magnetocaloric properties of Ni-Mn-Sn alloy," *Appl. Phys. Lett.*, vol. 104, no. 3, p. 031905, Jan. 2014.

[111] Z. D. Han, D. H. Wang, C. L. Zhang, H. C. Xuan, B. X. Gu, and Y. W. Du, "Low-field inverse magnetocaloric effect in Ni50−xMn39+xSn11 Heusler alloys," *Appl. Phys. Lett.*, vol. 90, no. 4, p. 042507, Jan. 2007.

[112] P. A. Bhobe, K. R. Priolkar, and A. K. Nigam, “Room temperature magnetocaloric effect in Ni–Mn–In,” *Appl. Phys. Lett.*, vol. 91, no. 24, p. 242503, Dec. 2007.

[113] M. Khan, N. Ali, and S. Stadler, “Inverse magnetocaloric effect in ferromagnetic Ni50Mn37+xSb13−x Heusler alloys,” *J. Appl. Phys.*, vol. 101, no. 5, p. 053919, Mar. 2007.

[114] Z. D. Han, D.H. Wang, C.L. Zhang, H.C. Xuan, J.R. Zhang, B.X. Gu, and Y.W. Du, “The phase transitions, magnetocaloric effect, and magnetoresistance in Co doped Ni–Mn–Sb ferromagnetic shape memory alloys,” *J. Appl. Phys.*, vol. 104, no. 5, p. 053906, Sep. 2008.

[115] D. Pal and K. Mandal, “Magnetocaloric effect and magnetoresistance of Ni–Fe–Ga alloys,” *J. Phys. Appl. Phys.*, vol. 43, no. 45, p. 455002, 2010.

[116] L. Pareti, M. Solzi, F. Albertini, and A. Paoluzi, “Giant entropy change at the co-occurrence of structural and magnetic transitions in the Ni Mn Ga Heusler alloy,” *Eur. Phys. J. B - Condens. Matter Complex Syst.*, vol. 32, no. 3, pp. 303–307, Apr. 2003.

[117] V. K. Sharma, M. K. Chattopadhyay, and S. B. Roy, “Large inverse magnetocaloric effect in Ni50Mn34In16,” *J. Phys. Appl. Phys.*, vol. 40, no. 7, p. 1869, Mar. 2007.

[118] L. Huang, D. Y. Cong, L. Ma, Z. H. Nie, M. G. Wamg. Z. L. Wang, H. L. Suo, Y. Ren, Y. D. Wang, “Large magnetic entropy change and magnetoresistance in a Ni41Co9Mn40Sn10 magnetic shape memory alloy,” *J. Alloys Compd.*, vol. 647, pp. 1081–1085, Oct. 2015.

[119] A. K. Nayak, K. G. Suresh, and A. K. Nigam, “Giant inverse magnetocaloric effect near room temperature in Co substituted NiMnSb Heusler alloys,” *J. Phys. Appl. Phys.*, vol. 42, no. 3, p. 035009, Jan. 2009.

[120] D. Bourgault, J. Tillier, P. Courtois, D. Maillard, and X. Chaud, “Large inverse magnetocaloric effect in Ni45Co5Mn37.5In12.5 single crystal above 300 K,” *Appl. Phys. Lett.*, vol. 96, no. 13, p. 132501, Mar. 2010.

[121] A. J. Millis, B. I. Shraiman, and R. Mueller, “Dynamic Jahn-Teller Effect and Colossal Magnetoresistance in La1-xSrxMnO,” *Phys. Rev. Lett.*, vol. 77, no. 1, pp. 175–178, Jul. 1996.

[122] M. Uehara, S. Mori, C. H. Chen, and S.-W. Cheong, “Percolative phase separation underlies colossal magnetoresistance in mixed-valent manganites,” *Nature*, vol. 399, no. 6736, pp. 560–563, Jun. 1999.

[123] S. Jin, T. H. Tiefel, M. McCormack, R. A. Fastnacht, R. Ramesh, and L. H. Chen, “Thousandfold Change in Resistivity in Magnetoresistive La-Ca-Mn-O Films,” *Science*, vol. 264, no. 5157, pp. 413–415, Apr. 1994.

[124] P. M. Levy, S. Zhang, and A. Fert, “Electrical conductivity of magnetic multilayered structures,” *Phys. Rev. Lett.*, vol. 65, no. 13, pp. 1643–1646, Sep. 1990.

[125] Z. H. Liu, H. Liu, X.X. Zhang, X. K. Zhang, J.Q. Xiao, Z.Y. Zhu, X.F. Dai, G.D. Liu, J.L. Chen, and G.H. Wu, "Large negative magnetoresistance in quaternary Heusler alloy Ni50Mn8Fe17Ga25 melt-spun ribbons," *Appl. Phys. Lett.*, vol. 86, no. 18, p. 182507, Apr. 2005.

[126] S. Y. Yu, Z.G. Liu, G.D. Liu, J.L. Chen, Z.X. Cao, G.H. Wu, B. Zhang, and X.X. Zhang, "Large magnetoresistance in single-crystalline Ni50Mn50−xInx alloys (x=14–16) upon martensitic transformation," *Appl. Phys. Lett.*, vol. 89, no. 16, p. 162503, Oct. 2006.

[127] S. Chatterjee, S. Giri, S. Majumdar, and S. K. De, "Giant magnetoresistance and large inverse magnetocaloric effect in Ni2Mn1.36Sn0.64alloy," *J. Phys. Appl. Phys.*, vol. 42, no. 6, p. 065001, Feb. 2009.

[128] M. Pugacheva and A. Jezierski, "Dependence of the magnetic moment on the local atomic order in Rh2MnX Heusler alloys," *J. Magn. Magn. Mater.*, vol. 151, no. 1, pp. 202–206, Nov. 1995.

[129] V. A. Chernenko, "Compositional instability of β-phase in Ni-Mn-Ga alloys," *Scr. Mater.*, vol. 40, no. 5, pp. 523–527, Feb. 1999.

[130] V. V. Khovailo, K. Oikawa, T. Abe, and T. Takagi, "Entropy change at the martensitic transformation in ferromagnetic shape memory alloys Ni2+xMn1−xGa," *J. Appl. Phys.*, vol. 93, no. 10, pp. 8483–8485, May 2003.

[131] J. Pons, V. A. Chernenko, R. Santamarta, and E. Cesari, "Crystal structure of martensitic phases in Ni–Mn–Ga shape memory alloys," *Acta Mater.*, vol. 48, no. 12, pp. 3027–3038, Jul. 2000.

[132] A. Cakir, L. Righi, F. Albertini, M. Acet, M. Farle, and S. Akturk, "Extended investigation of intermartensitic transitions in Ni-Mn-Ga magnetic shape memory alloys: A detailed phase diagram determination," *J. Appl. Phys.*, vol. 114, no. 18, p. 183912, Nov. 2013.

[133] K. R. Priolkar, P.A. Bhobe, D.N. Lobo, S.W. D´Souza, S.R. Barman, A. Chakrabarti, and S. Emura, "Antiferromagnetic exchange interactions in the Ni2Mn1.4In0.6 ferromagnetic Heusler alloy," *Phys. Rev. B*, vol. 87, no. 14, p. 144412, Apr. 2013.

[134] T. Kanomata, T. Yasuda, S. Sasaki, H. Nishihara, R. Kainuma, W. Ito, K. Oikawa, K. Ishida, K-U. Neumann, and K.R.A. Ziebeck, "Magnetic properties on shape memory alloys Ni2Mn1+xIn1−x," *J. Magn. Magn. Mater.*, vol. 321, no. 7, pp. 773–776, Apr. 2009.

[135] E. Krén, E. Nagy, I. Nagy, L. Pál, and P. Szabó, "Structures and phase transformations in the Mn-Ni system near equiatomic concentration," *J. Phys. Chem. Solids*, vol. 29, no. 1, pp. 101–108, Jan. 1968.

[136] M. Khan, I. Dubenko, S. Stadler, and N. Ali, "Magnetostructural phase transitions in $Ni_{50}Mn_{25+x}Sb_{25-x}$ Heusler alloys," *J. Phys. Condens. Matter*, vol. 20, no. 23, p. 235204, Apr. 2008.

[137] J. Smit, "Magnetism in Hume-Rothery alloys," *J. Phys. F Met. Phys.*, vol. 8, no. 10, pp. 2139–2143, Oct. 1978.

[138] X. Q. Chen, F. J. Yang, X. Lu, and Z. X. Qin, "The way composition affects martensitic transformation temperatures of Ni–Mn–Ga Heusler alloys," *Phys. Status Solidi B*, vol. 244, no. 3, pp. 1047–1053, 2007.

[139] E. Şaşıoğlu, L. M. Sandratskii, and P. Bruno, "Role of conduction electrons in mediating exchange interactions in Mn-based Heusler alloys," *Phys. Rev. B*, vol. 77, no. 6, p. 064417, Feb. 2008.

[140] J. Enkovaara, O. Heczko, A. Ayuela, and R. M. Nieminen, "Coexistence of ferromagnetic and antiferromagnetic order in Mn-doped Ni_2MnGa," *Phys. Rev. B*, vol. 67, no. 21, p. 212405, Jun. 2003.

[141] T. Krenke, E. Duman, M. Acet, X. Moya, L. Mañosa, and A. Planes, "Effect of Co and Fe on the inverse magnetocaloric properties of Ni-Mn-Sn," *J. Appl. Phys.*, vol. 102, no. 3, p. 033903, Aug. 2007.

[142] V. K. Sharma, M. K. Chattopadhyay, A. Khandelwal, and S. B. Roy, "Martensitic transition near room temperature and the temperature- and magnetic-field-induced multifunctional properties of $Ni_{49}CuMn_{34}In_{16}$ alloy," *Phys. Rev. B*, vol. 82, no. 17, p. 172411, Nov. 2010.

[143] C. O. Aguilar-Ortiz, D. Soto-Parra, P. Álvarez-Alonso, P. Lázpita, D. Salazar, P.O. Castillo-Villa, H. Flores-Zúñiga, and V.A. Chernenko, "Influence of Fe doping and magnetic field on martensitic transition in Ni–Mn–Sn melt-spun ribbons," *Acta Mater.*, vol. 107, pp. 9–16, Apr. 2016.

[144] Z. Li, C. Jing, H.L. Zhang, Y. F. Qiao, S.X. Cao, J.C. Zhang, and L. Sun, "A considerable metamagnetic shape memory effect without any prestrain in Ni46Cu4Mn38Sn12 Heusler alloy," *J. Appl. Phys.*, vol. 106, no. 8, p. 083908, Oct. 2009.

[145] B. Gao, J. Shen, F. X. Hu, J. Wang, J. R. Sun, and B. G. Shen, "Magnetic properties and magnetic entropy change in Heusler alloys Ni50Mn35−xCuxSn15," *Appl. Phys. A*, vol. 97, no. 2, p. 443, May 2009.

[146] C.-M. Li, H.-B. Luo, Q.-M. Hu, R. Yang, B. Johansson, and L. Vitos, "Site preference and elastic properties of Fe-, Co-, and Cu-doped Ni2MnGa shape memory alloys from first principles," *Phys. Rev. B*, vol. 84, no. 2, p. 024206, Jul. 2011.

[147] Z. H. Liu, M. Zhang, W.Q. Wang, W.H. Wang, J.L. Chen, G.H. Wu, F.B. Meng, H.Y. Liu, B.D. Liu, J.P. Qu, and Y.X. Li, "Magnetic properties and martensitic transformation in quaternary Heusler alloy of NiMnFeGa," *J. Appl. Phys.*, vol. 92, no. 9, pp. 5006–5010, Oct. 2002.

[148] D. E. Soto-Parra, X. Moya, L. Mañosa, A. Planes, H. Flores-Zúñiga, F. Alvarado-Hernández, R.A. Ochoa-Gamboa, J.A. Matutes-Aquino and D. Ríos-Jara, "Fe and Co selective substitution in Ni2MnGa: Effect of magnetism on relative phase stability," *Philos. Mag.*, vol. 90, no. 20, pp. 2771–2792, Jul. 2010.

[149] Y. Murakami, T. Yano, R. Y. Umetsu, R. Kainuma, and D. Shindo, “Suppression of ferromagnetism within antiphase boundaries in Ni50Mn25Al12.5Ga12.5 alloy,” *Scr. Mater.*, vol. 65, no. 10, pp. 895–898, Nov. 2011.

[150] L. Huang, D. Y. Cong, H. L. Suo, and Y. D. Wang, “Giant magnetic refrigeration capacity near room temperature in Ni40Co10Mn40Sn10 multifunctional alloy,” *Appl. Phys. Lett.*, vol. 104, no. 13, p. 132407, Mar. 2014.

[151] V. Recarte, J. I. Pérez-Landazábal, S. Kustov, and E. Cesari, “Entropy change linked to the magnetic field induced martensitic transformation in a Ni–Mn–In–Co shape memory alloy,” *J. Appl. Phys.*, vol. 107, no. 5, p. 053501, Mar. 2010.

[152] Metamagnetic shape memory effect in a Heusler-type Ni43Co7Mn39Sn11 polycrystalline alloy “Magnetic ordering in magnetic shape memory alloy Ni-Mn-In-Co,” *Phys. Rev. B*, vol. 92, no. 22, p. 224429, Dec. 2015.

[153] F. Orlandi, S. Fabbrici, F. Albertini, P. Manuel, D. D. Khalyavin, and L. Righi, “Long-range antiferromagnetic interactions in Ni-Co-Mn-Ga metamagnetic Heusler alloys: A two-step ordering studied by neutron diffraction,” *Phys. Rev. B*, vol. 94, no. 14, p. 140409, Oct. 2016.

[154] M. Kreissl *et al.*, “The influence of atomic order and residual strain on the magnetic and structural properties of Ni2MnGa,” *J. Magn. Magn. Mater.*, vol. 272–276, pp. 2033–2034, May 2004.

[155] A. Planes, L. Mañosa, E. Vives, J. Rodríguez-Carvajal, M. Morin, G. Guenin, and J.L. Macqueron, “Neutron diffraction study of long-range atomic order in Cu-Zn-Al shape memory alloys,” *J. Phys. Condens. Matter*, vol. 4, no. 2, p. 553, 1992.

[156] V. Sánchez-Alarcos, J. I. Pérez-Landazábal, V. Recarte, J. A. Rodríguez-Velamazán, and V. A. Chernenko, “Effect of atomic order on the martensitic and magnetic transformations in Ni–Mn–Ga ferromagnetic shape memory alloys,” *J. Phys. Condens. Matter*, vol. 22, no. 16, p. 166001, 2010.

[157] Sanchez-Alarcos, Perez-Landazabal, Cristina Gómez-Polo, and V. Recarte, “Influence of the atomic order on the magnetic characteristics of a Ni–Mn–Ga ferromagnetic shape memory alloy,” *J. Magn. Magn. Mater.*, vol. 320, no. 14, pp. 160–163, Jul. 2008.

[158] V. Sánchez-Alarcos, V. Recarte, J. I. Pérez-Landazábal, C. Gómez-Polo, and J. A. Rodríguez-Velamazán, “Role of magnetism on the martensitic transformation in Ni–Mn-based magnetic shape memory alloys,” *Acta Mater.*, vol. 60, no. 2, pp. 459–468, Jan. 2012.

[159] A. L. Alves, E. C. Passamani, V. P. Nascimento, A. Y. Takeuchi, and C. Larica, “Influence of grain refinement and induced crystal defects on the magnetic properties of Ni 50 Mn 36 Sn 14 Heusler alloy,” *J. Phys. Appl. Phys.*, vol. 43, no. 34, p. 345001, 2010.

[160] E. C. Passamani, V.P. Nasimento, C. Larica, A.Y. Takeuchi, A.L. Alves, J.R. Proveri, M.C. Pereira, and J.D. Favris, "The influence of chemical disorder enhancement on the martensitic transformation of the Ni50Mn36Sn14 Heusler-type alloy," *J. Alloys Compd.*, vol. 509, no. 30, pp. 7826–7832, Jul. 2011.

[161] A. Ghotbi Varzaneh, P. Kameli, V. R. Zahedi, F. Karimzadeh, and H. Salamati, "Effect of heat treatment on martensitic transformation of Ni47Mn40Sn13 ferromagnetic shape memory alloy prepared by mechanical alloying," *Met. Mater. Int.*, vol. 21, no. 4, pp. 758–764, Jul. 2015.

[162] I. Unzueta, J. López-García, V. Sánchez-Alarcos, V. Recarte, J.I. Pérez-Landazábal, J.A. Rodríguez-Velamazán, J.S. Garitaonandia, J.A. García, and F. Plazaola, "119Sn Mössbauer spectroscopy in the study of metamagnetic shape memory alloys," *Hyperfine Interact.*, vol. 239, no. 1, p. 34, Aug. 2018.

[163] J. Ortín and A. Planes, "Thermodynamic analysis of thermal measurements in thermoelastic martensitic transformations," *Acta Metall.*, vol. 36, no. 8, pp. 1873–1889, Aug. 1988.

[164] Z. Zhang, X. Ding, J. Sun, T. Suzuki, T. Lookman, K. Otsuka, and X. Ren, "Nonhysteretic Superelasticity of Shape Memory Alloys at the Nanoscale," *Phys. Rev. Lett.*, vol. 111, no. 14, p. 145701, Sep. 2013.

[165] G. B. Rao, J. Q. Wang, E. H. Han, and W. Ke, "Study of residual stress accumulation in TiNi shape memory alloy during fatigue using EBSD technique," *Mater. Lett.*, vol. 6, no. 60, pp. 779–782, 2006.

[166] H. Scherngell and A. C. Kneissl, "Generation, development and degradation of the intrinsic two-way shape memory effect in different alloy systems," *Acta Mater.*, vol. 2, no. 50, pp. 327–341, 2002.

[167] R. Niemann, O. Heczko, L. Schultz, and S. Fähler, "Metamagnetic transitions and magnetocaloric effect in epitaxial Ni–Co–Mn–In films," *Appl. Phys. Lett.*, vol. 97, no. 22, p. 222507, Nov. 2010.

[168] R. Caballero-Flores, T. Sánchez, W.O. Rosa, J. García, L. González-Lagarreta, D. Serantes, V.M. Prida, L. Escoda, JJ. Suñol, and B. Hernando, "On tuning the magnetocaloric effect in Ni–Mn–In Heusler alloy ribbons with thermal treatment," *J. Alloys Compd.*, vol. 545, pp. 216–221, Dec. 2012.

[169] C. Gómez-Polo, J. I. Pérez-Landazábal, V. Recarte, V. Sánchez-Alarcos, G. Badini-Confalonieri, and M. Vázquez, "Ni–Mn–Ga ferromagnetic shape memory wires," *J. Appl. Phys.*, vol. 107, no. 12, p. 123908, Jun. 2010.

[170] M. Acet, “Magnetic shape memory: Magnetoelastic sponges,” *Nat. Mater.*, vol. 8, no. 11, pp. 854–855, Nov. 2009.

[171] J. Liu, N. Scheerbaum, S. Kauffmann-Weiss, and O. Gutfleisch, “NiMn-Based Alloys and Composites for Magnetically Controlled Dampers and Actuators,” *Adv. Eng. Mater.*, vol. 14, no. 8, pp. 653–667, Aug. 2012.

[172] J. Feuchtwanger, M. L. Richard, Y. J. Tang, A. E. Berkowitz, R. C. O’Handley, and S. M. Allen, “Large energy absorption in Ni–Mn–Ga/polymer composites,” *J. Appl. Phys.*, vol. 97, no. 10, p. 10M319, May 2005.

[173] C. Suryanarayana, “Mechanical alloying and milling,” *Prog. Mater. Sci.*, vol. 46, no. 1, pp. 1–184, Jan. 2001.

[174] M. E. McHenry and D. E. Laughlin, “Nano-scale materials development for future magnetic applications,” *Acta Mater.*, vol. 48, no. 1, pp. 223–238, Jan. 2000.

[175] A. Calka and D. Wexler, “Mechanical milling assisted by electrical discharge,” *Nature*, vol. 419, no. 6903, pp. 147–151, Sep. 2002.

[176] P. Gorria, P. Álvarez, J. S. Marcos, J. L. Sánchez Llamazares, M. J. Pérez, and J. A. Blanco, “Crystal structure, magnetocaloric effect and magnetovolume anomalies in nanostructured Pr2Fe17,” *Acta Mater.*, vol. 57, no. 6, pp. 1724–1733, Apr. 2009.

[177] W. Dagula, O. Tegus, X.W. Li, L. Song, E. Brück, D.T. Cam Thanh, F.R. de Boer, and K.H.J. Buschow, “Magnetic properties and magnetic-entropy change of MnFeP0.5As0.5−xSix(x=0–0.3) compounds,” *J. Appl. Phys.*, vol. 99, no. 8, p. 08Q105, Apr. 2006.

[178] Y. D. Wang, Y. Ren, Z.H. Nie, D.M. Liu, L. Zuo, H. Choo, H. Li, P.K. Liaw, J.Q. Yan, R.K. McQueeney, J.W. Richardson, and A. Huq, “Structural transition of ferromagnetic Ni2MnGa nanoparticles,” *J. Appl. Phys.*, vol. 101, no. 6, p. 063530, Mar. 2007.

[179] B. Tian, F. Chen, Y. Liu, and Y. F. Zheng, “Structural transition and atomic ordering of Ni49.8Mn28.5Ga21.7 ferromagnetic shape memory alloy powders prepared by ball milling,” *Mater. Lett.*, vol. 62, no. 17–18, pp. 2851–2854, Jun. 2008.

[180] Y. V. B. de Santanna, M. A. C. de Melo, I. A. Santos, A. A. Coelho, S. Gama, and L. F. Cótica, “Structural, microstructural and magnetocaloric investigations in high-energy ball milled Ni2.18Mn0.82Ga powders,” *Solid State Commun.*, vol. 148, no. 7, pp. 289–292, Nov. 2008.

[181] K. V. Peruman, R. Chokkalingam, and M. Mahendran, “Annealing effect on phase transformation in nano structured Ni–Mn–Ga ferromagnetic shape memory alloy,” *Phase Transit.*, vol. 83, no. 7, pp. 509–517, Jul. 2010.

[182] D. M. Liu, Z.H. Nie,Y. Rien, Y. D. Wang, J. Pearson, P.K. Liaw, and D.E. Brown, “Structural Transitions and Magnetic Properties of Ni50Mn36.7In13.3 Particles with Amorphous-Like Phase,” *Metall. Mater. Trans. A*, vol. 42, no. 10, p. 3062, May 2011.

[183] X. P. Fei, W. Li, J. Liu, F. Xu, G.D. Tang, W.S. Tan, and S.D. Li *et al.*, “Phase Transition of Ball-Milled Ni50-xMn37In13Cox (x=0,5) Alloy Powders,” *Materials Science Forum*, vol. 809-810, pp. 377-383, 2015.

Chapter 2. Experimental techniques

Taking into account that this thesis is an experimental work, in this chapter we will describe the methods employed to prepare the samples and their subsequent characterization. The sample preparation and macroscopic characterization (thermal and magnetic measurements) were carried out in the Materials Laboratory of the Physics Department of Navarra Public University, while neutron scattering and synchrotron X-ray diffraction experiments were performed at Institut Laue-Langevin and at ALBA synchrotron, respectively.

2.1. SAMPLE PREPARATION

2.1.1. Synthesis

The polycrystalline samples studied in this work were synthesized in an arc furnace Edmund Bühler MAM-1 (see Figure 2. 1) using pure elements. Arc Melting is used for melting metals–typically to form alloys. The heating is produced by an electric arc between a tungsten electrode and the metals placed in a depression of a refrigerated copper crucible. The chamber is evacuated and then back filled with argon gas. Hence, melting is performed in argon atmosphere to avoid the oxidation of the alloy. Repeated melting is performed to improve the homogeneity of the alloy. Successive evacuations of the chamber avoid oxidation of the melt.

Figure 2. 1. Arc furnace Edmund Bühler MAM-1.

2.1.2. Homogenization and thermal treatments

After the synthesis of the alloys in the arc furnace it is necessary to submit the ingots to a long-time thermal treatment at high temperature. This is due to the high directionality and non-homogeneity of the solidification process in the arc furnace and to the great influence of the composition on the structural and magnetic properties of the shape memory alloys. Thus, once the sample has been melted several times in the arc furnace, the next step is the homogenization process, which is done at 1073K-1273K, depending on the alloys system, during few days. At these temperatures, thermal energy allows the atomic diffusion, producing a high degree of homogeneity throughout the sample. Afterwards, a controlled quenching process is carried out on the sample in order to modify the degree of atomic order at room temperature and therefore tailoring the martensitic transformation and magnetic ordering temperatures.

A quenching in iced water from different temperatures or a slow cooling in a controlled atmosphere are the typical thermal treatments carried out in this type of alloys. These procedures, which allow a control of the microstructural state and the atomic order degree of the alloy in a reproducible way, are performed in a vertical furnace described schematically in Figure 2. 2 [1] .The sample is placed inside a vertical quartz tube that runs through the vertical furnace, holding tied to a Kanthal wire that is fixed to an external metallic pin. When the pin is removed, the sample falls into the thermal bath (iced water). The quartz tube is connected to a vacuum pump and to an inert gas bottle (usually argon gas), which allows the control of the atmosphere avoiding the sample oxidation.

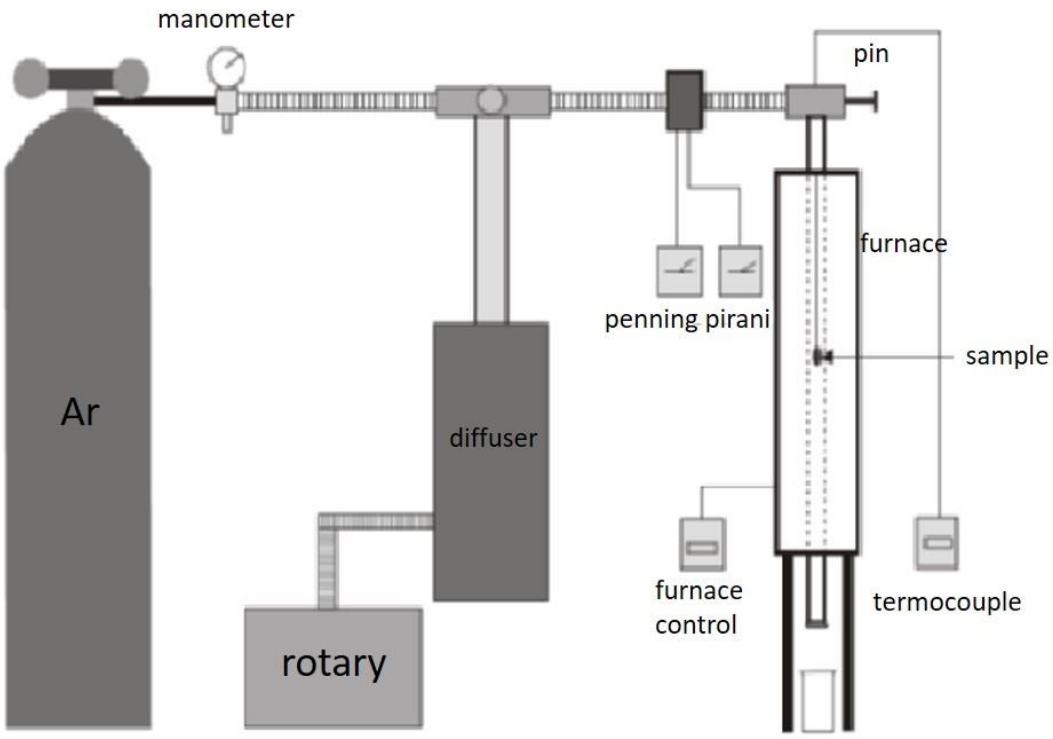

Figure 2. 2. Scheme of the vertical furnace used for the quenching and annealing thermal treatments [1].

Furthermore, this furnace was used also to perform thermal treatments in order to modify the atomic order and the microstructural parameters in powder samples, including samples previously treated by mechanical methods. In that case, the sample is introduced in a secondary quartz tube with tantalum balls to remove the oxygen from the atmosphere, avoiding oxidation in the powder.

2.1.3. Mechanical treatments

Mechanical treatments have been applied to the samples throughout this thesis with two objectives. On the one hand, to obtain, from the polycrystalline ingots, samples in powder state to perform the diffraction experiments avoiding the presence of textures. On the other hand, to modify in a controlled way the microestructural state of the samples introducing defects by mechanical alloying.

For the first purpose, hand milling in agate mortar, in some cases followed by sieving, was the method employed to obtain homogenous powders. In some cases, once the powder has been obtained, an annealing has been carried out to eliminate defects. When we wanted to study the influence of the defects and the microstructure in the magneto-mechanical properties of the alloys, ball milling at different milling times has been carried out. Thus, by modifying the milling parameters, the microstructure has been modified in a controlled and repetitive manner.

Ball milling is a mechanochemical technique used to induce deformation, grind, mix and cold welding of the particles for different materials as minerals, paints, ceramics or metals during repeated collisions with a ball.

Figure 2. 3. Ball-mill RETSCH E$_{MAX.}$

A planetary ball mill has been used in this work. The sample to be ground is introduced in a cylindrical container together with the milling balls, made of tungsten carbide in our case. The cylindrical container is located and fixed in a rotating platform producing the movement

of the balls that impact with the powder, reducing the size of the particles and changing their structure and their physical properties. The ratio between the volume of the powder and the balls, the milling time or the rotation energy are the adjustable parameters in this type of process. Controlling those variables allows the reproducibility of the final specimen.

One of the difficulties addressed during the milling process was that, due to the impacts between the balls, the cylinder and the sample, the temperature of the environment increases, and consequently the risk of sample oxidation. To avoid this issue, the process was carried out in short periods of milling of 5 minutes, interrupted by breaks of 30 minutes during which the cylinder was removed from the platform in order to cool it.

2.2. SAMPLE CHARACTERIZATION

2.2.1. Scanning Electron Microscopy (SEM) and Transmission Electron Microscopy (TEM)

These techniques have been used for the compositional and particle size analysis in an occasional way. Therefore, only a general description of the techniques and the instruments employed will be given.

Scanning Electron Microscopy (SEM) produces images of the surface of the sample with a focused high-energy electrons beam. The three most common signals used to characterize the sample are the secondary electrons, the backscattered and the characteristic X-rays. As effect of the interaction of the electron beam with the specimen, X-rays linked to the inner dexcitations of the atoms are emitted and are used to the compositional microanalysis, calling this technique *energy-dispersive X-rays spectroscopy (EDX)*. Moreover, the intensity and the angular distribution of the *back-scattered electrons* are sensitive to the atomic number of the probed atoms in the material and to the local direction of the surface, offering the possibility to make compositional analysis (different signals for phases with different compositions) and topography analysis (different orientations between grains in a single phase or between different phases with the same composition). On the other hand, low energy electrons from the sample can be extracted by the incident electron beam, named *secondary* emitted electrons which give topography information. During this thesis, a Jeol JSM-5610LV system was used for the analysis of the particle size after milling the alloys and also to check the composition of the synthetized samples.

Transmission Electron Microscopy (TEM) produces high-resolution images of the inside of a material using the transmitted electron from a focused high-energy electrons beam. Depending on the operating mode, the interaction between the transmitted electrons through the sample and the specimen creates an image what gives information about microstructure as the particle size, presence of defects as dislocations, twins, order domains, and crystal structure and symmetry. As the electrons have to be transmitted through the samples, these should be very thin; this technique is thus well adapted for the study of nano-sized objects. In this thesis, this technique was used to analyze the obtained particle size after high-energy ball-milling using (Hitachi H600 100keV TEM).

2.2.2. Thermal characterization. Differential scanning calorimetry (DSC)

Differential scanning calorimetry is a thermal analysis technique consisting on the measurement of the heat exchange required to keep the sample and a reference at the same temperature during temperature ramps or in isothermal measurements. Then, if the sample undergoes a first or second order transition or a chemical reaction, the heat required to keep the same temperature on the sample and on the reference will be different. In an exothermic process, the sample gives energy to the environment and the heat flow required is lower than in the reference, while in an endothermic one, the sample absorbs energy and, consequently, the heat flow should be higher in the sample than in the reference. Therefore, with this technique, it is possible to detect the different transformations that a material undergoes, determine the absorbed or liberated energy during the thermodynamic processes and the temperatures where those transitions or chemical reactions occur.

All the calorimetric measurements were carried out in a commercial DSC Q TA100 calorimeter. This device consists on a small furnace where two measurement pans (sample and reference) are located. The pans are connected to a thermal resistance and to a thermocouple to control the sample and reference temperatures, with another thermocouple located in the body of the furnace to control the temperature of the whole measurement system. To avoid possible oxidations and improve the thermal conductivity in the furnace, the sample environment is under a nitrogen gas flux.

Depending of the required range of temperatures, the calorimeter has different temperature control systems, allowing measurements between 90K and 1000K. The *FACS* system (Finned Air Cooling System), based in compressed air refrigeration, allows measuring from room temperature up to 1000K. On the other hand, the low temperature range is reached with the system *LNCS* (Liquid Nitrogen Cooling System) that works between 90K and 673K. Finally, the most used system during this thesis is the *RCS* (Refrigerated Cooling System), which using a vapor compressor allows measuring between 180K and 673K, the temperature range where most of the processes analyzed in this work occur.

In order to convert the electric signal of the sensors of the calorimeter into thermodynamic quantities, a calibration of the system is needed. Calibrations must be performed frequently, in particular after changes in the measurement conditions. From the calibration, we obtain a baseline and a *cell constant*, i.e. the ratio between the reference value of a given experimental variable and the measured one - in our case, the latent heat of an Indium sample. The baseline is obtained in two steps: first, the measurement of the empty furnace in the required temperature range; second, the repetition of the same measurement with two identical sapphire disks located in the sample and in the reference pans. Then, the latent heat of an Indium sample is measured, allowing calculating the values of enthalpy associated to the heat exchanges.

Due to the fast throughput of this technique, DSC measurements were the first characterization experiments performed after the sample preparation. By measuring ramps at 10K/min in cooling and heating modes it is possible to determine if the obtained alloys present a martensitic transformation, the temperatures where this transformation takes place and the enthalpy associated to the direct and reverse transitions. An example of the result obtained is shown the curve in Figure 2. 5. The critical temperatures are determined in the intersection of the tangents of the baseline and the peak where the exothermic and endothermic peaks start and finish. It this way, we identify the initial (M_S) and final (M_F) temperatures of the martensitic

transformation, and the initial (A_S) and final (A_F) temperatures of the reverse transformation from martensite to austenite structure. Moreover, the Curie temperature (T_C) indicating the onset of long-range magnetic order can be identified by a small variation in the baseline of the calorimetric curve.

Figure 2. 4. Differential Scanning Calorimeter Q-100 DSC, TA Instruments.

Furthermore, other types of processes can be detected and analyzed using this technique, like the appearance of secondary phases, atomic ordering, recrystallization, etc. with effects in the physical and magnetic properties of the shape memory alloys.

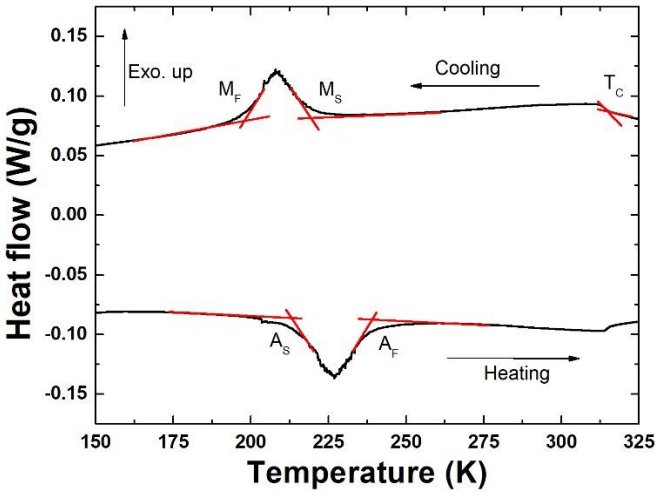

Figure 2. 5. Typical DSC curve with the determination of the critical temperatures obtained by tangents method.

2.2.3. Macroscopic magnetic characterization: magnetometry

The magnetic properties were analyzed in a SQUID magnetometer (Superconducting Quantum Interference Device). This system allows stuying the magnetization (M) and the

susceptibility (χ) of the magnetic alloys covering a broad range of temperatures (1.5K to 300K) and magnetic fields (-7T to 7T).

The SQUID is a very sensitive magnetometer consisting on a superconducting loop, containing one or two Josephson junctions, where an electric current circulates. The Josephson junctions are non-superconductiong links between superconductors where the electrons can flow through by quantum tunneling from a particular threshold value of the current. Figure 2.6 shows a scheme of the superconducting ring of a SQUID magnetometer. Since the magnetic flux enclosed by the superconducting loop should be constant, any change in an external magnetic field produces a current in the loop to counteract the change on the flux. The magnetic flux in the superconducting loop is quantized in multiples of the magnetic flux quantum $\phi_0 = 2\pi\hbar / 2e = 2.0678\text{x}10^{-15}$ Tm^2. If a constant current is maintained in the SQUID device, the output voltage in the setup of Figure 2. 6 oscillates with the changes in the magnetic flux produced by the presence of a magnetic sample that generate currents exceeding the critical currents of the junctions. Counting the oscillations allows evaluating the flux change due to the sample, since each oscillation corresponds to the increment of one flux quantum. The great sensitivity of the SQUID devices is therefore associated with the possibility of measuring changes in magnetic field associated with one flux quantum, making possible the detection of very small variations in the magnetic field over large absolute values of the field.

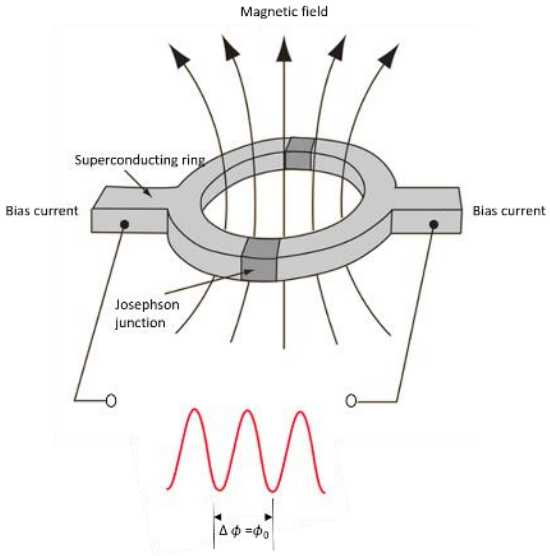

Figure 2. 6. Scheme of the superconducting loop of a SQUID magnetometer.

The magnetic characterization was carried our using the Quantum Design MPMS XL-7 SQUID magnetometer shown in Figure 2. 7. The magnetic measurements performed in this work were the dependence of the magnetization with the temperature at constant magnetic field *M(T)* and the variation in the magnetization with the applied magnetic field at constant temperatures *M(H)*. Additionally, one of the physical properties of technological interest of these alloys, the magnetocaloric effect, can be indirectly evaluated from the magnetometry measurements. According to classical thermodynamics, the magnetic entropy change ΔS as a consequence of a magnetic field increase can be indirectly measured by the magnetization curves using the following expression as explained in the first chapter [2, 3].

$$\Delta S = S(T,H) - S(T,0) = \int_0^H \left(\frac{\partial M}{\partial T}\right)_H dH \quad (2.1)$$

Negative (positive) values of the entropy change are expected when the magnetization decreases (increases) with temperature for the full set of applied fields. In the same way, a magnetic field reduction induces an entropy change $S(T,0) - S(T,H) = -\Delta S$.

Figure 2. 7. Quantum Design MPMS XL-7 SQUID magnetometer.

2.2.4. Mössbauer spectroscopy

Mössbauer spectroscopy is a technique based on the emission and absorption of gamma rays in solids when radioactive nuclei in excited states decay and might excite other stable nuclei, giving rise to nuclear resonant absorption and fluorescence. In brief, the sample is exposed to gamma radiation and a detector behind the sample measures the intensity of the transmitted beam. A radioactive parent atom that decays to the target isotope present in the sample produces the gamma radiation. Therefore, the incident radiation has approximately the correct energy to be absorbed by the target atoms, the only difference being due to the chemical environment, which in fact is the subject of study. Some of the incident gamma rays are absorbed producing a drop in the intensity in the measurement. The analysis of the number, the shape and the position of those (inverse) peaks in the spectrum gives information about the chemical environment.

Due to the high resolution on the energy measured, it is possible to detect really small changes in the atomic environment. Typically, there are three types of nuclear interactions that can be observed and analyzed:

- The *isomer shift* that gives information about the chemical order and is related with the electronic density. It is detected by a small shift of all peaks.

- The *quadrupole splitting* reveals the interaction between the nuclear quadrupole and the electric field gradient, giving rise to a splitting of the nuclear energy levels corresponding to different alignments of the quadrupole moment with respect to the principal axis of an asymmetric electric field gradient (produced by an asymmetric electronic charge distribution or ligand arrangement).
- The *magnetic hyperfine splitting* is the result of the interaction between the nuclear magnetic moment and the intrinsic magnetic field. This interaction splits the initial peaks. The splitting is proportional to the magnetic field strength at the nucleus. Therefore, the magnetic field can be readily determined from the splitting of the peaks.
- *Time-dependent effects*, can influence the spectral line shapes and the values of the Mössbauer hyperfine parameters.

The Mössbauer spectroscopy experiments presented in this thesis were performed in collaboration with I. Unzueta, J. S. Garitaonandia, J. A. García and F. Plazaola of the University of the Basque Country. Mössbauer spectra were obtained using a $Ba^{119}SnO_3$ source in a transmission setup and fitted using the NORMOS program ^{119}Sn isotopes instead of the most common ^{57}Fe were used as source. This allows for the study of alloys with presence of Sn, avoiding the otherwise needed doping of the sample with Fe.

2.3. CRYSTAL AND MAGNETIC STRUCTURE CHARACTERIZATION: X-RAY AND NEUTRON DIFFRACTION

It is straightforward that the physical properties of the alloys studied in this work are intimately related with their crystal structure, microstructure and magnetic structure, making crucial the insight into these. X-ray and neutron diffraction techniques are the methods of choice for this analysis, in particular neutron diffraction, since it presents several advantages for the study of these materials, as will be explained in the following sections.

2.3.1. Diffraction: powders and single crystals

The wave properties of photons and neutrons (and other particles like electrons) gives rise to diffraction phenomena when a beam of such particles scatters in an elastic way with a crystalline solid, due to the interference of the scattered waves. The wave vector, $\boldsymbol{k}$, in crystallographic convention, is defined a vector in the direction of the beam with modulus $1/\lambda$, being λ the wavelength of the radiation. In a scattering process, we can define the scattering vector $\boldsymbol{Q} = \boldsymbol{k} - \boldsymbol{k'}$ with $\boldsymbol{k}$ and $\boldsymbol{k'}$ the incident and scattered wave vectors, respectively. Being diffraction an elastic process, both $\boldsymbol{k}$ and $\boldsymbol{k'}$ have equal modulus, $1/\lambda$. The diffraction by a three dimensional lattice of points is equivalent to a reflection of the incident beam on a family of net planes (*hkl*), and the diffraction condition is described by the Bragg's law:

$$n\lambda = 2d_{hkl}\sin\theta \tag{2.2}$$

where d_{hkl} is the distance between the atomic planes (with Miller indexes *hkl*), and θ is the angle between the incident beam and the atomic planes. We can see that $\boldsymbol{Q}$ has modulus $2\sin\theta/\lambda$ and is perpendicular to the family of planes.

Therefore, with the equation (2.2), one can determine the distances between interatomic planes from the observed diffraction maxima, allowing obtaining the crystallographic unit cell of the studied sample. Moreover, it is possible to determine the content of the unit cell (the position of the atoms) from the intensity of the observed diffracted peaks, which is proportional to the squared modulus of the structure factor, which in turn depends of the position of each atom in the unit cell and the form factors of the different atoms:

$$F(\boldsymbol{Q}) = \sum_{j=1}^{N} a_j e^{i2\pi \boldsymbol{Q}\cdot \boldsymbol{r_j}} \tag{2.3}$$

where j are the labels of the N atoms of the unit cell, $\boldsymbol{r_j}$ is the position of atom j in the cell, $\boldsymbol{Q}$ is the scattering vector, and a_j is the atomic diffusion factor $f_j(Q)$ for X-rays of the Fermi length b_j for neutrons of atom j.

In a single crystal, i.e., a solid in which the atoms, ions, or molecules keep a three-dimensional order in a continuous way through the entire volume, the Ewald's construction (Figure 2. 8) provides a straightforward interpretation for the scattering condition:

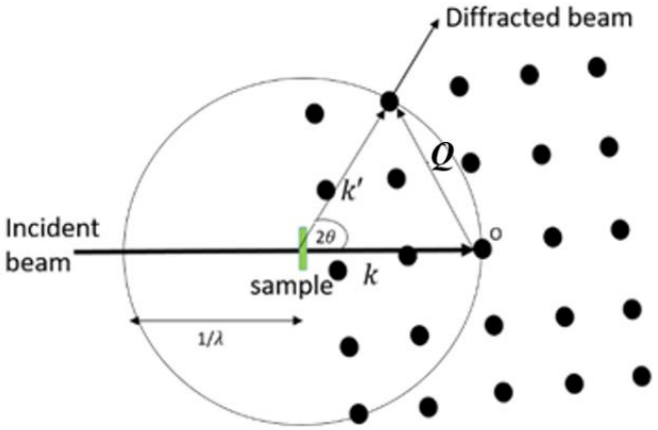

Figure 2. 8. Schematic representation of Ewald's sphere.

According with the Ewald's sphere configuration, only when the $\boldsymbol{Q}$ vector belongs to the reciprocal lattice and this vector intersects a sphere with radius$|\boldsymbol{k}| = 1/\lambda$, the crystal is in a Bragg position and diffraction maxima are produced.

In this work, most of the samples were in powder state. The principal characteristic of a powder specimen is the presence of a large amount of small crystals with different orientations and thus with different diffraction conditions, which implies a large number Ewald's spheres

with different orientations. As a result, the diffracted beams produce a geometrical figure known as *Debye-Scherrer cones*, as is shown in Figure 2. 9.

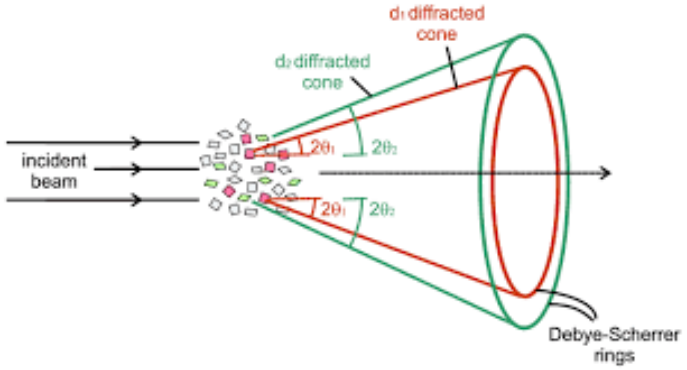

Figure 2. 9. Scheme of powder diffraction showing in different colors the different Debye-Scherrer cones due to the different diffraction conditions.

The intersection of such cones with a linear detector produces a diffractogram, as shown in Figure 2. 10, where the position and the intensity of those cones is recorded.

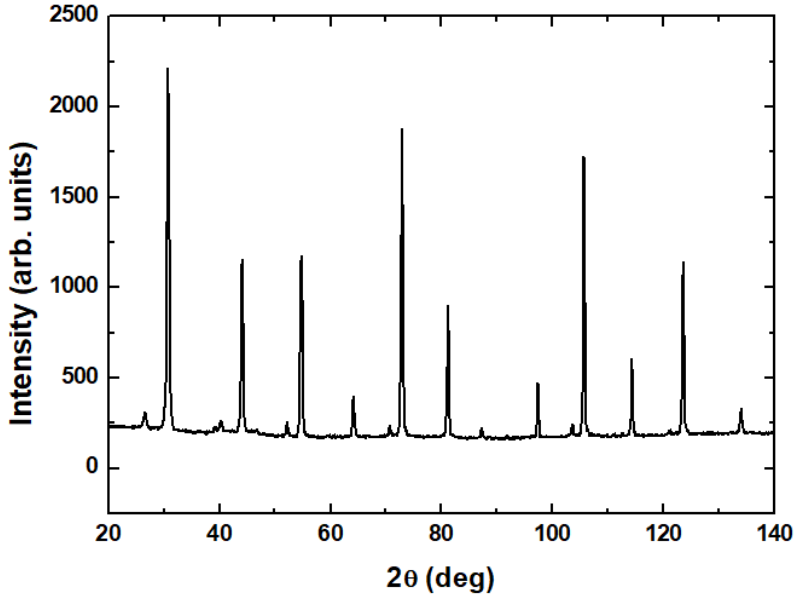

Figure 2. 10. Typical powder diffractogram for austenitic phase.

While the positions of the peaks depend on the periodicity (unit cell) of the system, the intensities are given by the expression:

$$I = C\frac{J_{hkl}A_{hkl}\bar{F}^2{}_{hkl}}{L} \tag{2.4}$$

where:

- *C* is an *instrumental constant* depending on the instrument characteristics, the beam intensity, the wavelength, the sample dimensions or its density.
- J_{hkl} is the *multiplicity* of the plane *hkl*, that is, the number of the reflections that participate in the intensity of the peak.
- A_{hkl} is the absorption factor, that accounts for the absorption effects produced in the sample
- $F(\boldsymbol{Q}) = F(hkl) = \sum_j a_j e^{2\pi i(hx_j+ky_j+lz_j)} e^{-B_j \left(sin^2\theta\right)/\lambda^2}$ is the *structure factor*, as deduced from eq. (2.3), that contains information about the position of the atoms in the unit cell, where *hkl* are the Miller indices that identify a family of planes; x_j, y_j, z_j are the coordinates of the atom *j* in the unit cell, and $e^{-B_j \left(sin^2\theta\right)/\lambda^2}$ is the Debye-Waller factor, with B_j the atomic displacement parameter, that accounts for the decrease of intensity at high angles produced by displacement of the atoms from their positions of equilibrium (because of thermal agitation, for example).
- *L* is the *Lorentz factor*, a geometric factor accounting for the length of time that a moving crystal remains in the diffracting position for any particular scattered beam.

2.3.2. Rietveld refinement

The analysis of the structures from the collected powder diffractograms is carried out by the Rietveld method, which consists on refining the crystal structure by fitting the entire profile of the diffraction pattern to a calculated profile using a least-squares approach. There is no intermediate step of extracting structure factors, and so patterns containing overlapping Bragg peaks can be analyzed. The equation to minimize is

$$\chi^2 = \sum_{i=1}^{n} w_i \{y_i - y_{c,i}(\boldsymbol{\beta})\}^2 \tag{2.5}$$

where *i* runs for the number of observations, y_i is the observed intensity and $y_{c,i}(\boldsymbol{\beta})$ is the intensity calculated by the model as a function of the parameter vector $\boldsymbol{\beta}$ ($\boldsymbol{\beta} = \beta_1, \beta_2, ..., \beta_p$), with the weight factor, w_i, given by the inverse of the square of the variance of the experimental observation, $w_i = 1/\sigma_i^2$. The optimization of the parameters is performed by imposing the condition $\frac{\partial \chi^2}{\partial \boldsymbol{\beta}_i} = 0$. A Taylor expansion of $y_{c,i}(\boldsymbol{\beta})$ around $\boldsymbol{\beta_0}$ allows the application of an iterative process. Several agreement factors allow assessing the quality of the refinement (the lower, the better), like the *R-profile* factor (R_p), *R-weighted profile* factor (R_{wp}) and the *expected R-weighted profile* factor (R_{exp}), or the *R-Bragg* factor (R_B), which are obtained as follows:

$$R_p = 100 \frac{\sum_{i=1}^{n} |y_i - y_{c,i}|}{\sum_{i=1}^{n} y_i} \tag{2.6}$$

$$R_{wp} = 100\left[\frac{\sum_{i=1}^{n} w_i|y_i - y_{c,i}|^2}{\sum_{i=1}^{n} w_i|y_i|^2}\right]^{1/2} \quad (2.7)$$

$$R_{exp} = 100\left[\frac{N-P}{\sum_{i=1}^{n} w_i|y_i|^2}\right]^{1/2} \quad (2.8)$$

$$R_B = 100\frac{\sum_{hkl}|I_{obs,hkl} - I_{calc,hkl}|}{\sum_h|I_{obs,hkl}|} \quad (2.9)$$

being the goodness of fit indicator $S = {R_{wp}}/{R_{exp}}$ or, most commonly used, the *reduced chi-square* $\chi^2 = \left({R_{wp}}/{R_{exp}}\right)^2 = S^2$. *N* in the expression of R_{exp} is the total number of points used in the refinement, *P* is the number of refined parameters and *N-P* is the number of degrees freedom. The Bragg factor, R_B, is calculated from the observed and calculated integrated intensities ($I_{obs,hkl}$and $I_{calc,hkl}$, respectively) of the Bragg reflections *(hkl)* in the pattern. When different reflections contribute to a region in the pattern, the observed integrated intensity is calculated by a *proportional sharing* between the different contributions according to the actual model.

All the nuclear and magnetic structures calculated during this thesis where refined using the programs of the *Fullprof Suite* [4].

2.3.3. Microstructural analysis

The combination of the Rietveld method together with a modeling of the shape of the peak is useful for the study of the microstructure of the samples. Dislocations, anti-phase domains, micro-strains and small crystallite sizes are structural defects that manifest in a broadening of the Bragg peaks in powder diffractograms.

The Voigt approximation is one of the most useful ways for modeling the peak shape and analyze the microstructural effects. Within this approximation, the instrument and sample intrinsic profiles are described as a convolution of Lorentzian and Gaussian components. Parameters as the volume averages of sizes and strains are derived from the integral breadths of the peaks. The normalized Gaussian and Lorentzian functions are defined as:

$$G(x) = a_G e^{-b_G x^2} \quad (2.10)$$

$$L(x) = \frac{a_L}{1 + b_L x^2} \quad (2.11)$$

where a_G, b_G, a_L and b_L are determined from the full width at half maximum value, *H*:

$$a_G = \frac{2}{H}\sqrt{\frac{ln2}{\pi}} \quad b_G = \frac{4\,ln2}{H^2} \quad a_L = \frac{2}{\pi H} \quad b_L = \frac{4}{H^2}$$

The integral breadths of the Gaussian and Lorentzian functions are described by the expressions

$$\beta_G = \frac{1}{a_G} = \frac{H}{2}\sqrt{\frac{\pi}{ln2}}\ ;\ \beta_L = \frac{1}{a_L} = \frac{\pi H}{2}$$

The psedo-Voigt function, *pV(x)*, is an approximation of the Voigt function in the form of a linear combination of a Lorentzian and a Gaussian function with the same full width at half maximum parameter, *H*, instead of two parameters coming from each contribution:

$$pV(x) = \eta L'(x) + (1-\eta)G'(x) \tag{2.12}$$

The integral breadth of a normalized pseudo-Voight function is the inverse of the maximum value, as described by the following expression, since when the function is multiplied by a constant (integrated intensity) the integral breadth does not change:

$$\beta_{pV} = \frac{\int I_i pV(x)dx}{I_i pV(0)} = \frac{1}{pV(0)} = \frac{\pi H/2}{\eta+(1-\eta)\sqrt{\pi\, ln2}} \tag{2.13}$$

The Scherrer formula relates the integral breadth of a particular reflection due to size effect, β_S , with the volume-average of the apparent size of the crystallites in the direction normal to the scattering planes:

$$\langle D\rangle_V = \frac{\lambda}{\beta_S \cos\theta} \tag{2.14}$$

In a diffraction pattern, the peak broadening due to size effects increases with 2θ as $(\cos\theta)^{-1}$. Except for spherical particles, the width depends on the direction in reciprocal space.

It is worth noting that the 'crystalline size' ere refers to the coherent-diffraction domains, which does not necessarily have to coincide with the 'particle size' observed by other techniques like electron microscopy. Moreover, the relation of the apparent size with physical dimensions of the coherent domains is not direct. We should normally assume a particular average shape of the crystallite (e.g. spheres) in order to relate the apparent sizes obtained for different Bragg reflections with characteristics dimensions (e.g. diameter).

The apparent size can be expressed in terms of a normalized *column-length* distribution *pv(l)*:

$$\langle D\rangle_V = \int_0^\infty p_V(l)\cdot l \cdot dl \tag{2.15}$$

where *l* is the length (column-length) normal to the scattering planes for each crystallite. The distribution $p_v(l)$ can be derived from the Gaussian and Lorentzian integral breadths:

$$p_V(l) = 2l[2\beta_L^2 - \pi\beta_G^2 + 4\pi\beta_L\beta_G^2 l + 2\pi^2\beta_G^4 l^2]exp\{-2l\beta_L - \pi\beta_G^2 l^2\} \tag{2.16}$$

Concerning the strain, the peak shape and width depend on both the particular reflection and the direction in reciprocal space, with the width of the peaks increasing with 2θ as $\tan\theta$. The so-called *maximum strain*, *e*, is related with the integral breadth of a particular reflection due to strain effect, β_D, by:

$$e = \beta_D /4\ tan\theta \tag{2.17}$$

Therefore, from the analysis and deconvolution of the integral breaths of the peaks in a diffractogram as implemented in Fullprof [4], microstructural parameters as the sizes and strains can be derived.

When the structure factors and the associated structural parameters (unit cell content) are not know or their knowledge is not the objective of the analysis, a lighter method, the so-called *Le Bail* fit, can be used as an alternative to the Rietveld method. The algorithm involves refining the unit cell and the profile parameters, with the peak intensities being also adjustable

parameters of the fit that are refined to match the measured powder diffraction pattern, avoiding considering the structure factors and their associated parameters. The *Le Bail* method is particularly useful when the aim of the analysis is focused on the determination of the microstructural parameters.

2.3.4. X-ray diffraction. Laboratory and synchrotron diffractometers

Powder X-ray diffraction (PXRD) has been used along this work to characterize the alloys and for microstructure analysis. We have employed both laboratory PXRD equipment and synchrotron PXRD instruments, taking advantage in the last case of the excellent resolution provided by this technique.

The laboratory PXRD measurements presented in this thesis were performed in a Siemens Diffractometer D5000 working at room temperature with Cu Kα radiation in reflection, in Bragg-Brentano configuration. This configuration is the most extended in laboratory PXRD instruments. The powder specimen is located in a plate with both source and detector at the same distance to the sample, describing a circle (see Figure 2. 11). The plate, the source and the detector can be rotated around the center of the diffractometer. In the Bragg-Brentano geometry, in contrast to other geometries, only one reflection can be well focused at a time. The focusing condition is fulfilled only when the angles between the specimen surface and incident and diffracted rays are equal (θ). The photon generator and the detector move around the circle covering all the real space to analyze the intensity of the scattered beam, obtaining peaks when the diffraction conditions are fulfilled [5].

The X-ray source is a vacuum tube where the electrons, due to a voltage difference, travel from the cathode to the metallic target constituting the anode, thus emitting the X-rays by fluorescence and as effect of the deceleration. Depending of the metal used as target the X-rays have different energies and wavelengths, with Cu and Mo being the most used targets for diffraction experiments, producing wavelengths of 1.54Å and 0.72Å, respectively.

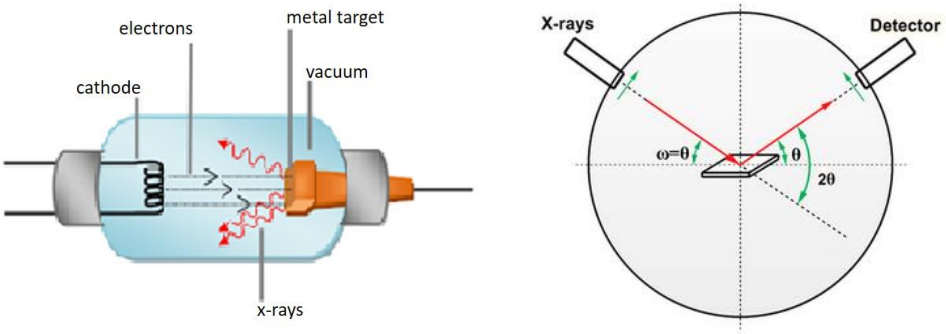

Figure 2. 11. Schematic representation of X-rays generation in an X-ray tube and scheme of Bragg-Brentano geometry.

We have also carried out PXRD experiments in the high-resolution powder diffraction station of BL04-MPSD beam line at ALBA synchrotron, in Barcelona, Spain, taking advantage of the high resolution of this instrument, the high photon flux allowing fast data acquisition,

and the possibility of performing variable-temperature measurements. In Figure 2. 12 a scheme of BL04-MPSD diffractometer is shown. This beam-line offers a broad range of operation energies between 8 and 50keV. The wavelength of the very intense and highly collimated synchrotron X-ray beam is selected by a monochromator consisting in a double Si crystal with (111) orientation. The diffractometer works in Debye-Scherrer configuration, in transmission, with the sample placed in a capillary (of 0.5 mm of diameter, in our case) that is fixed horizontally. During data acquisition, the capillary is spinning around its longitudinal axis to average out possible textures in the powder. An Oxford cryostream allows varying the temperature of the sample from 80 to 500K by a nitrogen gas blowing system. For higher temperatures, a FMB Oxford hot air blower can be employed, covering the temperature range from room temperature to 900C. Finally, two possible detectors are used to record the diffracted intensity. A MAD26 detector combined with an array of analyzer crystals gives the higher resolution, while a Mythen detector composed by 6 modules covering an angular range of 40 degrees in 2θ allows for faster data acquisition.

In the experiments carried out during this thesis the energy of the beam was set to 28 keV to avoid the energies where the alloys present absorption. Since the resolution of the diffraction patterns was sample-dominated, and in order to perform variable-temperature measurements, we used the Mythen detector, with the sample temperature controlled by the Oxford cryostream, which is well adapted for the temperature range of interest.

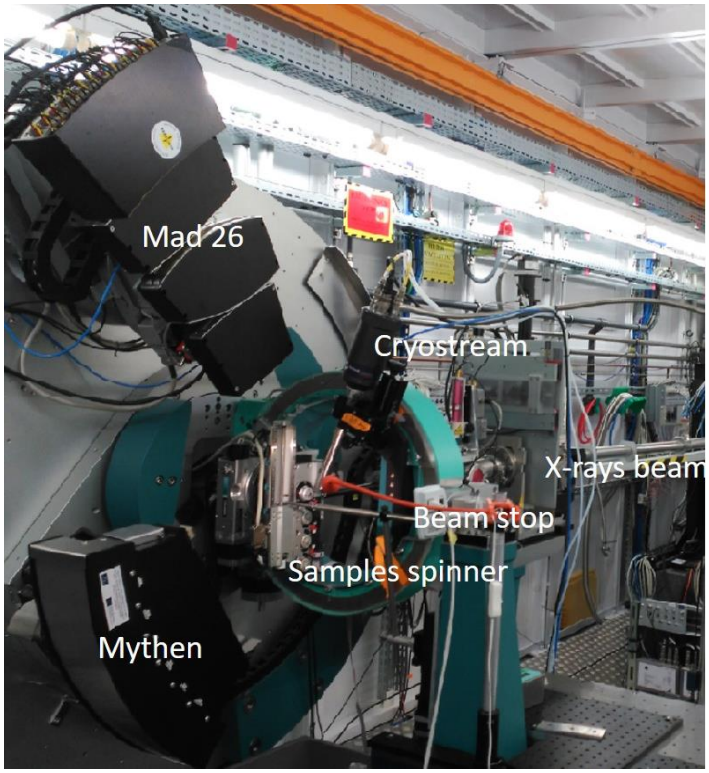

Figure 2. 12. Illustration of powder diffractometer BL04-MPSD at ALBA synchrotron.

2.3.5. Neutron properties and basic concepts on neutron scattering

Neutrons are heavy subatomic particles, which, together with protons, form the nuclei of the atoms. They were discovered in 1932 by Chadwick, and it was four years later, in 1936, when it was discovered that they can be diffracted, corroborating their wave-particle duality. The appearance of the first nuclear reactors in 1942, with the consequent increase of the available neutron flux, made possible their use for neutron scattering experiments. At present, neutron scattering experiments are carried out in nuclear reactors, where neutrons come from the fission of ^{235}U, or in spallation sources, where neutrons are produced by the incidence of accelerated protons in heavy elements as W, Pb or Hg.

The excellent properties that neutrons present for the study of condensed matter make of them an exceptional experimental tool for the study of the alloys addressed in this thesis:

- The wavelengths of the neutrons are of the same order of magnitude that the interatomic distances in the samples, and the energies of the neutrons are of the same order of the thermal excitations in solids and liquids. Therefore, neutrons can probe the structural and dynamical properties of the alloys.
- The neutron has no charge, the interaction with matter is weak, and consequently can penetrate more deeply in the matter than other probes like X-rays. That allows studying materials in bulk, and the use of different environments as cryostats, furnaces or pressure cells. The drawback is the need for relatively big samples to compensate for the low scattering probability.
- The scattering of neutrons is mainly produced in the nuclei, which can be considered as point object in comparison with the wavelength of the neutrons. Therefore, the scattering amplitude for neutrons, called scattering length or fermi length, b, is constant in the reciprocal space and there is no decay of the scattering amplitude with Q, which makes neutrons particularly adapted for precise structural determinations, since very small atomic displacements can be identified.
- The neutron has a magnetic moment (spin s=1/2), which means that it interacts with unpaired electrons in magnetic atoms. Therefore, the elastic scattering gives information about the arrangement of electron spins and the density of the distribution of unpaired neutrons. In the case of the inelastic scattering, the energy change in the neutron gives information about the magnetic excitations.
- The scattering cross section is not proportional to Z, which makes neutrons particularly advantageous for the investigation of materials with light atoms in presence of heavier elements in their composition and, as in the present case, for the study of alloys with elements that are neighbors in the periodic table. Moreover, they can distinguish isotopes of the same atom allowing the analysis of materials by isotopic substitution.

The basic quantity to describe a scattering process is the *scattering cross section*, σ, defined as the ratio between the number of neutrons scattered per second and the incident flux, Φ (number of neutrons per area and time unit). During a scattering process, a neutron with mass m, initial wavevector, $\boldsymbol{k}$, energy, E, and spin $\boldsymbol{\sigma}$, is scattered by the sample into a small solid angle, $d\Omega$, in the direction θ, ϕ, given by the vector $\boldsymbol{r}$, with final wavevector, $\boldsymbol{k'}$, energy, E' and

spin $\boldsymbol{\sigma'}$ (Figure 2. 13). If we consider only the neutrons scattered into the solid angle $d\Omega$ and as a function of their energy, we define the *partial differential cross section* $d^2\sigma/d\Omega dE'$, which is the quantity measured in experiments, i.e., the number of neutrons scattered per second into the solid angle $d\Omega$ with final energy between E' and $E'+d\,E'$, divided by Φ. Supposing that the energy of the scattered neutron is not analyzed but that simply all the neutrons scattered in the solid angle $d\Omega$ are counted, this is described by the *differential cross section*, $d\,\sigma/d\Omega$. The kinematical approximation (Born approximation) of neutron scattering supposes that the change of the incident neutron wave by the scattering center is almost negligible and can be treated as a perturbation. In this approximation, the *differential cross section* is derived from the Fermi's golden rule, considering neutrons with initial and final states $|k\rangle$ and $|k'\rangle$ scattered by a target with initial and final states $|\lambda\rangle$ and $|\lambda'\rangle$, as follows:

$$\left(\frac{d\sigma}{d\Omega}\right)_{\lambda\to\lambda'} = \frac{1}{\Phi}\frac{1}{d\Omega}\sum_{\boldsymbol{k'}} W_{\boldsymbol{k},\lambda\to\boldsymbol{k'},\lambda'} = \frac{2\pi}{\hbar}\rho_{\boldsymbol{k'}}|\langle \boldsymbol{k'}\lambda'|V|\boldsymbol{k}\lambda\rangle|^2 = |f(\Omega)|^2 \qquad (2.18)$$

where the $W_{\boldsymbol{k},\lambda\to\boldsymbol{k'},\lambda'}$ is the number of the transitions per second from the state ($\boldsymbol{k}$, λ) to the state ($\boldsymbol{k'}$, λ') , $\rho_{\boldsymbol{k'}}$ is the number of momentum states in $d\Omega$ per unit energy range for neutrons in the state $\boldsymbol{k'}$, and V is the interaction potential.* $f(\Omega)$ is the so-called scattering amplitude and it depends on the kind of interaction potential: nuclear or magnetic.

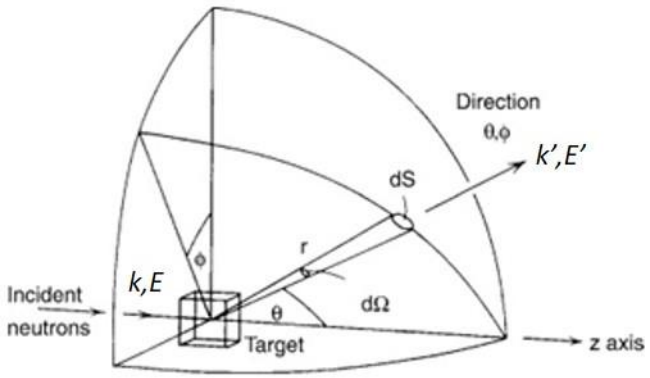

Figure 2. 13. Scheme of scattering process.

In the case of scattering by the nucleus, taking in to account that the nuclear force, which mainly causes the scattering, has an interaction range of about ~10^{-15}m, much smaller than the wavelength of thermal neutrons ~10^{-10}m , it is possible to consider the atom as a point scattered. As an approximation, we can describe the incident and scattered wavefunctions as flat and spherical waves, respectively, and the potential V in the equation (2.18) as a short range potential adopting the form of the *Fermi pseudopotential*

$$V(\boldsymbol{r}) = \frac{2\pi\hbar^2}{m} b\delta(\boldsymbol{r}-\boldsymbol{R_j}) \qquad (2.19)$$

* From ref. 6 (p.12) : It may be noted that although the sum on the left-hand side of 2.18 is over a range of neutron states, the expression on the right-hand side is evaluated at a particular state $\boldsymbol{k'}$

where $\delta(\boldsymbol{r} - \boldsymbol{R_j})$ is a three-dimensional Dirac delta function with $\boldsymbol{r}$, the neutron position and $\boldsymbol{R_j}$, the position of the scattering center j. b is the *scattering length*, a complex number with dimensions of length, where the real part accounts for the nuclear scattering and the imaginary one is related to the absorption. By convention, b is positive for repulsive potentials. The incident and scattered wavefunctions can be expressed as:

$$|k\rangle = e^{ikz} \tag{2.20}$$

$$|k'\rangle = -\frac{b}{r} e^{i\boldsymbol{k'r}} \tag{2.21}$$

In the case of the scattering by a single nucleus, $d\sigma/d\Omega = b^2$ and $\sigma_{tot} = 4\pi b^2$, which means that the cross section can be considered as the effective area of the nucleus.

Replacing Fermi's pseudopotential in eq. (2.18), applying the conservation of the energy, adding in λ' and averaging over λ, the expression for the cross section per energy unit becomes [6]:

$$\frac{d^2\sigma}{d\Omega dE'} = \sum_{\lambda\lambda'} p_\lambda \left(\frac{d^2\sigma}{d\Omega dE'}\right)_{\lambda\to\lambda'} = \frac{k'}{k}\frac{1}{2\pi\hbar}\sum_{jj'} b_j b_{j'} \int_{-\infty}^{\infty} \langle e^{-i\boldsymbol{Q}\cdot\boldsymbol{R_{j'}}(0)} e^{i\boldsymbol{Q}\cdot\boldsymbol{R_{j'}}(t)}\rangle\, e^{-i\omega t} dt \tag{2.22}$$

where $p_\lambda$is the probability that the target (sample) has initial state λ, $\boldsymbol{Q}$ is the scattering vector ($\boldsymbol{Q} = \boldsymbol{k} - \boldsymbol{k'}$) and ω is defined as $\hbar\omega = E - E'$. p_λ is given by the Boltzmann distribution $p_\lambda = \frac{1}{Z} e^{\left(-\frac{E_\lambda}{k_B T}\right)}$ where Z is the partition function introduced to ensure that $\sum_\lambda p_\lambda = 1$.

For a system of N scattering centers, the sum in $b_j b_{j'}$ gives a term in $\left(\bar{b}\right)^2$ related with the *coherent scattering* , implying correlation between the positions of different nuclei, j and j', and a term in $\overline{b^2} - \left(\bar{b}\right)^2$ related with the *incoherent scattering* , accounting for the correlation between the position of the same nucleus at time 0 and at time t:

$$\left(\frac{d^2\sigma}{d\Omega dE'}\right)_{coh} = \left(\bar{b}\right)^2 \frac{k'}{k}\frac{1}{2\pi\hbar}\sum_{jj'} \int_{-\infty}^{\infty} \langle e^{-i\boldsymbol{Q}\cdot\boldsymbol{R_{j'}}(0)} e^{i\boldsymbol{Q}\cdot\boldsymbol{R_j}(t)}\rangle\, e^{-i\omega t} dt \tag{2.23}$$

$$\left(\frac{d^2\sigma}{d\Omega dE'}\right)_{inc} = \left\{\overline{b^2} - \left(\bar{b}\right)^2\right\}\frac{k'}{k}\frac{1}{2\pi\hbar}\sum_{j} \int_{-\infty}^{\infty} \langle e^{-i\boldsymbol{Q}\cdot\boldsymbol{R_j}(0)} e^{i\boldsymbol{Q}\cdot\boldsymbol{R_j}(t)}\rangle\, e^{-i\omega t} dt \tag{2.24}$$

The coherent scattering depends on the direction of the scattering and can give interference effects between the waves dispersed by the different nuclei. The elastic (ω = 0) coherent scattering contains information about structures in equilibrium whereas inelastic ($\omega \neq 0$) coherent scattering provides information about the collective motions of the atoms. Incoherent scattering is isotropic and gives no interference effect and, since it depends on the correlation between the position of the same nucleus at different times, can give information about atomic motion.

When elastic coherent scattering gives interference effects between the waves dispersed by the different scattering centers, *diffraction* phenomena occur. In a periodic system, such as a crystalline solid, the partial differential cross section for *elastic coherent* scattering becomes:

$$\left(\frac{d^2\sigma}{d\Omega dE'}\right)_{\substack{coh\\el}} = \left(\bar{b}\right)^2 \frac{k'}{k}\frac{N}{2\pi\hbar} e^{(-i\boldsymbol{Q}\cdot\boldsymbol{u})^2} \sum_{\boldsymbol{l}} e^{i\boldsymbol{Q}\cdot\boldsymbol{l}} \int_{-\infty}^{\infty} e^{-i\omega t}\, dt \tag{2.25}$$

where we have considered the crystal as a Bravais lattice with N nodes with positions described by $\boldsymbol{l}+\boldsymbol{u}$, where $\boldsymbol{l}$ is the position of the cell in the lattice and $\boldsymbol{u}$ is the atomic displacement with respect to $\boldsymbol{l}$ (only one atom per unit cell).

The integral with respect to t is $\int_{-\infty}^{\infty} e^{-i\omega t}\,dt = 2\pi\hbar\delta(\hbar\omega)$ and since $\hbar\omega$ is the change in the energy of the neutron we see that the scattering is elastic and thus $|\boldsymbol{k}| = |\boldsymbol{k}'|$

Integrating in energy, that is, counting all the neutrons scattered in a given direction regardless of their energy, we obtain

$$\left(\frac{d\sigma}{d\Omega}\right)_{\substack{coh\\el}} = \int_0^{\infty}\left(\frac{d^2\sigma}{d\Omega dE'}\right)_{\substack{coh\\el}} dE' = \left(\bar{b}\right)^2 \frac{N}{2\pi\hbar} e^{(-i\boldsymbol{Q}\cdot\boldsymbol{u})^2} \sum_l e^{i\boldsymbol{Q}\cdot\boldsymbol{l}} \tag{2.26}$$

The lattice sum $\sum_l e^{i\boldsymbol{Q}\cdot\boldsymbol{l}}$ implies that diffraction maxima will occur when the interference of the waves is constructive, that is, when $e^{i\boldsymbol{Q}\cdot\boldsymbol{l}} = 1$, which occurs when $\boldsymbol{Q} = \boldsymbol{k} - \boldsymbol{k}' = \boldsymbol{\tau}$, with $\boldsymbol{\tau}$ a reciprocal lattice vector. This condition is the same as Bragg's law (see section 2.5.1).

If we consider that we can have different scattering centers inside the unit cell of the lattice with position vector $\boldsymbol{d}$ with respect to $\boldsymbol{l}$, then

$$\left(\frac{d^2\sigma}{d\Omega}\right)_{\substack{coh\\el}} = N\left(\sum_d b_d e^{i\boldsymbol{Q}\cdot\boldsymbol{d}}\, e^{-i\boldsymbol{Q}\cdot\boldsymbol{u}}\right)^2 \sum_l e^{i\boldsymbol{Q}\cdot\boldsymbol{l}} = N|F_N(Q)|^2 \sum_l e^{i\boldsymbol{Q}\cdot\boldsymbol{l}} \tag{2.27}$$

where $F_N(Q)$ is the nuclear *structure factor*, in a description equivalent to the one in section 2.5.1.

2.3.6. Magnetic diffraction

As mentioned before, the magnetic moment of the neutrons makes possible the interaction with the magnetic field produced by unpaired electrons of the atoms, since they present a magnetic dipole moment. Therefore, the coherent elastic scattering contains information about magnetic structures, while the coherent inelastic scattering provides information about the collective magnetic excitations (magnons).

Both, the neutron and the unpaired electron, present magnetic dipole moments that are given by:

$$\boldsymbol{\mu_n} = -\gamma\mu_N\boldsymbol{\sigma} \tag{2.28}$$

$$\boldsymbol{\mu_e} = -2\mu_B\boldsymbol{s} \tag{2.29}$$

where $\mu_N = e\hbar/2m_p$ is the nuclear magneton, determined by the proton mass m_p , its charge e and a positive constant $\gamma = 1.913$ (gyromagnetic constant); $\mu_B = e\hbar/2m_e$ is the Bohr magneton, determined by the electron mass m_e, and charge e; $\boldsymbol{\sigma}$ is the Pauli spin operator for the neutron, with eigenvalues ± 1 and $\boldsymbol{s}$ is the spin angular momentum operator for the electron with eigenvalues $\pm 1/2$. An important consequence of the dipolar nature of the magnetic interaction is that the scattering is not isotropic, and only the component of the magnetization of the sample that is perpendicular to the scattering vector $\boldsymbol{Q}$ is effective in scattering neutrons.

The magnetic interaction potential, V_m, between the neutron dipole moment and the magnetic field, $\boldsymbol{H}$, produced by a system of n unpaired electrons at $\boldsymbol{r_i}$ positions with spins $\boldsymbol{s_i}$ and momenta $\boldsymbol{p_i}$ is

$$V_m(\boldsymbol{r}) = \boldsymbol{\mu_n H} = -\gamma\mu_N \boldsymbol{\sigma} 2\mu_B \cdot \left[\sum_i^n \nabla \times \left(\frac{\boldsymbol{s_i}\times\boldsymbol{R_i}}{R_i^3}\right) - \frac{1}{\hbar}\frac{\boldsymbol{p_i}\times\boldsymbol{R_i}}{R_i^3}\right] \quad (2.30)$$

where $\boldsymbol{R_i} = \boldsymbol{r} - \boldsymbol{r_i}$. The first term inside the brackets accounts for the dipolar interaction of the spin of the neutron with those of the electrons, while the second term comes from the spin-orbit coupling between the neutron spin and the orbital motion of the electrons. The Fourier transform of V_m can be expressed as:

$$V_m(\boldsymbol{Q}) = \frac{2\pi\hbar^2}{m} p\boldsymbol{\sigma}\boldsymbol{Q}_\perp(\boldsymbol{Q}) \quad (2.31)$$

where p is a constant (2.696 10^{-13} cm/μ_{NB}) and $\boldsymbol{Q}_\perp(\boldsymbol{Q})$ is defined as:

$$\boldsymbol{Q}_\perp(\boldsymbol{Q}) = \sum_i^n e^{\boldsymbol{Q}\boldsymbol{r_i}} \frac{1}{Q^2}\left(\boldsymbol{Q}\times\boldsymbol{s_i}\times\boldsymbol{Q} - \frac{i}{\hbar}\boldsymbol{Q}\times\boldsymbol{p_i}\right) \quad (2.32)$$

If we define the spin and orbital magnetization densities $\boldsymbol{M_s(r)}$ and $\boldsymbol{M_L(r)}$ as follows:

$$\boldsymbol{M}_S(\boldsymbol{r}) = -2\mu_B \sum_i^n \boldsymbol{s_i}\ \delta(\boldsymbol{r} - \boldsymbol{r_i}) \quad (2.33)$$

$$\nabla \times \boldsymbol{M}_L(\boldsymbol{r}) = -\frac{e}{mc}\sum_i^n \boldsymbol{p_i}\ \delta(\boldsymbol{r} - \boldsymbol{r_i}) \quad (2.34)$$

we can write $\boldsymbol{Q}_\perp(\boldsymbol{Q})$ as:

$$\boldsymbol{Q}_\perp(\boldsymbol{Q}) = \frac{1}{2\mu_B}\int e^{\boldsymbol{Q}\boldsymbol{r}}\frac{1}{Q^2}(\boldsymbol{Q}\times\boldsymbol{M}(\boldsymbol{r})\times\boldsymbol{Q}) \quad (2.35)$$

where $\boldsymbol{M}(\boldsymbol{r}) = \boldsymbol{M}_S(\boldsymbol{r}) + \boldsymbol{M}_L(\boldsymbol{r})$ is the total magnetization density.

We can define a magnetic structure factor for the neutron diffraction by the magnetic field generated by the electrons, which is the Fourier transform of the magnetization, $\boldsymbol{M}$:

$$\boldsymbol{F_M}(\boldsymbol{Q}) = p\sum_i \boldsymbol{M}_i\, e^{i\boldsymbol{Q}\boldsymbol{r_i}} \quad (2.36)$$

(the Debye-Waller factor has been omitted for simplicity) and

$$\boldsymbol{F}_{\boldsymbol{M}\perp}(\boldsymbol{Q}) = \frac{1}{Q^2}(\boldsymbol{Q}\times\boldsymbol{F_M}\times\boldsymbol{Q}) \quad (2.37)$$

which is the quantity that plays the role of the nuclear structure factor in nuclear diffraction but that has a vector and not a scalar character.

The magnetic structures can have a periodicity that is different to the one of the nuclear structure. To describe it, we use the magnetic propagation vector $\boldsymbol{q}$ (denoted also often as $\boldsymbol{k}$), which relates the nuclear unit cell with the magnetic one. $\boldsymbol{q}$ describes the relation between a magnetic moment and its equivalent in the unit cell, the magnetic moment of an atom j in the nuclear unit cell being:

$$\boldsymbol{m}_{jl} = -\sum_q \boldsymbol{m}_{jq}\, e^{i\boldsymbol{q}\boldsymbol{l}} \quad (2.38)$$

with $\boldsymbol{l}$ a lattice vector. Then, in the magnetic case, diffraction maxima will occur when $\boldsymbol{Q} = \boldsymbol{\tau} + \boldsymbol{q}$, with $\boldsymbol{\tau}$ a reciprocal lattice vector. A magnetic structure can have several propagation vectors, but the most common case is the situation with only one. When the magnetic and the nuclear

cell are the same, as in the case of ferromagnetic structures, $\boldsymbol{q} = 0$ and the magnetic and nuclear diffraction peaks are superimposed.

Therefore, we can treat the magnetic diffraction in an analogous way to the case of nuclear scattering by using $\boldsymbol{F_{M\perp}}(\boldsymbol{Q})$ in the place of $F_N(\boldsymbol{Q})$ and introducing the magnetic propagation vectors to describe the periodicity. However, there are important differences that arise from the different nature of the interactions. As mentioned before, the magnetic scattering is not isotropic, and only the component of the magnetization of the sample that is perpendicular to the scattering vector $\boldsymbol{Q}$ can be probed. Also, contrarily to the case of nuclear scattering, the magnetic scattering amplitude decays with Q (or, equivalently, with 2θ) due to the fact that the interaction potential is not a delta function, but is spread in the space, and therefore its Fourier transform is not a constant in Q-space but decays at high Q. Moreover, the magnetic scattering is proportional to the ordered magnetic moment, and thus temperature-dependent (going to zero at temperatures higher than the magnetic ordering temperature)

In the general case, there may be nuclear and magnetic diffraction. If the incident neutron beam is not polarized, the nuclear and magnetic intensities simply add up. Nevertheless if we consider the possible polarization of the incident and scattered beams, there are interference terms between the nuclear and magnetic structure factors.

2.3.7. Polarized neutron diffraction

As seen in the previous section, the magnetic structure factors are the Fourier transform of the magnetization density. Then, the magnetization density distribution can be determined from the precise measurement of the magnetic structure factors. Polarized neutron diffraction [7] by the classical polarized beam technique is an experimental method that allows measuring magnetic structure factors in a precise way.

For unpolarized neutrons, when both magnetic and nuclear scattering are present, the diffracted intensity is simply the sum of the squared nuclear and magnetic structure factors:

$$I = |F_N|^2 + |\boldsymbol{F_{M\perp}}|^2 = |F_N|^2(1 + \gamma^2) \tag{2.39}$$

where γ is the ratio between the magnetic and nuclear structure factors. The fact that neutrons have spin can be used to polarize a neutron beam. In a polarized neutron diffraction experiment using the classical polarized beam technique, the incident neutron beam is polarized along the vertical axis, Z, and no polarization analysis is performed for the scattered neutrons. A vertical magnetic field is applied to the sample in order to have a net component of the magnetization in the vertical direction. Then, the diffracted intensity can be written, for the simplest cases (see below):

$$I^{\pm} = |F_N \pm F_{M\perp}|^2 = |F_N|^2(1 \pm 2\gamma + \gamma^2) \tag{2.40}$$

where the superscript indicates that the incident neutron beam is polarized parallel (+) or antiparallel (-) to the vertical axis. Since in eq. 2.40 γ appears as a first order term, in polarized neutron diffraction the sensitivity in the measurement of magnetic structure factors is improved thanks to the interference term between the nuclear and magnetic structure factors, compared with unpolarized neutrons diffraction, where γ appears as a second order term. Eq. 2.40 is only

valid when the magnetic structure is non chiral, the nuclear and magnetic diffraction peaks are superposed and the magnetization is parallel to the vertical direction. This condition is fulfilled by ferromagnetic materials (as the ones studied in this work), but also by ferromagnetic, antiferromagnetic and paramagnetic materials with a ferromagnetic component induced by an applied magnetic field.

In the experimental setup of a polarized neutron diffraction experiment using the classical polarized beam technique, the neutron beam is at the same time monochromated and polarized by a polarizing monochromator, which is a single crystal with a Bragg reflection for which $F_N = \pm F_{M_z}$, where F_{M_z} is the component of the magnetic structure factor in z direction. In this way, the interference between the nuclear and the magnetic terms of the scattering amplitude is constructive for one polarization state and destructive for the opposite. Once the neutrons are polarized, magnetic guide fields are used to maintain the polarization of the neutron beam, which can be reversed with a cryoflipper. A high magnetic field is applied to the sample in the vertical direction order to obtain a vertical magnetization component. This configuration introduces the limitation that only reflections close to the horizontal plane can be measured. The temperature of the sample can also be varied to choose the appropriate experimental conditions.

In this technique, the ratio, *R*, between the intensities detected for incoming beam polarized parallel or antiparallel to the vertical axis is measured instead of the integrated intensity; this method is called *flipping-ratio method.* This technique presents several advantages. Apart from the aforementioned increase in the sensitivity to the magnetic signal, several corrections in the intensity, like the absorption, are canceled out in the flipping-ratio expression. Finally, it is not necessary to measure all the diffracted intensity of a reflection, but only to compare the intensities for both neutron-spin polarizations for the same crystal position, avoiding the problems related to the integration of Bragg peaks and simplifying the measurements.

In the general case (for non chiral magnetic structures), the expression of the flipping ratio is:

$$R = \frac{I^+}{I^-} = \frac{|F_N|^2 + (F_N F_{M\perp z}^* + F_N^* F_{M\perp z}) + |\boldsymbol{F_{M\perp}}|^2}{|F_N|^2 - (F_N F_{M\perp z}^* + F_N^* F_{M\perp z}) + |\boldsymbol{F_{M\perp}}|^2} \tag{2.41}$$

This expression is much simplified if the magnetization is perfectly parallel to the vertical axis and if the structure is centrosymmetric (both nuclear and magnetic structure factors are real), as is the case for the alloys studied in this thesis. Considering the angle α between the scattering vector and the vertical axis, the flipping-ratio is written as

$$R = \frac{I^+}{I^-} = \frac{|F_N|^2 + 2sin^2\alpha F_N F_M + sin^2\alpha |F_M|^2}{|F_N|^2 + 2sin^2\alpha F_N F_M + sin^2\alpha |F_M|^2} \tag{2.42}$$

where both F_N and F_M are now scalar and real quantities. Therefore, if the nuclear structure factors are known from a different unpolarized neutron diffraction experiment at the same temperature, the magnetic structure factors can be extracted from the measured flipping ratios and their Fourier inversion gives directly the spin density distribution. Another important advantage of the flipping ratio method can be remarked at this point: the previous equation, valid for centrosymmetric structures, gives not only the amplitude of the magnetic structure

factor, but also its phase, which is usually lost in a diffraction experiment because what is actually measured is an intensity, i.e., the square of a structure factor.

The Fourier transform for the determination of the magnetization density distribution from the magnetic structure factors is a direct method that does not require the use of any model, but has important limitations. Since the Fourier inversion is only exact if all the reflections are measured (to infinity in *Q*), truncation effects appear in real experiments. Moreover, the Fourier inversion does not take into account the different experimental uncertainties of the measured magnetic structure factors, and all of them are given the same weight in the computation of the magnetization density. The maximum entropy method [8] is also a direct method (no model required) that circumvents the limitations of the Fourier inversion. It is a statistical method based in finding the most probable magnetization density map that can have generated the experimental magnetic structure factors, by applying the maximum entropy principle. The least informative map is chosen among the maps that are in agreement with the data. The maximum entropy method, as implemented in Dysnomia program [9] linked to the Fullprof Suite [4], was used to obtain spin density maps from the polarized neutron diffraction data presented in this thesis.

2.3.8. Examples of neutron diffraction instruments: D9 single-crystal diffractometer and D1B powder diffractometer

During this thesis, neutron diffraction data have been collected in a number of diffractometers of the instrument suite of the ILL, specifically D1B, D20 and D2B powder diffractometers, D9 single-crystal diffractometer and D3 polarized-neutron diffractometer. We will describe two of them as representative examples.

The single-crystal (unpolarized) neutron diffraction experiments carried out during this thesis were performed in D9 diffractometer. The purpose of the experiments was the detailed analysis of the structure and atomic order of the studied alloy and providing structural input for analyzing polarized neutron diffraction data collected in D3 instrument (see Chapter 5).

D9 is fed by high-energy neutrons from the ILL's reactor hot source, allowing working in a wavelength range between 0.35 and 0.86 Å. The appropriate wavelength for the experiment is selected by changing the takeoff angle of a Cu (220) monochromator. A set of filters is used to remove contamination from high-order harmonics. After the collimator, neutrons arrive to the sample, which is located in an Eulerian cradle where it can be set in the required orientation for diffraction to occur by rotation of the three angles of the cradle (namely ω, χ and ϕ), allowing large access to the reciprocal space. The two-dimensional position-sensitive detector, located 40 cm away for the sample and covering 64 x 64 mm^2 is rotated in the 2θ axis to collect the diffracted intensity. The sample is rotated around the vertical axis (ω) while the detector records the intensity of the diffracted beam of the selected Bragg reflection. The intensities of a large number of reflections are collected in this way in order to determine the crystal and/or magnetic structures of the studied samples.

The available sample environments cover a temperature range from 2 K, using different cryostats, to 1133 K, using a Peltier gas flow furnace, or even to 1273 K, using a closed shell furnace. Other sample environments allow applying high magnetic fields up to 6 Tesla or working at high pressures up to 10 GPa.

D1B instrument is a representative example of neutron powder diffractometer. This type of instrument is known as two axes diffractometer, because there are two points in the instrument where the direction of the neutrons is deflected: the monochromator and the sample. The neutrons travel through a neutron guide until the monochromator, which selects the wavelength of the neutrons that will reach the sample. In particular, this instrument works at a fixed takeoff angle with two possible monochromators: i) a set of crystals of pyrolytic graphite (002) that produces a wavelength of 2.52 Å with a neutron flux around $7.9x10^6$ neutrons·cm^{-2}·s^{-1} and ii) a germanium crystal (311) that produces a wavelength of 1.28 Å with a neutron flux around $0.4x10^6$ neutrons·cm^{-2}·s^{-1}. The neutrons diffracted by the sample reach the ^{3}He multidetector containing 1280 cells covering an angular range in 2θ of 128º. Different sample environments can be used in this instrument for high and low temperatures, high magnetic fields, high pressures, etc.

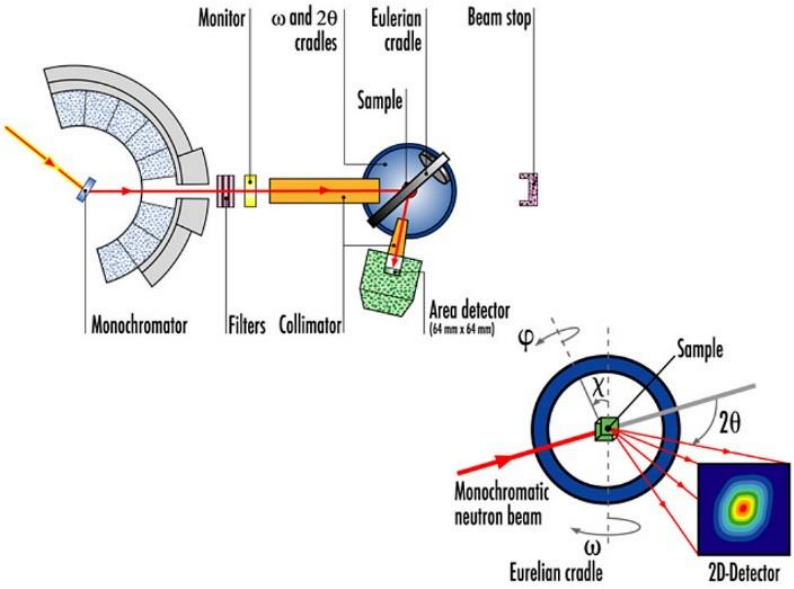

Figure 2. 14. Scheme of D9 single crystal neutron diffractometer at ILL.

During this thesis, this instrument was used with different environments, depending on the goal of the experiment. Most commonly, the environment used was a cryofurnace, which works from 1.5K to 500K, to study the nuclear and magnetic structures of the austenite and martensite phases of the alloys. A furnace allowing working from room temperature to 1200K was used in other experiments, like the ones aiming at analyzing the recrystallization processes in amorphous samples. All the experiments were performed at λ=1.28 Å because this wavelength allows recording a higher number of diffraction peaks in the angular range of the detector. In the following figure, a scheme of D1B diffractometer is shown.

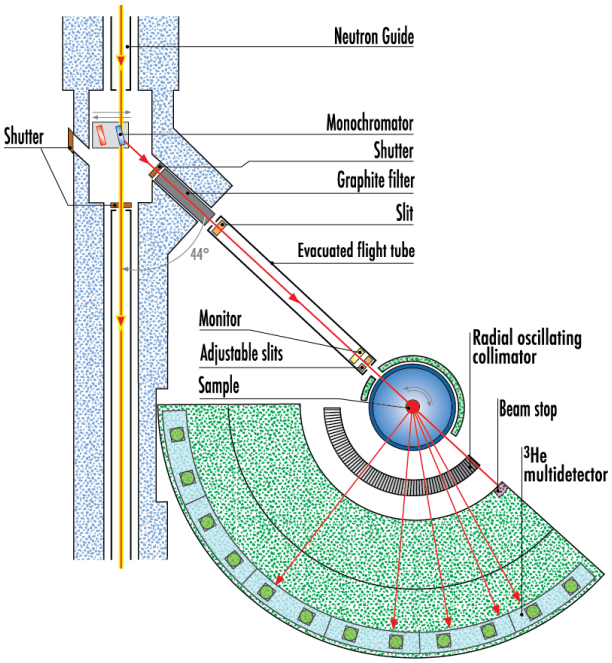

Figure 2. 15. Scheme of the powder diffractometer D1B at ILL.

Bibliography

[1] Vicente Recarte, “Estudio de los parámetros microstructurales que controlan la transformación martensítica en las aleaciones de Cu-Al-Ni con memoria de forma.,” Universidad del País Vasco UPV/EHU, 1997.

[2] V. K. Pecharsky, K. A. Gschneidner, A. O. Pecharsky, and A. M. Tishin, “Thermodynamics of the magnetocaloric effect,” *Phys. Rev. B*, vol. 64, no. 14, p. 144406, Sep. 2001.

[3] X. Moya, S. Kar-Narayan, and N. D. Mathur, “Caloric materials near ferroic phase transitions,” *Nat. Mater.*, vol. 13, no. 5, pp. 439–450, May 2014.

[4] J. Rodríguez-Carvajal, “Recent advances in magnetic structure determination by neutron powder diffraction,” *Phys. B Condens. Matter*, vol. 192, no. 1, pp. 55–69, Oct. 1993.

[5] L. A. Aslanov, G. V. Fetisov, and J. A. K. Howard, *Crystallographic Instrumentation*. International Union of Crystallography, 1998.

[6] G. L. Squires, *Introduction to the Theory of Thermal Neutron Scattering*. Mineola, N.Y: Dover Publications, 1997.

[7] E. Ressouche, “Polarized neutron diffraction,” *Éc. Thématique Société Fr. Neutron.*, vol. 13, p. 2002, 2014.

[8] R. J. Papoular and B. Gillon, “Maximum Entropy Reconstruction of Spin Density Maps in Crystals from Polarized Neutron Diffraction Data,” *EPL Europhys. Lett.*, vol. 13, no. 5, p. 429, 1990.

[9] K. Momma, T. Ikeda, A. A. Belik, and F. Izumi, “Dysnomia, a computer program for maximum-entropy method (MEM) analysis and its performance in the MEM-based pattern fitting,” *Powder Diffr.*, vol. 28, no. 3, pp. 184–193, Sep. 2013.

Chapter 3. Relation between microstructure, atomic order and magneto-structural properties in Ni-Mn-Sn system

3.1. INTRODUCTION

As explained in the general introduction, the Ni-Mn-Sn (and Ni-Mn-Sb) systems present a very high stability of the $L2_1$ structure. Therefore, standard thermal treatments (annealing and quenching) are unable to modify the atomic order [1], contrarily to what happens in Ni-Mn-In and its quaternary systems, where the long-range atomic order can be modified by those conventional thermal treatments and large shifts of the MT temperature can be achieved [2–4]. In Ni-Mn-Sn alloys, then, it appears that the only way to tune the functional properties is the modification of the microstructure, which can be controlled using thermo-mechanical treatments such as milling and post-milling annealing. Here, we undertake a systematic study of the different microstructural states caused by such thermo-mechanical treatments in the $Ni_{50}Mn_{35}Sn_{15}$ system, aiming at quantitatively correlate them with the magnetostructural properties of the alloy.

In order to create different microstructural states in a controlled way, a $Ni_{50}Mn_{35}Sn_{15}$ alloy has been mechanically milled and then annealed at different temperatures. The analysis of the microstructural parameters (crystallite size and internal stresses) was performed by means of X-rays diffraction at room temperature, while neutron diffraction has been used to establish the atomic order and the magnetic coupling between Mn atoms, determining the reason of the observed variations in the magnetization. Further insight into the magnetism of the alloys and the local environment of the Sn atoms has been obtained by ^{119}Sn-Mössbauer spectroscopy. The evolution of the microstructural parameters has been quantified and correlated to the evolution of the MT features and the magnetic properties, characterized by means of DSC and magnetometry measurements, in order to explain the observation that the relaxation processes brought by annealing leads to recovery of the MT and the enhancement of the magnetism at both macroscopic and local levels.

3.2. EXPERIMENTAL RESULTS AND DISCUSSION

The $Ni_{50}Mn_{35}Sn_{15}$ alloy was synthetized in an arc furnace using pure elements as described in Chapter 2. Once the ingot melted several times, it was homogenized at 1173K during 24 hours and quenched in iced water. The alloy was hand milled in agate mortar until obtaining a powder with homogenous particle size. The powder was divided into five samples: the first one was kept in the as-milled state (sample named AM273), while the rest were annealed at 573K (sample AN573), 673K (AN673), 773K (AN773) and 873K (AN873) for 5 minutes in order to further modify the microstructural properties. The study of the magneto-structural transformations was carried out by DSC in heating/cooling ramps at 10K/min. The thermal treatments were also performed "in situ" in the calorimeter. The magnetic behavior was analyzed by SQUID magnetometry by means of thermomagnetization measurements at 100Oe and 60kOe applied magnetic field and magnetization *versus* magnetic field measurements at constant temperatures. For the study of the microstructural parameters, X-ray diffraction patterns were collected at room temperature using Cu Kα radiation and analyzed using the FullProf package programs [5]. For the determination of the atomic order and the magnetic structure, powder neutron diffraction was performed in D2B instrument at ILL with a wavelength of 1.59Å. ^{119}Sn-Mössbauer spectra were obtained in collaboration with I. Unzueta, J. A. Garcia, F. Plazaola and J. S. Garitaonandia of the University of the Basque Country, using a $Ba^{119}SnO_3$ source in a transmission setup at 270K and fitted using NORMOS program.

3.2.1. Calorimetric measurements

The first step in this study is the characterization of the martensitic transformation and the determination of the magnetic ordering temperature by calorimetric measurements, which allow observing the presence of the exothermic and endothermic peaks corresponding to the direct and reverse martensitic transformation, respectively, and also the presence of the λ-type shoulder that indicates the Curie temperature of the austenite. As explained in Chapter 2, the values of the Curie temperature and the initial and final temperatures for forward and reverse transformation were obtained using the tangent method. The values of the enthalpy and entropy associated to the MT are also determined. The enthalpy, ΔH, is estimated from the average area, between cooling and heating, below the peaks, while the entropy change at the MT is $\Delta S = \Delta H / T_P$, with T_P the peak temperature. The calorimetric curves obtained for all the samples are shown in. The values of the structural and magnetic transformation temperatures and the enthalpy and entropy associated to the MT for all the studied samples are summarized in Table 3. I.

Table 3. I. Temperature of the DSC peak for the forward MT, M_P, for the reverse MT, A_P, enthalpy, ΔH, and entropy change, ΔS, and Curie temperature T_C for the set of samples.

Sample	$M_P(K)$	$A_P(K)$	$\Delta H(J/g)$	$\Delta S(J/kgK)$	$T_C(K)$
AM273	208 (1)	228 (1)	1.8 (4)	8 (2)	317 (1)
AN573	209 (1)	228 (1)	4.2 (3)	19 (1)	322 (1)
AN673	208 (1)	226 (1)	4.3 (3)	20 (1)	321 (1)
AN773	209 (1)	227 (1)	4.7 (3)	22 (1)	322 (1)
AN873	208 (1)	227 (1)	4.8 (4)	22 (2)	322 (1)

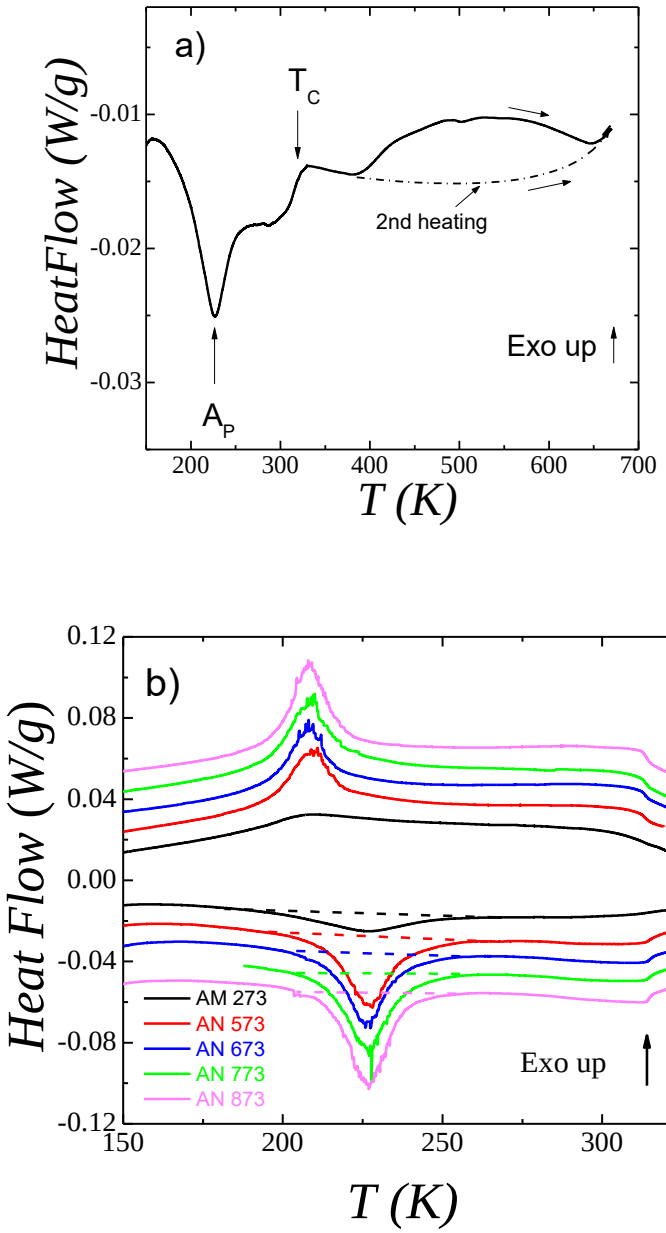

Figure 3. 1. a) DSC thermogram on heating the as-milled sample, AM273, up to 673 K. b) DSC thermograms around the martensitic transformation and the magnetic transition of the alloys studied in this chapter.

As can be seen in Figure 3. 1(a), a broad exothermic peak appears between 400 K and 600 K when the as-milled sample is heated for the first time, which is not observed on heating in a subsequent cycle. This feature must be linked to the microstructural recovery processes. In order to analyze the effect of such processes on both the MT and T_C, the annealing temperatures have been chosen inside and above the temperature range of this exothermic peak. As can be appreciated in Figure 3. 1(b) and Table 3. I, the values of the MT temperature and T_C do not change noticeably, remaining constant for all the studied samples. The biggest change is shown in the values of the enthalpy and entropy associated to the MT. In the as-milled sample, the MT

is hardly noticeable but present. As the annealing temperature increases, the peaks associated to the structural change become narrower and their associated enthalpy and entropy values become bigger, indicating an increase of the percentage of the alloy that undergoes the martensitic transformation (recovery of the MT) due to the effect of the thermal relaxation of the internal strains and defects. The enthalpy and entropy increase remarkably (more than doubling their values) after annealing at 573K (Figure 3. 2). Further increase of the annealing temperature produces only slight variations in ΔH and ΔS, indicating that the recovery of the MT is mainly produced after the treatment at the lowest temperature.

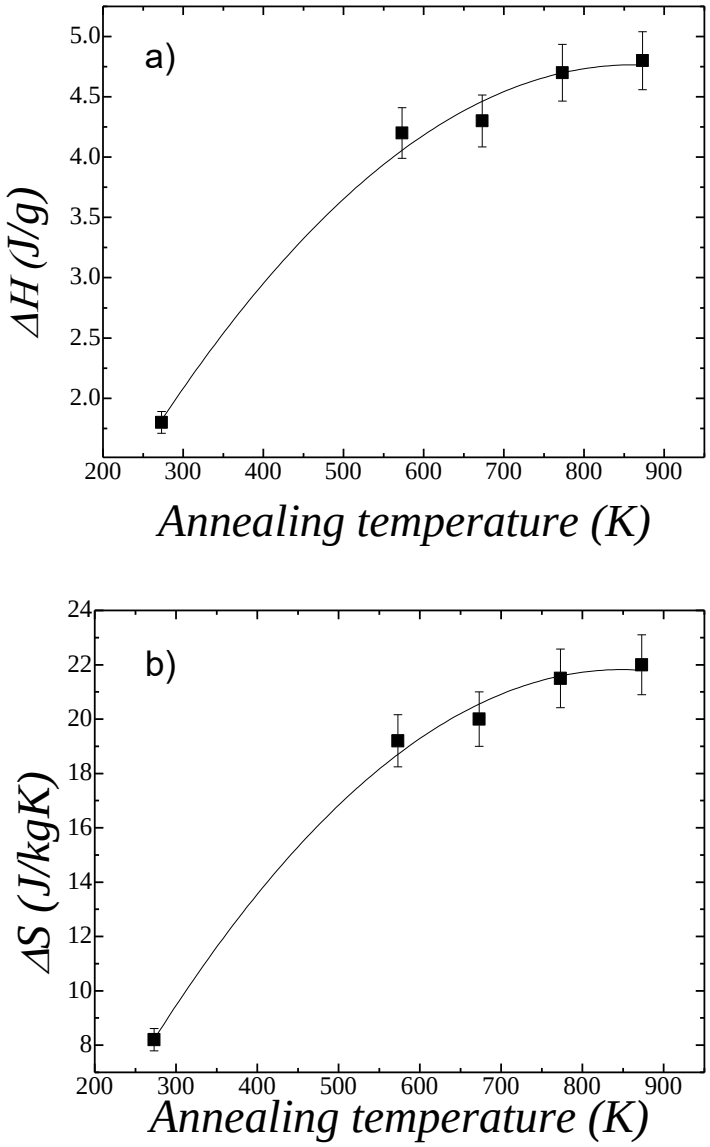

Figure 3. 2. Evolution of ΔH a) and ΔS b) at the MT with the annealing temperature for the set of samples.

As mentioned before, the MT peak temperatures remain practically unchanged for the different annealing treatments, and so does the associated hysteresis, defined as the temperature difference between heating and cooling transformation peaks (upper panel in Figure 3. 3). On the other hand, since these peaks become narrower as the annealing temperature increases, the temperature range in which the martensitic transformation takes place, ΔT, is reduced gradually (lower panel in Figure 3. 3). ΔT is determined as the average value of the difference between the MT starting and finishing temperatures: M_S-M_F for the forward transformation and A_F-A_S for the reverse transformation (taken as the temperatures corresponding to the 2% and 98% of the normalized integrated area below the peaks). Therefore, although the temperatures of the MT and the T_C remain constant, as corresponds to the expected lack of variation of the atomic order [1], the fact that ΔT decreases and ΔS increases indicates that the thermal induction of the transformation is strongly affected by the evolution of the microstructural parameters during the annealing.

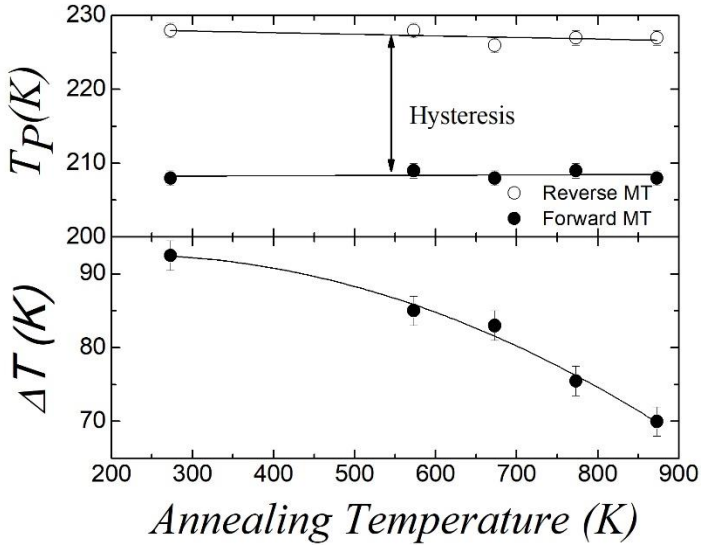

Figure 3. 3. Temperature of the forward and reverse martensitic transformation (upper panel) and variation of the temperature range of the transformation (lower panel) as a function of annealing temperature.

3.2.2. X-ray diffraction

In order to obtain quantitative values for the microstructural parameters, as grain size and internal stress, and correlate them with the thermo-mechanical treatments of the samples, X-ray diffraction measurements at room temperature were performed. Figure 3. 4 shows the diffractograms of the studied samples and the corresponding Lebail fits. All the diffractograms present the characteristic (220), (400) and (422) peaks that correspond to the well-known Heusler $L2_1$ cubic structure with space group $Fm\bar{3}m$ [1]. The position of the peaks remains almost unchanged with the different annealing treatments, indicating that the cell parameters remain nearly constant. The effect of the annealing treatment is instead appreciated in the width of the peaks that become narrower as the temperature of the treatment increases, which is an indication of a variation in the microstructural parameters. The values of crystallite size and

internal strains obtained from the analysis of the diffractograms are shown in Figure 3. 5 and Table 3. II. In the as-milled sample the obtained values of grain size and strain are 88.98 (2)Å and 9.33 (3) ‰, respectively. As the annealing temperature is increased, the values of the strains decrease down to 1.09 (4) ‰ in the case of the alloy annealed at 873K, which is accompanied by an increase on the grain size, reaching values of 222.08 (6)Å.

Table 3. II. Values of the grain size, internal strains and cell parameters obtained by Lebail fit refinement for the set of the samples.

Sample	Size (Å)	Strains (‰)	Cell Parameter (Å)
AM273	88.98 (2)	9.33 (3)	5.985 (3)
AN573	104.58 (3)	4.93 (2)	6.001 (2)
AN673	145.22 (4)	4.74 (2)	5.999 (2)
AN773	172.23 (9)	3.33 (6)	5.989 (1)
AN873	222.08 (6)	1.09 (4)	5.999 (1)

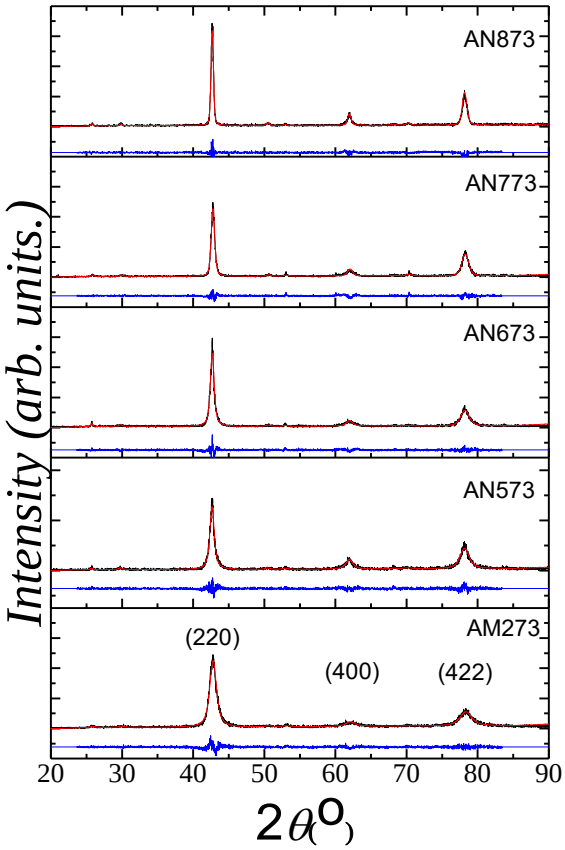

Figure 3. 4. X-ray diffractograms at room temperatures for the set of samples. The red, black and blue lines represent, respectively, the observed and calculated pattern, and the difference between both.

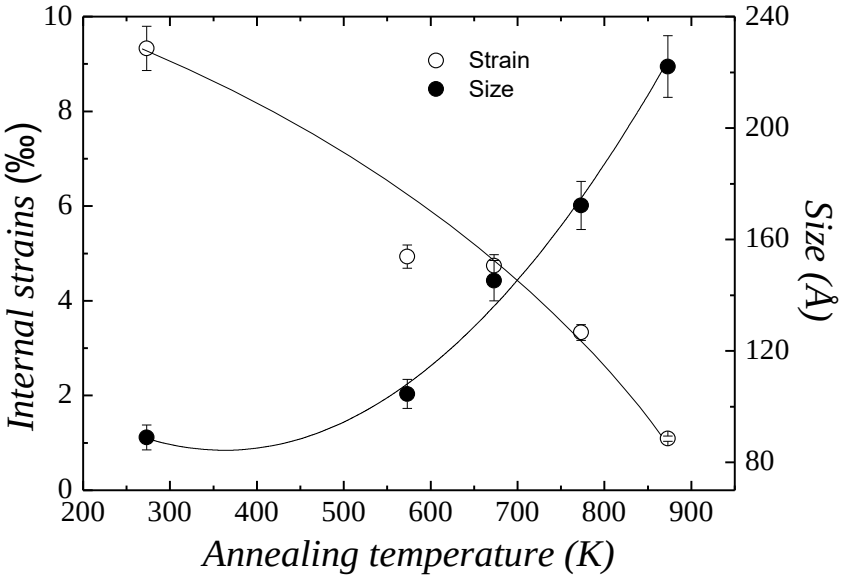

Figure 3. 5. Crystalline size and strains as a function of the annealing temperatures.

An estimation of the grain size distribution can be made from the Gaussian and Lorentzian integral breadths obtained from the peak profile analysis and using equation (2.16) shown in Chapter 2 (in the present case, the size broadening has only Lorentzian contribution). The distribution for the different samples is represented in Figure 3. 6.

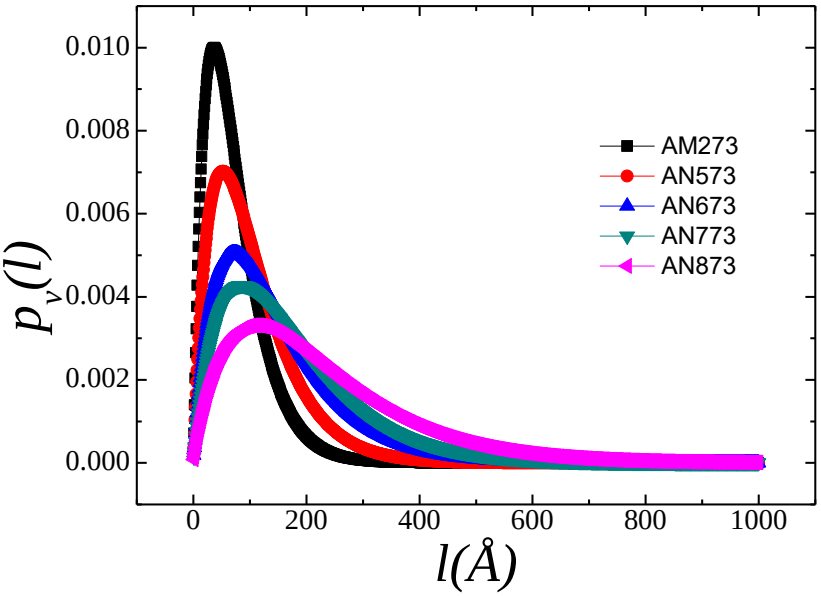

Figure 3. 6. Grain size distribution, $p_V(l)$, for the different samples.

Once the microstructural parameters are calculated, we can relate them with the MT features as a function of the thermal treatments. In Figure 3. 7 the relation between the variation in the temperature interval of the transformation, *ΔT,* and the internal strain is shown. It can be appreciated the linear relation between both parameters as a consequence of the elastic energy. In fact, due to the presence of elastic and frictional terms in the energy balance at the MT, the transformation takes place in a finite temperature range and showing hysteretic behavior [6], [7]. Thus, at $T<T_0$ a local equilibrium is achieved during the forward martensitic transformation when:

$$-\Delta G_{ch}^{a\to m} + E_{el}^{a\to m} + E_{fr}^{a\to m} = 0 \tag{3.1}$$

where $\Delta G_{ch}^{a\to m}$ is the difference in the free energy between austenite and martensite, and $E_{el}^{a\to m}$ and $E_{fr}^{a\to m}$ are the stored elastic energy and the dissipated frictional energy during the forward martensitic transformation, respectively. On a further cooling, the chemical term, $\Delta G_{ch}^{a\to m}$, acts as the driving force to overcome the elastic and frictional terms which impede the development of the transformation. As a result, the recovery of defects during the annealing reduces the non-chemical terms and hence the martensitic transformation becomes narrower.

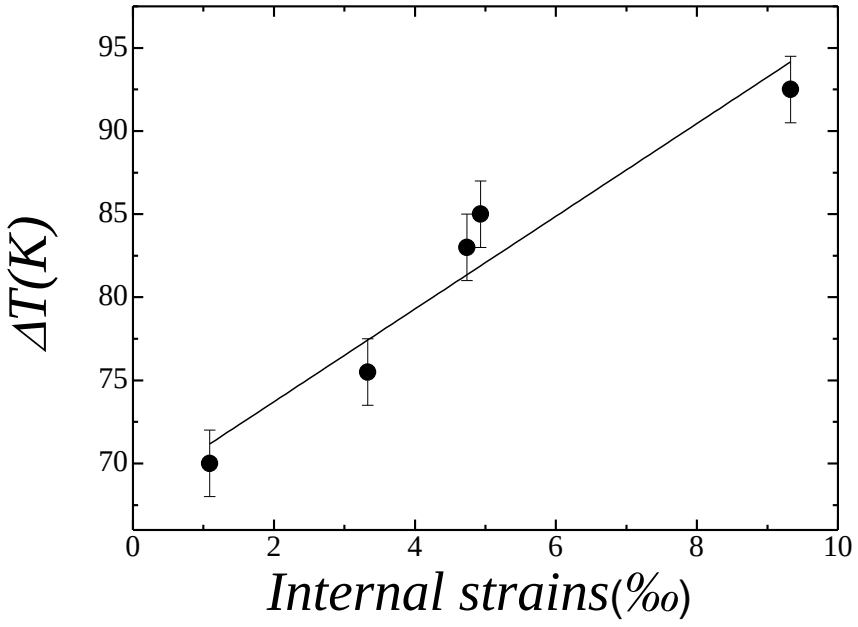

Figure 3. 7. Martensitic transformation temperature interval ΔT as a function of internal strains.

3.2.3. Magnetic measurements

Magnetic measurements have been carried out to establish the relation between the microstructural state and the magnetic behavior. Figure 3. 8a shows the thermo-magnetization curves at 100Oe applied magnetic field. As in the calorimetric results, the T_C in austenitic phase, indicated by a drastic jump of the magnetization, is observed in all the samples at the same temperature (ca. 320K). A drop in the magnetization at lower temperatures is indicative of the

martensitic transformation, which takes place from the ferromagnetic austenite phase to the martensite phase, characterized by a weaker magnetic character. This drop in the magnetization also appears in all the samples at the same temperatures, around 220K, in agreement with the calorimetric measurements, and confirming the null variation of the atomic order induced by thermal treatments. However, the annealing produces a remarkable increase of the magnetization in austenite and a bigger drop in the magnetization associated to the MT. The magnetization variation at the MT is better evaluated with measurements at high magnetic fields, since the measurements at low magnetic fields can suffer from spurious effects like those produced by demagnetization fields. Figure 3. 8.b shows the measurements of the temperature dependence of the magnetization at 60kOe. The temperature of the MT remains unchanged, which excludes the existence of magnetic arrest phenomena as the observed in other systems like Ni-Mn-In, Ni-Co-Mn-In or Ni-Co-Mn-Sn [8–10]. In those cases, the magnetic field stabilizes the phase with higher magnetization, decreasing the MT temperature. Concerning the effect of the annealing treatment in the present case, the variation in the magnetization at the MT increases with the temperature of the annealing, except for the case of the specimen treated at 873K where the variation in the magnetization is smaller in comparison with the alloys treated at lower temperatures, since the microstructural recovery induced by annealing produces a more pronounced increase of the magnetization in the martensite phase than in the austenite.

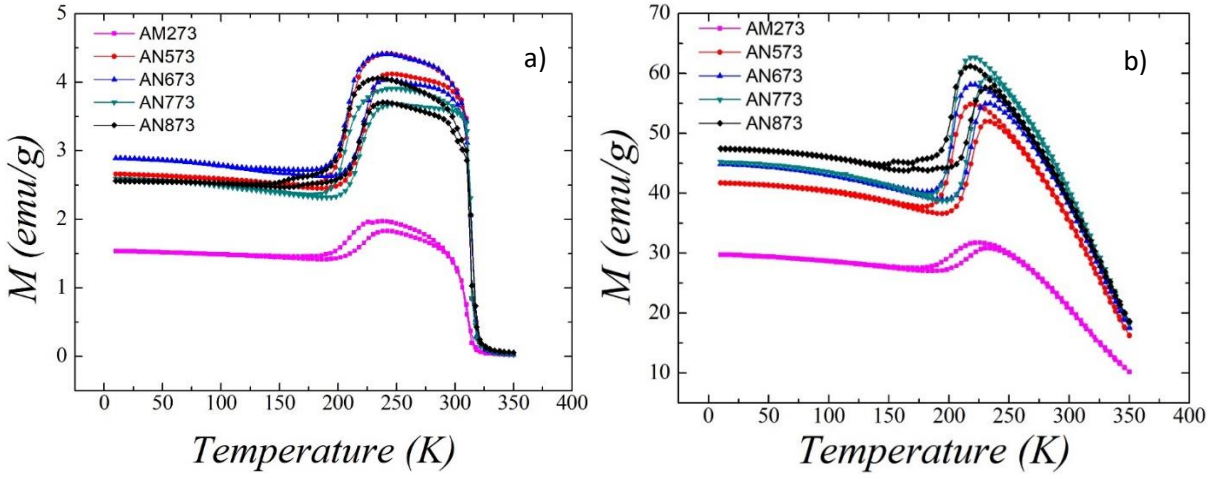

Figure 3. 8. Magnetization dependence with temperature of the set of samples at a) 100 Oe and b) 60kOe applied magnetic field.

In order to analyze the magnetocaloric effect associated to these compounds and evaluate the effect of the microstructural relaxation, two samples were selected to make a comparison: the as milled alloy (AM273) and the alloy treated at 673K (AN673). The magnetization of the samples is measured on heating under different applied fields (from 100Oe to 60kOe) after zero-field cooling, and the magnetic entropy change, $\Delta S_m(T,H)$ is evaluated using equation 1.11 (Chapter 1). In Figure 3. 9 are shown the different magnetization curves at different magnetic fields for the magnetocaloric effect evaluation.

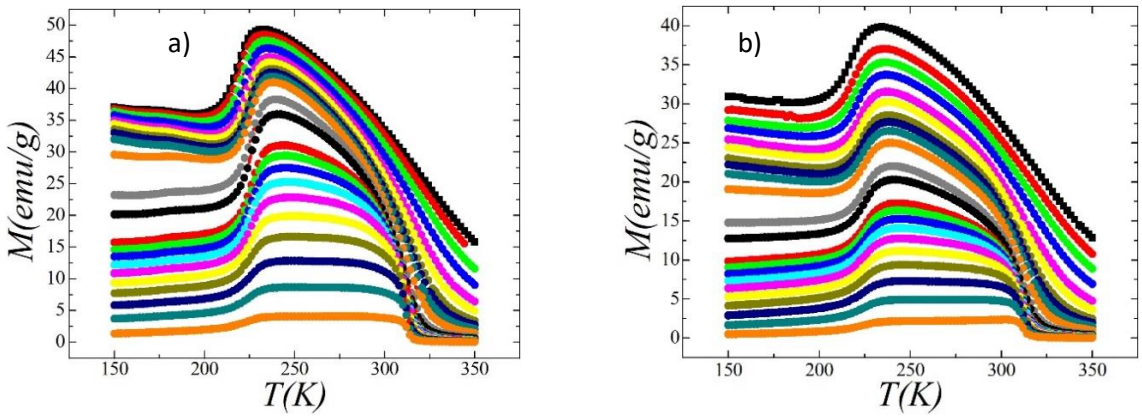

Figure 3. 9. Zero field cooled magnetization curves measured on heating under different applied magnetics fields ranging from 100Oe to 60kOe for a) the alloy treated at 673K (AN673) and b) the as-milled alloy (AM273).

Figure 3. 10 depicts the temperature dependence of the magnetically induced entropy change under an applied field of 60 kOe obtained after application of equation 1.11. The negative peaks observed (direct magnetocaloric effect) are associated to the magnetic transition at T_C, and the positive peaks (inverse magnetocaloric effect) that appear at lower temperatures are associated to the induction of the reverse martensitic transformation. In both cases, the microstructural recovery brought by annealing enhances the magnetocaloric effect, increasing the saturation magnetization and decreasing the martensitic transformation temperature range. As shown in Figure 3. 11, where the ΔS_m values for both transitions are plotted as a function of the maximum applied magnetic field, the increase in the entropic variation, and therefore the effect of microstructure, is more pronounced for the MT, a magnetostructural transition with a first order character, than for the magnetic ordering of the austenite, a second order transition.

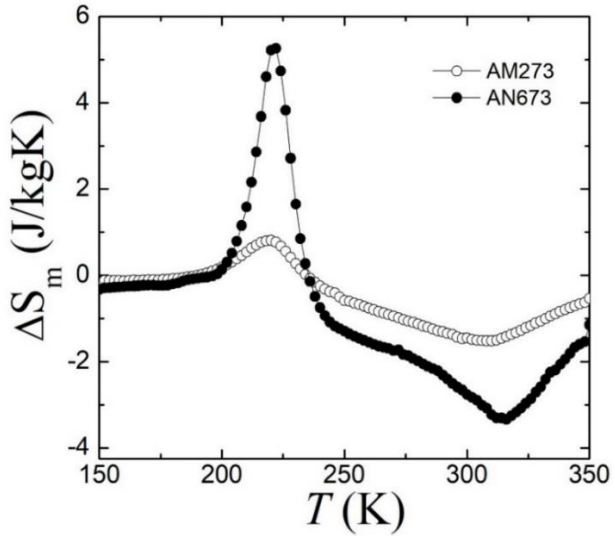

Figure 3. 10. Magnetically induced entropy change under an applied field of 60kOe, as a function of the temperature, for the AM273 and AN673 samples.

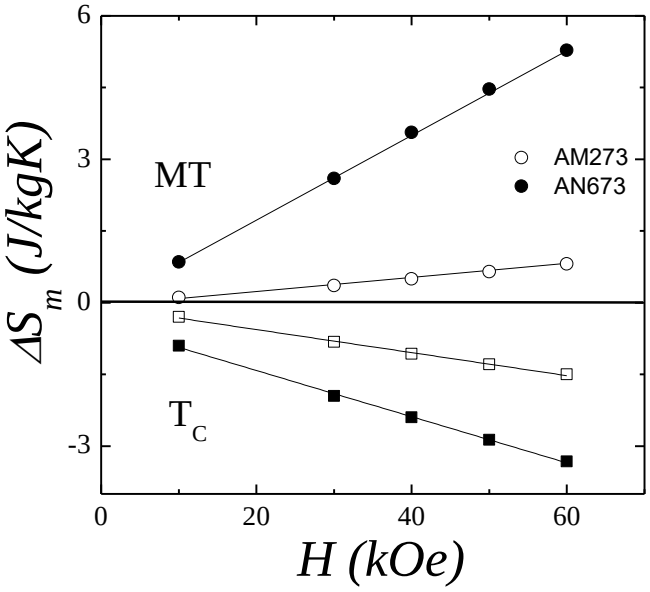

Figure 3. 11. Magnetically induced entropy change at the martensitic transformation and Curie temperature as a function of the applied magnetic field.

The significant change observed for the magnetocaloric effect manifests the outstanding influence of the microstructure on the functional properties of the alloy. This improvement of the magnetostructural parameters and the enhancement of the magnetocaloric effect by annealing treatments in ground samples is in agreement with the observed in other systems like $Ni_{40}Co_{10}Mn_{40}Sn_{10}$ [11]. The obtained results confirm that, once the transition temperature has been fixed by the composition, the modification of the microstructure through thermo-mechanical treatments appears as the best way to tune the functional properties of these alloys.

The magnetic properties of the martensite were measured at low temperatures in order to correlate them with the microstructural state. Figure 3. 12 shows the magnetization dependence with the applied magnetic field at a constant temperature of 10K for the whole set of samples. It is noticeable the increase of the saturation magnetization and the shape change of the curves with the increase of annealing temperatures. These variations can be attributed to the change in the magnetic coupling between Mn atoms caused by the changes in the microstructure, as will be discussed below.

The magnetization curves have been fitted using the law of approach to saturation expressed in the following equation [12]:

$$M = M_S\left(1 - \frac{a}{H} - \frac{b}{H^2}\right) + \chi H \tag{3.2}$$

where H is the applied magnetic field, M_S is the saturation magnetization, χ is the field independent susceptibility and a and b are coefficients related to magnetic and structural properties of the alloy [13]. In particular, the a parameter can be related with the stress field created by dislocations, vacancies and non-magnetic inclusions [14], that is, with the amount of magnetic defects that the specimen presents, and it can be approximated to:

$$a \approx 4\pi\rho M_S P_{eff} \tag{3.3}$$

where ρ is the density of the material and P_{eff} is the effective fraction of porosity and non-magnetic inclusions. The obtained values of P_{eff} and M_S are plotted in Figure 3. 13 as a function of the internal strains. The high value of effective non-magnetic inclusions corresponding to the as-milled alloy $P_{eff} = 0.2$ can be related, among other defects, with the high density of dislocations, where the local atomic disordering in their vicinity hinders the ferromagnetic coupling. The weakness of the magnetic coupling is also reflected in the low value of the saturation magnetization $M_S \approx 20\ emu/g$. The initial recovery of the microstructure, when the internal strains undergo a decrease of 50%, drastically reduces the density of defects (P_{eff} decreases by nearly a factor 10) and therefore increases M_S up to values close to 40 *emu/g*. The slight variations of P_{eff} and M_S during the subsequent reduction of internal strains indicate that the evolution of the macroscopic magnetic properties takes place mainly during the first stage of the microstructural recovery.

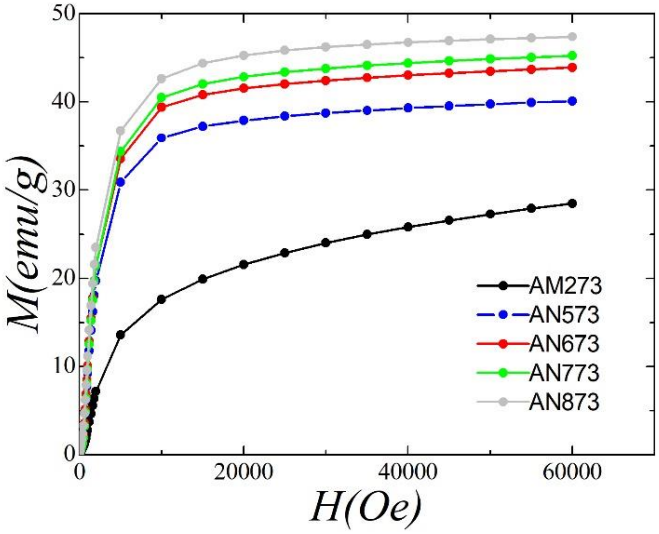

Figure 3. 12. Magnetic field dependence of magnetization at 10K.

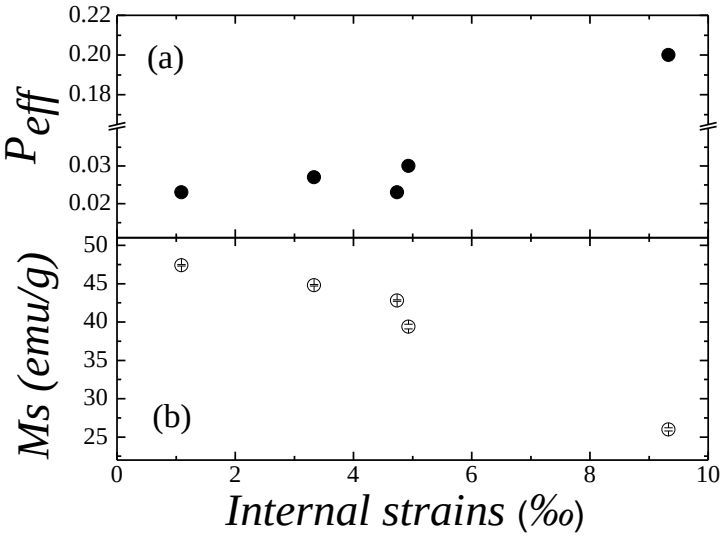

Figure 3. 13. a) Fraction of non-magnetic inclusions P_{eff} and b) saturation magnetization M_S as a function of internal strains.

3.2.4. Neutron diffraction: atomic order and magnetic structures

It has been proved by calorimetric and thermomagnetic measurements the high stability of the atomic order of the $Ni_{50}Mn_{35}Sn_{15}$ alloy, which is not modified by thermomechanical treatments, as manifested by the null variation of the equilibrium temperature between the austenitic and martensitic phases. Nevertheless, the temperature range of the martensitic transformation is considerably affected by the thermomechanical treatments, which also have a strong effect in the magnetic properties. In this section, the stability of the atomic order is verified at the atomic level and the magnetic structures are investigated by means of neutron diffraction, which is the appropriate probe for this type of analysis. With this aim, powder diffraction patterns in all the different structural and magnetic states were collected for the two representative samples AM273 and AN673.

Since the martensitic transformation is a diffusionless process and therefore the atomic order can be assumed the same in the austenite and martensite phases, the occupancies of the different crystallographic positions were determined in the austenitic phase in paramagnetic state (at 400 K) in order to simplify the analysis and avoid the magnetic contribution to the diffractogram. The diffraction patterns of both samples at 400 K correspond to a cubic $L2_1$ structure (space group $Fm\bar{3}m$). The data were first analyzed by a Lebail fit to obtain the cell parameters, the peak shapes and an estimation of the background. Both alloys present practically the same lattice parameter (a =6.004 (5) Å for the AM273 sample and a = 6.003 (11) Å for the AN673 sample). Subsequently, a Rietveld refinement was carried out, assuming as starting point the occupancies corresponding to an ordered system (i.e. the 4*a* sites fully occupied by Mn atoms, the 8*c* sites fully occupied by Ni atoms, and the 4*b* sites containing all the available Sn atoms and the Mn atoms exceeding the stoichiometric amount). Then, the different species were allowed in all crystallographic sites and the occupancies were refined, taking advantage of the negative scattering factor of Mn and using soft restraints according to the composition of the alloys to reduce the number of free parameters. When the refined occupancy for an atomic species in a particular site recurrently gave negative or negligible values, these were fixed to zero. This refinement was repeated until the convergence was reached, giving values of R_B of 4.06 % for the annealed sample and 2.42 % for the as-milled one. Figure 3. 14 andFigure 3. *15* show the experimental and calculated diffractograms obtained after the analysis for both samples. The results obtained are summarized in Table 3. III. Figure 3. 16 illustrates the crystallographic structure of the austenitic phase.

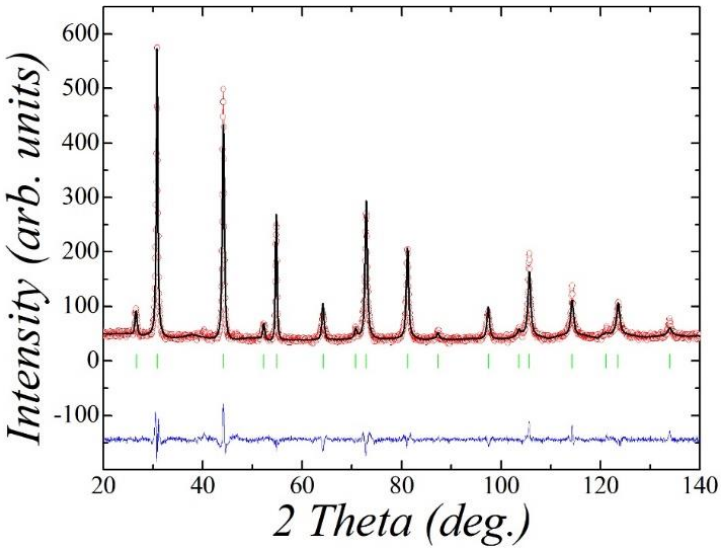

Figure 3. 14. Neutron diffraction patterns (wavelength 1.59Å) of the AN673 alloy at 400K, where the red dots are the observed pattern, the black line is the calculated one, the blue line is the difference between the observed and the calculated patterns and the green marks are the Bragg reflections.

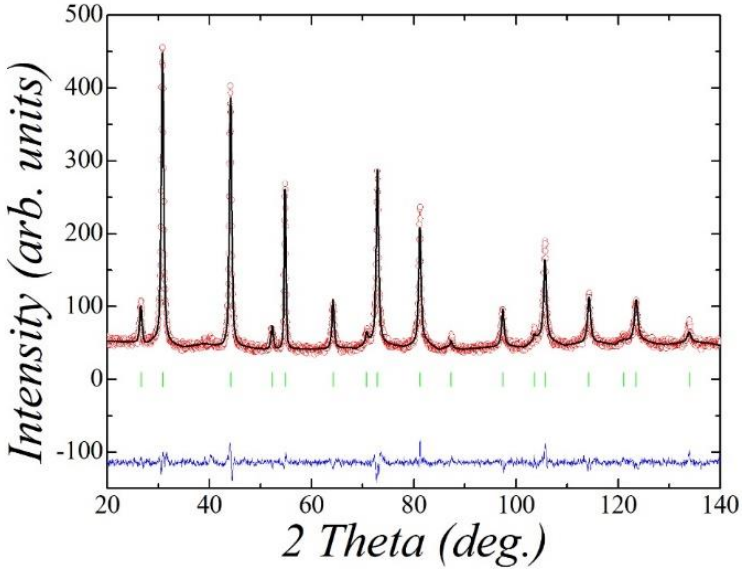

Figure 3. 15. Neutron diffraction patterns (wavelength 1.59Å) of the AM273 alloy at 400K, where the red dots are the observed pattern, the black line is the calculated one, the blue line is the difference between the observed and the calculated patterns and the green marks are the Bragg reflections.

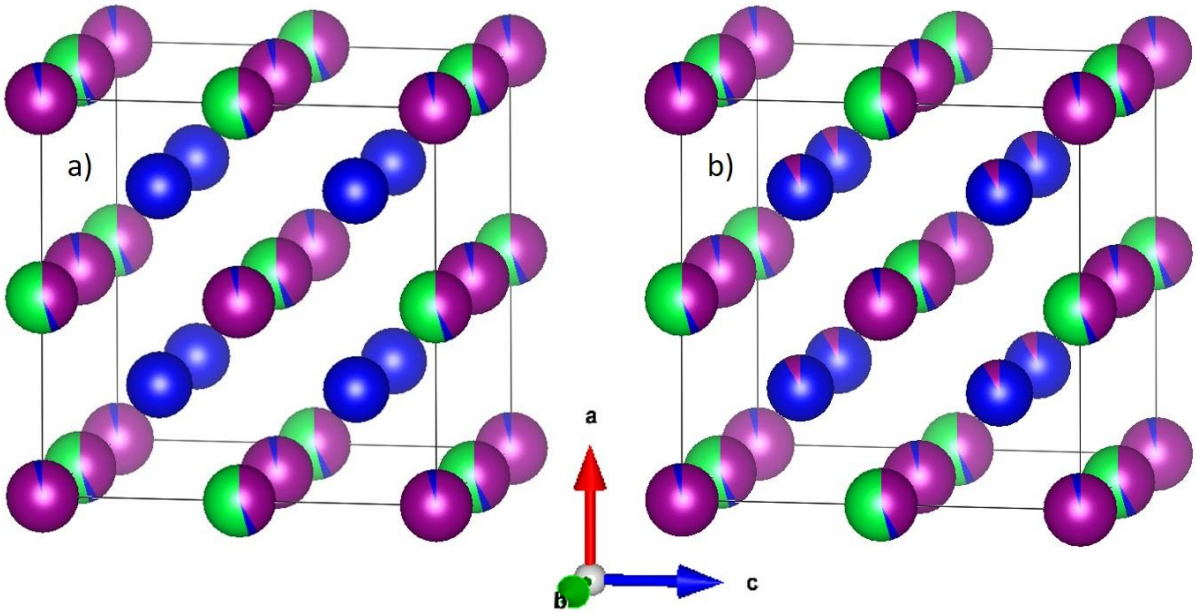

Figure 3. 16. Crystallographic representation of the structure of the austenitic phase where the purple color corresponds to Mn, green to Sn and blue to Ni in a) AN673 and b) AM273 alloys.

Table 3. III. Cell parameters and occupancies of 4a, 4b and 8c sites for the AM273 and AN673 alloys.

Site	**Atoms**	**Occupancy**	
		AN673	**AM273**
		a =6.004 (5) Å	a = 6.003 (11) Å
4*a*	Mn	0.94 (3)	0.95 (4)
(0,0,0)	Ni	0.06 (3)	0.05 (4)
4*b*	Mn	0.43 (3)	0.41 (4)
(1/2,1/2,1/2)	Ni	0.05 (3)	0.02 (4)
	Sn	0.523 (3)	0.57 (4)
8*c*	Ni	1.000 (0)	0.93 (5)
(1/4,1/4,1/4)	Mn		0.07 (5)

As shown in Table 3. III there is no change in the atomic order between the as-milled and the annealed alloy, in concordance with the results of the calorimetric and thermomagnetic measurements, where no variation is observed for the martensitic transformation and magnetic order temperatures in all the studied alloys.

Diffractograms in the ferromagnetic austenite phase were collected in order to give insight into the origin of the variation of the magnetization in the austenite produced by the different thermomechanical treatments. The magnetic contribution manifests in the diffraction patterns by an increase of the intensity of the peaks at lower angles (due to the decay of the magnetic form factor with Q). Figure 3. 17 shows the comparison of the diffractograms

corresponding to the paramagnetic and ferromagnetic states of the austenitic phase of the AM273 sample. In the present case, the magnetic contribution is manifested in the (111) peak, the intensity remaining nearly constant in the next peaks. The paucity of significant magnetic scattering compared to the total intensity implies that the absolute values of the magnetic moments obtained from the analysis may be taken with care, although conclusions may be drawn from the relative values and the tendencies observed.

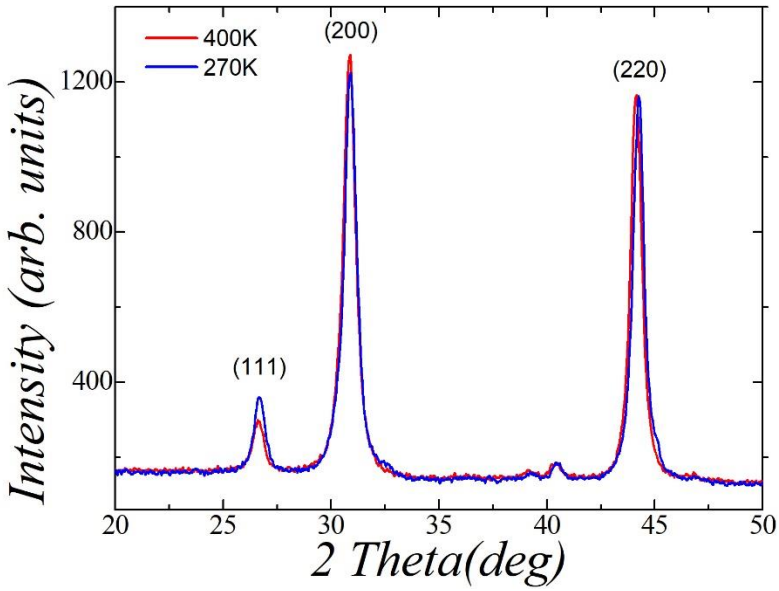

Figure 3. 17. Comparison of the paramagnetic and ferromagnetic states in austenitic phase for the AM273 alloy.

Figure 3. 18 and Figure 3. 19 show the experimental and calculated diffractograms obtained after the analysis for both samples. The obtained values for the magnetic parameters are summarized in Table 3. IV. In order to reduce the number of free parameters, the magnetic moments in the 8*c* site have been fixed to the values corresponding to Ni atoms carrying a moment of 0.2 μ_B, in accordance with theoretical calculations and with previous neutron diffraction studies [15].

Table 3. IV. Magnetic moments obtained by neutron diffraction in AM273 and AN673 at 270K.

Sample	Magnetic moment (μ_B)			
	4*a*	4*b*	8*c*	m_{total}
AM273	1.26 (6)	-0.45 (2)	0.2* (0)	1.21 (8)
AN673	2.58 (2)	0.37 (2)	0.2* (0)	3.35 (4)

*The value of site 8*c* was fixed at 0.2 μ_B corresponding to Ni atoms.

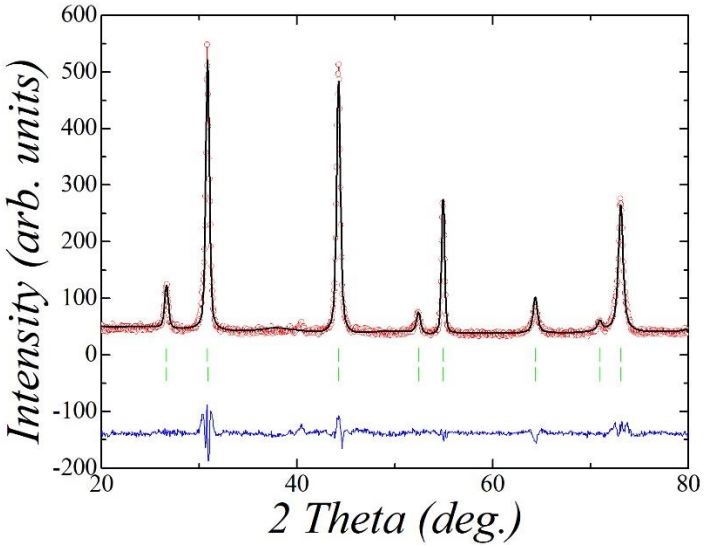

Figure 3. 18. Neutron diffraction patterns (wavelength 1.59Å) of the AN673 alloy at 270K, where the red dots are the observed pattern, the black line is the calculated one, the blue line is the difference between the observed and the calculated patterns and the green marks are the Bragg reflections.

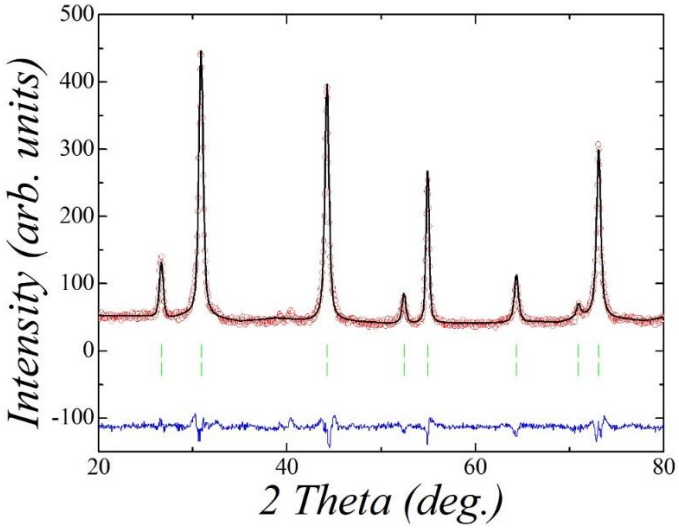

Figure 3. 19. Neutron diffraction patterns (wavelength 1.59Å) of the AM273 alloy at 270K, where the red dots are the observed pattern, the black line is the calculated one, the blue line is the difference between the observed and the calculated patterns and the green marks are the Bragg reflections.

As explained in chapter 1, the magnetic behavior in these alloys is mainly due to the Mn atoms, with the magnetic interactions being strongly dependent of the interatomic distances. For the atomically ordered stoichiometry alloys, the Mn atoms are located only in the 4*a* sites, at a distance $a/\sqrt{2}$ in the austenite cubic structure and presenting ferromagnetic coupling. When the composition is not stoichiometric or when atomic disorder is present, different studies propose that, since some Mn atoms locate in 4*b* sites (at shorter distance) these tend to couple antiferromagnetically with the rest [9, 10], although the final result is a net ferromagnetic

moment and a macroscopic ferromagnetic behavior, as observed in the magnetometry measurements.

Interestingly, in the present case, the magnetic coupling between Mn atoms in 4*a* and 4*b* positions drastically evolves from antiferromagnetic to ferromagnetic upon annealing (Table 3. IV and Figure 3. 20). This produces a change in the total magnetic moment from 1.21 (8) to 3.35 (4) μ_B that is in agreement with the observed drastic increase of the magnetization at high magnetic field in the austenite phase. The change in the magnetic coupling is produced despite the null variation in lattice parameter (a = 5.992 (8) Å for the AM273 sample and a = 5.989 (8) Å for the AN673 sample) and in atomic order. Since the amount of Mn atoms at 4*b* positions is practically the same for both alloys, the change in the magnetic structure must be due to the effect of the microstructural parameters. As discussed in the previous sections, the relaxation of the internal strains is accompanied by the reduction of the vacancies and non-magnetic inclusions and an increase of the grain size on the alloy. The combination of all these changes must be at the origin of the switch of the coupling between the Mn atoms located in 4*a* and 4*b* sites from antiferromagnetic to ferromagnetic, and the resulting increase in the magnetization.

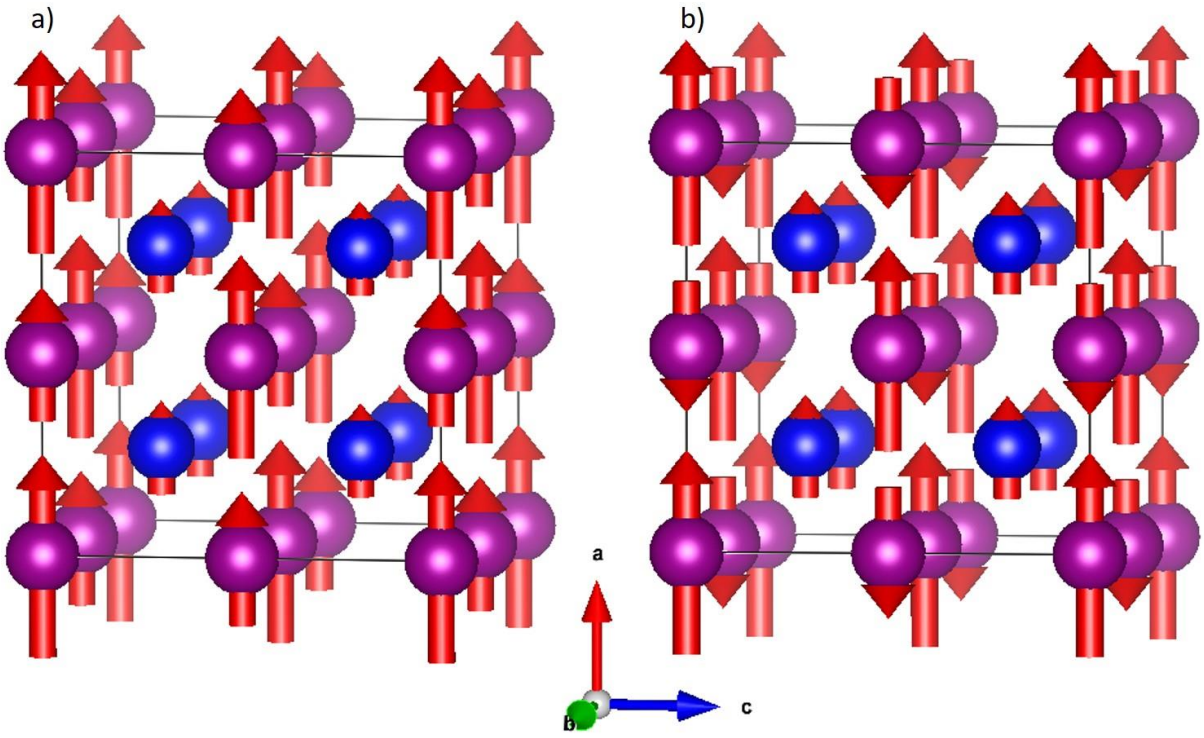

Figure 3. 20. Representation of the magnetic structure at 270K for a) AN673 and b) AM273 alloys.

Neutron diffraction patterns were also collected in martensite phase. In this case, it is not possible to analyze the nuclear and magnetic structures separately from different diffractograms, since the martensitic phase presents (weak) ferromagnetism in the whole temperature range. To avoid the presence of magnetic scattering, once the pattern indexed, only the $40^o < 2\theta < 140^o$ range of the diffraction pattern was used for the analysis of the nuclear part. The crystal structure of the martensite phase of the studied $Ni_{50}Mn_{35}Sn_{15}$ alloys corresponds to

the one determined by Brown et al. for the $Ni_{50}Mn_{36}Sn_{14}$ system,[17] that is, an orthorhombic structure with a two-fold modulation in the direction of the *a* axis, with space group *P m m a*. Figure 3. 21 shows an scheme of the crystallographic structure of the martensite phase, and its relation with the structure of the austenite. Both samples present the same global structure. The structural parameters obtained by the Rietveld refinements are summarized in Table 3. V. As mentioned before, assuming that the MT is a diffussionless process, the values used for the occupancies are those determined in the austenite phase (see Table 3. V). The values of the cell parameters remain nearly constant regardless of the themomechanical treatments, which means that also for the martensitic phase these affect mainly to the microstructural parameters. Nevertheless, slight variations in the atomic positions and therefore in the interatomic distances are observed between both samples, which can affect the magnetic coupling. In this case, the analysis of the magnetic structure becomes unreliable due to the number of free parameters, the cumbersome decoupling of nuclear and magnetic scattering, and the low magnetic signal. Different magnetic structure models have been tried [17], but no satisfactory results could be obtained. The only information that may be drawn is a tendency to refine lower magnetic moments than in austenite for both samples, being the lowest for the as-milled alloy, in agreement with the magnetization measurements. As an example, Figure 3. 22 shows the refinement of the data corresponding to the AN673 sample with the most simple model, that assumes magnetic moment only in the crystallographic positions completely filled by Mn (those deriving from the 4*a* site in austenite), with a refined value of 2.6(2) μ_B.

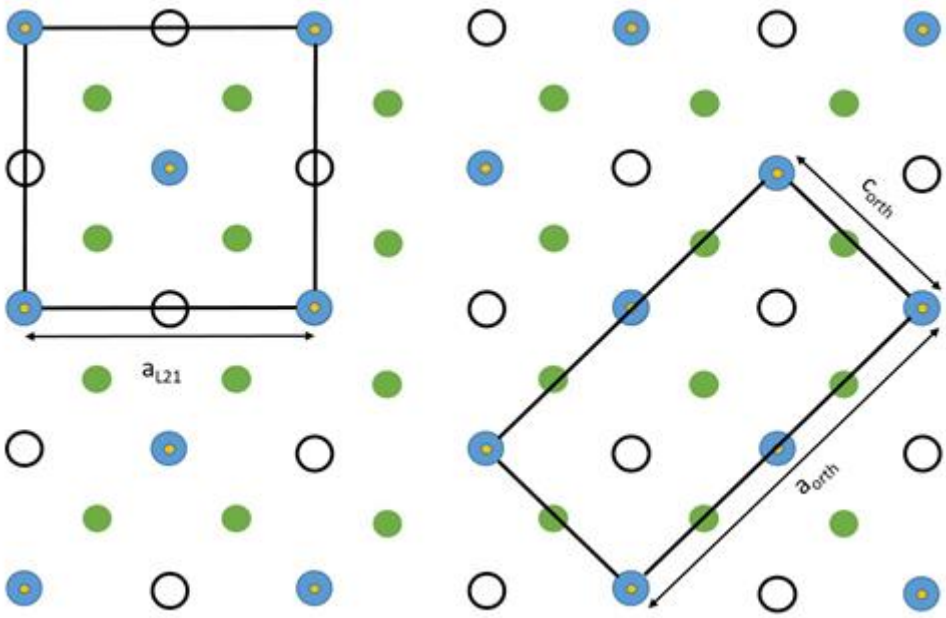

Figure 3. 21. Schematic representation of crystallograpic structure of martensite phase and its relation with the austenite $L2_1$ strucuture.

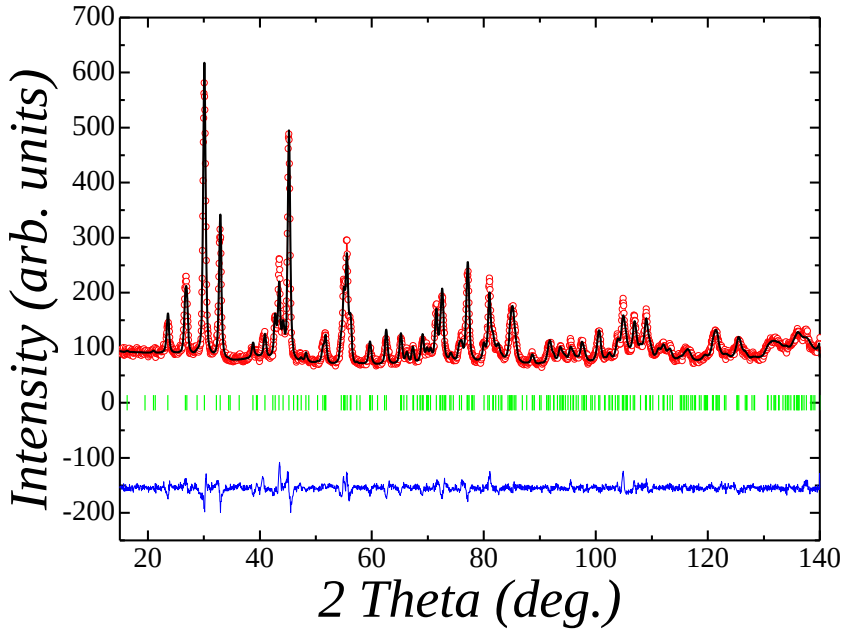

Figure 3. 22. Neutron diffraction patterns (wavelength 1.59Å) of the AN673 alloy at 50K, where the red dots are the observed pattern, the black line is the calculated one, the blue line is the difference between the observed and the calculated patterns and the green marks are the Bragg reflections.

Table 3. V. Obtained structural parameters at 50K in AN673 and AM273 alloys in martensite phase (space group P m m a).

Sites		AN673 *a*= 8.590 (21) *b*=5.612 (13) *c*=4.361 (13)			AM273 *a*=8.589 (26) *b*=5.614 (15) *c*=4.359 (15)		
	Occ	y	z	Occ	y	z
2*a*(0,0,0)	Mn 0.95 (3)			Mn 0.95 (4)		
2*f*(1/4,1/2,z)	Ni 0.06 (3)		0.559 (35)	Ni 0.05 (4)		0.564 (37)
2*b*(0,1/2,0)	Mn 0.43 (3)			Mn 0.41 (4)		
2*e*(1/4,0,z)	Ni 0.05 (3)		0.556 (51)	Ni 0.02 (4)		0.563 (53)
	Sn 0.52 (3)			Sn 0.57 (4)		
4*h*(0,y,1/2)	Ni 1.00 (0)	0.249 (10)	0.089 (40)	Ni 0.93 (5)	0.248 (12)	
4*k*(1/4,y,z)		0.240 (76)		Mn 0.07 (5)	0.240 (90)	0.090 (46)

** The values used for the occupancies are those determined in the austenite phase, with sites 2*a* and 2*f* in the martensite structure corresponding to sites 4*a* in austenite, sites 2*b* and 2*e* in martensite corresponding to sites 4*b* in austenite, and sites 4*h* and 4*k* in martensite corresponding to sites 8*c* in austenite.

3.2.5. Mössbauer spectroscopy

The magnetism of these alloys has been also analyzed at the atomic level using ^{119}Sn-Mössbauer spectroscopy. The experimental spectra obtained, together with the corresponding fits are shown in Figure 3. 23, and the results summarized in Table 3. VI. All the spectra have been satisfactorily fitted exclusively with two discrete contributions: a non-magnetic singlet and magnetic sextet. The relative intensities of both components change gradually with the annealing temperature. In this way, while for the AM273 sample the spectrum is dominated by a non-magnetic singlet with a non-resolved magnetic component as a minor contribution, the magnetic subspectrum is practically the only contribution to the spectrum of the AN873 sample.

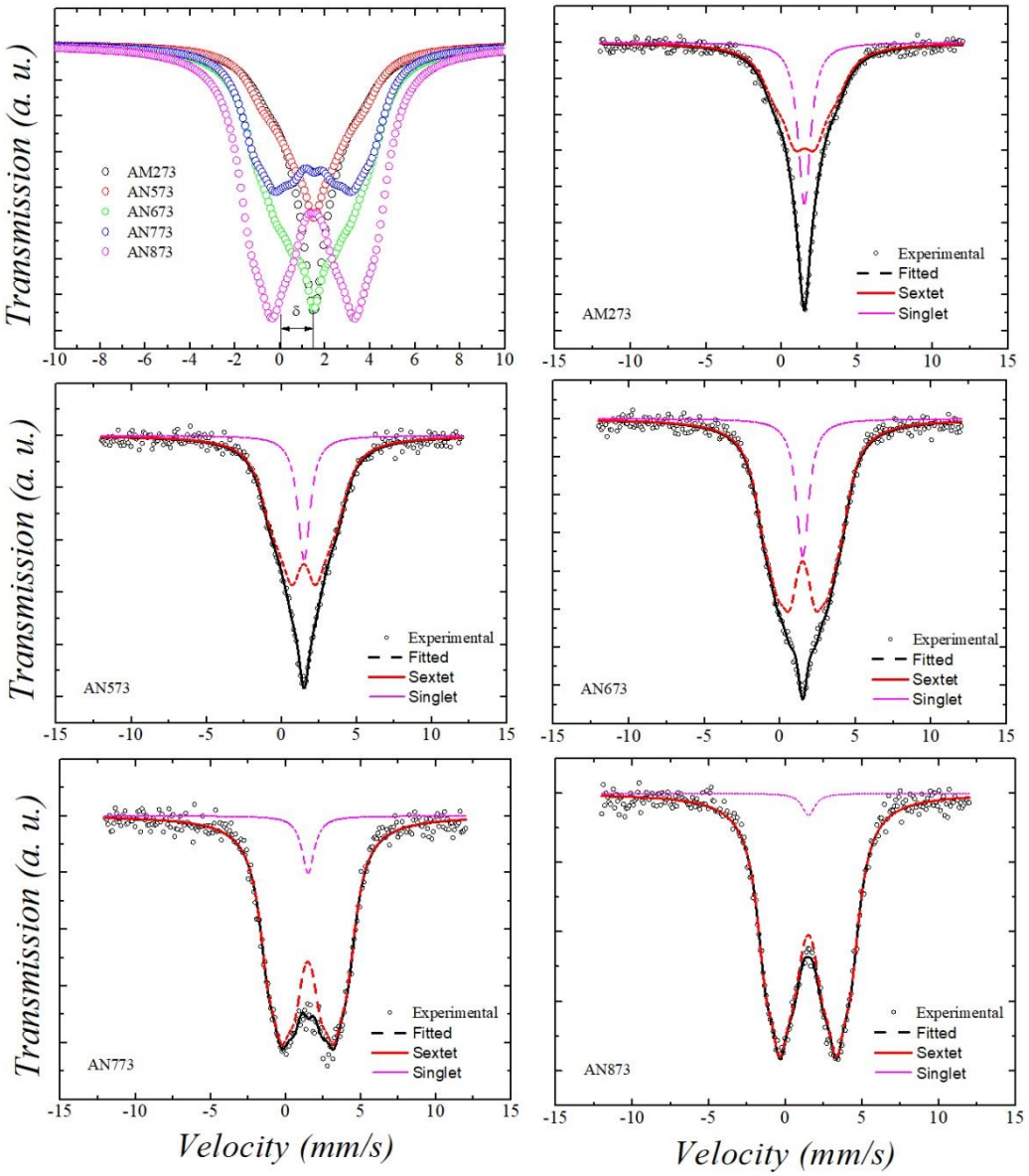

Figure 3. 23. Raw and fitted Mössbauer spectra for the set of samples at 240K.

Table 3. VI. Values obtained by the fitting of Mössbauer spectra for the whole set of samples.

Sample	δ (mm/s)	Γ (mm/s)	B_{hf} (T)	A_S (%)
AM273	1.53 (1)	1.96 (1)	4.1 (1)	31 (3)
AN573	1.48 (1)	1.67 (9)	4.6 (2)	18 (1)
AN673	1.48 (1)	1.54 (5)	5.1 (1)	15 (1)
AN773	1.48 (1)	1.51 (4)	5.3 (1)	6 (1)
AN873	1.48 (1)	1.50 (2)	5.6 (1)	1 (1)

According with the obtained results, Figure 3. 24 and Figure 3. 25 show the evolution of the magnetic hyperfine field, B_{hf}, and the singlet component, A_s, of the Mössbauer spectra with the internal strains. The main feature is the decrease of the singlet component and the increment of the hyperfine field as the annealing temperature increases. Moreover, the value of the δ isomer shift of both components, which contains information about the chemical order in the surrounding of Sn atoms and is therefore related with the atomic order on the alloy, does not change, in concordance with neutron powder diffraction results and with the null variation in the martensitic transformation and magnetic order temperatures observed by calorimetric and magnetic measurements. On the other hand, the line-width parameter, Γ , decreases as the annealing temperature increases. The value of Γ is related with the slight distortions of the local environment of the Mössbauer probe atoms [18] and therefore it is sensitive to the microstructure and consequently to the recovery of the defects created by milling. Thus, the observed changes on the magnetic properties and in the width of the martensitic transformation would rely on different internal stress states and on the presence of defects created during the milling. As previously reported in some Heusler alloys, several local distortions as dislocations and defects can be created during mechanical treatments while the atomic order is maintained [19, 20]. Dislocations in atomic ordered structures appear as super-dislocations: a pair of dislocations separated by an antiphase boundary where the atomic order is modified, and consequently the magnetic coupling related to it. Sn atoms do not carry intrinsic magnetic moment, but since a transferred hyperfine field can be induced from the neighboring magnetic ions (Mn ions in the case of Ni-Mn-Sn), [21] ^{119}Sn-Mössbauer spectroscopy would be sensitive to the local magnetic field felt by the Sn atoms. The singlet component (Figure 3. 25) is related to stressed regions caused by dislocations and antiphase boundaries where the local magnetic field is absent. In these regions the ferromagnetic order is altered in such a way that the total transferred dipolar field at Sn sites is zero. A_s decreases with annealing, implying a reduction of the density of antiphase boundaries as result of the annihilation of dislocations, while at the same time B_{hf} increases. This increase indicates a reinforcement of the transferred dipolar field with the annealing of defects and the recovery of the ferromagnetic coupling in the austenitic phase.

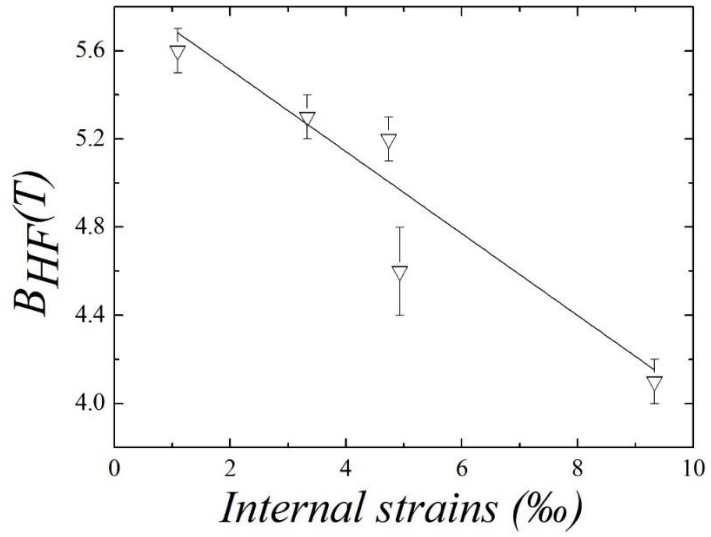

Figure 3. 24. Hyperfine field as a function of internal strains.

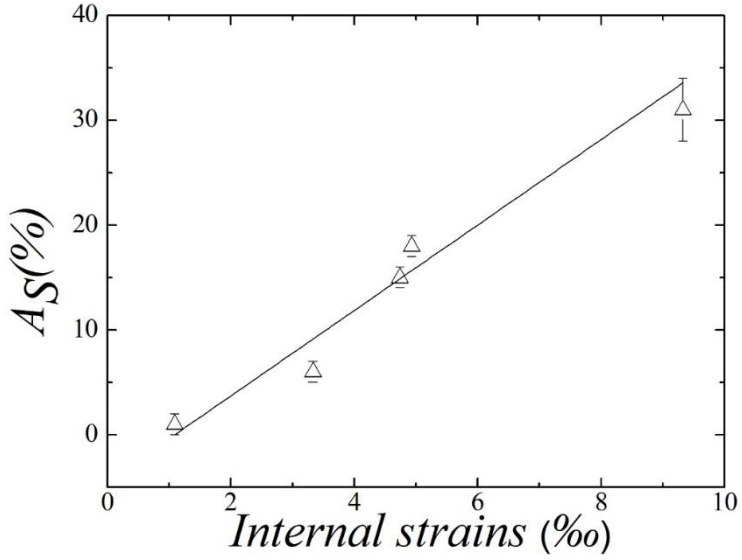

Figure 3. 25. Area of the singlet component as a function of internal strains.

3.3. SUMMARY AND CONCLUSIONS

In this chapter, the effect of the microstructure in the martensitic transformation and the related magnetostructural properties was studied in Ni-Mn-Sn alloys. The study was carried out by the analysis of macroscopic calorimetric and magnetic measurements and, at the microscopic level, by X-rays and neutron diffraction and Mössbauer spectroscopy. To evaluate the effect of microstructural parameters in the martensitic transformation and in the magnetic behavior, a milled $Ni_{50}Mn_{35}Sn_{15}$ alloy was annealed at different temperatures to induce different states of microstructural defects.

By means of calorimetry and magnetometry measurements, the martensitic transformation temperature and Curie temperature were determined, evidencing their null

variation with the different annealing treatments, although the temperature range in which the martensitic transformation takes place is reduced as the annealing temperature increases. The enthalpy and entropy values associated to the martensitic transformation point out that the martensitic transformation, significantly affected by milling, is mainly recovered after the treatment at the lowest temperature. Also, the significant change observed for the magnetocaloric effect manifests the outstanding influence of the microstructure on the functional properties of the alloy. Powder X-ray diffraction has been used to obtain information about the microstructural parameters as grain size and internal strains, showing the evolution of those values with the annealing temperatures. By combination of the magnetic measurements and the microstructural analysis by X-ray diffraction, the amount of the non-magnetic inclusions was quantified and related with the internal strains, showing a reduction of a factor of more than 10 by annealing, together with an associated increase of the saturation magnetization.

Powder neutron diffraction has shown the non-variation in the atomic order, which is in agreement with the absence of change in the temperatures of the martensitic transformation and magnetic ordering, proving the high stability of the atomic order of the Ni-Mn-Sn alloys. The crystal structure of the martensite phase has been resolved, obtaining a two-fold modulated orthorhombic structure. The analysis of the magnetic structure in the austenite phase has revealed the switch of the magnetic coupling of the Mn atoms from antiferromagnetic to ferromagnetic induced by annealing. Finally, Mössbauer spectroscopy has been used for the analysis of the microstructure and the magnetism of these alloys at the atomic level.

In conclusion, the evolution of the microstructural parameters has been quantified and correlated to the evolution of the martensitic transformation features and the magnetic properties. It is found that the relaxation processes brought by annealing leads to recovery of the martensitic transformation and the enhancement of the magnetism at both macroscopic and local level. In particular, the density of non-magnetic defects decreases upon annealing, thus leading to an increase of the saturation magnetization and a decrease of the martensitic transformation temperature range, respectively, which results in a higher magnetocaloric effect. The obtained results confirm that, once the transition temperature has been fixed by the composition, the modification of the microstructure through thermomechanical treatments appears as the best way to tune the functional properties of these alloys.

Bibliography.

[1] V. Sánchez-Alarcos, J. I. Pérez-Landazábal, V. Recarte, I. Lucia, J. Vélez, and J. A. Rodríguez-Velamazán, "Effect of high-temperature quenching on the magnetostructural transformations and the long-range atomic order of Ni–Mn–Sn and Ni–Mn–Sb metamagnetic shape memory alloys," *Acta Mater.*, vol. 61, no. 12, pp. 4676–4682, Jul. 2013.

[2] V. Recarte, J. Pérez-Landazábal, V. Sánchez-Alarcos, and J. A. Rodriguez-Velamazán, "Dependence of the martensitic transformation and magnetic transition on the atomic order in Ni–Mn–In metamagnetic shape memory alloys," *Acta Mater.*, vol. 60, pp. 1937–1945, Mar. 2012.

[3] V. Sánchez-Alarcos, V. Recarte, J. I. Pérez-Landazábal, E. Cesari, and J. A. Rodríguez-Velamazán, "Long-Range Atomic Order and Entropy Change at the Martensitic Transformation in a Ni-Mn-In-Co Metamagnetic Shape Memory Alloy," *Entropy*, vol. 16, no. 5, pp. 2756–2767, May 2014.

[4] S. Kustov, M. L. Corró, J. Pons, and E. Cesari, "Entropy change and effect of magnetic field on martensitic transformation in a metamagnetic Ni–Co–Mn–In shape memory alloy," *Appl. Phys. Lett.*, vol. 94, no. 19, p. 191901, May 2009.

[5] J. Rodríguez-Carvajal, "Recent advances in magnetic structure determination by neutron powder diffraction," *Phys. B Condens. Matter*, vol. 192, no. 1, pp. 55–69, Oct. 1993.

[6] J. Ortín and A. Planes, "Thermodynamics of thermoelastic martensitic transformations," *Acta Metall.*, vol. 37, no. 5, pp. 1433–1441, May 1989.

[7] J. Ortín and A. Planes, "Thermodynamic analysis of thermal measurements in thermoelastic martensitic transformations," *Acta Metall.*, vol. 36, no. 8, pp. 1873–1889, Aug. 1988.

[8] J. L. S. Llamazares, B. Hernando, J. J. Suñol, C. García, and C. A. Ross, "Kinetic arrest of direct and reverse martensitic transformation and exchange bias effect in Mn49.5Ni40.4In10.1 melt spun ribbons," *J. Appl. Phys.*, vol. 107, no. 9, p. 09A956, May 2010.

[9] R. Y. Umetsu, K. Ito, W. Ito, K. Koyama, T. Kanomata, K. Ishida, and R. Kainuma, "Kinetic arrest behavior in martensitic transformation of NiCoMnSn metamagnetic shape memory alloy," *J. Alloys Compd.*, vol. 509, no. 5, pp. 1389–1393, Feb. 2011.

[10] J. I. Pérez-Landazábal, V. Recarte, V. Sánchez-Alarcos, C. Gómez-Polo, S. Kustov, and E. Cesari, "Magnetic field induced martensitic transformation linked to the arrested austenite in a Ni-Mn-In-Co shape memory alloy," *J. Appl. Phys.*, vol. 109, no. 9, p. 093515, May 2011.

[11] X. Wang, F. Sung, J. Wang, Q. Yu, Y. Wu, H. Hua, and C. Jiang, "Influence of annealing temperatures on the magnetostructural transition and magnetocaloric effect of Ni40Co10Mn40Sn10 powders," *J. Alloys Compd.*, vol. 691, pp. 215–219, Jan. 2017.

[12] S. Chikazumi and C. D. Graham, *Physics of Ferromagnetism 2e*. OUP Oxford, 2009.

[13] E. Schlömann, "Properties of Magnetic Materials with a Nonuniform Saturation Magnetization. I. General Theory and Calculation of the Static Magnetization," *J. Appl. Phys.*, vol. 38, no. 13, pp. 5027–5034, Dec. 1967.

[14] G. F. Dionne, J. A. Weiss, and G. A. Allen, "Hysteresis loops modeled from coercivity, anisotropy, and microstructure parameters," *J. Appl. Phys.*, vol. 61, pp. 3862–3864, Apr. 1987.

[15] Umetsu, R. Y, A. Sheikh, B. Ouladdiaf, K. R. A. Ziebeck, T. Kanomata, and R. Kainuma, "The effect of Co substitution on the magnetic properties of the Heusler alloy $Ni_{50}Mn_{33}Sn_{17}$," *Appl. Phys. Lett.*, vol. 98, no. 4, p. 042507, Jan. 2011.

[16] T. Krenke, M. Acet, E. F. Wassermann, X. Moya, L. Mañosa, and A. Planes, "Ferromagnetism in the austenitic and martensitic states of Ni-Mn-In alloys," *Phys. Rev. B*, vol. 73, no. 17, p. 174413, May 2006.

[17] P. J. Brown, A.P. Gandy, K. Ishida, R. Kainuma, T. Kanomata, K. U. Neumann, K. Oikawa, B. Ouladdiaf, and K. R. A. Ziebeck, "The magnetic and structural properties of the magnetic shape memory compound $Ni_2Mn_{1.44}Sn_{0.56}$," *J. Phys. Condens. Matter*, vol. 18, no. 7, p. 2249, 2006.

[18] D. P. E. Dickson and F. J. Berry, *Mössbauer Spectroscopy*. Cambridge University Press, 2005.

[19] J. Schaf, K. L. Dang, P. Veillet, and I. A. Campbell, "Extended and local effects of cold work in Heusler alloys," *J. Phys. F Met. Phys.*, vol. 13, no. 6, pp. 1311–1316, Jun. 1983.

[20] T. Shinohara, K. Sasaki, H. Yamauchi, H. Watanabe, H. Sekizawa, and T. Okada, "On the Reduction in Magnetization by Clod Working on the Ferromagnetic Heusler Alloy Pd_2MnSn," *J. Phys. Soc. Jpn.*, vol. 50, no. 9, pp. 2904–2908, Sep. 1981.

[21] M. Kalvius and P. Kienle, *The Rudolf Mössbauer Story: His Scientific Work and Its Impact on Science and History*. Springer Science & Business Media, 2012.

Chapter 4. Enhancement of magnetocaloric effect by intrinsic defects and microstructure evolution by ball-milling in $Ni_{45}Co_5Mn_{35}Sn_{15}$ shape memory alloy

4.1. INTRODUCTION

As explained previously in the introduction chapter, the metamagnetic alloys based in the Ni-Mn-Z (Z=In, Sn, and Sb) systems in which the martensitic transformation (MT) takes place between a ferromagnetic austenite and a weak-magnetic martensite are among the most promising alloys for magnetocaloric applications. The MT characteristics and the magnetic properties of these alloys depend on composition, atomic order and, in principle to a lesser extent, on microstructure. The compositional dependence has been widely studied, being the complete phase diagrams of the appearing structural and magnetic phases well stablished [1–4]. Atomic order has been also systematically studied. In Ni-Mn-In and Ni-Mn-In-Co alloys it has been shown that the magnetostructural properties can be properly tuned varying the long-range atomic order, which can be easily controlled by means of thermal treatments [5–7]. In Ni-Mn-Sn and Ni-Mn-Sb alloys, in turn, the $L2_1$ structure is highly stable and the atomic order is then hardly modifiable by means of conventional thermal treatments [8]. In these alloys, the modification of the microstructural parameters (grain size, defects, internal stresses…) is the only way to modify the functional properties for a selected alloy composition. Mechanical milling and subsequent annealing treatments are one of the simplest and most used method to modify the microstructure. Typically, the grain size reduction and the presence of defects and internal stresses induced by milling degrade the MT and the magnetic properties, which can be then partially restored upon microstructural recovery processes brought by subsequent annealing [9–13]. In this respect, by comparing a Ni-Mn-Sn alloy in both the as-milled and the annealed states, we have shown that, even though no appreciable long-range atomic disorder was induced by milling, the saturation magnetization of both martensitic and austenitic phases are considerably higher after annealing, due to the reduction of the density of the anti-phase boundaries (linked to dislocations), which promote the antiferromagnetic coupling between Mn moments, as it was explained in Chapter 3. A similar magnetic deterioration at anti-phase boundaries was indeed evaluated in Ni-Mn-Al-Ga alloys by electron holography, and explained as a consequence of a local atomic disordering in the boundary region [14].

On the other hand, the addition of cobalt has been shown to enhance the magnetism of the austenite and to hinder ferromagnetic ordering in martensite in Ni-Mn-Z alloys, thus leading to an increase of ΔM and therefore to larger magnetically-induced shifts of the MT temperature and higher associated magnetocaloric effects [15–20]. In particular, in Ni-Mn-Sn alloys it has been also shown that the magnetic coupling between the Mn moments on the 4*a* (Mn sublattice) and 4*b* sites (Sn sublattice) of the austenitic cubic structure changes from being antiferromagnetic to ferromagnetic as a consequence of the substitution of Ni by Co [19] (the magnetic coupling between Mn atoms on the 4*a* sites is ferromagnetic both in the ternary and the quaternary alloys). In this regard, it could be thought that the influence of the presence of anti-phase boundaries (and any other microstructural defect resulting in local atomic disordering) on the magnetic properties will be different in the quaternary Co-doped alloys to that in the ternary ones. In this sense, in the first part of this chapter the effect of mechanically-induced defects on the magnetostructural properties, and in particular on the magnetocaloric effect, is analyzed on a quaternary Ni-Co-Mn-Sn alloy subjected to soft milling and subsequent annealing. It is found that the presence of microstructural defects, far for worsening, can make the magnetocaloric effect to be higher in the as-milled state than after subsequent annealing. This unusual beneficial presence of defects is explained as the result of the combination of the effect of defects on the Mn-Mn distance, the Co effect on the magnetic exchange coupling between Mn atoms, and the effect of defects on the vibrational entropy change at the martensitic transformation.

Due to this unconventional result, in a further step, ball milling has been used as a suitable way to induce a large amount of defects in the studied Ni-Co-Mn-Sn alloy in a controlled way, allowing a systematic study on the evolution of the microstructure. This technique provides some advantages like simplicity, high productivity, and cost-effectiveness in fabrication metallic particles compared with other methods. On the other hand, the high energy involved in the process modifies the characteristics of the MT as consequence of inducing a disordered phase. In addition, the null variation in the atomic order degree by thermal treatments those Ni-Mn-Sn systems present make them suitable to understand the effects of ball milling on the properties of the alloys. Therefore, the effect of high-energy ball milling has been analyzed in the Ni-Co-Mn-Sn alloy, quantifying the evolution of the microstructural parameters and the magnetostructural properties with the milling time.

4.2. EXPERIMENTAL RESULTS

A $Ni_{45}Co_5Mn_{35}Sn_{15}$ alloy was synthetized, as described in Chapter 2, from high purity elements by arc-melting under protective argon atmosphere. The obtained bulk was remelted several times and homogenized at 1173K during 24h and slowly cooled to room temperature. The composition was analyzed by EDS in a Jeol JSM-5610LV Scanning Electron Microscope (SEM). In order to induce defects, the alloy was subjected to hand milling in an agate mortar until reaching a uniform particle-size distribution. The mean particle size of the powder, estimated from SEM images, was $60 \pm 20\ \mu m$. A part of the obtained powder was then subjected to a 5 min annealing at 673K in order to remove some of the defects induced by

milling. The as-milled and the annealed samples were then analyzed and compared. The martensitic transformation was characterized by differential scanning calorimetry (Q-100 DSC, TA Instruments), by heating-cooling cycles performed form 140K up to 300K at 10K/min. The macroscopic magnetic characterization of the alloys was performed by recording thermomagnetization curves at 100Oe and 60kOe and the magnetization dependence on the magnetic field at constant temperature in both phases in SQUID magnetometer (QD MPMS XL-7). The neutron scattering experiments were carried out at Institut Laue-Langevin, in Grenoble, France. Nuclear and magnetic structures were analyzed by powder neutron diffraction, using data collected in D1B (λ=1.28Å and). As for all the diffraction work in this thesis, the data treatment was carried out using the programs of the Fullprof Suite [21]. Starting from the as-milled powder, a systematic ball milling in order to study the microstructure evolution was performed at different milling times (15, 30, 45, 60, 90, 120 minutes) in a RETSCH E_{MAX} ball-mill with ratio 5:1 at 800 rpm under argon atmosphere and controlled temperature avoiding the possibility of oxidation. For the microstructure analysis, High Resolution X-rays Powder Diffraction (HRXPD) was carried out in BL04_MPSD beam line (28keV) at ALBA synchrotron, Barcelona, Spain.

4.2.1. Macroscopic characterization

4.2.1.1. DSC measurements

The occurrence of martensitic transformation is confirmed by the appearance of endothermic peaks (see Figure 4. 1.) associated to the reverse MT on the heating curves in calorimetric measurements, obtaining also the corresponding values of the entropy change (ΔS) associated to the transformation. Taking into account the high sensibility of the transformation temperatures to long-range atomic order [22], the absence of evolution suggests a scarce effect of annealing on atomic order, as it could be indeed expected given the high stability of the $L2_1$ structure in the Ni-Mn-Sn system [8]. With respect to the entropy change, it is worth noting that the obtained value (see Table 4. I) is higher in the as-milled sample although ΔS typically increases as a consequence of the microstructural recovery processes brought by annealing (as in fact occurs in ternary Ni-Mn-Sn alloys, as shown in Chapter 3). This point will be analyzed later in detail.

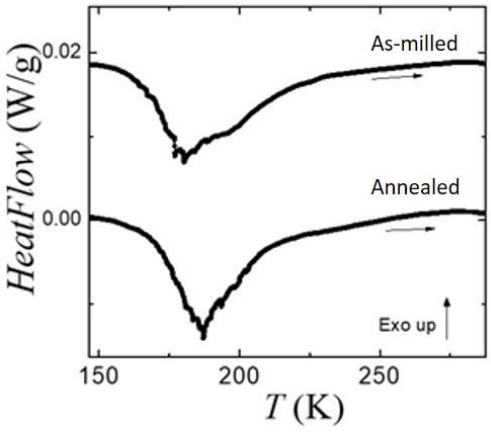

Figure 4. 1. Calorimetric measurements showing the reverse martensitic transformation.

4.2.1.2. Magnetic measurements

Figure 4. 2 shows the temperature dependence of the magnetization in the as-milled and annealed samples under a) 100 Oe and b) 60 kOe applied magnetic fields. The sequences of magnetostructural transformations can be clearly determined from the low-field *M(T)* curves: in both samples, the high temperature paramagnetic austenite becomes ferromagnetic around 360 K and a subsequent magnetization jump takes place around 180 K, coinciding with the appearance of the endothermic peaks in the calorimetric curves (Figure 4. 1), linked to the MT to a martensite with lower magnetization. The transformation temperatures and the magnetization change at the MT obtained from the different *M(T)* curves are summarized in Table 4. I along with the entropy change at the MT, ΔS, estimated from the DSC thermograms. As it was shown in Chapter 3 for ternary Ni-Mn-Sn alloys, neither the Curie temperature, T_C^a, nor the MT temperature, T_M, seem to evolve substantially with the annealing treatment. Furthermore, the thermal hysteresis linked to the MT is also practically unaffected by annealing (in fact, it is slightly larger in the annealed sample). As shown in Figure 4. 2.b, the MT shifts toward lower temperatures under the application of a 60 kOe magnetic field, being the shift (with respect to T_M obtained at 100 Oe) almost the same in both as-milled and annealed samples. On the contrary, the magnetization change at the MT, ΔM, is definitively affected by annealing, being ΔM quite lower in the annealed sample.

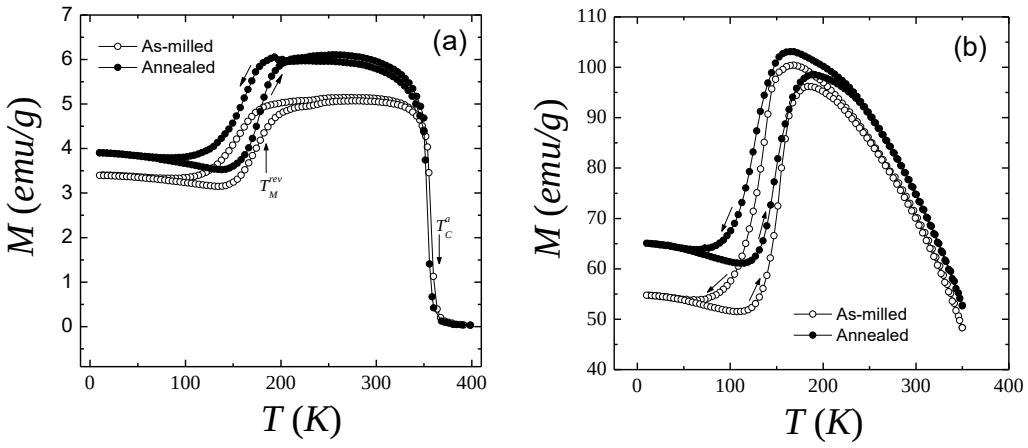

Figure 4. 2. Temperature dependence of magnetization of the as-milled and annealed samples under a) 100 Oe and b) 60 kOe applied magnetic field.

Table 4. I. Temperature of the reverse transformation (T_M^{rev}) at 100 and 60000 Oe, Curie temperature of the austenite (T_C^a), magnetization change at the MT (ΔM) and entropy change at the MT for the as-milled and annealed alloys.

Sample	T_M^{rev}*(100 Oe)(K)*	T_M^{rev}*(60 kOe)(K)*	T_C^a *(K)*	*ΔM (emu/g)*	*ΔS (J/kgK)*
As-milled	187	159	362	52	9.8
Annealed	188	159	360	40	8.1

The effect of annealing on the saturation magnetization, M_S, is illustrated in Figure 4. 3, where the magnetic-field dependence of magnetization is shown for both phases in both as-milled and annealed states. In all cases, the magnetization shows an initial abrupt increase and a subsequent trend to saturation, typical of a ferromagnetic behavior. Interestingly, the annealing treatment affects the magnetization in a different way in martensite and in austenite. In particular, the saturation magnetization significantly increases in martensite after annealing ($\Delta M_S^{mart}/ M_S^{mart} \sim 28\%$) whereas a very slight variation ($\Delta M_S^{aust}/ M_S^{aust} \sim 3\%$) is observed in austenite. This behavior is quite surprising as long as it is opposite to that found in similarly-milled ternary Ni-Mn-Sn alloys, for which the high-field magnetization increase linked to annealing is larger in austenite and in martensite as it was shown in Chapter 3.

In the same way as in in Chapter 3,the effect of defects on the magnetic properties has been qualitatively estimated from the fitting of the field-dependence of the magnetization to the classical law of approach to saturation for magnetization. As a reminder, this law is expressed as:

$$M = M_S\left(1-\frac{a}{H}-\frac{b}{H^2}\right)+\chi H \tag{4.1}$$

where H is the applied field, M_S the saturation magnetization, χ the field independent susceptibility and a and b are coefficients related to magnetic and structural properties of the sample [23–25]. In particular, the parameter a depends on the stresses field created by dislocations and non-magnetic inclusions and it can be approximated to $a \approx 4\pi\rho M_S P_{eff}$, where ρ is the density of the material and P_{eff} is the effective fraction of porosity and non-magnetic inclusions [26]. From the fitting of the magnetization curves in martensite at 10 K to the law of approach to saturation (Figure 4. 3.b) P_{eff} values of 0.021 and 0.014 are obtained for the as-milled and annealed samples, respectively. The higher value of effective fraction of non-magnetic inclusions in the as milled sample points out that the density of dislocations where the ferromagnetic coupling is lost by the local atomic disordering is higher in the as-milled sample than in the annealed one, in agreement with the expected reduction of defects upon heating treatment.

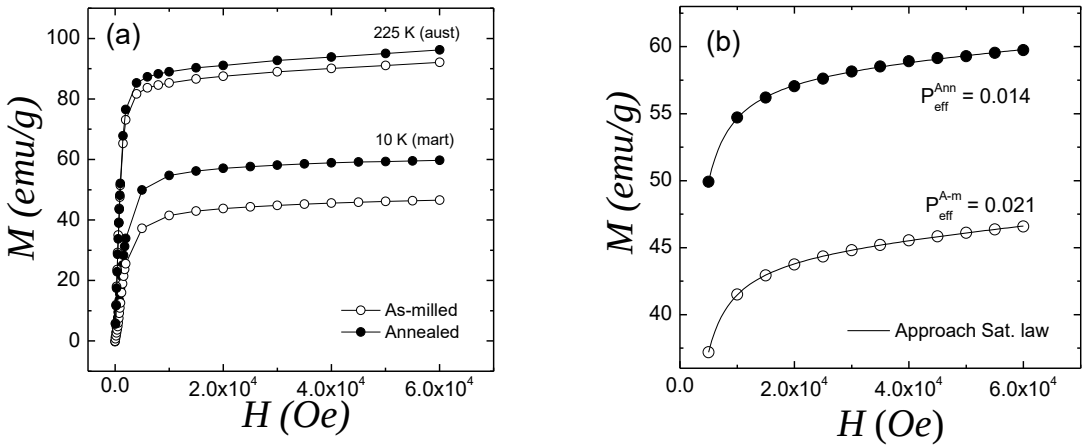

Figure 4. 3. a) Magnetization in the austenitic (at 225 K) and martensitic (at 10 K) phases of the as-milled and annealed samples, as a function of the applied magnetic field. b) Detail of the fitting of the magnetization curves in martensite at 10 K to the law of approach to saturation.

4.2.2. Neutron diffraction analysis

In order to ascertain the origin of the different evolution of the saturation magnetization in martensite and austenite upon annealing, neutron diffraction measurements were performed. The nuclear structures have been first refined from diffractograms obtained at 400 K in paramagnetic austenite, which allowed a more accurate determination of the atomic order, and then a combined nuclear and magnetic refinement has been performed for ferromagnetic austenite at 300 K and ferromagnetic martensite at 10K.

4.2.2.1. Nuclear and magnetic structures in austenite

Figure 4. 4 shows the Rietveld refinements in paramagnetic austenite at 400K in order to avoid all the magnetic contribution and obtain the nuclear structure. The atomic order in the form of site occupancies obtained by Rietveld refinement is shown in Table 4. II. The austenitic phases show the typical cubic $L2_1$ structure (space group $Fm\bar{3}m$) with almost the same lattice parameter. Some of the intensity peaks indexed according to the associated Bragg reflections are shown in the diffractograms. In particular, the (111), (200) and (220) reflections, linked to the $L2_1$, B2 and A2 types of ordering, respectively [8, 27], are clearly distinguished at low angles. As expected, no significant variation of the atomic order is observed, in agreement with the null evolution of the structural and magnetic transition temperatures.

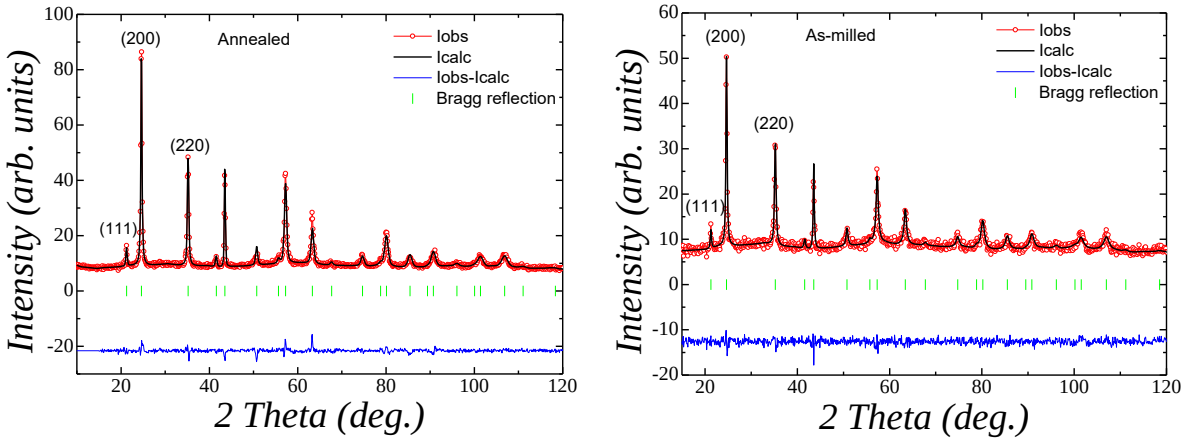

Figure 4. 4. Rietveld refinement in paramagnetic austenite phases at 400K in annealed and as-milled samples.

Figure 4. 5 shows a detail of the refinement combining nuclear and magnetic structures in the main magnetic reflections in ferromagnetic austenite at 300 K for the as-milled and annealed samples. The magnetic moments obtained by the analysis on the ferromagnetic austenite are summarized in Table 4. III. The magnetic structure shows a collinear arrangement with the magnetic moments of Mn atoms all positive in austenite, thus implying a ferromagnetic coupling between Mn atoms, even between those in the 4*a* and 4*b* sites. Interestingly also, the net magnetic moments in austenite are not affected by the annealing. As it was shown in Chapter 3, in the cubic phase of the ternary Ni-Mn-Sn alloys, the magnetic coupling between Mn atoms in the 4*a* sites is ferromagnetic whereas it is antiferromagnetic between Mn atoms in the 4*a* and

4*b* sites. Hence, the magnetic coupling between Mn atoms may change from ferromagnetic to antiferromagnetic across linear or planar defects, thus leading to a decrease in the net magnetic moment. In the austenitic phase of the quaternary alloy, in turn, the presence of Co on the Ni sites makes the Mn atoms at the 4*a* and 4*b* sites to couple ferromagnetically, and therefore the magnetic coupling between Mn atoms (whether nearest or next-nearest neighbors) will be always ferromagnetic, irrespectively of the presence of defects. Therefore, assuming that a similar annihilation process occurs on annealing the quaternary alloy, the almost null evolution of the saturation magnetization of austenite can be explained as a direct consequence of the ferromagnetic coupling between Mn atoms.

Table 4. II. Atomic order obtained by Rietveld refinement in paramagnetic austenite at 400K in as-milled and annealed samples.

Sites	Sample	
	As-milled	Annealed
4*a* (0,0,0)	0.94Mn+0.06Sn	0.97Mn+0.03Sn
4*b* (1/2,1/2,1/2)	0.47Mn+0.53Sn	0.49Mn+0.51Sn
8*c* (1/4,1/4,1/4)	0.88Ni+0.12Co	0.90Ni+0.10Co

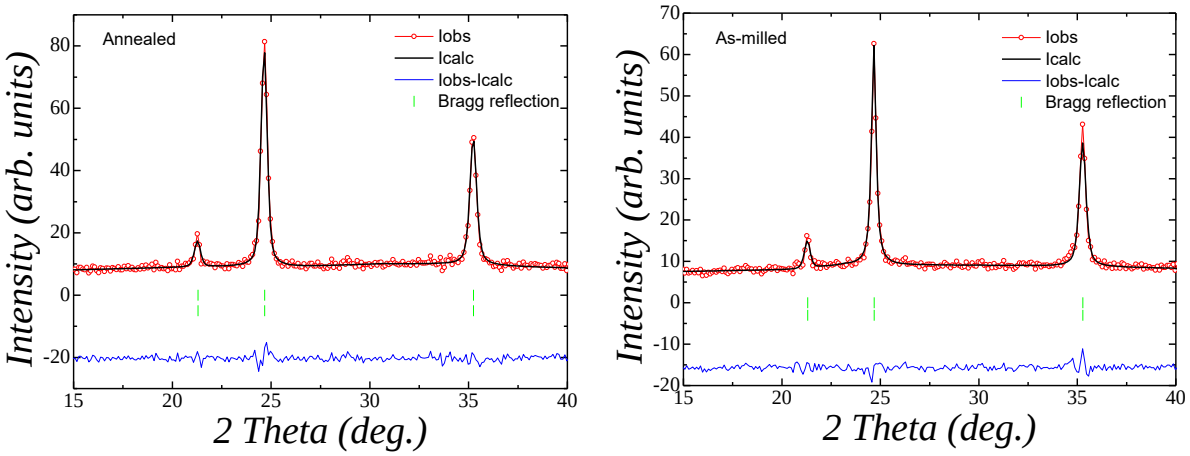

Figure 4. 5. Rietveld refinement in magnetic ordered austenite phases at 300K in annealed and as-milled samples.

Table 4. III. Magnetic moments values for as-milled and annealed samples at 300K.

Sample	**Sites**		
	4*a* (μ_B)	**4*b*** (μ_B)	**8*c*** (μ_B)
As-milled	3.11 (2)	1.14 (2)	0.296*
Annealed	3.11 (2)	1.19 (2)	0.28*

*Magnetic moments fixed to 0.2 μ_B and 1.0 μ_B for Ni and Co respectively

4.2.2.2. Nuclear and magnetic structures in martensite

The obtained martensitic structure is the same in both samples; a 3M modulated monoclinic structure (space group *P2/m*) with similar lattice parameters, no trace of austenitic phase being observed at all at 10 K. In order to reduce the number of parameters in the refinement of the martensitic structures, the same site occupancies obtained in paramagnetic austenite have been used in the sites related by the monoclinic distortion in martensite. With respect to the refined magnetic structure (a collinear magnetic structure, in all cases), it is worth noting that, contrarily to the situation observed in austenite, negative moments are obtained in martensite for Mn atoms in those sites related by the monoclinic distortion with the 4*b* sites (as expected due to the weakening of the exchange interactions as a consequence of the abrupt change in the Mn–Mn interatomic distances upon the MT). In the case of the martensite, the magnetic moments are significantly affected by the annealing, and a marked decrease in the negative antiferromagnetic contribution is observed. Figure 4. 6 shows the refinement combining nuclear and magnetic structures in ferromagnetic martensite at 10 K for the as-milled and annealed samples. The nuclear and magnetic structure parameters of both samples in ferromagnetic martensite are summarized in Table 4. IV. Figure 4. 7 shows an illustration of the nuclear and magnetic structures in the martensitic phase.

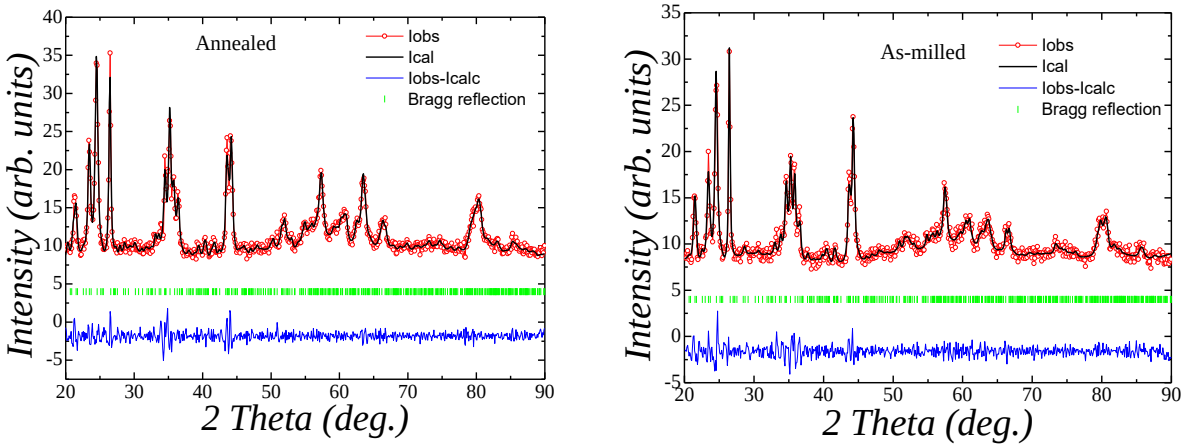

Figure 4. 6. Rietveld refinement of nuclear and magnetic structures at 10K in the samples studied.

Since neither crystallographic structure nor lattice parameters nor long-range atomic order evolve upon annealing, the observed evolution of the saturation magnetization and the magnetic moments in martensite must be purely attributable to a microstructural relaxation, just as it occurs in the similarly-milled ternary Ni-Mn-Sn alloy showed in Chapter 3. In that case, the increase of the saturation magnetization of austenite and martensite after annealing was ascribed to a reduction of the density of anti-phase boundaries as result of the annihilation of superlattice dislocations. In martensitic phase, the change in the interatomic distances upon the martensitic transformation makes the Mn atoms in the martensitic structure to couple antiferromagnetically or ferromagnetically depending on whether they are nearest or next-nearest neighbors, respectively, both in the ternary and the quaternary alloys. Therefore, the change of the Mn-Mn distance associated to the presence of defects (or even to internal stresses)

may explain the lower antiferromagnetic contribution in the annealed sample, where the amount of defects is presumably lower than in the as-milled one.

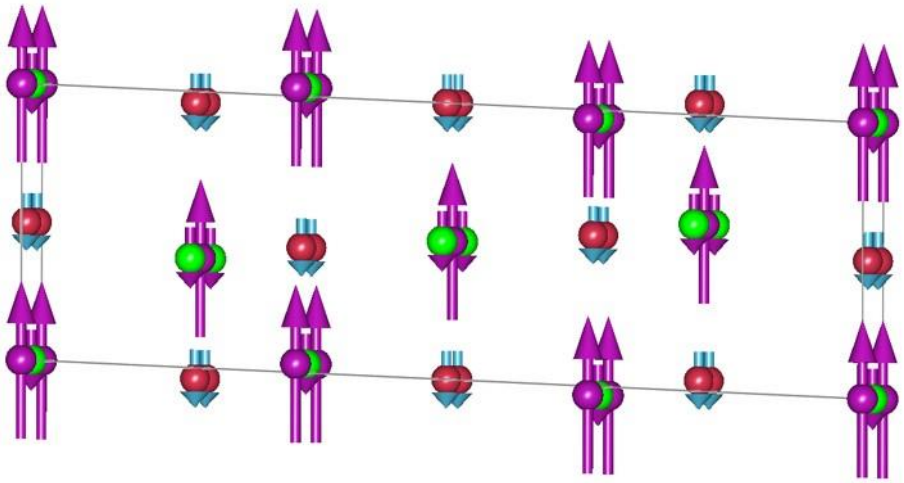

Figure 4. 7. Illustration of nuclear and magnetic structure in martensite of both as-milled and annealed samples, where purple balls are sites occupied mainly by Mn atoms, green ones are sites occupied by Sn and Mn atoms and red ones are sites occupied by Ni and Co atoms. Purple arrows are magnetic moments from Mn atoms and blue arrows for Ni and Co atoms.

Table 4. IV. Atomic coordinates and magnetic moments for martensitic structure with P2/m space group in as-milled and annealed samples at 10 K.

Sites	**As-milled**				**Annealed**			
	x	**y**	**z**	**μ (μB)**	**x**	**y**	**z**	**μ (μB)**
1*a*(0,0,0)				2.404(162)				2.502(208)
1*h*(1/2,1/2,1/2)								
2*n*(x,1/2,z)	0.397(1)		0.201(1)		0.397(1)		0.201(1)	
2*m*(x,0,z)	0.032(1)		0.326(1)		0.032(1)		0.326(1)	
1*b* (0,1/2,0)				-0.846(0)				-0.563(411)
1*g* (1/2,0,1/2)								
2*m* (x,0,z)	-0.034(4)		0.201(1)		-0.034(4)		0.201(1)	
2*n* (x,1/2,z)	0.453(5)		0.326(1)		0.453(5)		0.326(1)	
2*j* (1/2,y,0)		0.245(13)		*0.296		0.245(13)		*0.28
2*k* (0,y,1/2)		0.221(7)				0.221(7)		
4 (0,1/4,z)			0.201(1)				0.201(1)	
4 (1/2,1/4,z)			0.326(1)				0.326(1)	

*Magnetic moments fixed to 0.2 μ_B and 1.0 μ_B for Ni and Co respectively.

4.2.3. Magnetocaloric analysis

The magnetically-induced shift of the MT temperature T_M is directly related to ΔM through the Clausius-Clapeyron equation

$$\frac{dT_M}{dH} = -\mu_0 \frac{\Delta M}{\Delta S} \tag{4.2}$$

(where H is the applied magnetic field). The observed effect of annealing on the magnetic moments, and in particular on ΔM, suggests a possible influence of the mechanically-induced defects on the magnetic induction of the MT and therefore on the magnetocaloric effect (MCE).

The effect of magnetic field on the MT temperature has been analyzed from the temperature dependence of magnetization under different applied magnetic fields. Figure 4. 8 shows the *M(T)* curves obtained on heating under applied magnetic fields ranging from 100 Oe to 60 kOe around the martensitic transformation of the as-milled and the annealed samples. As expected, in both cases the magnetization jump associated to the MT occurs at lower temperatures on increasing the magnetic field, because of the magnetic stabilization of the austenite.

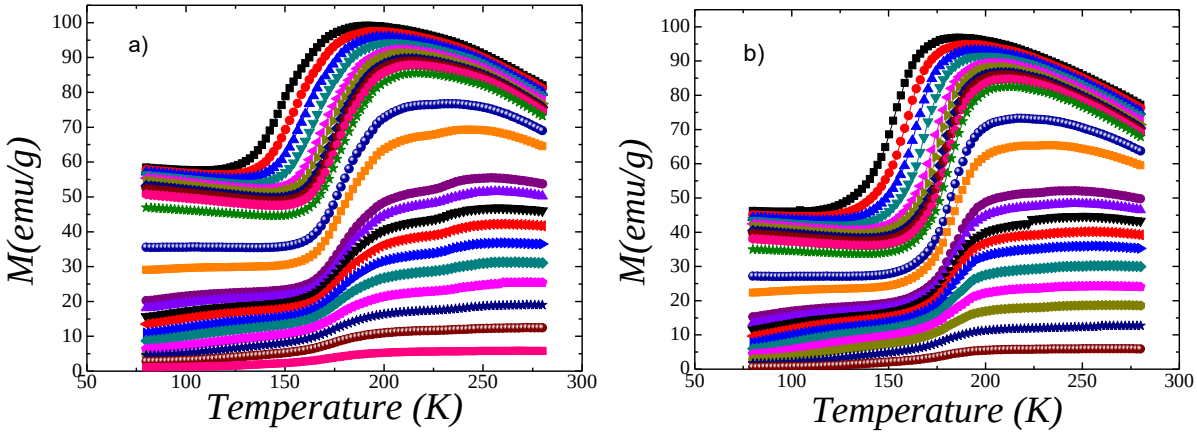

Figure 4. 8. ZFC M(T) curves on heating under different applied fields ranging from 100 Oe up to 60 kOe in the a) annealed and b) as-milled samples.

The shift of T_M (determined from the peaks of the derivative curve of magnetization measurements) is shown in Figure 4. 9 as a function of the applied field. The transformation temperatures linearly decrease with the increasing applied field, being the slope the same in both samples, $dT_M/dH \approx$ (0.5 K/kOe). It is worth noting that this slope is in agreement with the dT_M/dH values calculated by substituting into Equation 4.2 the values of ΔM and ΔS shown in Table 4.I.

The MCE, which can be defined as the entropy change in isothermal conditions, ΔS_{iso}, has been calculated from the ZFC magnetization measurements shown in Figure 4. 8 using the expression

$$\Delta S_{iso} = S(T,H) - S(T,0) = \int_0^H \left(\frac{\partial M}{\partial T}\right)_H dH \tag{4.3}$$

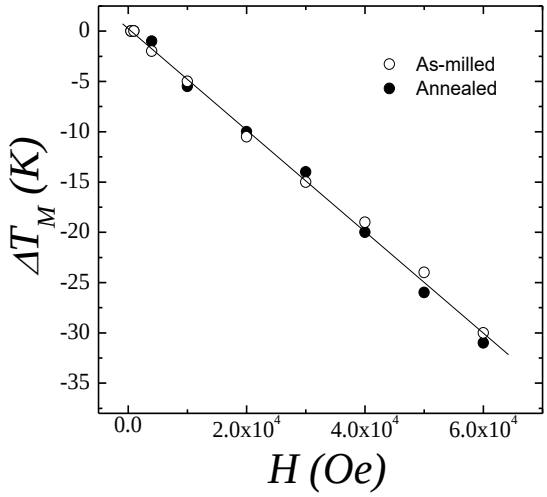

Figure 4. 9. Shift of the transformation temperature as a function of the applied magnetic field.

The numerical integration of $\partial M/\partial T$ from a set of magnetization versus temperature spectra at different constant values of applied field $M(T)_H$ is the correct procedure [28]. The obtained ΔS_{iso} values are shown in Figure 4. 10 as a function of temperature and applied magnetic field. In both cases, a positive peak (inverse MCE) is observed linked to the magnetostructural transformation at T_M^{rev} and the maximum MCE values increase with the increasing magnetic field. In particular, the maximum values, obtained under $4.77 \cdot 10^6$ A/m, are $\Delta S_{iso}^{Mill} \approx 8$ J/kgK and $\Delta S_{iso}^{Ann} \approx 6$ J/kgK for the milled and annealed samples, respectively. These values are much lower than the higher values obtained in Ni-Co-Mn-Sn alloys (around $\Delta S_{iso} \approx 32$ J/kgK [29]), but comparable or even greater than those obtained in the Ni-Mn-Sn system [9, 30, 31].

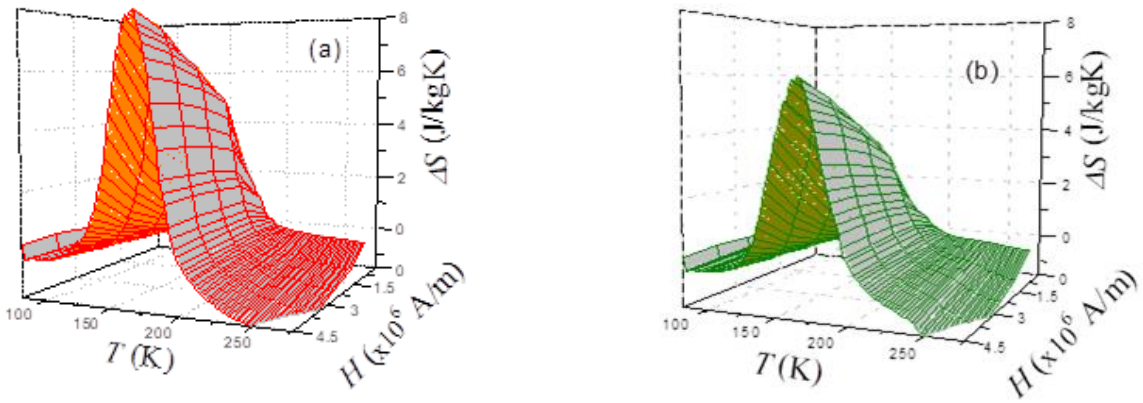

Figure 4. 10. Isothermal magnetically-induced entropy change as a function of temperature and applied magnetic field for a) as-milled sample and b) annealed sample.

In order to better compare the influence of annealing on the magnitude of the MCE, the ΔS_{iso} values obtained in both samples are plotted together as a function of temperature in *Figure 4. 11*. It can be seen that the magnetocaloric effect is considerably higher in the as-milled sample

than in the annealed one. Interestingly, this result suggests that the presence of defects, far for worsening, may be beneficial for MCE in these metamagnetic Heusler alloys. In these alloys, the magnetically-induced entropy change is linked to the magnetic induction of the MT. In both, the as-milled and annealed samples, a similar transformed fraction is induced since the shift of the MT temperature and the width of the MT temperature range is nearly the same. Therefore, the higher ΔS_{iso} obtained in the as-milled sample must be a consequence of its higher intrinsic MT entropy change (see Table 4. I). The entropy change linked to the reverse MT (which represents the maximum attainable ΔS_{iso}) can be considered as the sum of a vibrational $\Delta S_{vib}^{(+)}$ (positive) and a magnetic $\Delta S_{mag}^{(-)}$ (negative) term, in such a way that $\Delta S \approx \Delta S_{vib}^{(+)} + \Delta S_{mag}^{(-)}$ must be positive [32]. Since $\Delta S_{mag}^{(-)}$ (directly related to ΔM [27]) is higher in the as-milled sample, a lower total ΔS should be expected. Nevertheless, ΔS is actually higher indicating that the vibrational contribution ΔS_{vib} must be considerably higher in the as-milled sample than in the treated one. Taking into account that the crystallographic structures are exactly the same in both samples, the decrease of the entropy change in the treated sample should be attributable to the decrease in the concentration of mechanically-induced defects upon annealing.

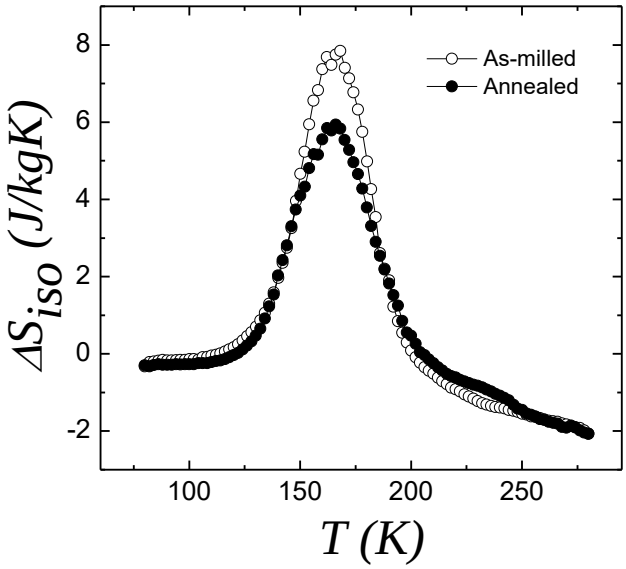

Figure 4. 11. Isothermal magnetically-induced entropy change under 60 kOe applied magnetic field as a function of temperature for the as-milled and annealed samples.

Assuming that in general the presence of defects increases the entropy of the alloy independently of the crystallographic structure (phase), the increase of the vibrational entropy change ΔS_{vib} is a consequence of the much stronger influence of the induced defects on the vibrational entropy of the austenite than on the vibration entropy of the martensite (opposite to the above mentioned higher influence of defects on the magnetism of the martensitic phase). Although the influence of defects (point defects, dislocations and anti-phase boundaries) in the vibrational properties of some metals has been analyzed in several theoretical studies [33–35], to the best of our knowledge this is the first indirect evidence of the effect of defects on the vibrational entropy change at the martensitic transformation. In any case, further works on the

analysis of the type and concentration of defects should be need in order to quantitatively correlate defects and magnetically-induced entropy change.

4.2.4. Systematic milling

Since, as we have seen in the previous sections, the inclusion of defects by hand-milling improves the magnetocaloric effect, a further step is the induction of a large amount of defects in a controlled way by high energy ball-milling. The objective is to modify the microstructure systematically, allowing the structural and microstructural changes to be correlated with the variation in the properties of the system. Starting from the hand-milled powder (as-milled sample), different samples have been obtained by ball milling at different milling times (15, 30, 45, 60, 90, 120 minutes)

4.2.4.1. Calorimetric characterization

As a first step of characterization, calorimetric measurements in all the obtained powders are carried out in order to identify the presence of the martensitic transformation and determine the thermodynamic properties. Figure 4. 12 displays the calorimetric curves on heating at 10K/min, showing the endothermic peaks associated to the reverse MT. The reverse MT temperature remains constant with the milling time, as expected from the result obtained on Ni-Mn-Sn alloys presented in Chapter 3. However, the enthalpy associated to the MT is reduced with milling time as effect of the inclusion of defects and the variation of the microstructural state. The reduction of the enthalpy of the MT by milling indicates the degradation of the MT, which vanishes for the samples milled more than 60 minutes, as Figure 4. 13 shows.

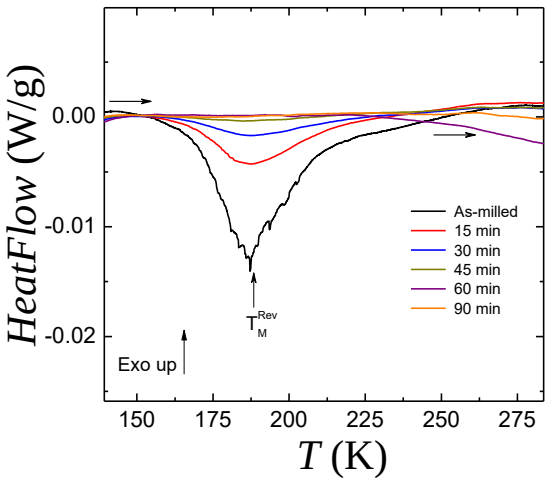

Figure 4. 12. DSC curves on heating at 10K/min of the samples studied in this section.

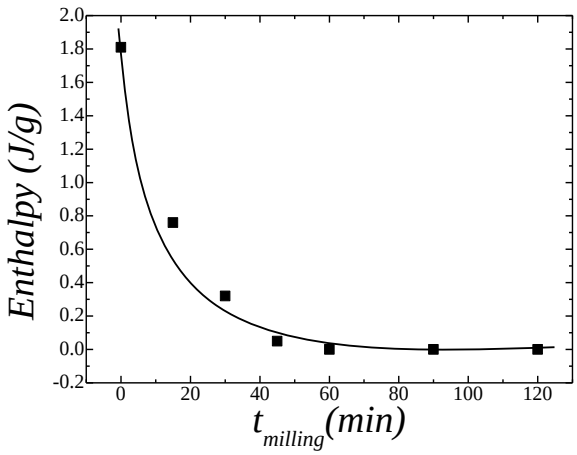

Figure 4. 13. Dependence of the MT enthalpy with milling time for the reverse MT.

4.2.4.2. Powder characterization

SEM microscopy was carried out in order to characterize the obtained powders after milling. Figure 4. 14 shows images of the Ni-Co-Mn-Sn powder samples with different milling times.

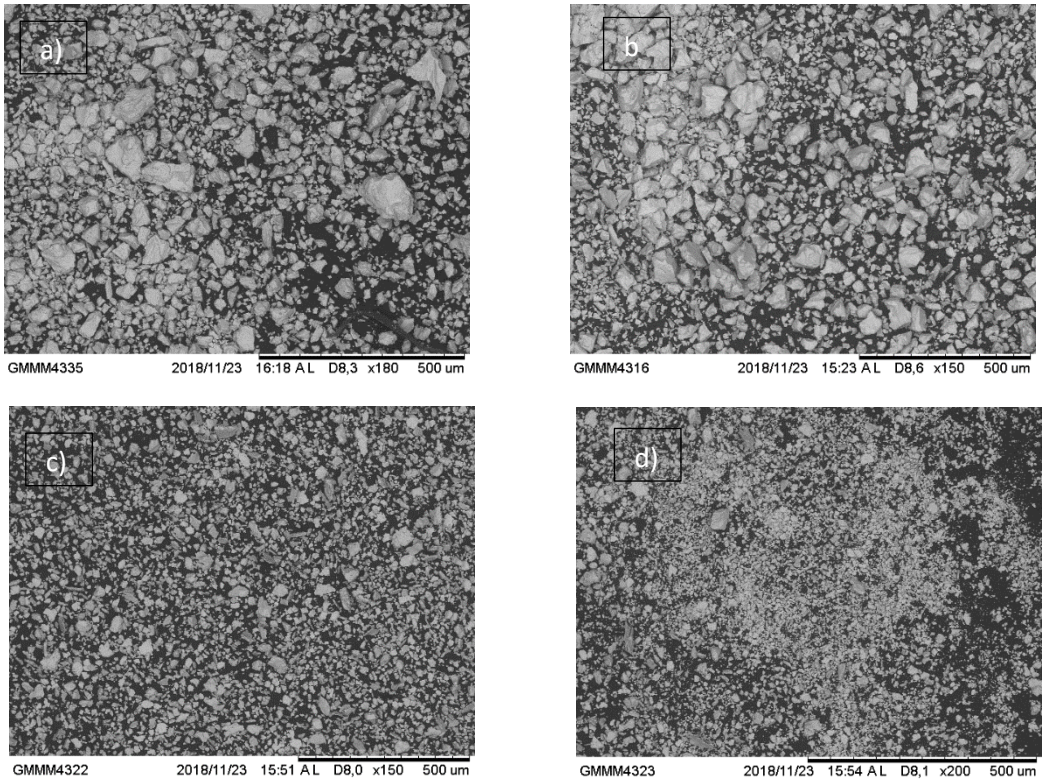

Figure 4. 14. SEM images on a) as-milled (hand-milled), b) 15 minutes, c) 45 minutes and d) 60 minutes ball-milled samples.

The as-milled sample (see Figure 4. 14.a) presents large particle sizes. It is worth recalling that this sample is only hand-milled in agate mortar. In this case, the powder particle size is not homogenous, with many big particles with 800 μm size. In the case of the sample milled during 15 minutes, the powder particles present sizes slightly smaller than the as-milled sample, around to 500 μm, but, more remarkable, a higher size homogeneity. This tendency is maintained at longer milling times: as the milling time increases, the obtained powders present a smaller particle size with higher homogeneity.

In order to obtain more information about the microstructure evolution, Figure 4. 15 shows the obtained TEM diffractograms at room temperature for the samples milled during 15, 30 and 45 minutes. For the samples milled during 15 and 30 minutes, the diffractograms show enlarged spots corresponding to the reciprocal lattice of the cubic austenite. The presence of these spots indicates that de diffraction volume corresponds to deformed single-crystals. In the case of the alloy milled during 45 minutes the presence of rings indicates the presence of different crystal orientations characteristic of a powder structure with very small crystal size.

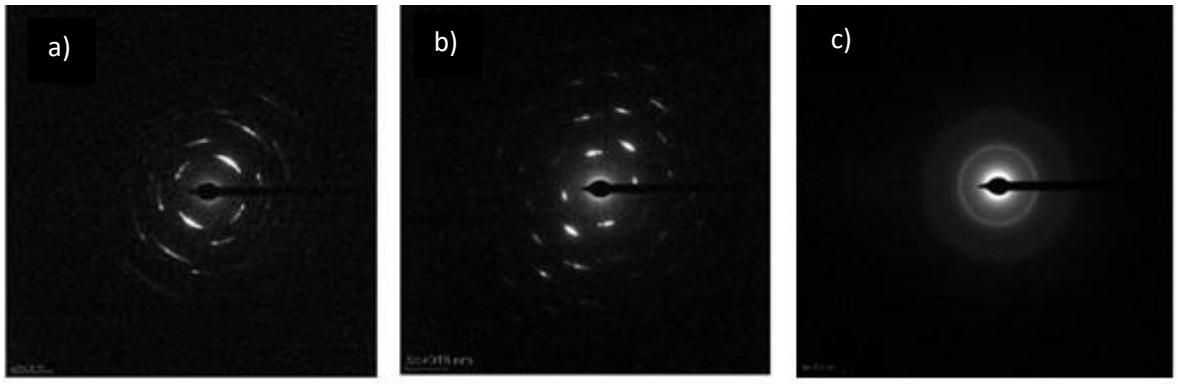

Figure 4. 15. TEM images corresponding to samples milled during a) 15 minutes, b) 30 minutes and c) 45 min.

4.2.4.3. Microstructural analysis

In order to obtain quantitative values for the microstructural parameters, as grain size and internal strains, and correlate them with the mechanical treatments of the samples, high-energy (28 keV - λ =0.4424 Å) X-ray diffraction measurements at room temperature were performed. Figure 4. 16 shows the evolution of the diffractograms of the studied samples. According to the increase in milling time, the intensity of the (111) peak, that corresponds to $L2_1$ structure [36–38], is reduced, while an amorphous phase induced by the mechanical treatment appears and increases with the milling time. Furthermore, as shown in Figure 4. 16.b, a certain percentage of martensite is present in all the samples, as indicated by the presence of the peak at $2\theta \sim 11.8^{\circ}$ that corresponds to the (200) reflection of a *I2/m* monoclinic structure. As it will be further explained hereafter, several processes occur at the same time during high-energy ball milling. First, the variation in microstructure parameters as grain size and internal stress, which decrease and increase respectively with the milling time (see Figure 4. 17.).

Secondly, the continuous reduction of the percentage of crystalline phases, the sample becoming more and more amorphous, as indicated by the disappearance of diffraction peaks. Finally, the induction of the martensitic phase and consequently the reduction of the volume fraction of the austenitic structure (see Figure 4. 16.b andFigure 4. *18*).

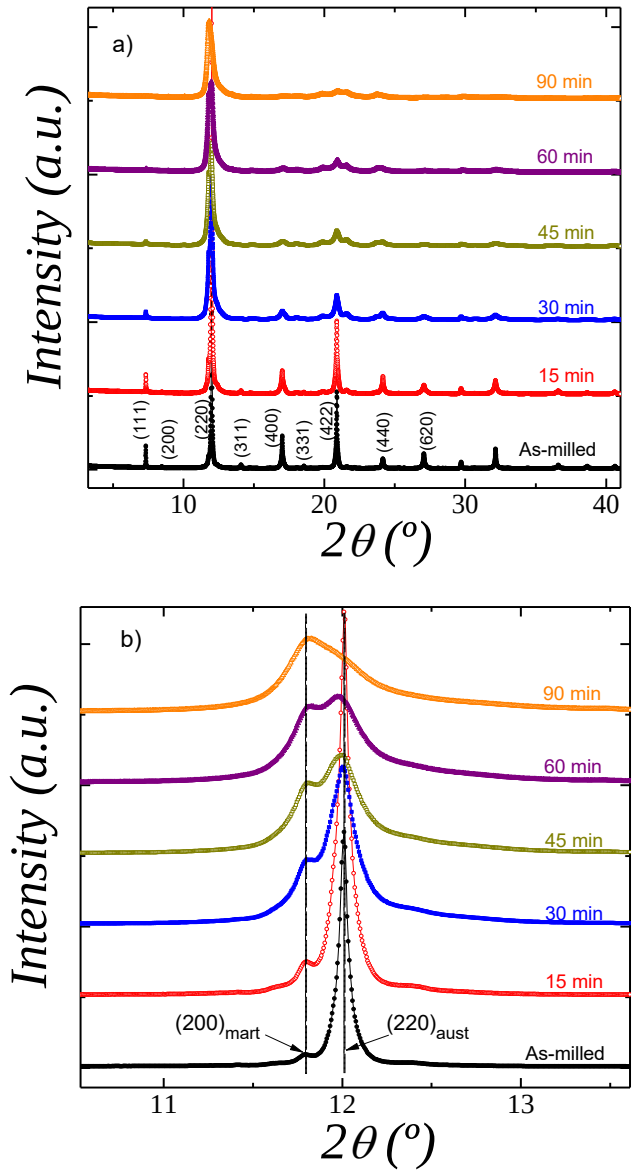

Figure 4. 16. (a) X-ray diffractograms at room temperature for the samples studied in this section. (b) Detail of the region around the most intense reflection of the austenite phase (2 2 0) showing the appearance of a peak corresponding to martensite phase.

Figure 4. 17 shows the evolution of the microstructure parameters as grain size and internal strains obtained by Lebail fit in the set of samples, in the same way as it was done in Chapter 3. In the as-milled alloy the values of the grain size and internal strains are 236.74 (2) Å and 0.31 (2) ‰ respectively. As the milling time is increased, the values of the grain size decrease

down to 65.4 (1) Å in the case of the alloy milled during 90 minutes, which is accompanied by an increase on the strains, reaching values of 10.86 (3) ‰.

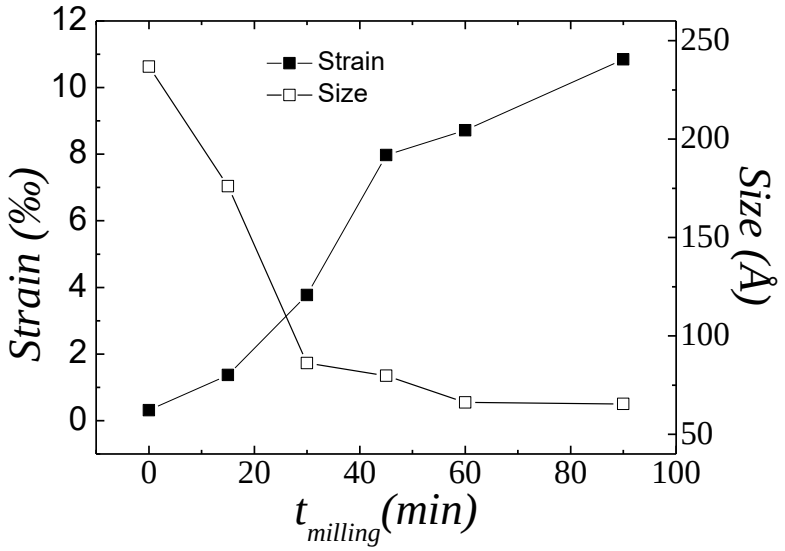

Figure 4. 17. Evolution of microstrains and grain size with milling time.

Additionally, as the Figure 4. 16.b shows, the intensity of a secondary peak at $2\theta \sim 11.8^{\circ}$, and the decrement of (220) peak with the milling time indicate the induction of a secondary martensitic phase that can be indexed as monoclinic structure with space group *I2/m*. On the other hand, the increase in the width of the peaks, together with the reduction of number of reflections noticeable in the diffraction patterns indicate that the samples undergo an amorphization process upon milling. In order to evaluate the amount of amorphous phase from the diffraction data, this phase was modelled as an A2 phase with space group $Im\bar{3}m$, which is the most atomic disordered structure found in this type of alloys [39–41], with all the elements present in the alloy sharing the 2*a* (0,0,0) atomic position. In this way, the powder diffraction patterns have been refined combining three phases: austenite ($L2_1$, $Fm\bar{3}m$), the induced martensite (*I2/m*) and the amorphous-like disordered phase (A2, $Im\bar{3}m$), and the percentage of each phase was obtained for all the samples studied. Figure 4.18 shows the evolution of the mentioned phases with the milling time, showing that, as the milling time increases, both the martensite and the amorphous-like phases increase in decrement of $L2_1$ phase, being the martensite almost constant for milling times higher than 60 minutes and reaching 54% of amorphous state after 90 minutes of milling.

Figure 4. 19 shows the relation between the amorphous-like phase fraction and the internal strains induced by milling, which shows a linear behavior. Therefore, the milling process not only produces an increase of the strains encompassing a reduction of the grain size and a degradation of the MT due to the presence of defects, but also an amorphization process.

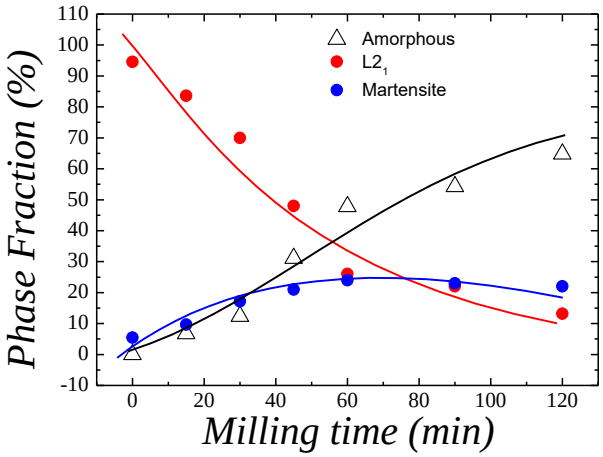

Figure 4. 18. Evolution of phase fractions of austenite, induced martensite and amorphous phase with milling time.

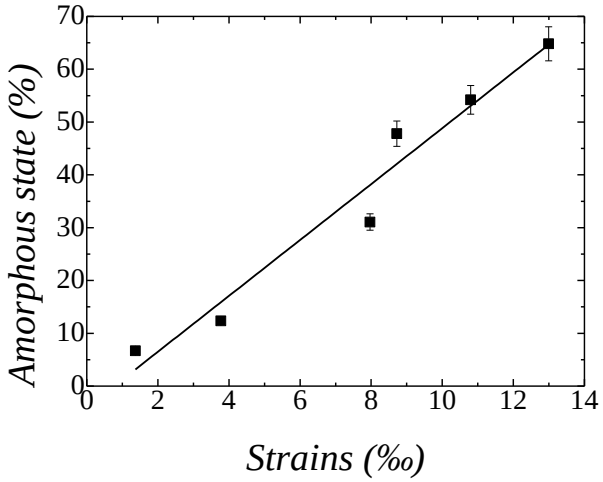

Figure 4. 19. Dependence of amorphous phase fraction with the internal strains.

4.2.4.4. Magnetic properties

Magnetic measurements have been carried out to establish the relation between the microstructural state and the magnetic behavior. Figure 4.20.a shows the thermo-magnetization curves at an applied magnetic field of 100 Oe. The T_C in austenite phase, indicated by a drastic jump of the magnetization, is observed in all the samples at the same temperature (ca. 365 K). In concordance with the results obtained by calorimetric measurements, a drop in the magnetization at lower temperatures, indicates the presence of the MT, which takes place from a ferromagnetic austenite phase to a martensite phase with lower magnetization. This drop in the magnetization also appears at the same temperatures in all the samples, around 150 K for the reverse MT. The fact that all samples present the same T_C and MT temperatures confirms the null variation in the atomic order by high-energy ball milling. However, the mechanical treatment produces a remarkable decrease of the magnetization change associated to the MT. The variation in the magnetization at the MT is better evaluated at higher magnetic fields. Figure 4. 20.b shows the thermo-magnetization curves at 60 kOe. The temperatures of the MT change with respect to the measurements at 100 Oe due to the shift of the MT to lower

temperatures under an applied magnetic field. Concerning the effect of mechanical treatment in the present case, the measurements at high magnetic fields confirm that the induction of defects and the variation of the microstructure by milling promote the degradation of the MT and consequently the reduction of the variation in the magnetization linked to the transformation.

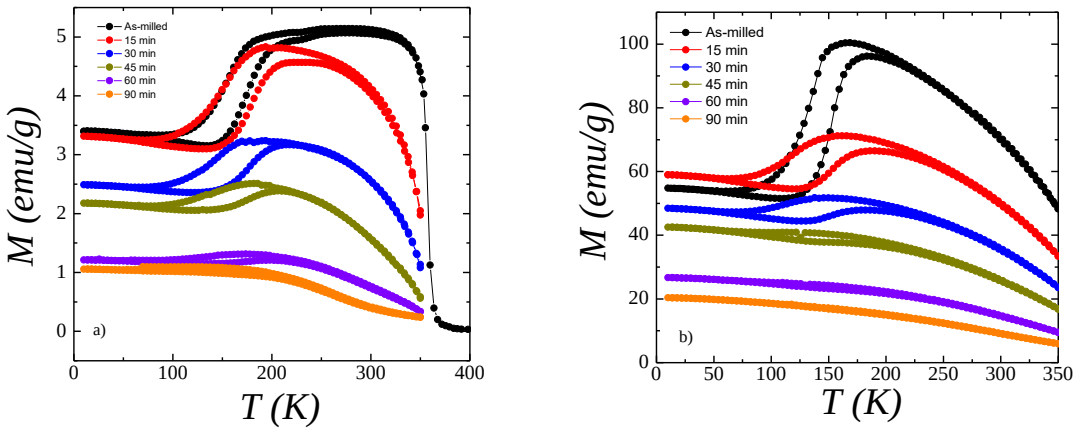

Figure 4. 20. Thermomagnetization at a) 100 Oe and b) 60 kOe in the set of samples.

The magnetization versus applied field was measured in both phases in order to correlate the results with the microstructural state. Figure 4. 21 shows the magnetization curves at constant temperatures of 10 K and 300 K corresponding to ferromagnetic order in martensite and austenite, respectively, and Figure 4. 22 shows the evolution of the saturation magnetization with the milling time. Due to the increase of the density of defects, the amorphization process and the induction of martensite by mechanical treatment, a decrease in the saturation magnetization is produced in both phases. The magnetic coupling between Mn atoms is affected by the mechanical treatment, and the induction of a paramagnetic amorphous state in decrement of crystalline structures degrades the magnetism on the alloy.

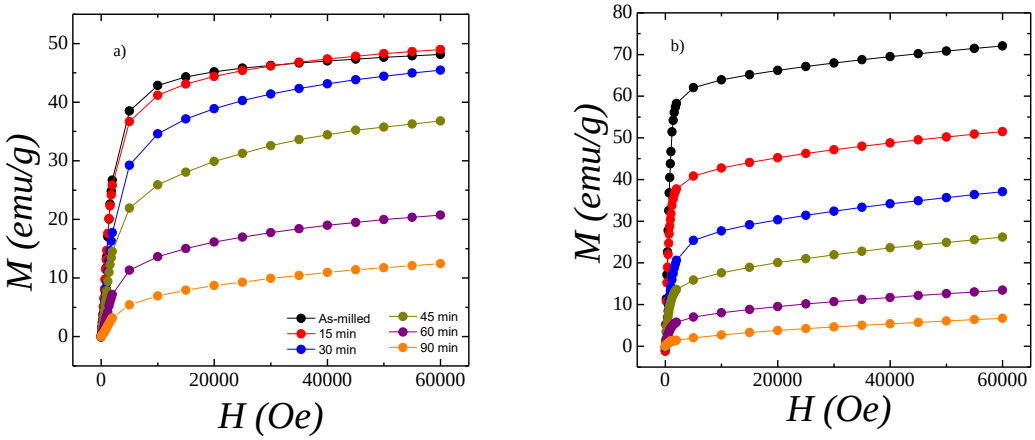

Figure 4. 21. Magnetization dependence of applied magnetic field in the set of samples in: a) martensite at 10 K and b) austenite at 300 K.

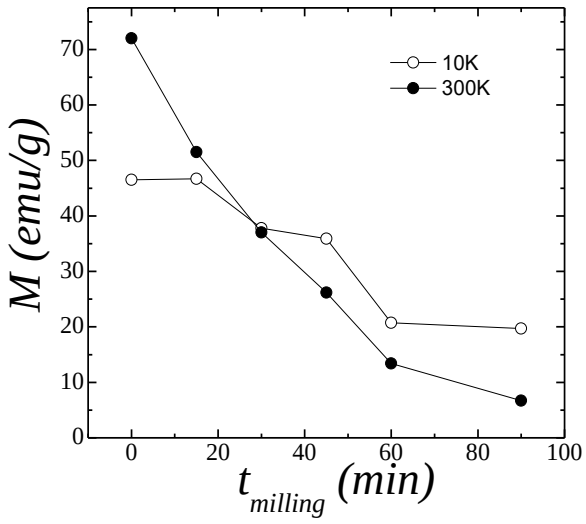

Figure 4. 22. Evolution of magnetization at 10K and 300K with the milling time.

4.2.4.5. Magnetic structures analyzed by neutron diffraction

The evolution of the atomic order and the magnetic structures with milling was analyzed by Rietveld refinement of the neutron powder diffraction data obtained in austenite in the samples milled 15, 30, and 45 minutes. Considering only the austenite and the induced martensite phases, the atomic order remains constant independently of the milling time, which is in agreement with the observed behavior in calorimetric and magnetic measurements, where the MT and Curie temperatures remain constant. On the other hand, the magnetic structure in austenite was obtained at 300K (see Figure 4. 23). In the milled samples, ferromagnetic coupling is observed between the magnetic moment of Mn atoms in 4*a* and 4*b* sites. The inclusion of defects by milling and the variation of the microstructural parameters has the effect of reducing the magnetic moment of the Mn atoms, without changing the type of coupling (in contrast with the change observed in the ternary alloy as a consequence of annealing (see Chapter 3).

Figure 4. 24 shows the evolution of the magnetic moments in the different studied alloys. The magnetic moment for the 4*a* sites is reduced by 56% with 45 minutes of milling, evolving from 3.11 μ_B to 1.74 μ_B in the as-milled and 45-minutes milled alloys, respectively. In the case of the 4*b* site, the reduction is of 31%,the magnetic moment changing from 1.14 μ_B to 0.35 μ_B. Therefore, in the Ni-Mn-Sn-Co system, doping with Co favors ferromagnetic coupling in the alloy. All the samples studied show ferromagnetic coupling, in contrast with the ternary alloy, where the as-milled state is characterized by an antiferromagnetic coupling that evolves into ferromagnetic upon annealing. Then, in the Ni-Co-Mn-Sn system, the variation of the microstructure, merely reduces the magnetic moments of the Mn atoms, and consequently the saturation magnetization in the alloy, but does not produce a switch of the type of magnetic coupling.

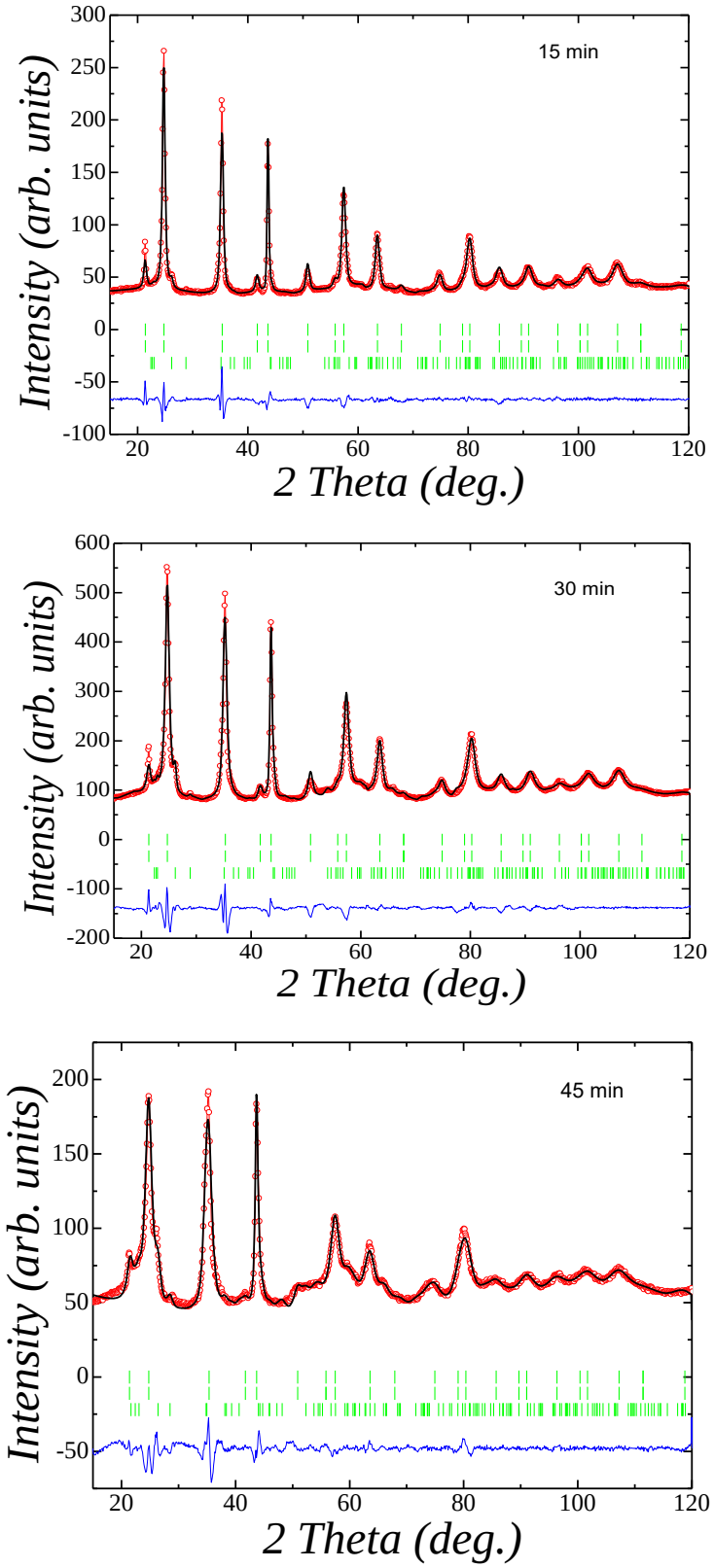

Figure 4. 23. Rietveld refinement at 300K in 15, 30 and 45 minutes milled alloys.

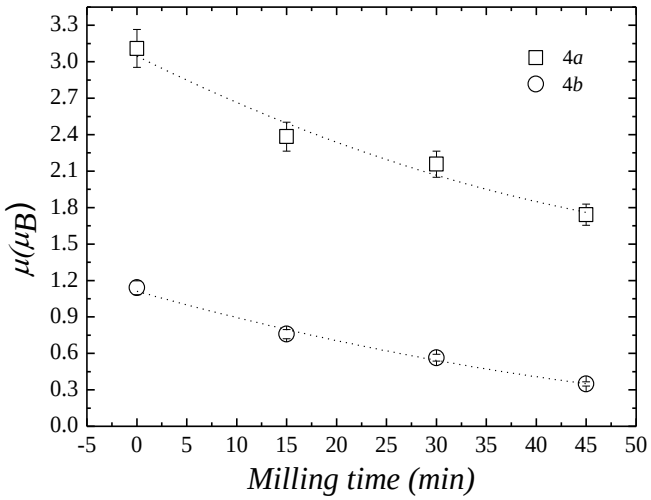

Figure 4. 24. Evolution of the magnetic moments for 4a and 4b sites with the milling time.

4.2.4.6. Magnetocaloric analysis

In order to analyze the magnetocaloric effect associated to these compounds and evaluate the effect of the microstructural changes, two samples were selected to make a comparison: the as-milled alloy and the alloy milled during 15 minutes (since further milling produces excessive degradation of the MT). Figure 4.25 depicts the temperature dependence of the magnetically-induced entropy change under a field of 60 kOe obtained after application of equation 1.11. The difference in the entropy change associated to MT is due to the variation of the microstructural state induced by high-energy ball milling. The higher value of the internal strains and the smaller grain size affect the magnetic coupling between Mn atoms, reducing the variation in the magnetization associated to the MT. Also, the phases induced by milling (martensite and amorphous) imply a reduction of the amount of material undergoing MT.

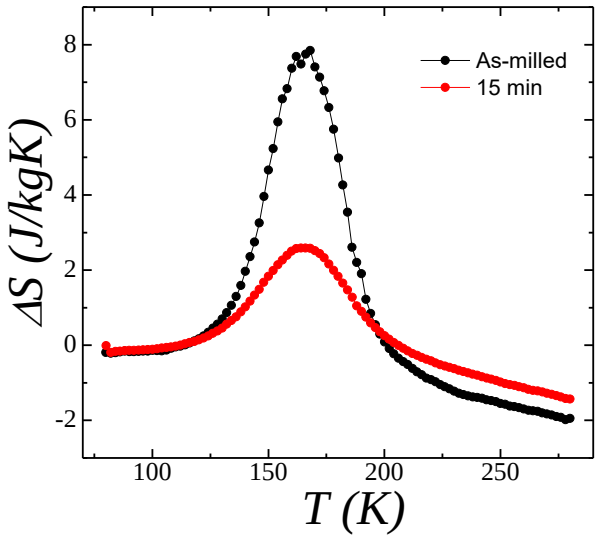

Figure 4. 25. Magnetically-induced entropy change under an applied field of 60kOe, as a function of the temperature, for the as-milled and the 15 minutes ball-milled samples.

4.3. SUMMARY AND CONCLUSIONS

In this chapter, the influence of mechanically-induced defects on the magnetostructural properties was analyzed in a non-stoichiometric $Ni_{45}Co_5Mn_{35}Sn_{15}$ alloy. The first part of the study was centered on the study of the influence of a hand-milling process, a mechanical "soft" method, and subsequent annealing, while the second part deals with the effect of a more severe milling process carried out on by ball-milling at increasing milling times. The first study was performed by combining macroscopic calorimetric and magnetic measurements with powder neutron diffraction. In the second part, synchrotron radiation diffraction was used for the microstructural characterization.

The comparative analysis of neutron powder diffractograms carried out on the as-milled (hand-milled) and annealed samples reveal no changes in the atomic order induced by these treatments and shows a ferromagnetic coupling of Mn atoms in austenite favored by the presence of Co in the Ni positions. Both samples present the same modulated monoclinic crystallographic structure with *P2/m* space group with antiferromagnetic coupling as consequence of the shorter distance between Mn-Mn atoms, although this antiferromagnetic coupling is weaker in the less defective annealed sample. As consequence of the lower magnetization in martensite and the null variation in the magnetization of the austenitic phase, the variation of the magnetization associated to the MT is larger in the as-milled alloy. Thus, the presence of the defects increases the magnetocaloric effect associated to the MT.

After the evidence of the enhancement of the magnetocaloric effect by hand-milling, a systematic ball-milling was performed in the same alloy. By means of calorimetry and magnetometry measurements, the martensitic transformation and Curie temperature were determined, evidencing their null variation with the milling time. The enthalpy values associated to the MT point out that the MT is affected by mechanical treatments and significantly reduced with the milling time. Powder X-ray diffraction has been used to obtain information about the microstructural parameters as grain size and internal strains, showing the evolution of those values, and the induction with the milling time of secondary phases identified as a non-modulated monoclinic martensitic structure (*I2/m*) and an amorphous phase. The amount of amorphous phase induced by milling was estimated. By combination of the magnetic measurements and the microstructural analysis by X-ray diffraction, the amount of the non-magnetic inclusion was quantified an related with the internal strains, showing an increment of a factor of more than 10 by milling, together with an associated reduction of the saturation magnetization. The magnetic structure was obtained by neutron diffraction in the samples milled during 15, 30 and 45 minutes showing the reduction of the magnetic moment when the milling time increases, while keeping ferromagnetic the coupling of the Mn atoms in 4*a* and 4*b* sites.

Magnetocaloric measurements carried out on the as-milled sample and the alloy milled during 15 minutes have revealed the drastic reduction by ball milling of the entropy change associated to the martensitic transformation, which is reduced by 33%.

In conclusion, the evolution of the microstructural parameters has been quantified and correlated to the evolution of the martensitic transformation features and the magnetic

properties. It is found that the inclusion of small amount of defects can improve the magnetocaloric properties on the alloy due to the variation in the magnetism of the martensite. On the other hand, high-energy milling creates a big amount of defects that reduce drastically the saturation magnetization and the variation in the magnetic entropy associated to the martensitic transformation. Additionally, it was found that milling not only produces variations in the microstructure, but also entails the induction of martensite, while keeping the atomic order invariant.

Bibliography

[1] Y. Sutou, Y. Imano, N. Koeda, T. Omori, R. Kainuma, K. Ishida and K. Oikawa, "Magnetic and martensitic transformations of NiMnX(X=In,Sn,Sb) ferromagnetic shape memory alloys," *Appl. Phys. Lett.*, vol. 85, no. 19, pp. 4358–4360, Nov. 2004.

[2] T. Krenke, M. Acet, E. F. Wassermann, X. Moya, L. Manosa, and A. Planes, "Martensitic transitions and the nature of ferromagnetism in the austenitic and martensitic states of Ni-Mn-Sn alloys," *Phys. Rev. B*, vol. 72, no. 1, p. 014412, Jul. 2005.

[3] T. Krenke, M. Acet, E. F. Wassermann, X. Moya, L. Manosa, and A. Planes, "Ferromagnetism in the austenitic and martensitic states of Ni-Mn-In alloys," *Phys. Rev. B*, vol. 73, no. 17, p. 174413, May 2006.

[4] M. Khan, I. Dubenko, S. Stadler, and N. Ali, "Magnetostructural phase transitions in $Ni_{50}Mn_{25+x}Sb_{25-x}$ Heusler alloys," *J. Phys. Condens. Matter*, vol. 20, no. 23, p. 235204, Apr. 2008.

[5] V. Recarte, J. Pérez-Landazábal, V. Sánchez-Alarcos, and J. A. Rodriguez-Velamazán, "Dependence of the martensitic transformation and magnetic transition on the atomic order in Ni–Mn–In metamagnetic shape memory alloys," *Acta Mater.*, vol. 60, pp. 1937–1945, Mar. 2012.

[6] V. Recarte, J. I. Pérez-Landazábal, and V. Sánchez-Alarcos, "Dependence of the relative stability between austenite and martensite phases on the atomic order in a Ni–Mn–In Metamagnetic Shape Memory Alloy," *J. Alloys Compd.*, vol. 536, pp. S308–S311, Sep. 2012.

[7] V. Sánchez-Alarcos, V. Recarte, J. I. Pérez-Landazábal, E. Cesari, and J. A. Rodríguez-Velamazán, "Long-Range Atomic Order and Entropy Change at the Martensitic Transformation in a Ni-Mn-In-Co Metamagnetic Shape Memory Alloy," *Entropy*, vol. 16, no. 5, pp. 2756–2767, May 2014.

[8] V. Sánchez-Alarcos, J. I. Pérez-Landazábal, V. Recarte, I. Lucia, J. Vélez, and J. A. Rodríguez-Velamazán, "Effect of high-temperature quenching on the magnetostructural transformations and the long-range atomic order of Ni–Mn–Sn and Ni–Mn–Sb metamagnetic shape memory alloys," *Acta Mater.*, vol. 61, no. 12, pp. 4676–4682, Jul. 2013.

[9] A. L. Alves, E. C. Passamani, V. P. Nascimento, A. Y. Takeuchi, and C. Larica, "Influence of grain refinement and induced crystal defects on the magnetic properties of Ni 50 Mn 36 Sn 14 Heusler alloy," *J. Phys. Appl. Phys.*, vol. 43, no. 34, p. 345001, 2010.

[10] E. C. Passamani, V.P. Nasimento, C. Larica, A.Y. Takeuchi, A.L. Alves, J.R. Proveri, M.C. Pereira, and J.D. Favris, "The influence of chemical disorder enhancement on the

martensitic transformation of the $Ni_{50}Mn_{36}Sn_{14}$ Heusler-type alloy," *J. Alloys Compd.*, vol. 509, no. 30, pp. 7826–7832, Jul. 2011.

[11] A. Ghotbi Varzaneh, P. Kameli, V. R. Zahedi, F. Karimzadeh, and H. Salamati, "Effect of heat treatment on martensitic transformation of Ni47Mn40Sn13 ferromagnetic shape memory alloy prepared by mechanical alloying," *Met. Mater. Int.*, vol. 21, no. 4, pp. 758–764, Jul. 2015.

[12] P. Czaja, J. Przewoźnik, M. Fitta, M. Bałanda, A. Chrobak, B. Kania, P. Zackiewicz, A. Wójcik, M.Szlezynger, and W. Maziarz, "Effect of ball milling and thermal treatment on exchange bias and magnetocaloric properties of Ni48Mn39.5Sn10.5Al2 ribbons," *J. Magn. Magn. Mater.*, vol. 401, pp. 223–230, Mar. 2016.

[13] X. Wang, F. Sun, J. Wang, Q. Yu, Y. Wu, H. Hua, and C. Jiang, "Influence of annealing temperatures on the magnetostructural transition and magnetocaloric effect of Ni40Co10Mn40Sn10 powders," *J. Alloys Compd.*, vol. 691, pp. 215–219, Jan. 2017.

[14] Y. Murakami, T. Yano, R. Y. Umetsu, R. Kainuma, and D. Shindo, "Suppression of ferromagnetism within antiphase boundaries in $Ni_{50}Mn_{25}Al_{12.5}Ga_{12.5}$ alloy," *Scr. Mater.*, vol. 65, no. 10, pp. 895–898, Nov. 2011.

[15] R. Kainuma, Y. Imano, W. Ito, Y. Sutou, H. Morito, S. Okamoto, O. Kitakami, K. Oikawa, A. Fujita, T. Kanomata, and K. Ishida, "Magnetic-field-induced shape recovery by reverse phase transformation," *Nature*, vol. 439, no. 7079, pp. 957–960, Feb. 2006.

[16] R. Kainuma, Y. Imano, W. Ito, H. Morito, Y. Sutou, K. Oikawa, A. Fujita, K. Ishida, S. Okamoto, O. Kitakami, and T. Kanomata, "Metamagnetic shape memory effect in a Heusler-type $Ni_{43}Co_7Mn_{39}Sn_{11}$ polycrystalline alloy," *Appl. Phys. Lett.*, vol. 88, no. 19, p. 192513, May 2006.

[17] A. K. Nayak, K. G. Suresh, and A. K. Nigam, "Giant inverse magnetocaloric effect near room temperature in Co substituted NiMnSb Heusler alloys," *J. Phys. Appl. Phys.*, vol. 42, no. 3, p. 035009, Jan. 2009.

[18] L. Huang, D. Y. Cong, H. L. Suo, and Y. D. Wang, "Giant magnetic refrigeration capacity near room temperature in $Ni_{40}Co_{10}Mn_{40}Sn_{10}$ multifunctional alloy," *Appl. Phys. Lett.*, vol. 104, no. 13, p. 132407, Mar. 2014.

[19] Umetsu, R. Y, A. Sheikh, B. Ouladdiaf, K. R. A. Ziebeck, T. Kanomata, and R. Kainuma, "The effect of Co substitution on the magnetic properties of the Heusler alloy $Ni_{50}Mn_{33}Sn_{17}$," *Appl. Phys. Lett.*, vol. 98, no. 4, p. 042507, Jan. 2011.

[20] S. Pandey, Z. Quetz, A. Aryal, I. Dubenko, D. Mazumdar, S. Stadler, and N. Ali, "Large Inverse Magnetocaloric Effects and Giant Magnetoresistance in Ni-Mn-Cr-Sn Heusler Alloys," *Magnetochemistry*, vol. 3, no. 1, p. 3, Mar. 2017.

[21] J. Rodríguez-Carvajal, "Recent advances in magnetic structure determination by neutron powder diffraction," *Phys. B Condens. Matter*, vol. 192, no. 1, pp. 55–69, Oct. 1993.

[22] V. Sánchez-Alarcos, V. Recarte, J. I. Pérez-Landazábal, C. Gómez-Polo, and J. A. Rodríguez-Velamazán, "Role of magnetism on the martensitic transformation in Ni–Mn-based magnetic shape memory alloys," *Acta Mater.*, vol. 60, no. 2, pp. 459–468, Jan. 2012.

[23] S. Chikazumi and C. D. Graham, *Physics of Ferromagnetism 2e*. OUP Oxford, 2009.

[24] E. Schlömann, "Properties of Magnetic Materials with a Nonuniform Saturation Magnetization. I. General Theory and Calculation of the Static Magnetization," *J. Appl. Phys.*, vol. 38, no. 13, pp. 5027–5034, Dec. 1967.

[25] H. Zhang, D. Zeng, and Z. Liu, "The law of approach to saturation in ferromagnets originating from the magnetocrystalline anisotropy," *J. Magn. Magn. Mater.*, vol. 322, no. 16, pp. 2375–2380, Aug. 2010.

[26] G. F. Dionne, J. A. Weiss, and G. A. Allen, "Hysteresis loops modeled from coercivity, anisotropy, and microstructure parameters," *J. Appl. Phys.*, vol. 61, pp. 3862–3864, Apr. 1987.

[27] V. Sánchez-Alarcos, J. I. Pérez-Landazábal, and V. Recarte, "Influence of Long-Range Atomic Order on the Structural and Magnetic Properties of Ni-Mn-Ga Ferromagnetic Shape Memory Alloys," *Mater. Sci. Forum*, vol. 684, pp. 85–103, 2011.

[28] L. Tocado, E. Palacios, and R. Burriel, "Entropy determinations and magnetocaloric parameters in systems with first-order transitions: Study of MnAs," *J. Appl. Phys.*, vol. 105, no. 9, p. 093918, May 2009.

[29] L. Huang, D. Y. Cong, L. Ma, Z. H. Nie, M. G. Wamg. Z. L. Wang, H. L. Suo, Y. Ren, Y. D. Wang, "Large magnetic entropy change and magnetoresistance in a $Ni_{41}Co_9Mn_{40}Sn_{10}$ magnetic shape memory alloy," *J. Alloys Compd.*, vol. 647, pp. 1081–1085, Oct. 2015.

[30] T. Krenke, E. Duman, M. Acet, X. Moya, L. Mañosa, and A. Planes, "Inverse magnetocaloric effect in ferromagnetic Ni–Mn–Sn alloys," *Nat. Mater.*, vol. 4, no. 6, pp. 450–454, Jun. 2005.

[31] A. Aryal, A. Quetz, S. Pandey, I. Dubenko, S. Stadler, and N. Ali, "Magnetocaloric effects and transport properties of rare-earth (R= La, Pr, Sm) doped $Ni_{50-x}R_xMn_{35}Sn_{15}$ Heusler alloys," *J. Alloys Compd.*, vol. 717, pp. 254–259, Sep. 2017.

[32] V. Recarte, J. I. Pérez-Landazábal, S. Kustov, and E. Cesari, "Entropy change linked to the magnetic field induced martensitic transformation in a Ni–Mn–In–Co shape memory alloy," *J. Appl. Phys.*, vol. 107, no. 5, p. 053501, Mar. 2010.

[33] M. Forsblom, N. Sandberg, and G. Grimvall , "Vibrational entropy of dislocations in Al," *Philos. Mag.*, vol. 84, no. 6, pp. 521–532, Feb. 2004.

[34] P. C. Schuck, J. Marian, J. B. Adams, and B. Sadigh, "Vibrational properties of straight dislocations in bcc and fcc metals within the harmonic approximation," *Philos. Mag.*, vol. 89, no. 31, pp. 2861–2882, Nov. 2009.

[35] V. R. Manga, S. L. Shang,, W. Y. Wang, Y. Wang, J. Liang, V. H. Crespi, Z. K. Liu, "Anomalous phonon stiffening associated with the (111) antiphase boundary in L12 Ni3Al," *Acta Mater.*, vol. 82, pp. 287–294, Jan. 2015.

[36] A. Planes, L. Mañosa, E. Vives, J. Rodríguez-Carvajal, M. Morin, G. Guenin, and J.L. Macqueron, "Neutron diffraction study of long-range atomic order in Cu-Zn-Al shape memory alloys," *J. Phys. Condens. Matter*, vol. 4, no. 2, p. 553, 1992.

[37] V. Sánchez-Alarcos, V. Recarte, J. I. Pérez-Landazábal, and G. J. Cuello, "Correlation between atomic order and the characteristics of the structural and magnetic transformations in Ni–Mn–Ga shape memory alloys," *Acta Mater.*, vol. 55, no. 11, pp. 3883–3889, Jun. 2007.

[38] V. Sánchez-Alarcos, J. I. Pérez-Landazábal, V. Recarte, J. A. Rodríguez-Velamazán, and V. A. Chernenko, "Effect of atomic order on the martensitic and magnetic transformations in Ni–Mn–Ga ferromagnetic shape memory alloys," *J. Phys. Condens. Matter*, vol. 22, no. 16, p. 166001, 2010.

[39] R. Kainuma, F. Gejima, Y. Sutou, I. Ohnuma, and K. Ishida, "Ordering, Martensitic and Ferromagnetic Transformations in Ni–Al–Mn Heusler Shape Memory Alloys," *Mater. Trans. JIM*, vol. 41, no. 8, pp. 943–949, 2000.

[40] T. Omori, K. Ando, M. Okando, X. Xu, Y. Tanaka, I. Ohnuma, R. Kainuma, K. Ishida, "Superelastic Effect in Polycrystalline Ferrous Alloys," *Science*, vol. 333, no. 6038, pp. 68–71, Jul. 2011.

[41] P. Entel, V. D. Buchelnikov, M. E. Gruner, A. Hucht, V. V. Khovailo, S. K. Nayak, A. T. Zayak, "Shape Memory Alloys: A Summary of Recent Achievements," *Materials Science Forum*, Vol. 583, pp21-41, May 2008.

Chapter 5. Analysis of the improvement of the magnetic properties in Ni-Mn-In alloys by thermal treatment and cobalt doping

5.1. INTRODUCTION

As explained in the general introduction, the so-called metamagnetic shape memory alloys – Ni_2MnX (X=In, Sn, Sb) – present a particularly large variation in the magnetization (ΔM) associated to the MT, which allows inducing the reverse MT with moderate magnetic fields [1–3]. Their applicability in areas like magnetic refrigeration – based on magnetocaloric effect [4–6] – or in sensing – based on giant magnetoresistance [7, 8] – is therefore significantly improved. It appears straightforward that the control of the magneto-structural properties and the comprehensive understanding of the physics of the system is crucial to develop these materials. In this chapter, we focus in the magnetic coupling between magnetic atoms in the different crystallographic sites in the austenite phase, and how this coupling can be modified to produce improved magnetic properties.

As a reminder, in magnetic SMAs the magnetic moments are mainly confined to the Mn atoms, which are not nearest neighbors, the indirect exchange interactions being strongly dependent on the interatomic distances [9, 10]. In ordered stoichiometric $Ni_{50}Mn_{25}X_{25}$ all the Mn atoms locate in the 4*a* sites of the austenite, with the moments aligned parallel. In off-stoichiometry compositions and/or disordered structures, the ferromagnetic coupling is in principle reduced by the presence of Mn moments at 4*b* sites that tend to couple antiferromagnetically. As regards the martensitic phase, the change of the interatomic distances occurring in the MT gives rise to a magnetic phase showing different behaviors ranging from weak ferromagnetism to antiferromagnetism or superparamagnetism and spin-glass-like behavior [11–14].

Composition and atomic order are therefore key parameters that govern the magnetostructural properties of these systems. In particular, Co doping in Ni-Mn-In and Ni-Mn-Sn metamagnetic SMAs has been shown to increase both the Curie temperature (T_C) and the spontaneous magnetization of the austenite by the enhancement of the ferromagnetic coupling [11, 15] while hindering the ferromagnetic ordering in martensite, thus leading to an increase of the change ΔM at the MT and consequently improving the magnetic properties relevant for applications [1, 13, 16, 17]. On the other hand, the Curie and MT temperatures, as well as the spontaneous magnetization, are particularly sensitive to the long-range atomic order,

[18–21] thermal treatments being one of the most direct ways to tune such a parameter. We have selected the $Ni_{50}Mn_{34}In_{16}$ and $Ni_{45}Co_5Mn_{37}In_{13}$ alloys in two different states induced by thermal treatments (water quenching, WQ, and slow cooling, SC) to study in detail the effect of cobalt doping and atomic order in the magnetic properties of these metamagnetic SMAs in terms of the magnetic coupling between the different magnetic moments. These alloys have been chosen by balancing compositional similarity, transforming character (occurrence of MT), and available temperature range in both paramagnetic and ferromagnetic austenitic phases. Besides, both specific compositions have been extensively studied in the literature. Following the characterization of the macroscopic magnetic behavior by magnetometry measurements, we have employed neutron powder diffraction and single-crystal polarized neutron diffraction to study in detail the atomic order and magnetic structures in the austenitic phases of the alloys. Atomically-ordered and, particularly, cobalt-doped samples show an increase of the ferromagnetic coupling between the magnetic moments located in 4*a* and 4*b* sites, which explains the increase of the magnetization. We have delved into this point by means of polarized neutron diffraction on a single-crystal of atomically-ordered $Ni_{45}Co_5Mn_{37}In_{13}$ alloy, a technique that allows studying in detail the coupling between magnetic moments [22] and obtaining spin density maps that reveal the magnetic interaction pathways responsible for this coupling scheme.

5.2. EXPERIMENTAL RESULTS

The $Ni_{50}Mn_{36}In_{14}$ and $Ni_{45}Co_5Mn_{37}In_{13}$ alloys were synthetized from high purity elements by arc-melting under protective argon atmosphere. The obtained bulks were remelted several times and homogenized at 1173K during 24h and quenched in ice water or slow cooled in order to induce different atomic order degrees. A single crystal of slow-cooled $Ni_{45}Co_5Mn_{37}In_{13}$ alloy, grown by the Bridgman method and cut into a small cube of 3x3x3mm was used for the single-crystal neutron diffraction experiments. The macroscopic magnetic characterization of the alloys was performed by recording thermomagnetization curves at 100Oe and the magnetization dependence with the magnetic field at constant temperature. All the neutron scattering experiments were carried out at Institut Laue-Langevin, in Grenoble, France. Nuclear and magnetic structures were analyzed by powder neutron diffraction, using data collected in D1A (λ=1.9Å), D1B (λ=1.28Å and 2.52Å) and D2B (λ=1.59Å) instruments (D2B data were used in the final refinements). Additionally, single-crystal neutron diffraction data were taken in D9 (λ=0.8Å and 0.5Å) instrument for the quaternary SC alloy and combined with powder diffraction data to improve the reliability of the atomic order analysis results. The polarized neutron single-crystal diffraction experiment was carried out in D3 (λ=0.8Å) instrument with an applied magnetic field of 8T along the *c*-axis. As for all the diffraction work in this thesis, the data treatment was carried out using the programs of the Fullprof Suite [23]. The maximum entropy method [24], as implemented in Dysnomia program [25], was used to obtain spin density maps from the polarized neutron diffraction data.

5.2.1. Macroscopic magnetic characterization

Figure 5. 1 and Figure 5. 2 show the magnetic measurements. The temperatures associated to the MT and magnetic ordering have been determined from the temperature

dependence of the magnetization (Figure 5. 1). The values of the critical temperatures are summarized in Table *5. I.* On cooling from ca. 380 K, a second order transition takes place, characterized by a significant increase of the magnetization of the alloy and indicating the onset of the magnetic ordering of the austenitic phase (T_C). On further cooling, an abrupt decrease in the magnetization reveals the occurrence of the MT, the first order character of this transition being confirmed by the hysteresis observed on warming. Finally, at lower temperatures, changes in the magnetic signal indicate different magnetic transitions in the martensite depending on the composition and order degree. The comparison of the curves of the four different samples (Figure 5. 1) reveals the effects of thermal treatment and Co doping. Regarding the transition temperatures, Co-doping produces increments in both the T_C and the MT. For the quenched alloys, the increase is ca. 60 K in the T_C and ca. 80 K in the MT, while for the slow-cooled samples the increments are of ca. 85 K and ca. 40 K for the T_C and the MT, respectively. On the other hand, the thermal treatment produces a displacement of the MT to lower temperatures (ca. 40 K and ca. 75 K for the ternary and quaternary alloys, respectively) and an increase of the T_C (ca. 10K and ca. 35 K for the ternary and quaternary alloys, respectively), when comparing SC with WQ samples.

Once the critical temperatures determined, the magnetization dependence with the applied magnetic field, M(H), was measured for all samples at similar reduced temperatures ($T/Tc \approx 0.8$) to allow comparison, that is, ca. 265 K and 310 K for the ternary and quaternary alloys, respectively. Figure 5. 2 shows the M(H) curves. Co-doping gives the most pronounced effect in ΔM at low fields, due to the substantial increase produced in the magnetization of the austenite phase (Figure 5. 1). If we consider the saturation magnetization (Figure 5. 2), atomic ordering (slow cooling treatment) and Co-doping are shown to produce a similar increase of ca. 35 % with respect to the ternary WQ alloy, with the increment reaching ca. 60 % by the combination of both in the SC quaternary alloy. This behavior is in concordance with previous works. [13, 15, 20, 26]

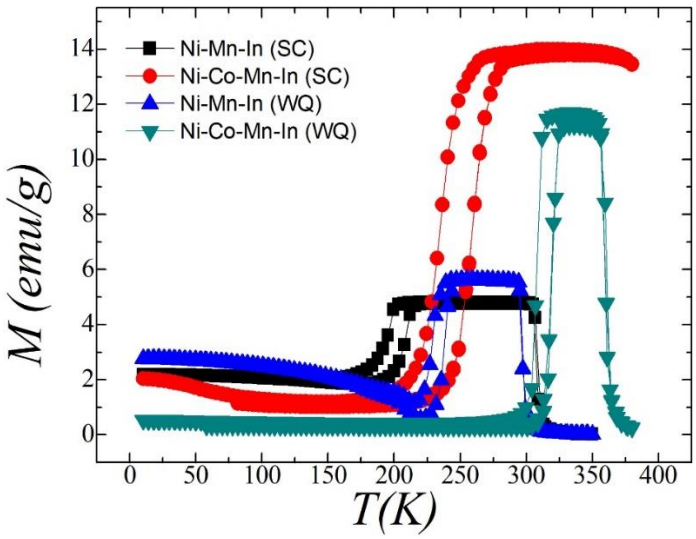

Figure 5. 1.Thermomagnetization curves at 100Oe applied magnetic field for the set of samples.

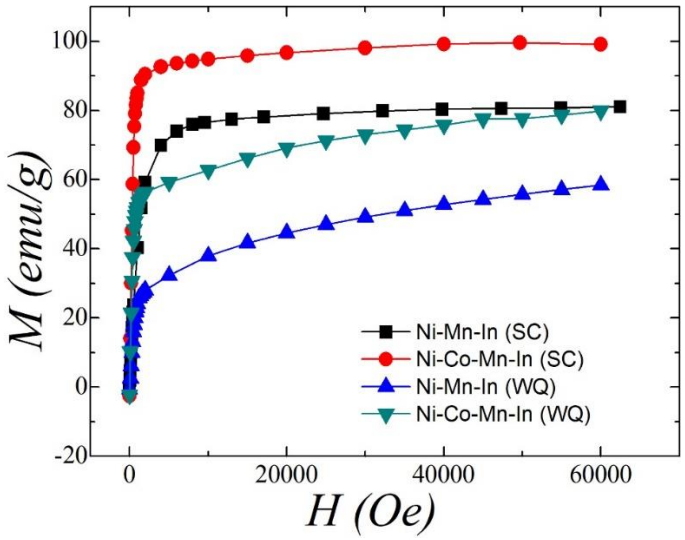

Figure 5. 2. Magnetization dependence with applied magnetic field for the set of samples in austenitic ferromagnetic state.

Table 5. I. Transition temperatures of the studied samples obtained by magnetic meauserements.

Sample	Martensitic transformation (K)	T_C(K)
Ni-Mn-In- WQ	227	298
Ni-Mn-In SC	190	309
Ni-Mn-In-Co- WQ	305	360
Ni-Mn-In-Co- SC	232	395*

* Estimated from the values given in ref. [27]

5.2.2. Microscopic insight: Neutron diffraction

In order to provide in-depth physical insight into the reasons behind the changes of the magnetization, neutron diffraction experiments were performed. We have employed powder and single-crystal neutron diffraction to analyze in detail the atomic order of the selected alloys. The magnetic structures in the ferromagnetic austenite phase have been determined from unpolarized neutron powder diffraction, and we have furthered the understanding of the magnetic coupling by means of polarized neutron diffraction on a single-crystal of atomically-ordered $Ni_{45}Co_5Mn_{37}In_{13}$ alloy.

5.2.2.1. Atomic order

To study the long-range atomic order of the different samples, a powder diffractogram was recorded for each alloy in paramagnetic austenitic phase and analyzed by Rietveld refinement. In the case of the quaternary SC alloy, powder and single crystal data have been combined, improving the reliability of the analysis. The results, in the form of occupancies of the different crystallographic sites, are summarized in Table 5. II.

The data obtained correspond to the Heusler $L2_1$ structure with space group $F\,m\bar{3}m$. The occupancies have been determined assuming as starting point an ordered system. Then, using soft restraints according to the composition of the alloys to reduce the number of free parameters and taking advantage of the negative scattering factor of Mn, the different species were allowed in all crystallographic sites. Since for some of the species the refined occupancy recurrently gave negative or close-to-zero values, these were fixed to zero. The refined occupancies show how the atomic order increases in SC alloys with respect to WQ ones. In the SC samples, a maximum atomic order is obtained, with the Mn atoms fully occupying the 4*a* sites (only a small amount of 2% of In is refined in this position) and practically all the available In and Ni atoms located in the 4*b* and 8*c* sites, respectively. The Mn atoms in excess with respect to the stoichiometric composition complete the occupancy of the 4*b* sites, while in the quaternary alloy the Co atoms complete the occupancy of the 8*c* site, which is not fully occupied by Ni since the composition of this alloy is defective in Ni with respect to the stoichiometric one. The atomic disorder in the ternary quenched alloy is driven by Ni atoms that are present in all sites, letting space for In in 8*c* site, with some Mn migrating from 4*a* to 4*b* position to complete the occupancy of this last one. In the quaternary WQ alloy, Mn fully occupies the 4*a* sites and the excess of this element locates in the 4*b* site. In turn, a certain amount of In and, to a lesser extent, Co, moves from its corresponding site, being both present in the 4*b* and 8*c* sites.

Table 5. II. Occupancies obtained by neutron diffraction in paramagnetic state.

Alloy	Occupancy		
	4*a*	4*b*	8*c*
Ni-Mn-In WQ	0.94(1)Mn 0.06(1)Ni	0.41(2)Mn 0.47(2)In 0.09(1)Ni	0.88(5)Ni 0.12(5)In
Ni-Mn-In SC	0.98(2)Mn 0.02(2)In	0.38(1)Mn 0.62(1)In	1.00(5)Ni
Ni-Co-Mn-In WQ	1.00(2)Mn	0.57(1)Mn 0.41(1)In 0.02(2)Co	0.88(2)Ni 0.09(6) Co 0.03(4) In
Ni-Co-Mn-In SC	0.969(5)Mn 0.020(6)In	0.484(5)Mn 0.503(4)In	0.898(8)Ni 0.094(8)Co

5.2.2.2. Magnetic structures

The diffractograms recorded in the ferromagnetic austenite phase in both SC and WQ conditions for the determination of the magnetic structure were measured (as for the M(H) curves) at similar reduced temperatures, T/Tc ≈ 0.8, to facilitate the comparison, that is, ca. 245 K and 310 K for the ternary and quaternary alloys, respectively. The magnetic intensity in the diffraction pattern is revealed at low angle. The patterns in ferromagnetic phase show an increase of the intensity of some nuclear peaks (namely the (2 0 0) and the (1 1 1) reflections) due to a magnetic ordering with a propagation vector $\boldsymbol{k}$=0. This magnetic intensity (see insets in Figure 5. 3) gives a first indication about the magnetic coupling, since the magnetic intensity ratio between the (2 0 0) and the (1 1 1) reflections should increase as the coupling between the atoms in 4*a* and 4*b* sites becomes more ferromagnetic. In line with the magnetometry results, Co-doping produces a noticeable increase of the ferromagnetic coupling.

In order to avoid correlations of the magnetic structure analysis with other parameters, we have carefully extracted the magnetic intensity by subtraction of the data taken in the paramagnetic phase. The magnetic integrated intensities have been used to obtain the magnetic moments by the simulated annealing method, [28, 29] and then these values have been applied in the Rietveld fit of the diffraction patterns of the ferromagnetic phase, together with the site occupancies determined in the paramagnetic phase. In order to reduce the number of free parameters, the magnetic moments in the 8*c* site have been fixed to the values corresponding to Ni and Co atoms carrying a moment of 0.2 and 1.0 μ_B respectively, in accordance with theoretical calculations [30] and with previous neutron diffraction studies [15]. The ferromagnetic patterns refined with the magnetic contributions are shown in Figure 5. 3.

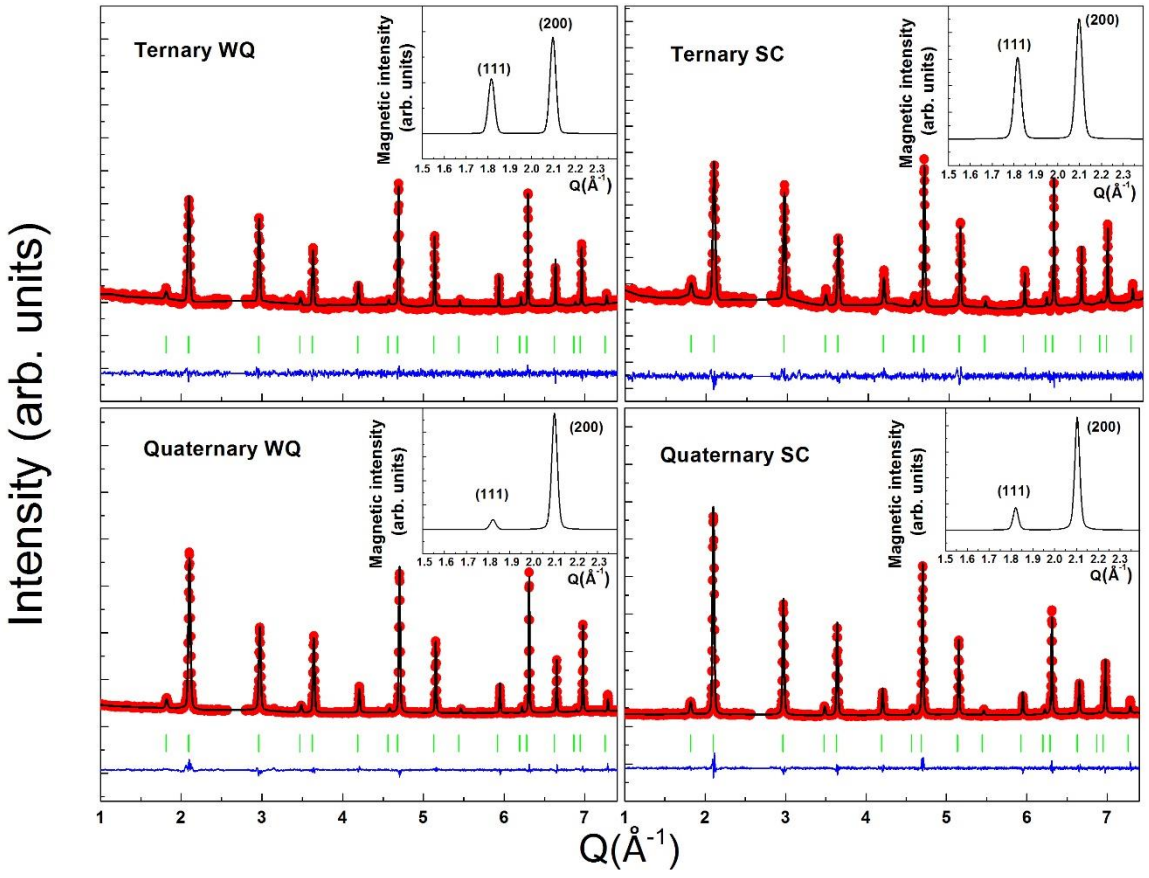

Figure 5. 3. Powder neutron diffraction patterns on ferromagnetic state of austenitic phase of $Ni_{50}Mn_{36}In_{14}$ and $Ni_{45}Co_5Mn_{37}In_{13}$ with different thermal treatments, where the red dots, the black and blue lines are the observed calculated and difference between the observed and calculated patterns, respectively; the green marks are the Bragg reflections. Contamination from aluminum of the sample environment around 2.7 Å-1 has been removed from the diffractograms. The insets represent the magnetic intensities for the (111) and (200) reflections.

Most of the magnetic moment is carried by Mn atoms. The values of the magnetic moments vary with the position where the Mn atoms are located, approaching to $2\mu_B$ and $1\mu_B$

in the 4*a* and 4*b* octahedral sites, respectively. Similar results were reported previously by Brown et al. for the ternary $Ni_{46}Mn_{41}In_{13}$ alloy [31]. Although the absolute values of the magnetic moments can be affected by the weak magnetic signal compared to the total intensity and the large error bars, several conclusions may be drawn by the relative values. In the ternary alloys, the overall magnetic coupling between 4*a* and 4*b* sites is ferromagnetic, but with relatively lower values of the magnetic moment in the 4*b* position with respect to the quaternary alloys. The lower values are observed in the WQ specimen due to the atomic disorder induced by the quenching process and the presence of defects, which are reduced by the slow cooling treatment. Therefore, the total magnetic moment increases in the SC alloy, with a marked increase in the 4*a* site and the coupling of the moment in the 4*b* becoming slightly more ferromagnetic. The reduced presence of Mn moments at 4*b* sites, which tend to couple antiferromagnetically, [15] appears as a possible cause for the enhancement of the ferromagnetic coupling. Additionally, the thermal relaxation reduces the strain and the antiphase boundaries in the sample and, as a consequence, favors the ferromagnetic coupling. [32]

However, the most pronounced effect in the coupling between 4*a* and 4*b* sites is that of Co-doping, with values of the magnetic moment in the 4*b* sites markedly higher despite the higher amount of Mn atoms in these sites with respect to the ternary alloy. In a similar way, in the NiMnSn system [15], it has been observed that Co-doping produces a substantial increase of the ferromagnetic coupling, involving even a switch of the coupling between sites 4*a* and 4*b* from antiferromagnetic to ferromagnetic. Finally, both effects add up in the ordered quaternary alloy when Co-doping is combined with the slow cooling thermal treatment, resulting in enhanced magnetic moments with stronger ferromagnetic coupling and giving a total increase of the total ordered magnetic moment reaching ca. 60 % with respect to the ternary disordered alloy (in concordance with the results obtained by macroscopic magnetization measurements). The magnetic moments for each crystallographic position and sample are summarized in Table 5. III.

Table 5. III. Magnetic moments obtained by neutron powder diffraction. Calculated total magnetic moment obtained from neutron diffraction (m_{tot}) and macroscopic magnetization at 60kOe (m_{60kOe}) measured in the ferromagnetic austenitic phase.

Sample	**Magnetic moment (μ_B)**			**Magnetic moment ($\mu_B/f.u.$)**	
	4*a*	4*b*	8*c**	m_{tot}	m_{60kOe}
Ternary WQ	1.76 (10)	0.65 (15)	0.176	2.76 (25)	2.78
Ternary SC	2.18 (17)	0.71(16)	0.200	3.29 (33)	3.74
Quaternary WQ	1.63 (13)	1.16 (23)	0.268	3.33 (36)	3.70
Quaternary SC	2.06 (12)	1.20 (19)	0.274	3.81 (31)	4.44

*Magnetic moments for Ni and Co atoms are fixed to 0.2 and 1.0μ_B respectively.

5.2.2.3. Polarized neutron diffraction

Polarized neutron diffraction is a powerful technique for analyzing magnetic structures and magnetic interaction pathways that has been previously used with success in the study of magnetic shape memory alloys [22]. In order to gain more insight into the magnetic structure and magnetic coupling, we have employed this technique in the analysis of a single crystal of the quaternary SC alloy. The obtained spin density maps show the magnetic moments in all sites with parallel polarization and therefore with ferromagnetic coupling, in agreement with the unpolarized neutron diffraction results explained before. From the observation of the spin density distribution between sites, it is possible to deduce that the stronger interaction takes place between 4*a* and 4*b* sites, corresponding to a distance of $a/2$ in the $L2_1$ cubic structure, followed in intensity by the interaction 4*a*-4*a* or 4*b*-4*b* sites, corresponding to a distance $a/\sqrt{2}$. According to these maps, the interaction of the 8*c* with the 4*a* and 4*b* ones, with distance $\sqrt{3}/4$, should be very weak, but of great importance since the replacement of Ni by Co, occurring mainly in the 8*c* position, has been seen to produce a significant increase in the ferromagnetic coupling. Observing the Bethe-Slater curve, that qualitatively describes the variation in the intensity of the exchange coupling as a function of the ratio of the interatomic distance to the radius of the 3d electron shell, [33] one can understand this behavior. As Co has a bigger 3d electron shell radius than Ni, the strength of the ferromagnetic interaction increases. The introduction of Co, that mainly shares the 8*c* site with Ni atoms, produces an increment on the ferromagnetic interactions, and since the magnetic moments in 8*c* positions have ferromagnetic coupling with its nearest neighbors in 4*a* and 4*b* sites, which in turn are coupled by strong interactions, this favors the ferromagnetic coupling of the Mn atoms. Figure 5. 4 shows the spin density map obtained by maximum entropy method.

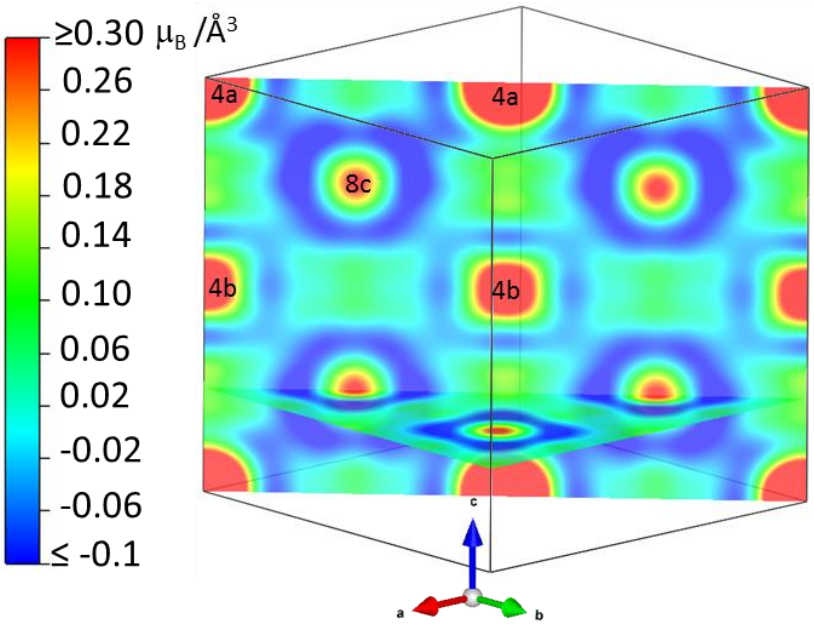

Figure 5. 4. Spin density map obtained by maximum entropy method in (110) and (001) planes for $Ni_{45}Co_5Mn_{37}In_{13}$ single crystal measured in paramagnetic austenite phase.

5.3. SUMMARY AND CONCLUSIONS

In this chapter, the macroscopic magnetic properties, together with the atomic order and magnetic structure in austenitic phase were analyzed in non-stoichiometric $Ni_{50}Mn_{36}In_{14}$ and $Ni_{45}Co_5Mn_{37}In_{13}$ alloys with two different thermal treatments, namely water quenching and slow cooling. The study was performed by means of macroscopic magnetometry measurements, unpolarized powder and single-crystal neutron diffraction and polarized single-crystal neutron diffraction.

Thermomagnetization curves reveal the variation in the Curie and martensitic transformation temperatures due to the different thermal treatment and Co doping. Thermal treatment by slow cooling produces a shift to higher temperatures in T_C with respect to WQ samples, while the martensitic transformation moves to lower temperatures. On the other hand, Co-doping produces an increment in both transition temperatures. Both slow cooling thermal treatment and Co-doping produce an increase in the saturation magnetization of the austenite phase, reaching ca. 60% of increase when both methods are combined.

Neutron diffraction has been used to investigate the microscopic origin of these effects by analyzing the atomic order and magnetic arrangement in the austenite phase. The higher degree of atomic order, together with the reduction of strains and defects induced by slow cooling thermal treatments produces an increase in the total ordered magnetic moment and a slight enhancement of the ferromagnetic coupling between the magnetic moments located in octahedral sites, while cobalt doping has a stronger effect in increasing the ferromagnetic coupling, which explains the noticeable effect in the magnetization.

The spin density maps obtained from polarized neutron diffraction reveal the magnetic interactions responsible for this coupling scheme. Despite the weak interaction of the moments in 8*c* sites with the rest of the magnetic moments, Co, that mainly replace Ni in 8*c* positions, tends to couple ferromagnetically with its nearest neighbors in 4*a* and 4*b* sites, where the magnetic atoms are mainly Mn, which in turn are coupled by strong interactions, favoring the overall ferromagnetic coupling.

Bibliography.

[1] R. Kainuma, Y. Imano, W. Ito, Y. Sutou, H. Morito, S. Okamoto, O. Kitakami, K. Oikawa, A. Fujita, T. Kanomata, and K. Ishida, "Magnetic-field-induced shape recovery by reverse phase transformation," *Nature*, vol. 439, no. 7079, pp. 957–960, Feb. 2006.

[2] K. Koyama, K. Watanabe, T. Kanomata, R. Kainuma, K. Oikawa, and K. Ishida, "Observation of field-induced reverse transformation in ferromagnetic shape memory alloy Ni50Mn36Sn14," *Appl. Phys. Lett.*, vol. 88, no. 13, p. 132505, Mar. 2006.

[3] K. Oikawa, W. Ito, Y. Imano, Y. Sutou, R. Kainuma, K. Ishida, S. Okamoto, O. Kitakami, and T. Kanomata, "Effect of magnetic field on martensitic transition of $Ni_{46}Mn_{41}In_{13}$ Heusler alloy," *Appl. Phys. Lett.*, vol. 88, no. 12, p. 122507, Mar. 2006.

[4] A. Planes, L. Mañosa, and M. Acet, "Magnetocaloric effect and its relation to shape-memory properties in ferromagnetic Heusler alloys," *J. Phys. Condens. Matter*, vol. 21, no. 23, p. 233201, 2009.

[5] J. Liu, T. Gottschall, K. P. Skokov, J. D. Moore, and O. Gutfleisch, "Giant magnetocaloric effect driven by structural transitions," *Nat. Mater.*, vol. 11, no. 7, pp. 620–626, Jul. 2012.

[6] J. I. Perez-Landazabal, V. Recarte, V. Sanchez-Alarcos, J.J. Beato-Lopez, J.A. Rodríguez-Velamazán, J. Sánchez-Marcos, C. Gómez-Polo, and E. Cesari, "Giant direct and inverse magnetocaloric effect linked to the same forward martensitic transformation," *Sci. Rep.*, vol. 7, p. 13328, Oct. 2017.

[7] Z. Li, W. Hu, F. Chen, M. Zhang, Z. Li, B. Yang, X. Zhao, L. Zuo, "Large magnetoresistance in a directionally solidified $Ni_{44.5}Co_{5.1}Mn_{37.1}In_{13.3}$ magnetic shape memory alloy," *J. Magn. Magn. Mater.*, vol. 452, pp. 249–252, Apr. 2018.

[8] S. Pandey, Z. Quetz, A. Aryal, I. Dubenko, D. Mazumdar, S. Stadler, and N. Ali, "Large Inverse Magnetocaloric Effects and Giant Magnetoresistance in Ni-Mn-Cr-Sn Heusler Alloys," *Magnetochemistry*, vol. 3, no. 1, p. 3, Mar. 2017.

[9] E. Şaşıoğlu, L. M. Sandratskii, and P. Bruno, "First-principles calculation of the intersublattice exchange interactions and Curie temperatures of the full Heusler alloys Ni_2MnX (X=Ga, In, Sn, Sb)," *Phys. Rev. B*, vol. 70, no. 2, p. 024427, Jul. 2004.

[10] E. Şaşıoğlu, L. M. Sandratskii, and P. Bruno, "Role of conduction electrons in mediating exchange interactions in Mn-based Heusler alloys," *Phys. Rev. B*, vol. 77, no. 6, p. 064417, Feb. 2008.

[11] K. Ollefs, C. Schöppner,I. Titov, R. Meckenstock, F. Wilhelm, A. Rogalev, J. Liu, O. Gutfleisch, M. Farle, H. Wende, and M. Acet, "Magnetic ordering in magnetic shape memory alloy Ni-Mn-In-Co," *Phys. Rev. B*, vol. 92, no. 22, p. 224429, Dec. 2015.

[12] S. Aksoy, M. Acet, P. P. Deen, L. Mañosa, and A. Planes, "Magnetic correlations in martensitic Ni-Mn-based Heusler shape-memory alloys: Neutron polarization analysis," *Phys. Rev. B*, vol. 79, no. 21, p. 212401, Jun. 2009.

[13] R. Kainuma, Y. Imano, W. Ito, H. Morito, Y. Sutou, K. Oikawa, A. Fujita, K. Ishida, S. Okamoto, O. Kitakami, and T. Kanomata, "Metamagnetic shape memory effect in a Heusler-type $Ni_{43}Co_7Mn_{39}Sn_{11}$ polycrystalline alloy," *Appl. Phys. Lett.*, vol. 88, no. 19, p. 192513, May 2006.

[14] J. I. Pérez-Landazábal, V. Recarte, V. Sánchez-Alarcos, C. Gómez-Polo, and E. Cesari, "Magnetic properties of the martensitic phase in Ni-Mn-In-Co metamagnetic shape memory alloys," *Appl. Phys. Lett.*, vol. 102, no. 10, p. 101908, Mar. 2013.

[15] Umetsu, R. Y, A. Sheikh, B. Ouladdiaf, K. R. A. Ziebeck, T. Kanomata, and R. Kainuma, "The effect of Co substitution on the magnetic properties of the Heusler alloy $Ni_{50}Mn_{33}Sn_{17}$," *Appl. Phys. Lett.*, vol. 98, no. 4, p. 042507, Jan. 2011.

[16] V. Recarte, J. I. Pérez-Landazábal, S. Kustov, and E. Cesari, "Entropy change linked to the magnetic field induced martensitic transformation in a Ni–Mn–In–Co shape memory alloy," *J. Appl. Phys.*, vol. 107, no. 5, p. 053501, Mar. 2010.

[17] L. Huang, D. Y. Cong, H. L. Suo, and Y. D. Wang, "Giant magnetic refrigeration capacity near room temperature in $Ni_{40}Co_{10}Mn_{40}Sn_{10}$ multifunctional alloy," *Appl. Phys. Lett.*, vol. 104, no. 13, p. 132407, Mar. 2014.

[18] V. Sánchez-Alarcos, V. Recarte, J. I. Pérez-Landazábal, and G. J. Cuello, "Correlation between atomic order and the characteristics of the structural and magnetic transformations in Ni–Mn–Ga shape memory alloys," *Acta Mater.*, vol. 55, no. 11, pp. 3883–3889, Jun. 2007.

[19] W. Ito, M. Nagasako, R. Y. Umetsu, R. Kainuma, T. Kanomata, and K. Ishida, "Atomic ordering and magnetic properties in the $Ni_{45}Co_5Mn_{36.7}In_{13.3}$ metamagnetic shape memory alloy," *Appl. Phys. Lett.*, vol. 93, no. 23, p. 232503, Dec. 2008.

[20] V. Recarte, J. I. Pérez-Landazábal, and V. Sánchez-Alarcos, "Dependence of the relative stability between austenite and martensite phases on the atomic order in a Ni–Mn–In Metamagnetic Shape Memory Alloy," *J. Alloys Compd.*, vol. 536, pp. S308–S311, Sep. 2012.

[21] S. Kustov, M. L. Corró, J. Pons, and E. Cesari, "Entropy change and effect of magnetic field on martensitic transformation in a metamagnetic Ni–Co–Mn–In shape memory alloy," *Appl. Phys. Lett.*, vol. 94, no. 19, p. 191901, May 2009.

[22] P. Lázpita, J. M. Barandiarán, J. Gutiérrez, C. Mondelli, A. Sozinov, and V. A. Chernenko, "Polarized Neutron Study of Ni-Mn-Ga Alloys: Site-Specific Spin Density Affected by Martensitic Transformation," *Phys. Rev. Lett.*, vol. 119, no. 15, p. 155701, Oct. 2017.

[23] J. Rodríguez-Carvajal, "Recent advances in magnetic structure determination by neutron powder diffraction," *Phys. B Condens. Matter*, vol. 192, no. 1, pp. 55–69, Oct. 1993.

[24] R. J. Papoular and B. Gillon, "Maximum Entropy Reconstruction of Spin Density Maps in Crystals from Polarized Neutron Diffraction Data," *EPL Europhys. Lett.*, vol. 13, no. 5, p. 429, 1990.

[25] K. Momma, T. Ikeda, A. A. Belik, and F. Izumi, "Dysnomia, a computer program for maximum-entropy method (MEM) analysis and its performance in the MEM-based pattern fitting," *Powder Diffr.*, vol. 28, no. 3, pp. 184–193, Sep. 2013.

[26] S. Singh, I. Glavatskyy, and C. Biswas, "The influence of quench atomic disorder on the magnetocaloric properties of Ni–Co–Mn–In alloys," *J. Alloys Compd.*, vol. 601, pp. 108–111, Jul. 2014.

[27] V. Sánchez-Alarcos, V. Recarte, J. I. Pérez-Landazábal, E. Cesari, and J. A. Rodríguez-Velamazán, "Long-Range Atomic Order and Entropy Change at the Martensitic Transformation in a Ni-Mn-In-Co Metamagnetic Shape Memory Alloy," *Entropy*, vol. 16, no. 5, pp. 2756–2767, May 2014.

[28] J. Rodríquez-Carvajal, "Magnetic Structure Determination from Powder Diffraction Symmetry Analysis and Simulated Annealing," *Mater. Sci. Forum*, vol. 378–381, pp. 268–273, Oct. 2001.

[29] S. Kirkpatrick, C. D. Gelatt, and M. P. Vecchi, "Optimization by Simulated Annealing," *Science*, vol. 220, no. 4598, pp. 671–680, May 1983.

[30] Y. Kurtulus, R. Dronskowski, G. D. Samolyuk, and V. P. Antropov, "Electronic structure and magnetic exchange coupling in ferromagnetic full Heusler alloys," *Phys. Rev. B*, vol. 71, no. 1, Jan. 2005.

[31] P. J. Brown, A.P. Gandy, R. Kainuma, T. Kanomata, K. U. Neumann, K. Oikawa, B. Ouladdiaf, A. Sheikh, and K. R. A. Ziebeck, "The field and temperature dependence of the magnetic and structural properties of the shape memory compound $Ni_{1.84}Mn_{1.64}In_{0.52}$," *J. Phys. Condens. Matter*, vol. 23, no. 45, p. 456004, 2011.

[32] I. Unzueta, J. López-García, V. Sánchez-Alarcos, V. Recarte, J.I. Pérez-Landazábal, J.A. Rodríguez-Velamazán, J.S. Garitaonandia, J.A. García, and F. Plazaola, "^{119}Sn Mössbauer spectroscopy for assessing the local stress and defect state towards the tuning of Ni-Mn-Sn alloys," *Appl. Phys. Lett.*, vol. 110, no. 18, p. 181908, May 2017.

[33] S. Chikazumi and C. D. Graham, *Physics of Ferromagnetism 2e*. OUP Oxford, 2009.

Chapter 6. Recrystallization process in NiCoMnSn and NiCoMnIn magnetic shape memory alloys

6.1. INTRODUCTION

The poor mechanical properties of metamagnetic shape memory alloys (brittleness, cracks after thermal cycling, etc.) constitute one of the main drawbacks for applications[1, 2]. To overcome the mechanical limitations of the bulk material, nanostructuration, processing in form of ribbons or wires or, in particular, the integration of powder alloys into a polymer to form composites have been reported as interesting options [3, 4]. Regarding the magnetocaloric applications, optimum mechanical properties are not necessary since the active material is not subject to mechanical stresses. However, it is important to optimize the magnetocaloric effect and the heat exchange between the active material and the transmitting fluid. In principle, the metamagnetic shape memory alloys in powder form meet the requirements to be used as a magnetocaloric element for refrigeration systems [5]. Nevertheless, in all cases, a complete characterization of the powdered alloys is needed in order to properly tune the functional properties. A proper analysis of the powder may provide valuable information concerning the influence of microstructure on both the martensitic transformation and the magnetic properties.

As stated in the general introduction (Chapter 1), ball milling is one of the simplest and cheapest methods to produce nanostructured materials and to modify the properties of alloys by mechanical treatment, with the appearance of interesting physical and chemical phenomena [6–8]. For instance, an optimization of the MCE may be produced in different magnetic systems through the reduction of the particle size by ball milling, either by increasing the temperature range [9] or by reducing the hysteresis loss when linked to a magnetostructural first order transformation [10].

The magnetostructural properties of metamagnetic shape memory alloy have been deeply studied in polycrystalline bulk alloys. Nevertheless, up to now, much less work has been devoted to the analysis of the martensitic transformation at reducing sizes, even though the grain size and the state of internal tensions are known to be two parameters highly influencing the characteristics of the MT through the variation of elastic energy term [11]. The effect of ball milling on the magnetostructural properties has been studied in Ni-Mn-Ga [12–15] and nanoparticles of Ni-Mn-Sn and Ni-Mn-In were recently obtained by ball milling [16–18]. In the previous chapters, we have delved into the effect of milling in ternary metamagnetic shape memory alloys and in quaternary systems with cobalt. The variations observed in the properties

and the appearance of new phases stimulates the continuation of the investigation with the study of the recovery and recrystallization processes induced by temperature in the milled alloys.

This chapter is therefore devoted to the study of the influence of the ball milling and the subsequent microstructural recovery under heating in Ni-Mn-In-Co and Ni-Mn-Sn-Co milled particles. We have chosen these alloys because mechanical milling in quaternary systems with Co has been much less studied than in the corresponding ternary systems. Furthermore, as shown in this thesis work, Co doping is a way to improve the magnetic properties, and consequently magnetocaloric effect, Ni-Mn-In and Ni-Mn-Sn systems. In previous chapters, we have studied the influence of milling the magnetostructural properties and the correlation with the microstructure of these systems, showing also the occurrence of an amorphization process. Hereafter, by means of neutron thermodiffraction, DSC, SEM and TEM measurements, the crystallization process taking place on heating the milled alloys and the properties of the resulting ordered structures have been characterized. A relaxation process occurs on annealing above 700 K, concurrently with a B2-$L2_1$ atomic ordering, in both systems, while a disordering process takes place at high temperature in the Ni-Mn-In-Co alloy giving rise to an anomalous two-step thermal expansion.

6.2. EXPERIMENTAL RESULTS

$Ni_{45}Co_5Mn_{37}In_{13}$ and $Ni_{45}Co_5Mn_{35}Sn_{15}$ alloys (In-Co and Sn-Co hereafter) were prepared from high purity elements by arc melting under protective Ar atmosphere. The as-cast ingots were homogenized at 1073 K during 24h and then quenched into iced water. The composition of the elaborated alloy was analyzed by EDS in a Jeol JSM-5610/LV Scanning Electron Microscope (SEM). The alloys were subjected to a ball milling process in an argon atmosphere at 800 rpm during an effective time of 2 h at room temperature using a ball:powder ratio of 5:1 in the ball mill described in Chapter 2. The structural transformations and the possible recovery processes taking place on annealing the as-milled powder samples were characterized by differential scanning calorimetry (Q-100 DSC, TA Instruments). The size and shape of the particles were observed by scanning and transmission electron microscopy (SEM, Jeol JSM-5610/LV). The evolution of crystal structure, long-range atomic order, crystallite size and microstrains was determined from in-situ powder neutron diffraction measurements performed on the high-flux D1B two-axis diffractometer, at the Institute Laue-Langevin (Grenoble, France). The diffraction patterns were measured on heating from RT up to 1173K at 1K/min using a neutron wavelength of 1.28 Å. The structures were refined by the Rietveld method using the Fullprof package programs [19].

6.2.1. Bulk and powder characterization

DSC cooling/heating measurements have been carried out to determine the transformation cycle of the bulk samples, shown in Figure 6. 1. The occurrence of a first-order

MT is evidenced by the presence in both alloys of the hysteretic exothermic and endothermic peaks linked to the forward and reverse MT respectively. The MT temperatures for the forward transformation (austenite to martensite) were determined taking the maximum of the exothermic peak on cooling; being T_{MT}=175 K and T_{MT}=300 K for Ni-Mn-Sn-Co and Ni-Mn-In-Co alloys respectively. The second-order magnetic transition taking place in the austenitic phase, inferred from the λ-type shoulder above the MT, has only been observed for the In-Co sample around 375 K.

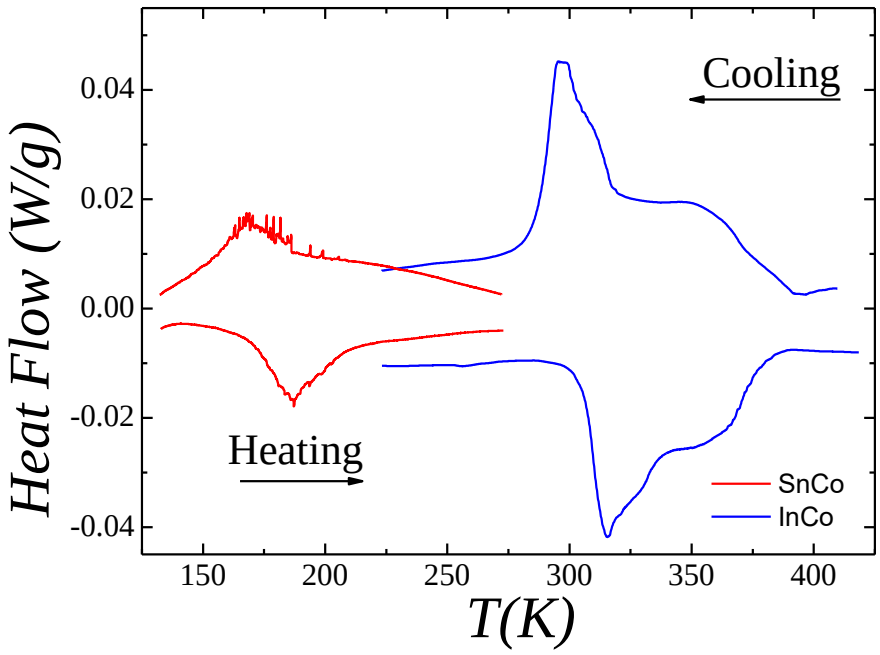

Figure 6. 1. DSC thermograms performed on cooling/heating the reference bulk alloys at 10 K/min.

The transformation temperature of the In-Co alloy is higher than the milling temperature, ≥ RT, and therefore the phase that is subjected to mechanical stress is the martensite. In the case of the Sn-Co alloy the transformation temperature, $T_M < 200K$, is well below the milling temperature. Due to the first-order character of the MT and the deformation associated therewith, the transition can be induced by the application of a mechanical stress at temperatures above $T_M(0)$, the transformation temperature for null stresses. According to Clausius-Clapeyron expression $dT_M/d\sigma = \varepsilon^{A\to M}/\Delta S^{A\to M}$>0, where T_M is the MT temperature, σ the applied stress, $\varepsilon^{A\to M}$ and $\Delta S^{A\to M}$ the deformation and entropy associated with the transformation, respectively. Thus, for an alloy with a transformation temperature below room temperature, the martensite could be induced by the stresses generated by the ball milling. Nevertheless, in the case of the Sn-Co alloy, the transformation temperature is well below the milling temperature, the difference between both temperatures being ~100K. This fact could imply that the necessary stresses to induce the MT would be so high that before inducing the transition the elastic limit of the austenite would be exceeded [20]. Therefore, we could presume

that the milling process is carried out on the cubic structure. However, from the previous results shown in Chapter 4, where the microstructural evolution with milling time has been studied in this alloy, we know that with long milling times the martensite phase is induced. Thus, in the milling process there is a change in the structure deformed over time. For short times the crystallographic structure subjected to milling is the austenite and for longer times the martensite is being induced. Then, the In-Co sample was milled in martensite phase and in the Sn-Co sample there is an evolution in the milled phase. This difference could be reflected in the morphology of the obtained particles after 2 hours of milling, Figure 6. 2. A different morphology of the particles is observed depending on which crystalline phase they have been milled. Thus, the sample that is in the austenite phase when milling starts shows a more homogeneous distribution of particle size and a more equiaxial form thereof. On the other hand, the particles initially in martensitic state show a planar morphology and a greater tendency to agglomerate. The presence of platelets-like particles can thus be related with the fact that the milling was done in martensite structure. When the sample is in this phase, the alloy presents variants with different directions and the presence of external strains due to the ball-milling can induce the break of the sample by the grain border letting the obtained powder in this platelet-like shape [21]. Other factors as plastic deformation, higher ductility of InCo than SnCo alloy and the cold welding effect on the alloy during milling can be the responsible of the flake-like shape [22–25]. The tendency to agglomerate can be due to the small particle size obtained by crushing the alloy that produces a large free energy or to the small volume/surface relation [26].

Figure 6. 3 shows the room temperature neutron diffraction pattern of the as-milled samples. The absence of well-defined Bragg reflections confirms the achievement of an almost amorphous phase as a result of the structural distortion and the associated introduction of structural defects caused by milling. In fact, the presence of small and broad peaks would indicate the presence of some marginal degree of crystallinity in the particles. In order to determine the percentage of amorphous phase, we have modeled it by a disordered A2 phase with space group $Im\bar{3}m$. The percentage of the disordered A2 phase, corresponding to the amorphous state in SnCo and InCo at room temperature is 64% and 78%, respectively. The microstructural evolution and the recovery processes taking place on heating the as-milled samples has been studied by means of ‘in-situ’ powder neutron diffraction and DSC experiments.

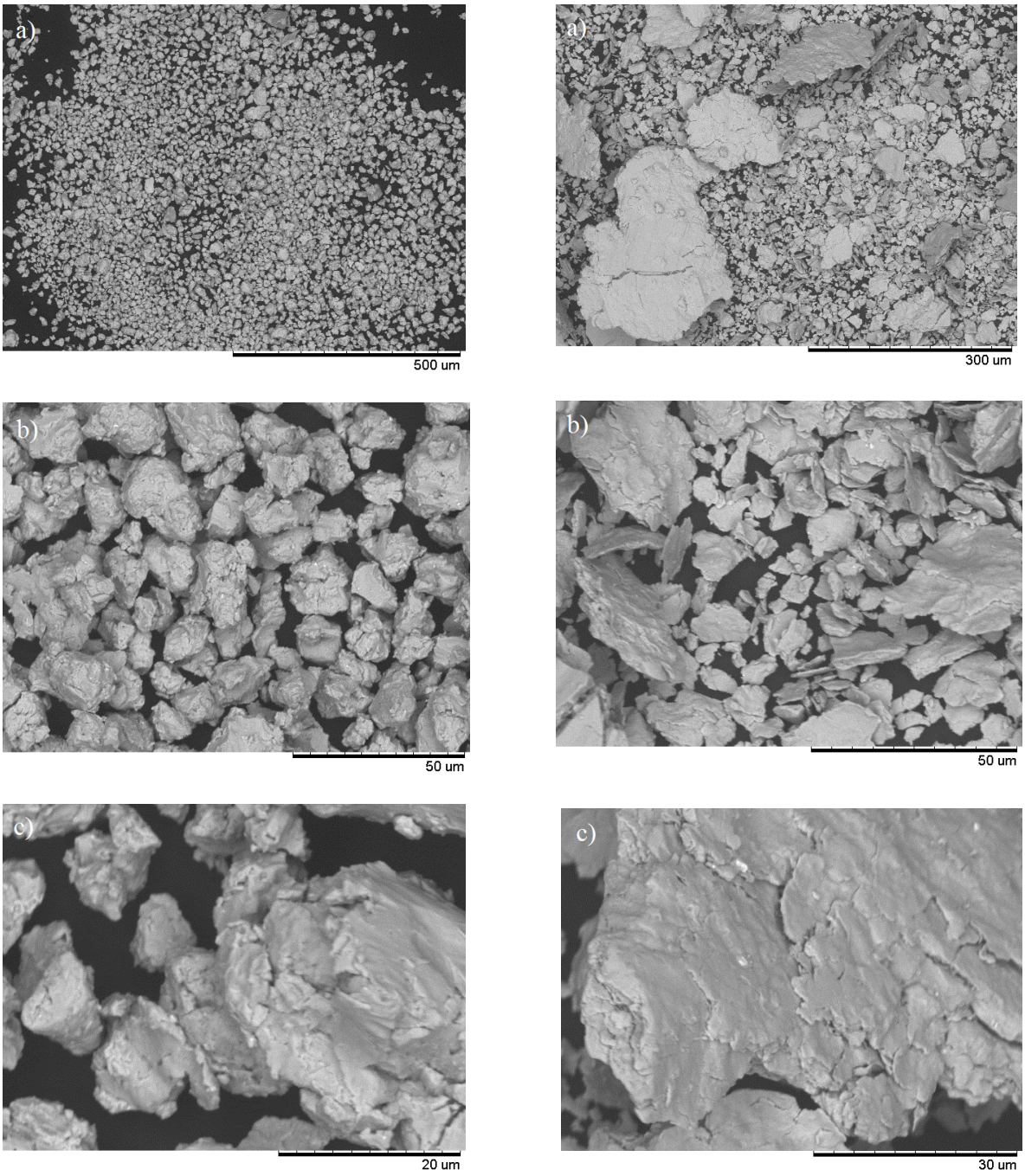

Figure 6. 2. SEM micrographs of the as-milled samples. Left column corresponds to Sn-Co alloy. Right column corresponds to In-Co alloy.

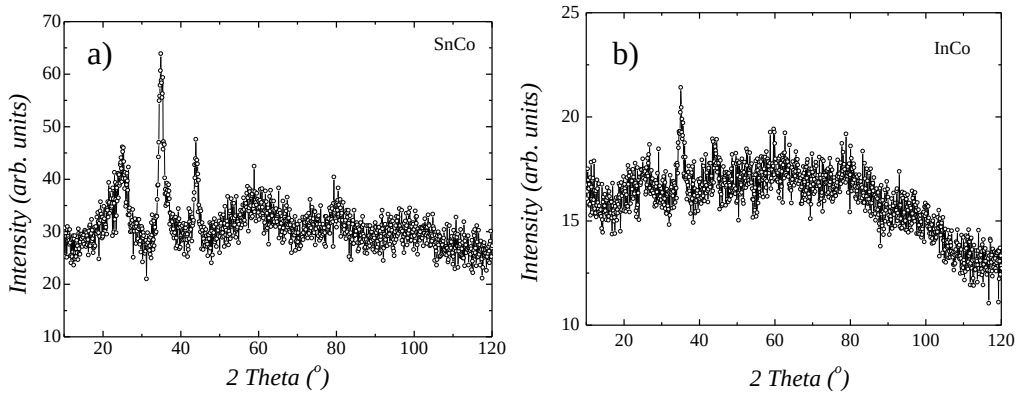

Figure 6. 3. Room temperature diffraction patterns of the as milled samples. a) Sn-Co sample, b) In-Co sample.

6.2.2. Recrystallization process

Figure 6. 4 shows the thermo-diffractograms of the Sn-Co sample obtained on heating from RT up to 1100 K at a 1 K/min constant rate. The evolution with the temperature of the amorphous state could be determined by Rietveld refinement. The 64% of amorphous phase determined as starting point at room temperature starts decreasing for temperatures higher than 400 K reaching 10% at temperatures close to 600 K.

Recrystallization is evidenced by the sudden appearance of Bragg reflections at temperatures above 500 K. Specifically, the sample crystallizes in B2 cubic structure with nearest-neighbors long-range atomic order, with $Pm\bar{3}m$ space group (Figure 6. 5.a). In this structure, the Ni-Co atoms tend to occupy the $(1/4, 1/4, 1/4)$ positions, the rest atomic positions being randomly occupied by atoms of Mn and Sn (actually, in Figure 6. 5.a, 8 cells of phase B2 are drawn, because when ordering to $L2_1$ takes place the cell parameter is doubled). Therefore, if we consider the crystallographic structure composed by four FCC sub-lattices, three of them have the same atomic occupation. On heating around 700 K, the appearance of $L2_1$ superstructure reflections (those in which the h, k, l indices are all odd, according to the corresponding unit cell structure factor) indicates the occurrence of an ordering process from B2 to a $L2_1$ cubic structure with next-nearest-neighbors long-range atomic order, with $Fm\bar{3}m$ space group (Figure 6. 5.b). In this case, the atoms of Mn and Sn tend to occupy different atomic positions and therefore the lattice parameter doubles. A similar recovery process has been observed on heating the as-milled In-Co sample, showing the same temperature range for crystallization, with the difference of the observation of a disordering $L2_1$-B2 transition at temperatures close to 850 K, where the (111) peak disappears reveling the disappearance the of $L2_1$ superstructure.

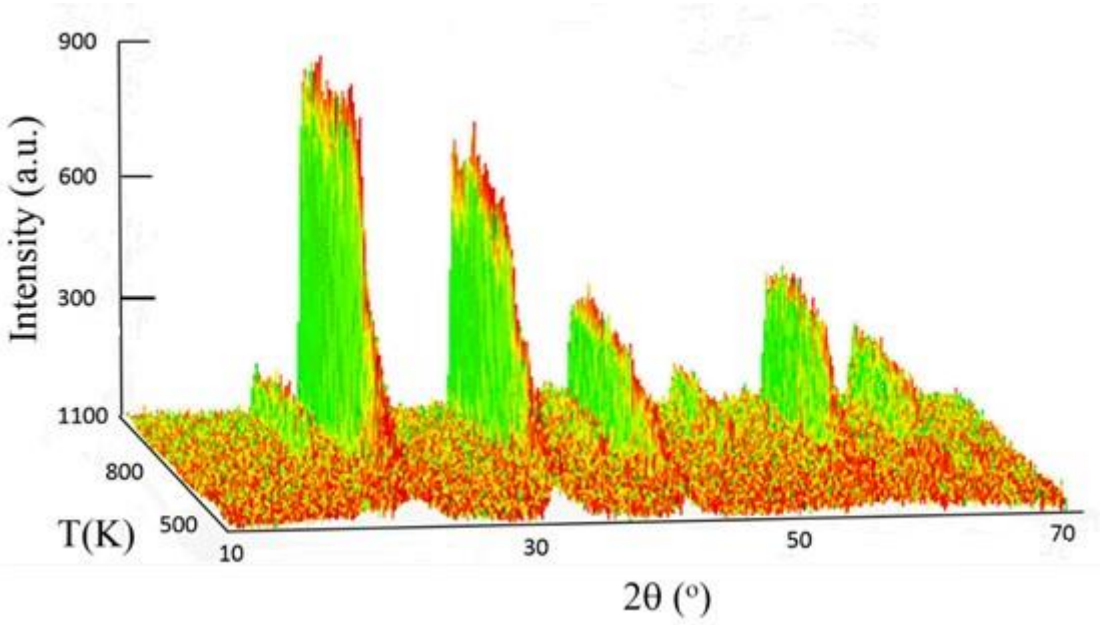

Figure 6. 4. In-situ neutron powder thermodiffractograms on heating between 500 K and 1100 K at 1 K/min for the Sn-Co alloy.

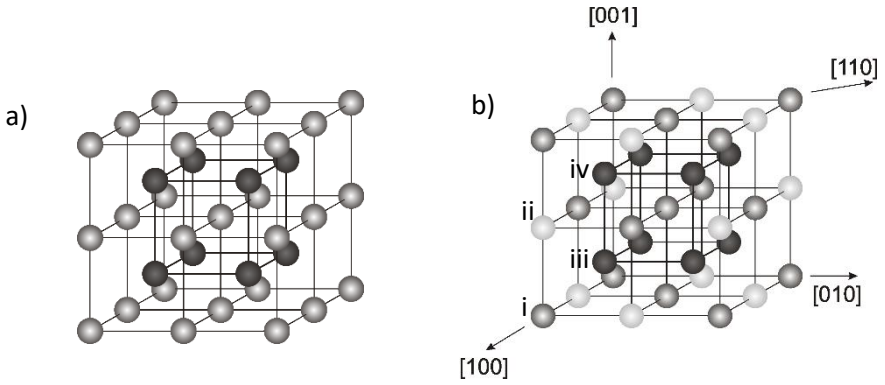

Figure 6. 5. a) B2 structure where three of the four FCC sub-lattices have the same atomic occupation. b) $L2_1$ structure, i and ii sub-lattices have different occupancy and the cell parameter doubles.

The crystallization process observed by thermodiffraction has been also analyzed by DSC measurements. Figure 6. 6 shows the thermograms obtained on heating the amorphous powders up to 700 K at a 10 K/min heating rate. A broad exothermic peak is observed, for both alloys, between 400 K and 700 K. The temperature of the maximum of the exothermic peak is slightly higher for the In-Co system, with a difference of around 50 K. On the other hand, the enthalpy of the whole peak is higher for the Sn-Co system. ($\Delta H \approx 60$ J/g and $\Delta H \approx 45$ J/g for Sn-Co and In-Co respectively).

The thermodiffraction shows that the crystallization process occurs abruptly in a narrow range of temperatures. However, the exothermic peak shown in both thermograms extends over a range of 300 K. Although the major contribution to the release of heat is linked to the process of crystallization, other contributions related to recovery processes must be included in the

enthalpy measured in the calorimeter. Figure 6. 6 also shows the fraction of amorphous phase as a function of temperature. There is a slight mismatch between the beginning of the crystallization processes and the peaks of calorimetry. In this sense, it should be noted that the heating ramp of the calorimetry was performed at a higher speed, 10 K/min. A higher heating rate implies a displacement towards high temperatures of any exothermic process. If they had been carried out at the same low heating rate as the thermodifraction, the peaks would appear less displaced but, on the other hand, the signal would be worse.

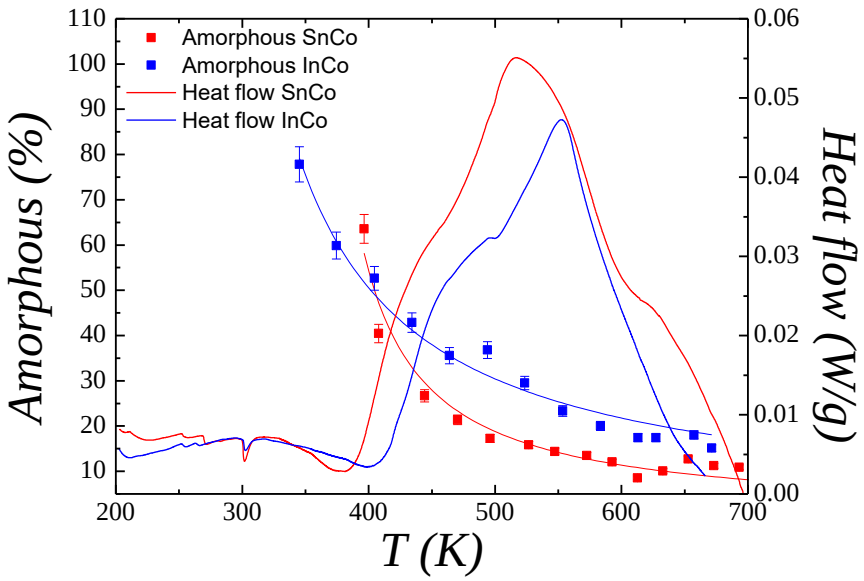

Figure 6. 6. DSC thermograms on heating at 10 K/min of the milled samples. Points indicate the evolution of the fraction of amorphous phase during heating.

In both systems the crystallization process takes place in the same temperature range and with the same sequence of atomic ordering, that is, first a crystallization in a B2 structure, and subsequently the ordering at next-nearest-neighbors, giving a $L2_1$ structure. Nevertheless, differences in the process of the microstructural recovery during the heating ramp after crystallization have been observed between both systems.

The kind of atomic order and its evolution with temperature has been determined from the analysis of the thermodiffraction spectra. The microstructural relaxation can be also analyzed from the width and shape of the Bragg peaks of the diffraction patterns. As an example, Figure 6. 7.a and Figure 6. 7.b show the diffractograms obtained for both alloy systems, SnCo and InCo respectively, at three different temperatures, together with the respective fits by Rietveld method. It can be seen, as a common behavior, that the broadening of the reflections significantly decreases pointing out a relaxation of the microstructure on heating up to 1173 K.

In the case of SnCo system the $L2_1$ is maintained on heating the sample up to 1173 K. In the first diffractogram, at 600 K, just after crystallization, the long-range atomic order

corresponds to a B2 structure, i.e. ordered only at nearest-neighbors. A next-nearest-neighbors ordering process, that is, a B2→$L2_1$ transition, takes place under further heating; this state of order is maintained until the highest temperature reached in the heating ramp. This is evidenced by the presence of (111) reflection, characteristic of the $L2_1$ structure, in diffractograms at 800K and 1000K.

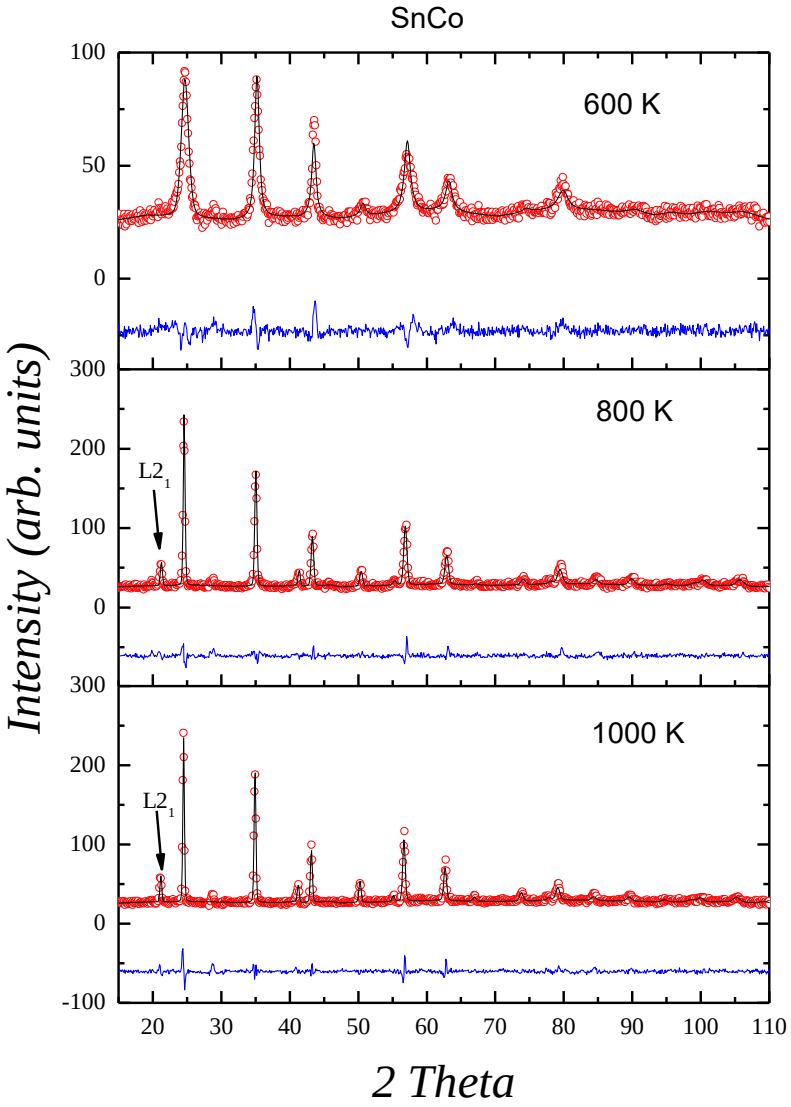

Figure 6. 7.a). Measured neutron diffraction pattern (dots), calculated profile (full line) and difference between the measured and calculated profiles (dashed line) for the milled alloy at 600 K, 800 K and 1000 K, for the SnCo alloy.

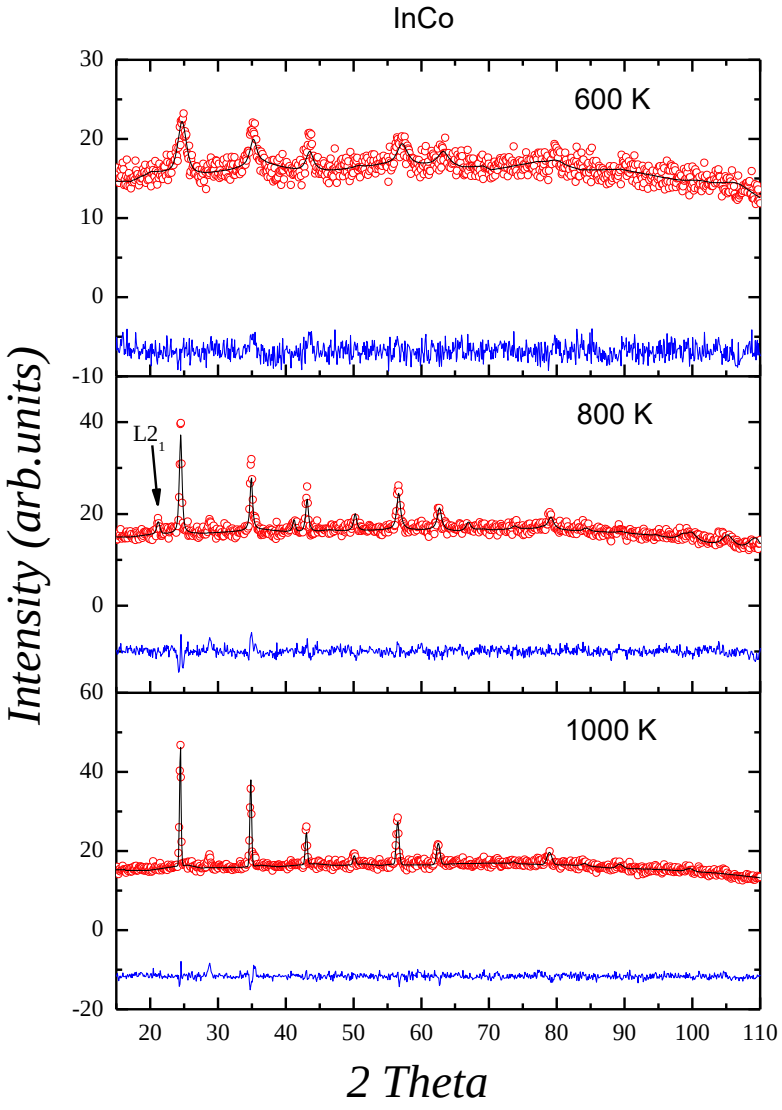

Figure 6.7.b). Measured neutron diffraction pattern (dots), calculated profile (full line) and difference between the measured and calculated profiles (dashed line) for the milled alloy at 600 K, 800 K and 1000 K, for the InCo alloy.

On the other hand, in the InCo system, the kind of atomic order observed at 600 K and 800 K, Figure 6. 7.b, is the same as in the SnCo system: order B2 at 600 K and order L21 at 800K, as evidenced by the peak (111) at this temperature. However, the L21 peak disappears in the diffractogram at 1000 K, indicating the loss of atomic order at next nearest-neighbors on heating.

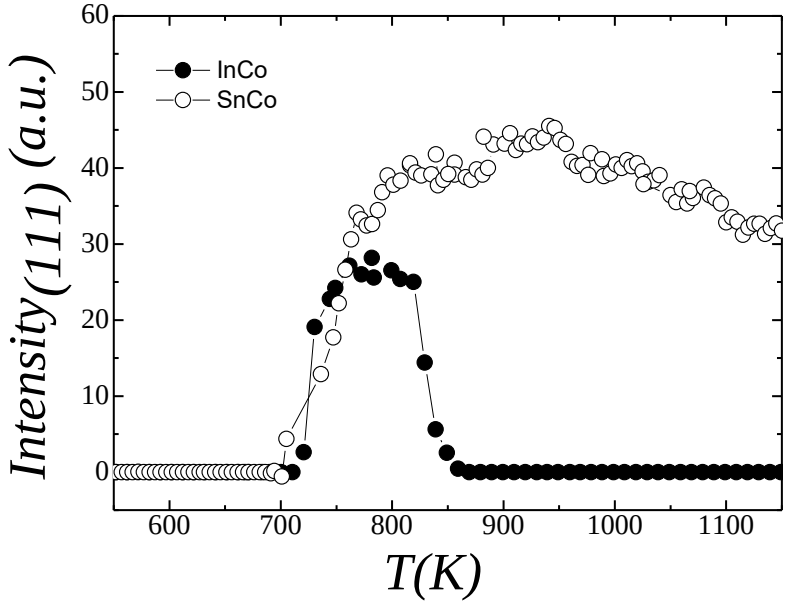

Figure 6. 8. Integrated intensity of the (111) reflection as a function of temperature for both alloys.

The temperature dependence of the integrated intensity of the (111) reflection shown in Figure 6. 8 illustrates the evolution of long-range atomic order of both alloys with temperature. The two consecutive order-disorder processes, B2→$L2_1$ and $L2_1$→ B2, for the InCo alloy are clearly identifiable from the appearance and subsequent disappearance of the superstructure reflection. It should be mentioned that the same sequence of order-disorder processes has been previously observed in ternary Ni-Mn-In as-milled samples [18]. On the other hand, the SnCo alloy undergoes the ordering B2→$L2_1$, at the same temperature, maintaining the presence of the peak (111) up to the highest temperature.

Comparing with the ordering processes observed in the corresponding bulk samples, similar ordering processes has been observed on heating the corresponding bulk alloys previously quenched from high temperatures, thought in that case the ordering temperatures (which indeed depend on the degree of disorder retained by quenching) typically lie between 500 K and 600 K. On further heating the intensity of the $L2_1$ reflections for Ni-Mn-In and Ni-Mn-In-Co gradually decreases until it vanishes completely as a consequence of the $L2_1$-B2 order-disorder transition [27–29]. In contrast, no $L2_1$-B2 disordering transition takes place in bulk Ni-Mn-Sn alloys demonstrating an extraordinary stability of the $L2_1$ structure [30], which is also evidenced in the milled sample presented here.

6.2.3. Microstructural analysis

The evolution of both microstrain and crystallite size with temperature is shown in Figure 6. 9.a and Figure 6. 9.b. The main microstructural relaxation takes place between 500 K and 800 K, where the microstrain abruptly decreases from 10.16 (1) ‰ to 0.93 (1) ‰ and

from 19.48 (3) ‰ to 2.45 (1) ‰ in SnCo and InCo alloys respectively. This is precisely the temperature range in which the B2-$L2_1$ ordering process occurs (see Figure 6. 8). Taking into account that atomic ordering implies atomic diffusion, as long as it is meditated by vacancies, it points to vacancy elimination and/or vacancy-assisted dislocation annihilation as the main recovery processes. On the other hand, the crystallite size for both systems increases with the increasing temperature, from 50 Å at RT to 750 Å at 1100K, approximately. As expected, the higher growth rate is reached above 800 K, just after recovery. It should be noted the different behavior shown in both systems by the microstrain and the crystalline size in its evolution with temperature. In the case of the SnCo alloy both magnitudes show an evolution of sigmoidal type, unlike the exponential behavior shown in the InCo alloy, Figure 6. 9.

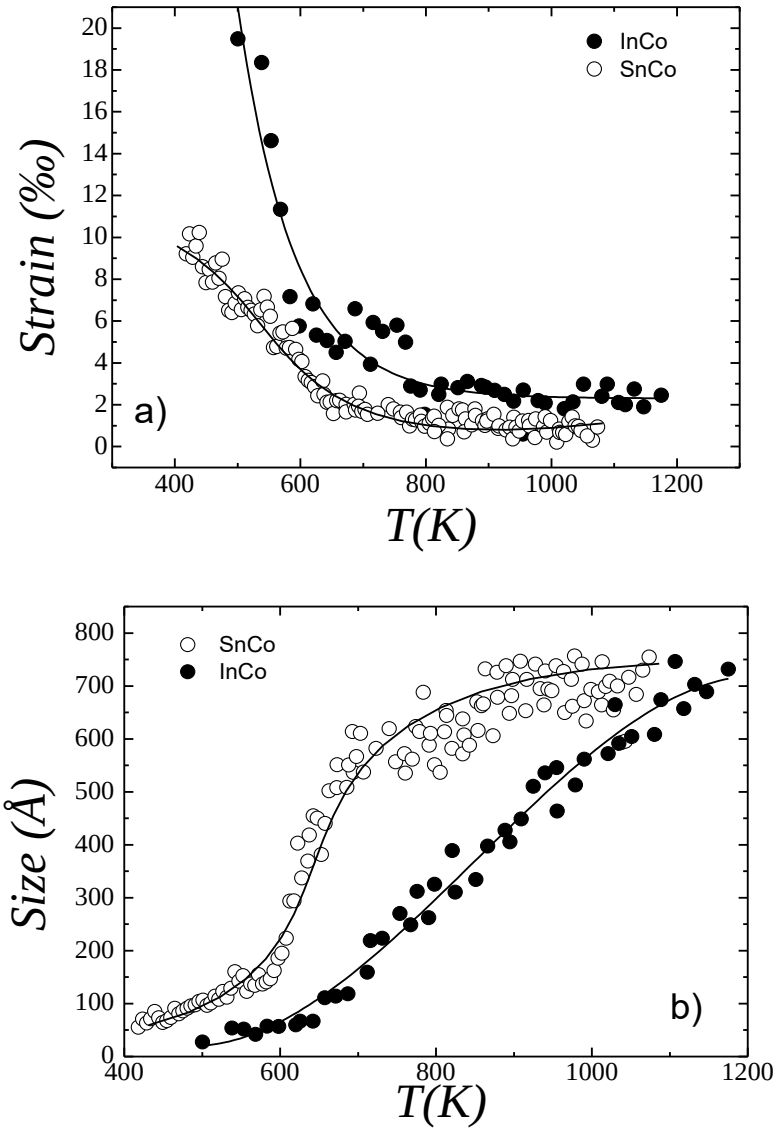

Figure 6. 9. a) Microstrain and b) crystalline size as a function of temperature for SnCo and InCo alloys.

Likewise, it is interesting to note that the temperature dependence of the lattice volume of the

austenite in the InCo alloy, Figure 6. 10, shows a marked change of slope at around 800 K, giving rise to an anomalous two-step thermal expansion. On the contrary, the thermal expansion of the SnCo alloy shows a monotonous behavior. According to the temperature dependence of the integrated intensity of the (111) reflection (i.e. the $L2_1$ order degree) shown in Figure 6. 8, the $L2_1$-B2 order-disorder transition for the InCo alloy starts at 800 K. The same two-step behavior of the thermal expansion has been previously observed in a ternary Ni-Mn-In as-milled sample [18] and also the change of the slope coincides with the initial temperature of the $L2_1$-B2 disordering process. Therefore, the anomalous behavior of the thermal expansion would be linked to the disorder process present in the Ni-Mn-In and Ni-Mn-In-Co alloys.

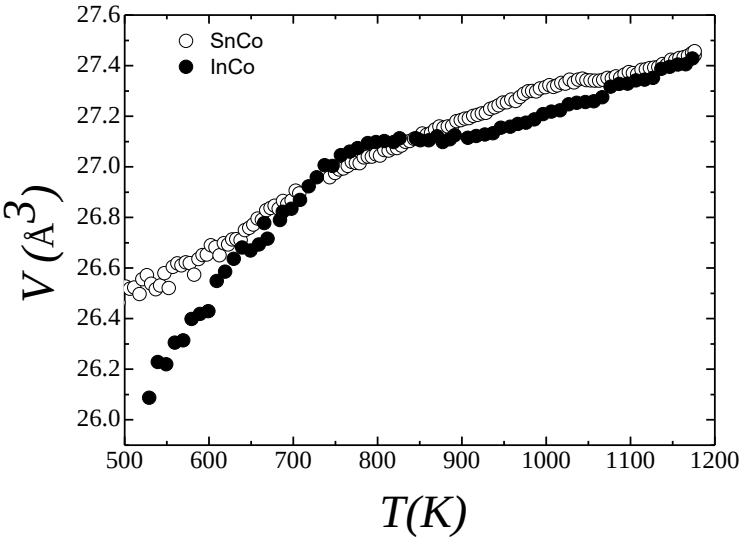

Figure 6. 10. Evolution of lattice volume (in terms of the B2 cell) with temperature for both alloys.

In order to obtain more information about the recrystallization and recovery processes undergone by the as-milled samples, the thermal evolution of their cell parameter and the degree of atomic order of austenite has been compared with the corresponding of the bulk samples. For this purpose, the Ni-Mn-In-Co and Ni-Mn-Sn alloys of the references [30, 31] were analyzed. In the first case, the composition of the In-Co quaternary alloy is very close to the sample of the present thesis. On the other hand, although the Sn alloy is not quaternary, the main difference is the substitution of Co for Ni. In both cases, the heat treatment undergone by both bulk samples consists of a slow cooling from high temperature to obtain the maximum degree of order allowed by the stoichiometry. The thermal behavior of the degree of order would be within the stable phase diagram of the austenite phase.

Figure 6. 11 summarizes the thermal behavior of the cell parameter and the atomic order of the four samples, bulk and as-milled. Focusing on the evolution of the degree of order, as has been previously mentioned, once the samples crystallized (B2 order) undergo the next-nearest

neighbors order transition B2-$L2_1$, the subsequent thermal evolution of the degree of order is the same as that of the bulk samples. Thus, after crystallization, in the intermediate temperature range, the degree of order of the milled samples would follow the diagram of stable phases. However, the cell parameters show a different behavior. The parameter of the cubic cell (in terms of the B2 cell) of the bulk samples presents a practically linear dependency with temperature without showing signatures of the order-disorder transitions. Nevertheless, the cell parameter behavior of the counterpart milled samples is very far from linearity, showing a clear influence of the recovery processes that takes place at intermediate temperatures, this effect being even greater in the InCo alloy. An estimate of the macrostrain of milled samples ε can be made from the deviation from the linear dependence with the temperature shown by the cell parameter of the bulk ones, according to the expression:

$$\varepsilon = \frac{a^{milled}(T) - a^{bulk}(T)}{a^{bulk}(T)} \tag{6.1}$$

where $a^{milled}(T)$ and $a^{bulk}(T)$ are the cell parameter of the milled and counterpart bulk alloys.

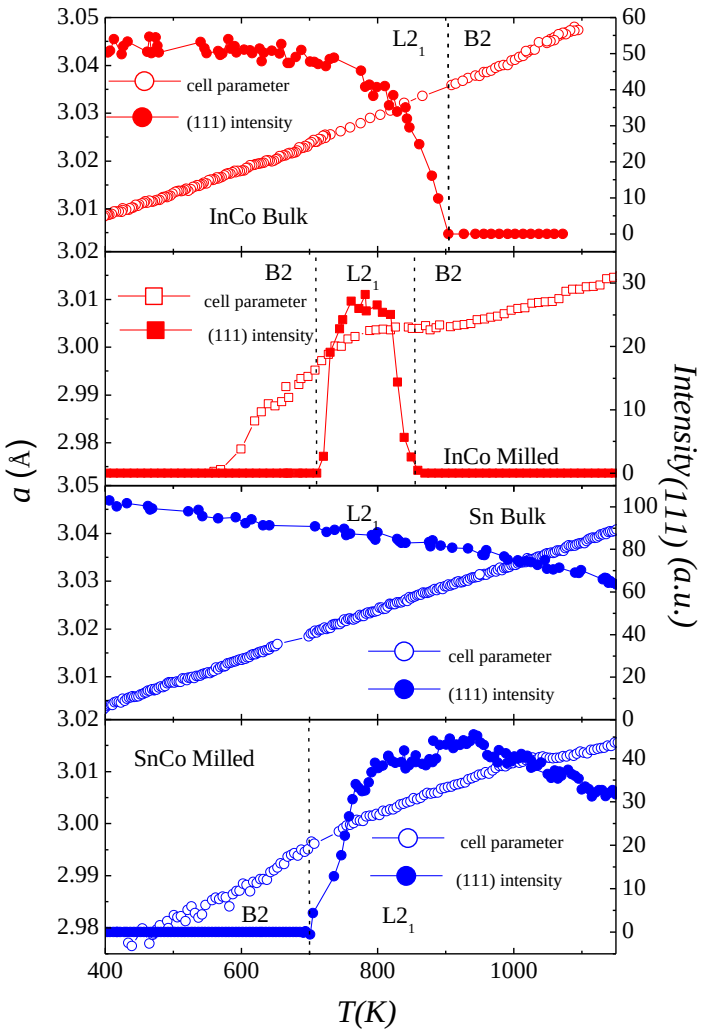

Figure 6. 11. Cell parameter (B2 cell reference) and degree of atomic order (intensity of (1 1 1) reflection) as a function of temperature of the cubic austenite for bulk and milled samples.

Thus, the analysis of the in-situ neutron thermodiffractograms has allowed estimating the evolution of the micro and macro strains during the crystallization and structural recovery process that takes place in the warming ramp of the milled samples, Figure 6. 12.

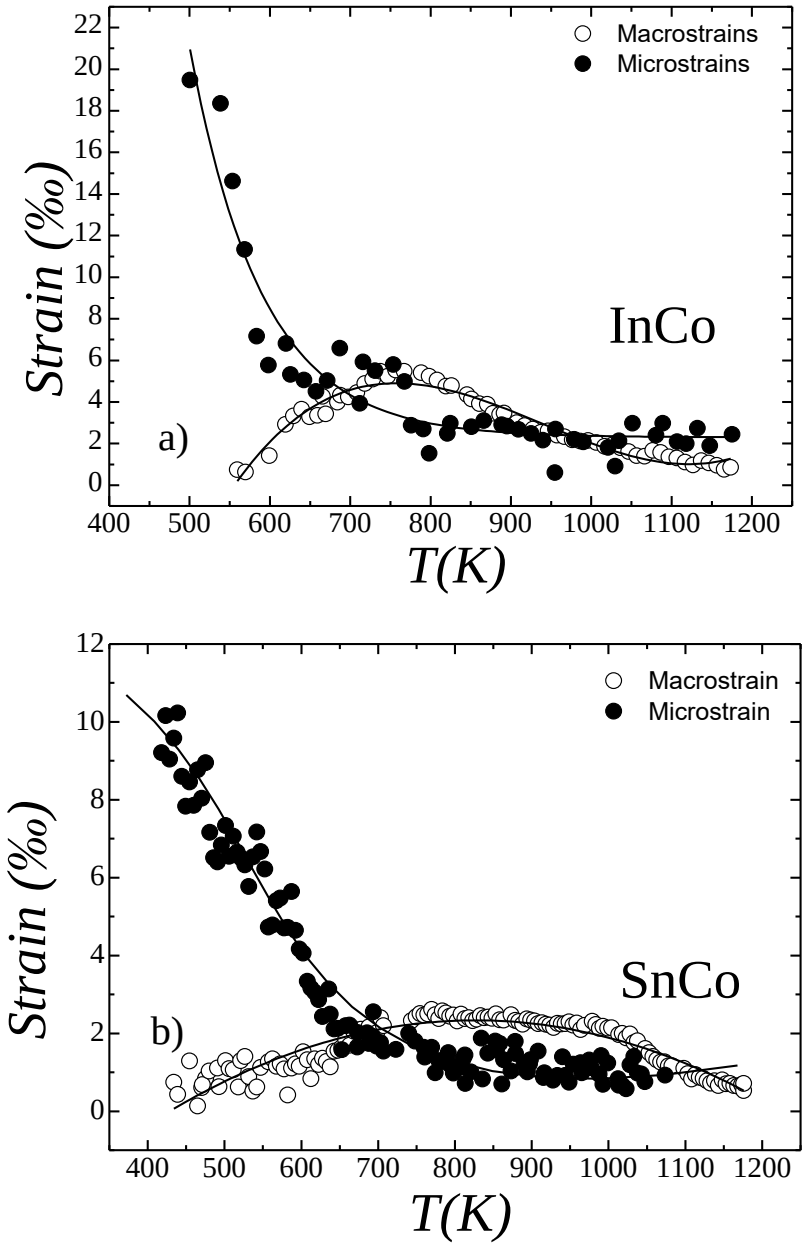

Figure 6. 12. Micro and macro strains as a function of temperature. a) InCo, b) SnCo

Both samples show the same general trend, being the values larger for the InCo system. The fact that this sample has been milled in martensite should give rise to a greater degree of initial deformation as corroborate the SEM micrographs. At low temperatures, just after the dominant role of the microstrain indicates that the highly energetic milling process has generated a high level of local stress/strains that are recovered in the first part of the heating process until

approximately 700 K. In this temperature range the thermal energy is enough to relax the system locally, dropping the microstrain values, but the long-range recovery has not taken place as evidenced by the fact that the atomic order B2-$L2_1$ has not yet been produced, Figure 6. 11. During the subsequent heating, the thermal energy allows diffusion and long-range atomic movement, producing the atomic order variations and the completion of the microstructural recovery. This recovery results in a maximum of long-range homogeneous deformation at around 800 K as it is reflected in the evolution of the macrostrain in both systems.

Finally, concerning the difference of the order of magnitude between the values of the particle size observed by SEM and the values obtained by diffraction, it should be noted that in this last technique the value obtained is related to the coherent diffraction volume. Thus, if the particles are not monocrystalline the values do not have to match. The TEM micrograph, Figure 6. 13, shows the high resolution image in a SnCo particle after recrystallization. It is observed that it is formed by multiple grains, whose size is of the order of magnitude of the nanometers, in agreement with the values obtained by diffraction.

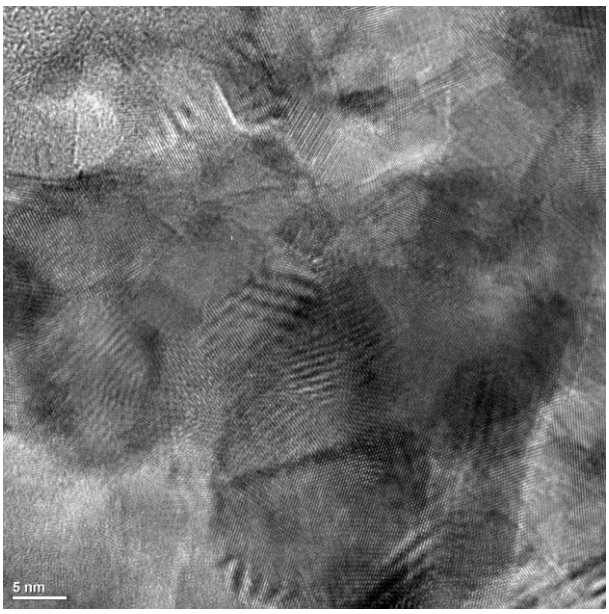

Figure 6. 13. TEM micrography of SnCo alloy after recrystallization.

6.3. SUMMARY AND CONCLUSIONS

In this chapter, the recrystallization process from an almost amorphous state was studied in Ni-Mn-Sn-Co and Ni-Mn-In-Co alloys subjected to two hours of high-energy ball milling, and ground in austenite and martensite, respectively. The study was carried out by the analysis of macroscopic calorimetric measurements and, from the microscopical point of view, by neutron

diffraction, SEM and TEM micrography. The evolution of microstructural and cell parameters was determined by Rietveld refinements during the recrystallization process.

By means of SEM micrography, the particle size of the obtained powder was determined in both studied specimens, obtaining values close to 100 μm with different morphology associated to ductility of the alloy and to the phase in which the samples were milled. In this sense, Ni-Co-Mn-Sn presents polyhedral particles while Ni-Mn-In-Co displays flake-like shaped particles, as a result of having been milled in martensite and the possible occurrence of cold welding due to the higher ductility that this last system presents.

Powder neutron diffraction in the initial state has revealed that, together with a prevailing amorphous phase, the alloys retain some degree of crystallinity after milling, as shown by the reflections present in the diffractograms. The amount of amorphous phase was estimated by modelling it by a disordered A2 phase, yielding values close to 64% and 78% for Ni-Mn-Sn-Co and Ni-Mn-In-Co alloys in the as-milled state, respectively. The higher degree of amorphization shown by the InCo system is in agreement with the higher strains and lower grain size determined in the initial state for this alloy. The recrystallization process occurs in two steps for both alloys. Both evolve from amorphous state to disordered B2 phase at temperatures close to 500 K and undergo a B2-$L2_1$ transition at 700 K. However, the Heusler $L2_1$ structure remains in SnCo up to temperatures as high as 1200 K, while InCo alloy undergoes a $L2_1$-B2 order-disorder transition at 850 K, pointing out the high stability of $L2_1$ structure in the SnCo system. Moreover, the evolution of microstructural parameters as grain size and internal strains was obtained from the refinement of the diffraction patterns measured during the recrystallization. An anomalous behavior of the cell parameter as a function of temperature has been clearly observed in the temperature range where the B2-$L2_1$ transition takes place. Finally, the grain size determined by TEM micrography is in agreement with the values obtained from Rietveld refinement, corroborating the polycrystalline structure of the particles after the recrystallization process. Although the particle sizes are large, the order of magnitude of the size of the recrystallized grains is in agreement with those obtained by neutron diffraction.

Bibliography

[1] G. B. Rao, J. Q. Wang, E. H. Han, and W. Ke, "Study of residual stress accumulation in TiNi shape memory alloy during fatigue using EBSD technique," *Mater. Lett.*, vol. 6, no. 60, pp. 779–782, 2006.

[2] H. Scherngell and A. C. Kneissl, "Generation, development and degradation of the intrinsic two-way shape memory effect in different alloy systems," *Acta Mater.*, vol. 2, no. 50, pp. 327–341, 2002.

[3] J. Feuchtwanger, M. L. Richard, Y. J. Tang, A. E. Berkowitz, R. C. O'Handley, and S. M. Allen, "Large energy absorption in Ni–Mn–Ga/polymer composites," *J. Appl. Phys.*, vol. 97, no. 10, p. 10M319, May 2005.

[4] J. Liu, N. Scheerbaum, S. Kauffmann-Weiss, and O. Gutfleisch, "NiMn-Based Alloys and Composites for Magnetically Controlled Dampers and Actuators," *Adv. Eng. Mater.*, vol. 14, no. 8, pp. 653–667, Aug. 2012.

[5] M. Acet, L. Manosa, and A. Planes, *Handbook of Magnetic Materials*, K. H. J. Buschow., vol. 19. Amsterdam: Elsevier, 2011.

[6] C. Suryanarayana, "Mechanical alloying and milling," *Prog. Mater. Sci.*, vol. 46, no. 1, pp. 1–184, Jan. 2001.

[7] M. E. McHenry and D. E. Laughlin, "Nano-scale materials development for future magnetic applications," *Acta Mater.*, vol. 48, no. 1, pp. 223–238, Jan. 2000.

[8] A. Calka and D. Wexler, "Mechanical milling assisted by electrical discharge," *Nature*, vol. 419, no. 6903, pp. 147–151, Sep. 2002.

[9] P. Gorria, P. Álvarez, J. S. Marcos, J. L. Sánchez Llamazares, M. J. Pérez, and J. A. Blanco, "Crystal structure, magnetocaloric effect and magnetovolume anomalies in nanostructured Pr2Fe17," *Acta Mater.*, vol. 57, no. 6, pp. 1724–1733, Apr. 2009.

[10] W. Dagula, O. Tegus, X.W. Li, L. Song, E. Brück, D.T. Cam Thanh, F.R. de Boer, and K.H.J. Buchow, "Magnetic properties and magnetic-entropy change of MnFeP0.5As0.5−xSix(x=0–0.3) compounds," *J. Appl. Phys.*, vol. 99, no. 8, p. 08Q105, Apr. 2006.

[11] J. Ortín and A. Planes, "Thermodynamic analysis of thermal measurements in thermoelastic martensitic transformations," *Acta Metall.*, vol. 36, no. 8, pp. 1873–1889, Aug. 1988.

[12] Y. D. Wang, Y. Ren, Z.H. Nie, D.M. Liu, L. Zuo, H. Choo, H. Li, P.K. Liaw, J.Q. Yan, R.K. McQueeney, J.W. Richardson, and A. Huq, "Structural transition of ferromagnetic Ni2MnGa nanoparticles," *J. Appl. Phys.*, vol. 101, no. 6, p. 063530, Mar. 2007.

[13] B. Tian, F. Chen, Y. Liu, and Y. F. Zheng, "Structural transition and atomic ordering of Ni49.8Mn28.5Ga21.7 ferromagnetic shape memory alloy powders prepared by ball milling," *Mater. Lett.*, vol. 62, no. 17–18, pp. 2851–2854, Jun. 2008.

[14] Y. V. B. de Santanna, M. A. C. de Melo, I. A. Santos, A. A. Coelho, S. Gama, and L. F. Cótica, "Structural, microstructural and magnetocaloric investigations in high-energy ball milled Ni2.18Mn0.82Ga powders," *Solid State Commun.*, vol. 148, no. 7, pp. 289–292, Nov. 2008.

[15] K. V. Peruman, R. Chokkalingam, and M. Mahendran, "Annealing effect on phase transformation in nano structured Ni–Mn–Ga ferromagnetic shape memory alloy," *Phase Transit.*, vol. 83, no. 7, pp. 509–517, Jul. 2010.

[16] A. L. Alves, E. C. Passamani, V. P. Nascimento, A. Y. Takeuchi, and C. Larica, "Influence of grain refinement and induced crystal defects on the magnetic properties of Ni 50 Mn 36 Sn 14 Heusler alloy," *J. Phys. Appl. Phys.*, vol. 43, no. 34, p. 345001, 2010.

[17] A. Ghotbi Varzaneh, P. Kameli, V. R. Zahedi, F. Karimzadeh, and H. Salamati, "Effect of heat treatment on martensitic transformation of Ni47Mn40Sn13 ferromagnetic shape memory alloy prepared by mechanical alloying," *Met. Mater. Int.*, vol. 21, no. 4, pp. 758–764, Jul. 2015.

[18] V. Sánchez-Alarcos, V. Recarte, J.I. Pérez-Landazábal, S. Larumbe, R. Caballero-Flores, I. Unzueta, J.A. García, F. Plazaola, J.A. Rodríguez-Velamazán, "Mechanically induced disorder and crystallization process in Ni-Mn-In ball-milled alloys," *J. Alloys Compd.*, vol. 689, pp. 983–991, Dec. 2016.

[19] J. Rodríguez-Carvajal, "Recent advances in magnetic structure determination by neutron powder diffraction," *Phys. B Condens. Matter*, vol. 192, no. 1, pp. 55–69, Oct. 1993.

[20] B. Lu and J. Liu, "Elastocaloric effect and superelastic stability in Ni–Mn–In–Co polycrystalline Heusler alloys: hysteresis and strain-rate effects," *Sci. Rep.*, vol. 7, no. 1, Dec. 2017.

[21] B. Tian, F. Chen, Y.X. Tong, L. Li, Y.F. Zheng, Y. Liu, and Q.Z. Li, "Phase transition of Ni–Mn–Ga alloy powders prepared by vibration ball milling," *J. Alloys Compd.*, vol. 509, no. 13, pp. 4563–4568, Mar. 2011.

[22] E. Sakher, N. Loudjani, M. Benchiheub, and M. Bououdina, “Influence of Milling Time on Structural and Microstructural Parameters of Ni50Ti50 Prepared by Mechanical Alloying Using Rietveld Analysis,” *J. Nanomater.*, p. 2560641, 2018.

[23] O. Güler, T. Varol, Ü. Alver, and A. Çanakçı, “The effect of flake-like morphology on the coating properties of silver coated copper particles fabricated by electroless plating,” *J. Alloys Compd.*, vol. 782, pp. 679–688, Apr. 2019.

[24] S. S. Razavi-Tousi and J. A. Szpunar, “Effect of ball size on steady state of aluminum powder and efficiency of impacts during milling,” *Powder Technol.*, vol. 284, pp. 149–158, Nov. 2015.

[25] B. Tian, Y. X. Tong, F. Chen, L. Li, and Y. F. Zheng, “Effect of aging and ball milling on the phase transformation of Ni50Mn25Ga17Cu8−xZrx alloys,” *Intermetallics*, vol. 58, pp. 56–61, Mar. 2015.

[26] H. S. Akkera, I. Singh, and D. Kaur, “Martensitic phase transformation of magnetron sputtered nanostructured Ni–Mn–In ferromagnetic shape memory alloy thin films,” *J. Alloys Compd.*, vol. 642, pp. 53–62, Sep. 2015.

[27] V. Recarte, J. Pérez-Landazábal, V. Sánchez-Alarcos, and J. A. Rodriguez-Velamazán, “Dependence of the martensitic transformation and magnetic transition on the atomic order in Ni–Mn–In metamagnetic shape memory alloys,” *Acta Mater.*, vol. 60, pp. 1937–1945, Mar. 2012.

[28] V. Sánchez-Alarcos, V. Recarte, J. I. Pérez-Landazábal, C. Gómez-Polo, and J. A. Rodríguez-Velamazán, “Role of magnetism on the martensitic transformation in Ni–Mn-based magnetic shape memory alloys,” *Acta Mater.*, vol. 60, no. 2, pp. 459–468, Jan. 2012.

[29] V. Sánchez-Alarcos, V. Recarte, J. I. Pérez-Landazábal, E. Cesari, and J. A. Rodríguez-Velamazán, “Long-Range Atomic Order and Entropy Change at the Martensitic Transformation in a Ni-Mn-In-Co Metamagnetic Shape Memory Alloy,” *Entropy*, vol. 16, no. 5, pp. 2756–2767, May 2014.

[30] V. Sánchez-Alarcos, J. I. Pérez-Landazábal, V. Recarte, I. Lucia, J. Vélez, and J. A. Rodríguez-Velamazán, “Effect of high-temperature quenching on the magnetostructural transformations and the long-range atomic order of Ni–Mn–Sn and Ni–Mn–Sb metamagnetic shape memory alloys,” *Acta Mater.*, vol. 61, no. 12, pp. 4676–4682, Jul. 2013.

[31] V. Sánchez-Alarcos, V. Recarte, J. I. Pérez-Landazábal, E. Cesari, and J. A. Rodríguez-Velamazán, “Long-Range Atomic Order and Entropy Change at the Martensitic Transformation in a Ni-Mn-In-Co Metamagnetic Shape Memory Alloy,” *Entropy*, vol. 16, no. 5, pp. 2756–2767, May 2014.

Chapter 7. Summary and conclusions

In the so-called metamagnetic shape memory alloys the fact that the martensitic transformation takes place between a ferromagnetic austenite and a weakly magnetic martensitic phase gives rise to multifunctional properties of great technical interest for practical applications, like sensing or magnetic refrigeration. Despite many topics as the compositional dependence and the effect of the atomic order on the magnetostructural properties have been deeply analyzed in several previous works, the role of the microstructure, in turn, has been less investigated, in spite of its potential for tuning the magnetostructural properties of these systems.

In this work we have focused on the study of the influence of the microstructure in metamagnetic shape memory alloys (Ni-Mn-In and Ni-Mn-Sn systems) together with the effect of Co-doping, in order to gain insight into these effects and to control and improve the properties of these materials. In order to modify their microstructure in a controlled way, the samples were subjected to thermo-mechanical treatments (hand milling, ball milling, and thermal annealing at different temperatures). The alloys have been characterized macroscopically by calorimetric and magnetic measurements, and studied at the microscopic level mainly through X-ray and neutron diffraction, which provided us information about the crystal structures, the atomic order in the alloys, the microstructural parameters as grain size and internal strains, and the magnetic structures. The combination of the results obtained in the microscopic study with the calorimetric and magnetic macroscopic characterization allowed us to gain a better understanding of the role of the microstructure and cobalt doping in the magnetostructural properties of these metamagnetic shape memory alloys and identify routes to obtain improved functional properties.

As main conclusions of the obtained results we can summarize.

- First, the effect of the microstructure on the martensitic transformation and the related magnetostructural properties was studied in Ni-Mn-Sn alloys. The study was carried out macroscopically with calorimetric and magnetic measurements and microscopically by X-rays and neutron diffraction and by Mössbauer spectroscopy in a milled $Ni_{50}Mn_{35}Sn_{15}$ alloy annealed at different temperatures. The conclusions drawn are:

  - Macroscopic measurements have evidenced the null variation in the martensitic transformation temperature with different annealing treatments, although the temperature range in which this structural transition takes place is reduced as the annealing temperature increases. The enthalpy and entropy values associated to the martensitic transformation point out that the martensitic transformation, significantly affected by milling, is mainly recovered after the treatment at the

lowest temperature. Moreover, the variation in the magnetocaloric effect manifests the outstanding influence of the microstructure on the functional properties of the alloy.

- By X-ray diffraction, the evolution of the microstructural parameters as grain size and internal strains has been analyzed as a function of the annealing temperatures. The amount of the non-magnetic inclusions was quantified and related with the internal strains by means of a combination of the magnetic measurements and the microstructural analysis, showing a reduction of a factor more than 10 by annealing, together with an associated increase of the saturation magnetization.

- The null variation in the atomic order obtained by powder neutron diffraction is consistent with the absence of change in the temperatures of the martensitic transformation, proving the high stability of the atomic order of the Ni-Mn-Sn alloys. The crystal structure of the martensite phase was resolved as a two-fold modulated orthorhombic structure. On the other hand, the magnetic structure of austenite reveals the switch of the magnetic coupling of Mn atoms from antiferromagnetic to ferromagnetic induced by the recovery of the microstructure induced by the annealing.

- Mössbauer spectroscopy has been used for the analysis of the magnetism at the atomic level and was related with the internal strains, demonstrating the importance of the microstructure in the hyperfine field, which is reduced with the increment of the internal strains, and pointing out the usefulness of this technique in the analysis of the microstructure.

- Doping with Co has proved to be a way to increase the metamagnetic character of the martensitic transformation in ternary systems. Then, the next step was the study of the influence of mechanically-induced defects on the magnetostructural properties in non-stoichiometric $Ni_{45}Co_5Mn_{35}Sn_{15}$ alloy in milled and post-annealed state. In a further stage, systematic high-energy ball-milling was performed and the samples analyzed by calorimetry, magnetometry and high-energy X-ray diffraction.

  - The long-range atomic order was determined in as-milled and annealed samples by Rietveld refinement of neutron powder diffractograms showing the non-variation in the atomic occupancies between both states and the presence of Co mainly in 8*c* sites. Those results are in good agreement with the observed by calorimetric and magnetic measurements where the martensitic transformation and Curie temperatures remain constant in both specimens.

  - The magnetic structure of austenite in both samples shows a ferromagnetic coupling between Mn atoms located in 4*a* and 4*b* sites due to the presence of Co atoms in 8*c* sites sharing occupancy with Ni. The presence of Co in these sites increases the magnetic interaction between Mn atoms, producing an increment of the

ferromagnetism in this phase. On the other hand, the annealing treatment increases slightly the saturation magnetization of austenite, due to the recovery of defects.

- Regarding the martensitic structure, both the as-milled and annealed samples present the same three-layered modulated monoclinic crystal structure with space group *P2/m* and antiferromagnetic coupling between Mn atoms. The annealed alloy presents weaker antiferromagnetic coupling, which explains the increase of the saturation magnetization in martensite that reduces the change of magnetization linked to the martensitic transformation. This fact implies that the as-milled alloy, with higher density of defects, presents higher magnetocaloric effect. Thus, the inclusion of a small amount of defects can improve the magnetocaloric properties on the alloy, due to the variation in the magnetism of the martensite.

- High resolution X-rays diffraction shows how the microstructural parameters are modified with the increase of the milling time: the grain size becomes smaller and the internal strains increase. We can also observe a degradation to an amorphous state, together with the induction of a secondary phase during milling identified as a monoclinic *I2/m* martensite. Moreover, the magnetic structure of the austenite in the alloys milled 45 minutes was calculated, determining a progressive reduction on the magnetic moment and although the ferromagnetic character of the magnetic coupling is maintained.

- SEM and TEM where carried out in order to obtain more information about the evolution of the microstructure. TEM was performed in a single particle in the samples that present martensitic transformation, showing how the diffraction evolves from patterns characteristic of single-crystals to patterns characteristic of powders, revealing the reduction of the grain size inside the particles.

- In order to get further insight into the influence of Co doping on the magnetic coupling, the macroscopic magnetic properties, together with the atomic order and magnetic structure in austenite phase were analyzed in non-stoichiometric $Ni_{50}Mn_{36}In_{14}$ and $Ni_{45}Co_5Mn_{37}In_{13}$ alloys with two different thermal treatments: water quenched and slow cooled from 1173 K. The combination of macroscopic magnetic measurements with unpolarized powder and single-crystal neutron diffraction and polarized single-crystal neutron diffraction allows drawing the following conclusions:

  - The variation in the thermal treatment and Co-doping modify the atomic order and as consequence the martensitic transformation and Curie temperatures. In the case of the slow cooled alloys the T_C shifts to higher temperatures with respect to the water quenched samples, while the martensitic transformation moves to lower temperatures. On the other hand, Co doping produces an increment in both transition temperatures. An increase of 60% in the saturation magnetization of the austenite phase can be reached by the combination of Co doping and slow cooling treatment.

- The higher degree of atomic order, together with the reduction of strains and defects induced by slow cooling thermal treatments produces an increase in the total ordered magnetic moment and a slight enhancement of the ferromagnetic coupling between the magnetic moments located in octahedral sites, while cobalt doping has a stronger effect in increasing the ferromagnetic coupling, which explains the noticeable effect in the magnetization.

- By spin density maps obtained from polarized neutron diffraction, the magnetic interaction responsible for this coupling was obtained. Despite the weak interaction of the moments in 8*c* sites with the rest of the magnetic moments, Co, that mainly replaces Ni in 8*c* positions, tends to couple ferromagnetically with its nearest neighbors in 4*a* and 4*b* sites, where the magnetic atoms are mainly Mn, which in turn are coupled by strong interactions, favoring the overall ferromagnetic coupling.

- Finally, the recrystallization process was studied in Ni-Mn-Sn-Co and Ni-Mn-In-Co alloys subjected to high-energy ball-milling during two hours in austenite and martensite, respectively. The evolution of the microstructure during the recrystallization was deduced from the analysis of parameters as grain size and internal strains from 'in-situ' neutron powder diffraction.

  - The average particle size was obtained in both alloys in as-milled states, giving values of ~100 μm. The morphology of the obtained powder changes from polyhedral in the SnCo alloy to flake-like shape in the InCo one, which is related with the fact that the second alloy was milled in martensitic phase.

  - Powder neutron diffractograms in the as-milled state present few reflections, indicating that, together with a prevailing amorphous phase, the alloys retain some degree of crystallinity after milling. The amount of amorphous phase in the as-milled state was estimated by modelling it by a disordered A2 phase, giving values close to 64% and 78% for Ni-Mn-Sn-Co and Ni-Mn-In-Co alloys, respectively.

  - Differential scanning calorimetry shows that the crystallization process occurs between 400 K and 700 K. Neutron powder diffraction experiments have shown that both samples undergo a first crystallization at 500 K from an amorphous state to a B2 structure. Besides, at 700 K the appearance of (111) reflection indicates the B2-$L2_1$ transition. This structure remains stable up to 1200 K in SnCo alloy, corroborating the high stability of this ordered structure in Sn-based systems. In contrast, in InCo a $L2_1$-B2 order-disorder transition is observed at 850 K.

  - The evolution during the recrystallization of microstructural parameters was obtained from the refinement of the diffraction patterns measured during the recrystallization. The evolution of the cell parameter of the austenite, in both

systems, was also determined during the crystallization process showing a deviation from linearity in its dependence at temperatures coinciding with the B2-$L2_1$ transition. Finally, the grain size determined by TEM micrography is in agreement with the values obtained from Rietveld refinement, corroborating the polycrystalline structure of the particles after the recrystallization process.

List of papers published by the author

The work developed during this thesis has led to the publication of the following papers in international peer-reviewed journals:

- I. Unzueta, J. López-García, V. Sánchez-Alarcos, V. Recarte, J. I. Pérez-Landazábal, J. A. Rodríguez-Velamazán, J. S. Garitaonandia, J. A. García, F. Plazaola, "^{119}Sn Mösbauer spectroscopy for assessing the local stress and defect state towards the tuning of Ni-Mn-Sn alloys" *Applied Physics Letters* 110 (2017) 181908.

- J. López-García, I. Unzueta, V. Sánchez-Alarcos, V. Recarte, J. I. Pérez-Landazábal, J.A. Rodríguez-Velamazán, J. A. García, F. Plazaola, "Correlation between defects and magneto-structural properties in Ni-Mn-Sn metamagnetic shape memory alloys" *Intermetallics* 94 (2018) 133-137.

- I. Unzueta, J. López-García, V. Sánchez-Alarcos, V. Recarte, J. I. Pérez-Landazábal, J. A. Rodríguez-Velamazán, J. S. Garitaonandia, J. A. García, F. Plazaola, "^{119}Sn Mösbauer spectroscopy in the study of metamagnetic shape memory alloys" *Hyperfine Interactions* 239 (2018) 34.

- V. Sánchez-Alarcos, J. López-García, I. Unzueta, J. I. Pérez-Landazábal, V. Recarte, J. J. Beato-López, J. A. García, F. Plazaola, J. A. Rodríguez-Velamazán, "Magnetocaloric effect enhancement dirven by intrinsic defects in a $Ni_{45}Co_5Mn_{35}Sn_{15}$ alloy" *Journal of Alloys and Compounds* 774 (2019) 586-592.

- J. López-García, V. Sánchez-Alarcos, V. Recarte, J. I. Pérez-Landazábal, O. Fabelo, E. Cesari, J. A. Rodríguez-Velamazán, "Routes for enhanced magnetism in Ni-Mn-In metamagnetic shape memory alloys" *Scripta Materialia* 167 (2019) 21-25.